

MEMOIRS
OF THE
FACULTY OF ENGINEERING
OSAKA CITY UNIVERSITY

VOL. 52

DECEMBER 2011

PUBLISHED BY THE
GRADUATE SCHOOL OF ENGINEERING
OSAKA CITY UNIVERSITY

This Memoirs is annually issued. Selected original works of the members of the Faculty of Engineering are compiled herein. Abstracts of paper presented elsewhere during the current year are also compiled in the latter part of the volume.

All communications with respect to Memoirs should be addressed to:

Dean of the Graduate School of Engineering
Osaka City University
3-3-138, Sugimoto, Sumiyoshi-ku
Osaka 558-8585, Japan

Editors

Kenji KATOH

Ayumu SUGITA

Daisuke MIYAZAKI

Hideki AZUMA

Tatsuhiko KIUCHI

Minako NABESHIMA

MEMOIRS OF THE FACULTY OF ENGINEERING
OSAKA CITY UNIVERSITY

VOL. 52

DECEMBER 2011

CONTENTS

Regular Articles 1

Mechanical and Physical Engineering

Applied Mathematics

Energy Estimates for Regularly Hyperbolic Operators with Non-classical Symbols
Shigeo TARAMA 1

Physical Electronics and Informatics

Information and Communication Engineering

An Improved Pedestrian Detection Method for DSS (Driver Supporting System) Using an Attitude Measurement Unit
Yukie HASHIMOTO, THI THI ZIN, Takashi TORIU and Hiromitsu HAMA 15

Urban Engineering

Civil Engineering

A Numerical Model to Simulate the Time Dependent Behavior of Rock
Kenichi NAKAOKA, Koji HATA, Hiroaki KITO and Yujing JIANG 21

Evaluation of the Bolt Axial Force in High Strength Bolted Joints by Using Strain Gauges
Chao PAN, Takashi YAMAGUCHI and Yasuo SUZUKI 37

Finite Element Analysis on the Mechanical Behavior of High Strength Bolted Friction Type Joints Considering Fluctuation of Bolt Axial Forces
Xue PENG and Takashi YAMAGUCHI 43

An Analysis on Influence of Regional and Individual Conditions to Intended Needs and Actual Demands of Bus Service	
<i>Naoki OKAMOTO and Yasuo HINO</i>	49
Waterfront Functions Required from a Ship Transport Perspective	
<i>Yasumasa FUKUSHIMA and Takashi UCHIDA</i>	55
Abstracts of Papers Published in Other Journals	63
<i>Mechanical and Physical Engineering</i>	
<i>Mechanical Engineering</i>	65
<i>Intelligent Materials Engineering</i>	75
<i>Machine Workshop</i>	83
<i>Physical Electronics and Informatics</i>	
<i>Electrical Engineering</i>	85
<i>Applied Physics</i>	87
<i>Information and Communication Engineering</i>	97
<i>Applied Chemistry and Bioengineering</i>	
<i>Applied Chemistry</i>	99
<i>Bioengineering</i>	109
<i>Urban Engineering</i>	
<i>Architecture and Building Engineering</i>	119
<i>Civil Engineering</i>	123
<i>Environmental Urban Engineering</i>	141

MEMOIRS
OF THE
FACULTY OF ENGINEERING
OSAKA CITY UNIVERSITY

VOL. 52

DECEMBER 2011

PUBLISHED BY THE
GRADUATE SCHOOL OF ENGINEERING
OSAKA CITY UNIVERSITY

Energy estimates for regularly hyperbolic operators with non-classical symbols

Shigeo TARAMA*

(Received September 30, 2011)

Synopsis

Energy estimates for regularly hyperbolic operators with $S_{1,2/3}^m$ class symbols are drawn.

KEYWORDS: energy estimates, regularly hyperbolic

1. Introduction

Consider the wave operator with an oscillating coefficient

$$L_\varepsilon u = \partial_t^2 u - a_\varepsilon^2(t) \partial_x^2 u = 0$$

with $a_\varepsilon(t) = a(t/\varepsilon)$. Here $a(t)$ is a positive and periodic smooth function and ε is a small positive parameter. For the standard energy $E(t) = \|u_t\|^2 + \|u_x\|^2$ of a solution u , we have

$$E(t) \leq e^{C\frac{t}{\varepsilon}} E(0).$$

In order to improve the above estimate, we consider the decomposition of $\hat{L}_\varepsilon = \frac{d^2}{dt^2} + a_\varepsilon^2(t)\xi^2$:

$$\left(\frac{d}{dt} \pm ia_\varepsilon(t)\xi + a_0(t) \pm \frac{i}{\xi}a_1(t)\right)\left(\frac{d}{dt} \mp ia_\varepsilon(t)\xi - a_0(t) \mp \frac{i}{\xi}a_1(t)\right) = \hat{L}_\varepsilon + R_\pm(t, \xi) \quad (1)$$

with $a_0(t) = \frac{-a'_\varepsilon(t)}{2a_\varepsilon(t)}$, $a_1(t) = \frac{1}{2a_\varepsilon(t)}(a'_0(t) + a_0(t)^2)$ and

$$R_\pm(t, \xi) = \mp \frac{i}{\xi}(2a_1(t)a_0(t) + a'_1(t)) + \frac{a_1(t)^2}{\xi^2}.$$

Then we see that

$$\hat{u}_\pm = a_\varepsilon^{-1/2}(t)\left(\frac{d}{dt} \mp ia_\varepsilon(t)\xi - a_0(t) \mp \frac{i}{\xi}a_1(t)\right)\hat{u}$$

satisfies

$$\left(\frac{d}{dt} \pm ia_\varepsilon(t)\xi \pm \frac{i}{\xi}a_1(t)\right)\hat{u}_\pm = a_\varepsilon^{-1/2}(t)\hat{L}_\varepsilon\hat{u} + R_\pm(t, \xi)\hat{u}_\pm. \quad (2)$$

We define the energy $e_1(t)$ by

$$e_1(t) = \frac{1}{2}(|\hat{u}_+|^2 + |\hat{u}_-|^2) = \frac{1}{a_\varepsilon}\left(|\frac{d}{dt}\hat{u} - a_0\hat{u}|^2 + |(a_\varepsilon\xi + \frac{a_1}{\xi})\hat{u}|^2\right).$$

Note that

$$|a_0(t)| \leq \frac{C}{\varepsilon}, \quad |a_1(t)| \leq \frac{C}{\varepsilon^2}, \quad \text{and } |R_\pm(t, \xi)| \leq C\left(\frac{1}{|\xi|\varepsilon^3} + \frac{1}{|\xi|^2\varepsilon^4}\right).$$

Then, when $|\xi|\varepsilon$ is large, we see $C^{-1}e_1(t) \leq (|\hat{u}_t|^2 + \xi^2|\hat{u}|^2) \leq Ce_1(t)$ with some $C > 0$. Hence from (2) follows that a solution \hat{u} of $\hat{L}_\varepsilon\hat{u} = 0$ satisfies, when $|\xi|\varepsilon$ is large,

$$\frac{d}{dt}e_1(t) \leq \frac{C}{|\xi|^2\varepsilon^3}e_1(t),$$

*Professor, Laboratory of Applied Mathematics

from which we obtain

$$e_1(t) \leq e^{\frac{Ct}{|\xi|^{2\varepsilon^3}}} e_1(0), \quad (t \geq 0).$$

Hence, the high frequency energy $E_\varepsilon(t) = \int_{|\xi| \geq C\varepsilon^{-3/2}} (|\hat{u}_t|^2 + \xi^2 |\hat{u}|^2) d\xi$ with large C of a solution $L_\varepsilon u = 0$, has the estimate

$$E_\varepsilon(t) \leq C_1 e^{C_2 t} E_\varepsilon(0) \quad (t \geq 0)$$

(see the related results ^{1),2)}).

In order to obtain a similar estimate for the regularly hyperbolic operator

$$P_\varepsilon u = D_t^m u + \sum_{1 \leq j \leq m, |\alpha| \leq j} a_{j,\alpha} \left(\frac{t}{\varepsilon}, \frac{x}{\varepsilon} \right) D_t^{m-j} D_x^\alpha u,$$

we are led to study the property of the operator P_ε in the case where $\varepsilon |\xi|^{2/3}$ is large.

Noting, if $\varepsilon^{-1} \leq C |\xi|^{2/3}$,

$$|\partial_t^k \partial_x^\alpha a_j \left(\frac{t}{\varepsilon}, \frac{x}{\varepsilon} \right)| \leq C_1 \varepsilon^{-(k+|\alpha|)} \leq C_2 |\xi|^{(k+|\alpha|) \frac{2}{3}},$$

we consider, in this paper, the regularly hyperbolic operator P whose symbol $p(t, x, \tau, \xi)$ is given by

$$p(t, x, \tau, \xi) = \tau^m + \sum_{j=1}^m a_j(t, x, \xi) \tau^{m-j}$$

with real $a_j(t, x, \xi)$ satisfying

$$|\partial_t^k \partial_x^\alpha \partial_\xi^\beta a_j(t, x, \xi)| \leq C \langle \xi \rangle^{j-|\beta|+(k+|\alpha|) \frac{2}{3}}$$

that is, a_j in $S_{1,2/3}^j$ where

$$\langle \xi \rangle = (1 + |\xi|^2)^{1/2}.$$

More precisely, for given $T > 0$, we denote by $S_{\rho,\delta}^k([0, T])$ the set of symbols $a(t, x, \xi) \in C^\infty([0, T] \times \mathbb{R}^n \times \mathbb{R}^n)$ satisfying for any non-negative integer l and any multi-index $\alpha, \beta \in \mathbb{N}^n$, where $\mathbb{N} = \{0, 1, 2, \dots\}$,

$$|\partial_t^l \partial_x^\alpha \partial_\xi^\beta a(t, x, \xi)| \leq C_{l,\alpha,\beta} \langle \xi \rangle^{k-\rho|\beta|+\delta(l+|\alpha|)}$$

on $[0, T] \times \mathbb{R}^n \times \mathbb{R}^n$.

Let P be an operator on $[0, T] \times \mathbb{R}^n$:

$$Pu = D_t^m u + \sum_{j=1}^m A_j(t, x, D_x) D_t^{m-j} u$$

whose symbol $p(t, x, \tau, \xi) = \tau^m + \sum_{j=1}^m a_j(t, x, \xi) \tau^{m-j}$ with real symbols $a_j(t, x, \xi) \in S_{1,2/3}^j([0, T])$ has a factorization : if $|\xi| \geq R_0$ with some $R_0 > 0$,

$$p(t, x, \tau, \xi) = \prod_{j=1}^m (\tau - \lambda_j(t, x, \xi)) \quad (3)$$

with real $\lambda_j(t, x, \xi)$ satisfying, with some $\delta > 0$,

$$|\lambda_j(t, x, \xi) - \lambda_k(t, x, \xi)| \geq \delta \langle \xi \rangle \quad (t, x, \xi) \in [0, T] \times \mathbb{R}^n \times \mathbb{R}^n \text{ with } |\xi| \geq R_0 \quad (4)$$

for any $j, k \in I$ with $j \neq k$.

Here $I = \{1, 2, \dots, m\}$ and $D_t = \frac{1}{i} \partial_t$. For a symbol $a(t, x, \xi) \in S_{1,2/3}^j([0, T])$, we define the operator $A(t, x, D_x)$ by

$$A(t, x, D_x)u = \frac{1}{(2\pi)^n} \int e^{i(x-y)\xi} a(t, x, \xi) u(y) dy d\xi$$

and for $q(t, x, \tau, \xi) = \sum_{j=0}^l a_j(t, x, \xi) \tau^{l-j}$

$$Q(t, x, D_t, D_x) = \sum_{j=0}^l A_j(t, x, D_x) D_t^{l-j}.$$

We show the following energy estimate for P .

Theorem 1. *We assume that the operator P satisfies the above mentioned conditions (3) and (4). Then we have the following:*

$$\sum_{j=0}^{m-1} \sum_{|\alpha| \leq m-1-j} \|D_t^j D_x^\alpha u(t, \cdot)\|_{-(m-1)/2} \leq C \left(\sum_{j=0}^{m-1} \sum_{|\alpha| \leq m-1-j} \|D_t^j D_x^\alpha u(0, \cdot)\|_{-(m-1)/2} + \int_0^t \|(P + P_{sb})u(s, \cdot)\|_{-(m-1)/2} ds \right) \quad (5)$$

for any $u(t, x) \in C^\infty([0, T] \times \mathbb{R}^n)$ that is rapidly decreasing with respect to x , where P_{sb} is the operator whose symbol $p_{sb}(t, x, \tau, \xi)$ is given by $p_{sb}(t, x, \tau, \xi) = \frac{1}{2i} \sum_{\mu=0}^n \partial_{x_\mu} \partial_{\xi_\mu} p(t, x, \tau, \xi)$ with $x_0 = t, \xi_0 = \tau$.

Here $D_{x_j} = \frac{1}{i} \partial_{x_j}$ and $D_x^\alpha = D_{x_1}^{\alpha_1} \dots D_{x_n}^{\alpha_n}$. The norm $\|\cdot\|_\sigma$ stands for the standard Sobolev norm given by $\|u(\cdot)\|_\sigma^2 = \int (1 + |\xi|^2)^\sigma |\hat{u}(\xi)|^2 d\xi$ with the Fourier transform $\hat{u}(\xi)$ of $u(x)$.

Remark 1. The differential operator whose principal symbol has only real roots satisfying (3) and (4) is called the regularly hyperbolic operator.

Remark 2. We remark that the above estimate (5) does not necessarily imply the wellposedness of the Cauchy problem for $P + P_{sb}$. The application of the above estimate to the operator with oscillating coefficients will be discussed in a forthcoming paper.

If $m = 1$, Theorem 1 is evident. We assume $m \geq 2$ from now on. In order to draw the estimate (5), we use the decomposition of P similar to (1). For the simplicity of expression, we use the Weyl calculus of pseudodifferential operators. For the properties of such calculus, refer to the section 14 in Chapter 7 of Taylor's book³⁾. For symbols $a(t, x, \xi)$ and $q = \sum_{j=1}^l a_j(t, x, \xi) \tau^{l-j}$, we define operators A^w and Q^w by

$$A^w(t, x, D_x)u = \frac{1}{(2\pi)^n} \int e^{i(x-y)\xi} a(t, \frac{x+y}{2}, \xi) u(y) dy d\xi \quad (6)$$

and

$$Q^w(t, x, D_t, D_x)u = \sum_{j=0}^l \frac{1}{(2\pi)^{n+1}} \int e^{i((t-s)\tau + (x-y)\xi)} a_j(\frac{t+s}{2}, \frac{x+y}{2}, \xi) \tau^{l-j} u(s, y) ds dy d\tau d\xi$$

with some appropriately extended $a_j(t, x, \xi)$ on $\mathbb{R} \times \mathbb{R}^n \times \mathbb{R}^n$. The same operator $Q^w(t, x, D_t, D_x)$ can also be given by

$$Q^w(t, x, D_t, D_x)u = \sum_{j=0}^l D_s^{l-j} (A_j^w(\frac{t+s}{2}, x, D_x)u(s, x))|_{s=t}. \quad (7)$$

For the proof of Theorem 1 we use the following.

Proposition 2. Let $p(t, x, \tau, \xi) = \tau^m + \sum_{j=1}^m a_j(t, x, \xi)\tau^{m-j}$ with real $a_j(t, x, \xi) \in S_{1,2/3}^j([0, T])$. Suppose that we have

$$p(t, x, \tau, \xi) = \prod_{j=1}^m (\tau - \lambda_j(t, x, \xi))$$

with real $\lambda_j(t, x, \xi) \in S_{1,2/3}^1([0, T])$ satisfying, with some $\delta > 0$,

$$|\lambda_j(t, x, \xi) - \lambda_k(t, x, \xi)| \geq \delta \langle \xi \rangle \quad (t, x, \xi) \in [0, T] \times \mathbb{R}^n \times \mathbb{R}^n \quad (8)$$

for any $j, k \in I$ with $j \neq k$. Then we have the following:

$$\sum_{j=0}^{m-1} \sum_{|\alpha| \leq m-1-j} \|D_t^j D_x^\alpha u(t, \cdot)\|_{-(m-1)/2} \leq C \left(\sum_{j=0}^{m-1} \sum_{|\alpha| \leq m-1-j} \|D_t^j D_x^\alpha u(0, \cdot)\|_{-(m-1)/2}^2 + \int_0^t \|P^w u(s, \cdot)\|_{-(m-1)/2} ds \right) \quad (9)$$

for any $u(t, x) \in C^\infty([0, T] \times \mathbb{R}^n)$ that is rapidly decreasing with respect to x .

In order to see that Proposition 2 implies Theorem 1, first we remark that an operator $A^w(t, x, D_x)$ with $a(t, x, \xi) \in S_{1,2/3}^s([0, T])$ has the order s , that is, we have $\|Au\|_\sigma \leq C\|u\|_{\sigma+s}$ (see Proposition 5.5 and the section 14 in Chapter 7 in Taylor's book³⁾) and that, for an operator $Q^w(t, x, D_t, D_x)$ with the symbol $q(t, x, \tau, \xi) = \sum_{j=0}^k a_j(t, x, \xi)\tau^{k-j}$ with $a_j(t, x, \xi) \in S_{1,2/3}^{s-k+j}([0, T])$, we have $\|Q(t, x, D_t, D_x)u\|_\sigma \leq C \sum_{j=0}^k \|D_t^{k-j} u\|_{j-k+s+\sigma}$ (see (7)).

Suppose that p satisfies the assumptions of Theorem 1. Set $q = \frac{-1}{8} \sum_{\mu, \nu=0}^n \partial_{\xi_\mu} \partial_{\xi_\nu} \partial_{x_\mu} \partial_{x_\nu} p$. Then we see that $q = \sum_{j=1}^m b_j(t, x, \xi)\tau^{m-j}$ with real symbols $b_j(t, x, \xi) \in S_{1,2/3}^{j-2/3}([0, T])$ and we have

$$\|P^w(t, x, D_t, D_x)u - (P + P_{sb} + Q)u\|_{-(m-1)/2} \leq C \sum_{j=0}^{m-1} \|D_t^j u\|_{m-j-1-(m-1)/2}. \quad (10)$$

Noting

$$\|Q^w u - Qu\|_{-(m-1)/2} \leq C \sum_{j=0}^{m-1} \|D_t^j u\|_{m-j-1-(m-1)/2}, \quad (11)$$

we have

$$\|(P^w - Q^w)u - (Pu + P_{sb}u)\|_{-(m-1)/2} \leq C \sum_{j=0}^{m-1} \|D_t^j u\|_{m-j-1-(m-1)/2}.$$

See (14.8) on page 60 in Taylor's book³⁾ for the above two claims (10) and (11).

On the other hand, $p - q = \tau^m + \sum_{j=1}^m (a_j(t, x, \xi) - b_j(t, x, \xi))\tau^{m-j}$ has the factorization : when $|\xi|$ is large,

$$p - q = \prod (\tau - \tilde{\lambda}_j(t, x, \xi))$$

with real $\tilde{\lambda}_j(t, x, \xi)$ satisfying, with some $R_1 > 0$ and $\delta > 0$,

$$|\tilde{\lambda}_j(t, x, \xi) - \tilde{\lambda}_k(t, x, \xi)| \geq \delta \langle \xi \rangle \quad (t, x, \xi) \in [0, T] \times \mathbb{R}^n \times \mathbb{R}^n \text{ with } |\xi| \geq R_1$$

for any $j, k \in I$ with $j \neq k$. See the appendix for the proof of this claim.

The above $\tilde{\lambda}_j(t, x, \xi)$ ($j = 1, \dots, m$) can be extended as a real symbol in $S_{1,2/3}^1([0, T])$ satisfying (8). See the appendix for the proof of this claim. Using the extended $\tilde{\lambda}_j(t, x, \xi)$ ($j = 1, \dots, m$), we set $\tilde{p}(t, x, \tau, \xi) = \prod_{j=1}^m (\tau - \tilde{\lambda}_j(t, x, \xi))$. Then $\tilde{p} = p - q$ when $|\xi|$ is large. Hence we have

$$\|\tilde{P}^w u - (Pu + P_{sb}u)\|_{-(m-1)/2} \leq C \sum_{j=0}^{m-1} \|D_t^j u\|_{m-1-j-(m-1)/2}.$$

While, applying Proposition 2 to $\tilde{p}(t, x, \tau, \xi)$, we obtain

$$\begin{aligned} & \sum_{j=0}^{m-1} \sum_{|\alpha| \leq m-1-j} \|D_t^j D_x^\alpha u(t, \cdot)\|_{-(m-1)/2} \leq \\ & C \left(\sum_{j=0}^{m-1} \sum_{|\alpha| \leq m-1-j} \|D_t^j D_x^\alpha u(0, \cdot)\|_{-(m-1)/2} + \int_0^t \|\tilde{P}^w u(s, \cdot)\|_{-(m-1)/2} ds \right). \end{aligned}$$

Then, noting that $\sum_{|\alpha| \leq m-1-j} \|D_x^\alpha u\|_\sigma$ is equivalent to $\|u\|_{m-1-j+\sigma}$, we have

$$\begin{aligned} & \sum_{j=0}^{m-1} \sum_{|\alpha| \leq m-1-j} \|D_t^j D_x^\alpha u(t, \cdot)\|_{-(m-1)/2} \leq \\ & C \left(\sum_{j=0}^{m-1} \sum_{|\alpha| \leq m-1-j} \|D_t^j D_x^\alpha u(0, \cdot)\|_{-(m-1)/2} \right. \\ & \left. + \int_0^t (\|Pu(s, x) + P_{sb}u(s, \cdot)\|_{-(m-1)/2} + \sum_{j=0}^{m-1} \sum_{|\alpha| \leq m-1-j} \|D_t^j D_x^\alpha u(s, \cdot)\|_{-(m-1)/2}) ds \right). \end{aligned}$$

Then, by Gronwall's inequality we obtain the estimate (5). Hence Proposition 2 implies Theorem 1.

In the next section, we prove Proposition 2 by using the decomposition of P^w given in Proposition 3 that is proved in the section 3.

We denote by $L(k, s)$ with a non-negative integer k and a real s , the set of symbols $q(t, x, \tau, \xi) = \sum_{j=0}^k a_j(t, x, \xi) \tau^{k-j}$ with $a_j(t, x, \xi) \in S_{1,2/3}^{j-k+s}([0, T])$. $L(0, s) = S_{1,2/3}^s([0, T])$. For operators Q and R , we write $Q = R \pmod{L(k, s)}$ when $Q - R$ can be given by $V^w(t, x, D_t, D_x)$ with some $v(t, x, \tau, \xi) \in L(k, s)$. While, for an operator Q , $Q \in S_{1,2/3}^k([0, T])$ means that Q can be given by $Q = A^w$ with $a(t, x, \xi) \in S_{1,2/3}^k([0, T])$.

For the operator $Q^w(t, x, D_t, D_x)$ whose symbol is $q(t, x, \tau, \xi) = \sum_{j=0}^k a_j(t, x, \xi) \tau^{k-j} \in L(k, s)$, the expression (7) implies that there exist $b_j(t, x, \xi) \in S_{1,2/3}^{j-k+s}([0, T])$ such that $b_j(t, x, \xi) - a_j(t, x, \xi) \in S_{1,2/3}^{j-1/3-k+s}([0, T])$ and

$$Q^w(t, x, D_t, D_x)u = \sum_{j=0}^k B_j^w(t, x, D_x) D_t^{k-j} u.$$

We recall some properties of the Weyl calculus. See (14.24) on page 62 in Taylor's book³. We define the Poisson bracket $\{q, r\}$ of $q(t, x, \tau, \xi) \in L(k, s_1)$ and $r(t, x, \tau, \xi) \in L(l, s_2)$, by

$$\{q, r\} = \sum_{\mu=0}^n (\partial_{\xi_\mu} q \partial_{x_\mu} r - \partial_{x_\mu} q \partial_{\xi_\mu} r),$$

and $(q, r)_2$ by

$$(q, r)_2 = \frac{-1}{4} \sum_{\mu, \nu=0}^n (q^{(\mu, \nu)} r_{(\mu, \nu)} + q_{(\mu, \nu)} r^{(\mu, \nu)} - 2q_{(\mu)}^{(\nu)} r_{(\nu)}^{(\mu)}) \quad (12)$$

where $q^{(\mu,\nu)} = \partial_{\xi_\mu} \partial_{\xi_\nu} q$, $q_{(\mu,\nu)} = \partial_{x_\mu} \partial_{x_\nu} q$ and $q_{(\mu)}^{(\nu)} = \partial_{x_\mu} \partial_{\xi_\nu} q$ with $x_0 = t$ and $\xi_0 = \tau$. We use also the notation $q^{(\mu)} = \partial_{\xi_\mu} q$, $q_{(\mu)} = \partial_{x_\mu} q$.

Here we note $\{q, r\} = -\{r, q\}$ and $(q, r)_2 = (r, q)_2$.

We set

$$d_0 = qr, \quad d_1 = \frac{1}{2i} \{q, r\}, \quad d_2 = \frac{1}{2} (q, r)_2.$$

We remark that $d_j \in L(k+l, s_1+s_2-j/3)$ ($j=0, 1, 2$). We have, for $j_0=0, 1, 2$,

$$Q^w R^w = \sum_{j=0}^{j_0} D_j^w \pmod{L(k+l, s_1+s_2-(j_0+1)/3)} \quad (13)$$

and

$$Q^w R^w - R^w Q^w = 2D_1^w \pmod{L(k+l, s_1+s_2-1)}$$

Furthermore when $q(t, x, \tau, \xi) - \tau^k \in L(k-1, s_1)$ or $r(t, x, \tau, \xi) - \tau^l \in L(l-1, s_2)$, we have for $j_0=0, 1, 2$,

$$Q^w R^w = \sum_{j=0}^{j_0} D_j^w \pmod{L(k+l-1, s_1+s_2-(j_0+1)/3)} \quad (14)$$

and

$$Q^w R^w - R^w Q^w = 2D_1^w \pmod{L(k+l-1, s_1+s_2-1)} \quad (15)$$

In the following we use the following notations. We denote the inner product in the space of square integrable functions on \mathbb{R}^n , by (\cdot, \cdot) , that is,

$$(v, w) = \int_{\mathbb{R}^n} v(x) \overline{w(x)} dx$$

and its norm by $\|v(\cdot)\| = (v, v)^{1/2}$.

We use C or C with some suffix in order to denote a positive constant which may be different line by line.

2. Proof of Proposition 2.

In this section, because we use only the Weyl calculus, the operator define by (6) or (7) is denoted by A or Q instead of A^w or Q^w .

Suppose that the assumption of Proposition 2 is fulfilled. Recall $I = \{1, 2, \dots, m\}$. For $j \in I$ we set

$$p_j(t, x, \tau, \xi) = \sum_{k \in I \setminus \{j\}} (\tau - \lambda_k(t, x, \tau, \xi)).$$

We have the following.

Proposition 3. *We set, for $j \in I$,*

$$e_j^0(t, x, \xi) = \sum_{k \in I \setminus \{j\}} \frac{-1}{2i} \frac{\{\tau - \lambda_j, \tau - \lambda_k\}}{\lambda_j - \lambda_k}.$$

There exist a real symbol $e_j^1(t, x, \xi) \in S_{1,2/3}^{1/3}([0, T])$ and a symbol $r_j(t, x, \tau, \xi) \in L(m-1, m-1/3)$ such that

$$(D_t - \Lambda_j + E_j^0 + E_j^1)(P_j + R_j) - P \in L(m-1, m-1). \quad (16)$$

For the moment admitting the validity of the above proposition, we draw the estimates (9). In the following, we denote by u a C^∞ function on $[0, T] \times \mathbb{R}^n$, which is rapidly decreasing with respect to x .

Set

$$w_j(t, x, \xi) = \prod_{k \in I \setminus \{j\}} |\lambda_j - \lambda_k|^{-1/2}.$$

We see from (8) that $w_j \in S_{1,2/3}^{-(m-1)/2}([0, T])$ and $w_j(t, x, \xi) \geq C(1 + |\xi|)^{-(m-1)/2}$. We have

$$\{\tau - \lambda_j, w_j\} = w_j \left(- \sum_{k \in I \setminus \{j\}} \frac{1}{2(\lambda_j(t, x, \xi) - \lambda_k(t, x, \xi))} \{\tau - \lambda_j, \lambda_j - \lambda_k\} \right).$$

Then $\frac{1}{i} \{\tau - \lambda_j, w_j\} = w_j e_j^0$. Setting $g = w_j e_j^0$, we get from (15)

$$(D_t - \Lambda_j)W_j - W_j(D_t - \Lambda_j) = G \pmod{S_{1,2/3}^{-(m-1)/2}}.$$

While with $\tilde{e}_j^1 \in S_{1,2/3}^{1/3}$ given by $\tilde{e}_j^1 = -\frac{1}{2i} \{w_j, e_j^0\} / w_j$ which is real-valued, we have

$$W_j E_j^0 = G - \tilde{E}_j^1 W_j \pmod{S_{1,2/3}^{-(m-1)/2}([0, T])}.$$

Then we have

$$(D_t - \Lambda_j)W_j - W_j(D_t - \Lambda_j) - W_j E_j^0 - \tilde{E}_j^1 W_j \in S_{1,2/3}^{-(m-1)/2},$$

which and $E_j^1 W_j = W_j E_j^1 \pmod{S_{1,2/3}^{-(m-1)/2}([0, T])}$, where $e_j^1 \in S_{1,2/3}^{1/3}([0, T])$, imply that

$$W_j(D_t - \Lambda_j + E_j^0 + E_j^1) - (D_t - \Lambda_j + E_j^1 + \tilde{E}_j^1)W_j \in S_{1,2/3}^{-(m-1)/2}. \quad (17)$$

Then we see from (16) and (17) that there exists $v_j(t, x, \tau, \xi) \in L(m-1, (m-1)/2)$ such that

$$(D_t - \Lambda_j + E_j^1 + \tilde{E}_j^1)W_j(P_j + R_j) = W_j P + V_j. \quad (18)$$

Since $-\lambda_j(t, x, \xi) + e_j^1(t, x, \xi) + \tilde{e}_j^1(t, x, \xi)$ is real-valued, then $-\Lambda_j(t, x, D_x) + E_j^1(t, x, D_x) + \tilde{E}_j^1(t, x, D_x)$ is formally selfadjoint with respect to the inner product (u, v) . Then we see that

$$\frac{d}{dt} \|u\|^2 = 2\Re(iD_t u(t, \cdot), u(t, \cdot)) = 2\Re(i(D_t - \Lambda_j + E_j^1 + \tilde{E}_j^1)u(t, \cdot), u(t, \cdot)).$$

Hence $\frac{d}{dt} \|W_j u\|^2 = 2\Re(i(D_t - \Lambda_j + E_j^1 + \tilde{E}_j^1)W_j u(t, \cdot), W_j u(t, \cdot))$. Then

$$\frac{d}{dt} \|W_j u\|^2 \leq 2\|(D_t - \Lambda_j + E_j^1 + \tilde{E}_j^1)W_j u\| \|W_j u\|.$$

Therefore, noting $w_j \in S_{1,2/3}^{-(m-1)/2}([0, T])$, we obtain from (18)

$$\frac{d}{dt} \|W_j(P_j + R_j)u\|^2 \leq C(\|Pu\|_{-(m-1)/2} + \sum_{k=0}^{m-1} \|D_t^k u\|_{-k+(m-1)/2}) \|W_j(P_j + R_j)u\|,$$

from which we obtain

$$\begin{aligned} \|W_j(P_j + R_j)u(t, \cdot)\| &\leq \|W_j(P_j + R_j)u(0, \cdot)\| \\ &\quad + C \int_0^t (\|Pu(s, \cdot)\|_{-(m-1)/2} + \sum_{k=0}^{m-1} \|D_t^k u(s, \cdot)\|_{-k+(m-1)/2}) ds. \end{aligned}$$

See for example Lemma 23.1.1 in the book of Hörmander⁴).

Since $w_j \in S_{1,2/3}^{-(m-1)/2}([0, T])$ and $w_j \geq C(1 + |\xi|)^{-(m-1)/2}$, we have $\|u\|_{-(m-1)/2} \leq C(\|W_j u\| + \|u\|_{-(m-1)/2-1})$. Hence we see

$$\begin{aligned} \|(P_j + R_j)u(t, \cdot)\|_{-(m-1)/2} &\leq C \left(\sum_{k=0}^{m-1} \|D_t^k u(t, \cdot)\|_{-k+(m-1)/2-1} \right. \\ &\quad + \sum_{k=0}^{m-1} \|D_t^k u(0, \cdot)\|_{-k+(m-1)/2} \\ &\quad \left. + \int_0^t (\|Pu(s, \cdot)\|_{-(m-1)/2} + \sum_{k=0}^{m-1} \|D_t^k u(s, \cdot)\|_{-k+(m-1)/2}) ds. \right. \end{aligned} \quad (19)$$

Now we draw the estimate of the norm of $D_t^k u$ from the estimate of $\|(P_j + R_j)u\|_{-(m-1)/2}$ ($j = 1, \dots, m$). First we note that $r_j \in L(m-2, m-1-1/3)$ implies that

$$\|R_j u\|_{-(m-1)/2} \leq C \sum_{k=0}^{m-2} \|D_t^k u\|_{-k+(m-1)/2-1/3} \quad (20)$$

Note that we have

$$p_j(t, x, \tau, \xi) = \tau^{m-1} + \sum_{k=2}^m a_{jk}(t, x, \xi) \tau^{m-k} \langle \xi \rangle^{k-1}$$

with $a_{jk}(t, x, \xi) \in S_{1,2/3}^0([0, T])$.

Let A be a m by m matrix whose (j, k) element is $a_{jk}(t, x, \xi)$. Here we set $a_{j1}(t, x, \xi) = 1$. We remark that

$$p_j(t, x, \tau, \xi) / \langle \xi \rangle^{m-1} = \sum_{k=1}^m a_{jk}(t, x, \xi) \left(\frac{\tau}{\langle \xi \rangle} \right)^{m-k}$$

Then we have $|\det A| \geq C$ with $C > 0$. Indeed, since

$$p_j(t, x, \lambda_l(t, x, \xi), \xi) = \begin{cases} \prod_{k \in I \setminus \{j\}} (\lambda_j(t, x, \xi) - \lambda_k(t, x, \xi)) & l = j \\ 0 & \text{otherwise,} \end{cases}$$

and

$$p_j(t, x, \lambda_l(t, x, \xi), \xi) / \langle \xi \rangle^{m-1} = \sum_{k=1}^m a_{jk}(t, x, \xi) \left(\frac{\lambda_l(t, x, \xi)}{\langle \xi \rangle} \right)^{m-k},$$

then we obtain the desired estimate $|\det A| \geq C$ from (8) and the Vandermonde determinant.

Hence each element of A^{-1} belongs to $S_{1,2/3}^0([0, T])$. Then there exists an m by m matrix $L \in S_{1,2/3}^0([0, T])$ satisfying $L(t, x, D_x)A(t, x, D_x) - I \in S_{1,2/3}^{-1}([0, T])$. Noting that

$$\|P_j u - \sum_{k=1}^m A_{jk}(t, x, D_x) D_t^{m-k} \langle D_x \rangle^{k-1} u\|_{-(m-1)/2} \leq C \sum_{l=0}^{m-2} \|D_t^l u\|_{-l+(m-1)/2-1/3},$$

we see that, for $k \in I$,

$$\left\| \sum_{j=1}^m L_{kj}(t, x, D_x) P_j u - D_t^{m-k} \langle D_x \rangle^{k-1} u \right\|_{-(m-1)/2} \leq C \sum_{l=0}^{m-1} \|D_t^l u\|_{-l+(m-1)/2-1/3},$$

where L_{kl} is the (k, j) element of the L . Then we obtain from the above estimate and (20)

$$\sum_{k=0}^{m-1} \|D_t^{m-1-k} u(t, \cdot)\|_{k-(m-1)/2} \leq C \left(\sum_{j=1}^m \|(P_j + R_j)u\|_{-(m-1)/2} + \sum_{k=0}^{m-1} \|D_t^k u(t, \cdot)\|_{-k+(m-1)/2-1} \right). \quad (21)$$

Here we used the property of Sobolev norm: $\|u\|_{\sigma-1/3} \leq \varepsilon \|u\|_{\sigma} + C_{\varepsilon} \|u\|_{\sigma-1}$ for any $\varepsilon > 0$ with some C_{ε} .

It follows from (19) and (21)

$$\begin{aligned} \sum_{k=0}^{m-1} \|D_t^k u(t, \cdot)\|_{-k+(m-1)/2} &\leq C \left(\sum_{k=0}^{m-1} \|D_t^k u(t, \cdot)\|_{-k+(m-1)/2-1} + \sum_{k=0}^{m-1} \|D_t u(0, \cdot)\|_{-k+(m-1)/2} \right. \\ &\quad \left. + \int_0^t (\|Pu(s, \cdot)\|_{-(m-1)/2} + \sum_{k=0}^{m-1} \|D_t^k u(s, \cdot)\|_{-k+(m-1)/2}) ds \right). \quad (22) \end{aligned}$$

Note that for $0 \leq k \leq m-2$

$$\frac{d}{dt} \|D_t^k u(t, \cdot)\|_{-k+(m-1)/2-1}^2 \leq 2 \|D_t^k u(t, \cdot)\|_{-k+(m-1)/2-1} \|D_t^{k+1} u(t, \cdot)\|_{-k+(m-1)/2-1}.$$

and

$$\begin{aligned} \frac{d}{dt} \|D_t^{m-1} u(t, \cdot)\|_{-(m-1)/2-1}^2 \\ \leq 2 \|D_t^{m-1} u(t, \cdot)\|_{-(m-1)/2-1} (\|Pu(t, \cdot)\|_{-(m-1)/2-1} + \sum_{k=0}^{m-1} \|D_t^k u(t, \cdot)\|_{(m-k-(m-1)/2-1)}). \quad (23) \end{aligned}$$

Then we have

$$\begin{aligned} \frac{d}{dt} \left(\sum_{k=0}^{m-1} \|D_t^k u(t, \cdot)\|_{-k+(m-1)/2-1}^2 \right) \\ \leq C (\|Pu\|_{-(m-1)/2-1} + \sum_{k=0}^{m-1} \|D_t^k u(t, \cdot)\|_{-k+(m-1)/2}) \left(\sum_{k=0}^{m-1} \|D_t^k u(t, \cdot)\|_{k-(m-1)/2-1}^2 \right)^{1/2}, \end{aligned}$$

from which we obtain

$$\begin{aligned} \sum_{k=0}^{m-1} \|D_t^k u(t, \cdot)\|_{-k+(m-1)/2-1} &\leq C \left(\sum_{k=0}^{m-1} \|D_t^k u(0, \cdot)\|_{-k+(m-1)/2-1} \right. \\ &\quad \left. + \int_0^t (\|Pu(s, \cdot)\|_{-(m-1)/2-1} + \sum_{k=0}^{m-1} \|D_t^k u(s, \cdot)\|_{-k+(m-1)/2}) ds \right). \end{aligned}$$

Hence from the above estimate and (22), we obtain

$$\begin{aligned} \sum_{k=0}^{m-1} \|D_t^k u(t, \cdot)\|_{-k+(m-1)/2} &\leq C \left(\sum_{k=0}^{m-1} \|D_t^k u(0, \cdot)\|_{-k+(m-1)/2} \right. \\ &\quad \left. + \int_0^t (\|Pu(s, \cdot)\|_{-(m-1)/2} + \sum_{k=0}^{m-1} \|D_t^k u(s, \cdot)\|_{-k+(m-1)/2}) ds \right). \quad (24) \end{aligned}$$

Then we obtain from (24) the desired estimate (9), by using Gronwall's inequality.

3. Proof of Proposition 3.

In this section also, we use only the Weyl calculus. Then the operator define by (6) or (7) is denoted by A or Q instead of A^w or Q^w .

First we show two lemmas on symbols.

Recall $I = \{1, 2, \dots, m\}$. For $j, k \in I$ with $j \neq k$, we set

$$p_j = \prod_{l \in I \setminus \{j\}} (\tau - \lambda_l(t, x, \xi)), \quad p_{kj} = \prod_{l \in I \setminus \{k, j\}} (\tau - \lambda_l(t, x, \xi)).$$

When $m = 2$, we set $p_{jk} = 1$.

Lemma 4. For $j \in I$, we set

$$a_j^0 = - \sum_{k \in I \setminus \{j\}} \frac{1}{2i} \frac{\{\tau - \lambda_j, \lambda_k - \lambda_j\}}{\lambda_k - \lambda_j}$$

and for $k \in I \setminus \{j\}$,

$$b_{jk}^0 = \frac{1}{2i} \frac{\{\tau - \lambda_j, \lambda_k - \lambda_j\}}{\lambda_k - \lambda_j}.$$

We set also

$$r_j^0 = \sum_{k \in I \setminus \{j\}} b_{jk} p_{jk}.$$

Then we have

$$\frac{1}{2i} \{\tau - \lambda_j, p_j\} + a_j^0 p_j + (\tau - \lambda_j) r_j^0 = 0.$$

Proof. Indeed, by the definition of the Poisson bracket, we see that $\{\tau - \lambda_j, p_j\} = \sum_{k \in I \setminus \{j\}} \{\tau - \lambda_j, \tau - \lambda_k\} p_{jk}$. Since $1 = \frac{(\tau - \lambda_j) - (\tau - \lambda_k)}{\lambda_k - \lambda_j}$, noting $(\tau - \lambda_j) p_{jk} = p_k$ and $(\tau - \lambda_k) p_{jk} = p_j$, we get

$$p_{jk} = \frac{p_k - p_j}{\lambda_k - \lambda_j}. \quad (25)$$

Since $\{\tau - \lambda_j, \tau - \lambda_j\} = 0$ and $(\tau - \lambda_k) - (\tau - \lambda_j) = \lambda_j - \lambda_k$, we see that $\{\tau - \lambda_j, \tau - \lambda_k\} = \{\tau - \lambda_j, \lambda_j - \lambda_k\}$. Hence

$$\{\tau - \lambda_j, p_j\} = \sum_{k \in I \setminus \{j\}} \{\tau - \lambda_j, \lambda_j - \lambda_k\} \frac{p_k - p_j}{\lambda_k - \lambda_j}.$$

Then, noting $(\tau - \lambda_j) p_{jk} = p_k$, we obtain

$$\frac{1}{2i} \{\tau - \lambda_j, p_j\} + a_j^0 p_j + (\tau - \lambda_j) r_j^0 = 0. \quad \square$$

Lemma 5. There exist real symbols $a_j^{1,h}, b_{jk}^{1,h} \in S_{1,2/3}^{1/3}([0, T])$ ($h = 1, 2, 3, 4$) such that

$$(\tau - \lambda_j, p_j)_2 = a_j^{1,1} p_j + \sum_{k \in I \setminus \{j\}} b_{jk}^{1,1} p_k \quad (26)$$

$$\frac{1}{2i} \{a_j^0, p_j\} = a_j^{1,2} p_j + \sum_{k \in I \setminus \{j\}} b_{jk}^{1,2} p_k \quad (27)$$

$$\frac{1}{2i} \{\tau - \lambda_j, r_j^0\} = a_j^{1,3} p_j + \sum_{k \in I \setminus \{j\}} b_{jk}^{1,3} p_k \quad (28)$$

$$a_j^0 r_j^0 = a_j^{1,4} p_j + \sum_{k \in I \setminus \{j\}} b_{jk}^{1,4} p_k \quad (29)$$

where a_j^0 and r_j^0 are symbols defined in Lemma 4.

Proof. For three distinct elements j, k, l in I , we set

$$p_{jkl} = \prod_{h \in I \setminus \{j, k, l\}} (\tau - \lambda_h).$$

When $m = 3$, we set $p_{jkl} = 1$.

Lagrange's interpolation formula implies that, for three distinct elements $j, k, l \in I$,

$$1 = \frac{(\tau - \lambda_j)(\tau - \lambda_k)}{(\lambda_l - \lambda_j)(\lambda_l - \lambda_k)} + \frac{(\tau - \lambda_k)(\tau - \lambda_l)}{(\lambda_j - \lambda_k)(\lambda_j - \lambda_l)} + \frac{(\tau - \lambda_l)(\tau - \lambda_j)}{(\lambda_k - \lambda_l)(\lambda_k - \lambda_j)}$$

Then we have

$$p_{jkl} = \frac{p_l}{(\lambda_l - \lambda_j)(\lambda_l - \lambda_k)} + \frac{p_j}{(\lambda_j - \lambda_k)(\lambda_j - \lambda_l)} + \frac{p_k}{(\lambda_k - \lambda_l)(\lambda_k - \lambda_j)} \quad (30)$$

Note that we have for $\mu, \nu \in \{0, 1, 2, \dots, n\}$

$$p_{j(\mu, \nu)} = \sum_{k \in I \setminus \{j\}} (\tau - \lambda_k)_{(\mu, \nu)} p_{jk} + \sum_{k, l \in I \setminus \{j\}, k \neq l} (\tau - \lambda_k)_{(\mu)} (\tau - \lambda_l)_{(\nu)} p_{jkl}.$$

Then we see from (25) and (30) that

$$\begin{aligned} (\tau - \lambda_j)_{(\mu, \nu)} p_{j(\mu, \nu)} &= \sum_{k \in I \setminus \{j\}} (\tau - \lambda_j)_{(\mu, \nu)} (\tau - \lambda_k)_{(\mu, \nu)} \frac{p_k - p_j}{\lambda_k - \lambda_j} \\ &\quad + \sum_{k, l \in I \setminus \{j\}, k \neq l} (\tau - \lambda_j)_{(\mu, \nu)} (\tau - \lambda_k)_{(\mu)} (\tau - \lambda_l)_{(\nu)} \\ &\quad \times \left(\frac{p_l}{(\lambda_l - \lambda_j)(\lambda_l - \lambda_k)} + \frac{p_j}{(\lambda_j - \lambda_k)(\lambda_j - \lambda_l)} + \frac{p_k}{(\lambda_k - \lambda_l)(\lambda_k - \lambda_j)} \right). \end{aligned} \quad (31)$$

Since λ_k ($k \in I$) is real-valued, we see that there exist real symbols $a_k \in S_{1,2/3}^{1/3}([0, T])$ so that we have

$$(\tau - \lambda_j)_{(\mu, \nu)} p_{j(\mu, \nu)} = \sum_{k \in I} a_k p_k.$$

Since this argument can be applied to other terms of $(\tau - \lambda_j, p_j)_2$ (see (12)), we see that the assertion for (26) is valid. Noting that $\frac{a_j^0}{i} \in S_{1,2/3}^{2/3}([0, T])$ is real valued, we see that the assertion for (27) follows from

$$\begin{aligned} \frac{1}{2i} \{a_j^0, p_j\} &= \sum_{k \in I \setminus \{j\}} \frac{1}{2i} \{a_j^0, \tau - \lambda_k\} p_{jk} \\ &= \sum_{k \in I \setminus \{j\}} \frac{1}{2i} \{a_j^0, \tau - \lambda_k\} \frac{p_k - p_j}{\lambda_k - \lambda_j}. \end{aligned}$$

Since

$$\frac{1}{2i} \{\tau - \lambda_j, b_{jk}^0 p_{jk}\} = \frac{1}{2i} \{\tau - \lambda_j, b_{jk}^0\} p_{jk} + \frac{b_{jk}^0}{2i} \{\tau - \lambda_j, \tau - \lambda_l\} p_{jkl},$$

noting that $\frac{b_{jk}^0}{i} \in S_{1,2/3}^{2/3}([0, T])$ is real valued, we see from (25) and (30), the assertion for (28) is valid. Finally, noting that $a_j^0 r_j^0$ is real-valued, we see from the definition of a_j^0 and r_j^0 and from (25) that the assertion for (29) is valid. \square

We see from (14) that

$$(D_t - \Lambda_j)P_j = P + Q_{j,1} + Q_{j,2} \pmod{L(m-1, m-1)}$$

with $q_{j1} = \frac{1}{2i}\{\tau - \lambda_j, p_j\}$ and $q_{j2} = \frac{1}{2}(\tau - \lambda_j, p_j)_2$.

Setting $h_1(t, x, \tau, \xi) = \frac{1}{2i}\{a_j^0, p_j\} + \frac{1}{2i}\{\tau - \lambda_j, r_j^0\}$, we see from Lemma 4 and (14) that

$$A_j^0 P_j + (D_t - \Lambda_j)R_j^0 + Q_{j1} = H_1 \pmod{L(m-2, m-1)}.$$

Then, setting $h_2(t, x, \tau, \xi) = h_1(t, x, \tau, \xi) + q_{j2} + a_j^0 r_j^0$, we see that

$$(D_t - \Lambda_j + A_j^0)(P_j + R_j^0) = P + H_2 \pmod{L(m-1, m-1)}.$$

Since

$$h_2(t, x, \tau, \xi) = \frac{1}{2i}\{a_j^0, p_j\} + \frac{1}{2i}\{\tau - \lambda_j, r_j^0\} + \frac{1}{2}(\tau - \lambda_j, p_j)_2 + a_j^0 r_j^0,$$

Lemma 5 shows the following expression of h_2 with real symbols $a_j^1, b_{jk}^1 \in S_{1,2/3}^{1/3}([0, T])$

$$h_2(t, x, \tau, \xi) = -a_j^1 p_j - \sum_{k \in I \setminus \{j\}} b_{jk}^1 p_k$$

With $r_j^1 = \sum_{k \in I \setminus \{j\}} b_{jk}^1 p_k \in L(m-2, m-2+1/3)$ we have

$$h_2(t, x, \tau, \xi) = -a_j^1 p_j - (\tau - \lambda_j) r_j^1$$

Then we see that

$$H_2 = -A_j^0 P_j - (D_t - \Lambda_j)R_j^1 \pmod{L(m-2, m-1)}.$$

Then we obtain

$$(D_t - \Lambda_j + A_j^0 + A_j^1)(P_j + R_j^0 + R_j^1) = P \pmod{L(m-1, m-1)}.$$

Since $a_j^1(t, x, \xi)$ is real-valued, Proposition 3 is proved. \square

4. Appendix.

We show the validity of two claims stated in Introduction. Assume that the symbol $p(t, x, \tau, \xi) = \tau^m + \sum_{j=1}^m a_j(t, x, \xi) \tau^{m-j}$ with real $a_j(t, x, \xi) \in S_{1,2/3}^j([0, T])$ has the following factorization when $|\xi| \geq R_0$ with some $R_0 > 0$.

$$p(t, x, \tau, \xi) = \prod_{j=1}^m (\tau - \lambda_j(t, x, \xi)) \tag{32}$$

with real $\lambda_j(t, x, \xi)$ satisfying, with some $\delta > 0$,

$$|\lambda_j(t, x, \xi) - \lambda_k(t, x, \xi)| \geq \delta \langle \xi \rangle \quad (t, x, \xi) \in [0, T] \times \mathbb{R}^n \times \mathbb{R}^n \text{ with } |\xi| \geq R_0 \tag{33}$$

for any $j, k \in I$ with $j \neq k$.

The first claim is the following. For any $q(t, x, \tau, \xi) = \sum_{j=1}^m b_j(t, x, \xi) \tau^{m-j}$ with real $b_j(t, x, \xi) \in S_{1,2/3}^{j-2/3}([0, T])$, $p(t, x, \tau, \xi) + q(t, x, \tau, \xi)$ has the factorization similar to (32) and (33) when $|\xi| \geq R_1$ with some $R_1 > 0$. Indeed, when $|\xi| \geq R_0$, set $p_j = \prod_{l \in I \setminus \{j\}} (\tau - \lambda_l(t, x, \xi))$. Then, by Lagrange's interpolation formula, we have

$$q(t, x, \tau, \xi) = \sum_{j=1}^m \frac{d_j}{p_j}$$

with

$$d_j = \frac{q(t, x, \lambda_j(t, x, \xi), \xi)}{p_j(t, x, \lambda_j(t, x, \xi), \xi)}.$$

Since $p_j(t, x, \lambda_j(t, x, \xi), \xi) = \prod_{l \in I \setminus \{j\}} (\lambda_j(t, x, \xi) - \lambda_l(t, x, \xi))$, we see from (33)

$$|p_j(t, x, \lambda_j(t, x, \xi), \xi)| \geq C \langle \xi \rangle^{m-1} \quad (|\xi| \geq R_0).$$

Note that the estimates $|a_j| \leq C \langle \xi \rangle^j$ ($j = 1, \dots, m$) imply $|\lambda_j| \leq C \langle \xi \rangle$ ($j = 1, \dots, m$). Then from $b_j(t, x, \xi) \in S_{1,2/3}^{j-2/3}([0, T])$ we obtain $|q(t, x, \lambda_j(t, x, \xi), \xi)| \leq C \langle \xi \rangle^{m-1-2/3}$. Hence $|d_j| \leq C \langle \xi \rangle^{-2/3}$. Then d_j is small when $|\xi|$ is large. Since $b_j(t, x, \xi)$ is real-valued, d_j is real-valued. From $p + q = p(1 + \sum_{j=1}^m \frac{d_j}{\tau - \lambda_j})$ and from (33), by considering the change of sign, follows that there exists a positive R_1 such that, when $|\xi| \geq R_1$, we have the factorization of $p + q$ similar to (32) and (33). Then we see that the first claim is valid.

The second claim is the following. Each $\lambda_j(t, x, \xi)$ ($j = 1, \dots, m$) appearing in (32) has an real extention $\tilde{\lambda}_j \in S_{1,2/3}^1([0, T])$ satisfying, with some $\delta > 0$,

$$|\tilde{\lambda}_j(t, x, \xi) - \tilde{\lambda}_k(t, x, \xi)| \geq \delta \langle \xi \rangle \quad (t, x, \xi) \in [0, T] \times \mathbb{R}^n \times \mathbb{R}^n \quad (34)$$

for any $j, k \in I$ with $j \neq k$.

We show this claim by using Nuij's theorem⁵⁾. We assume $\lambda_1 < \lambda_2 < \dots < \lambda_m$ when $|\xi| \geq R_0$. Let a non-negative function $\chi(s) \in C^\infty(\mathbb{R})$ satisfy

$$\chi(s) = \begin{cases} 1 & |s| \leq 3/2 \\ 0 & |s| \geq 2. \end{cases}$$

Note that by the implicit function theorem and (33), we see $(1 - \chi(|\xi|/R_0))\lambda_j(t, x, \xi) \in S_{1,2/3}^1([0, T])$. Set $\tilde{p} = \prod_{j=1}^m (\tau - (1 - \chi(|\xi|/R_0))\lambda_j(t, x, \xi))$. The polynomial \tilde{p} has only real roots that are distinct when $|\xi| \geq 2R_0$. Thanks to Nuij's theorem, we see that

$$\tilde{p} = (1 + \chi(\frac{|\xi|}{2R_0})\partial_\tau)^{m-1} \tilde{p}$$

has only simple real roots $\tilde{\lambda}_j$ ($j = 1, \dots, m$). We assume $\tilde{\lambda}_1 < \tilde{\lambda}_2 < \dots < \tilde{\lambda}_m$. Since $\tilde{p} = p$ when $|\xi| \geq 4R_0$, we see that $\lambda_j = \tilde{\lambda}_j$ there. Then (34) is verified when $|\xi| \geq 4R_0$. When $|\xi| \leq 4R_0$, the coefficients of \tilde{p} are bounded. Then as a polynomial in τ , the set $\{\tilde{p}(t, x, \tau, \xi) \mid (t, x, \xi) \in [0, T] \times \mathbb{R}^n \times \mathbb{R}^n \text{ with } |\xi| \leq 4R_0\}$ is a bounded set. For any \tilde{p} belonging to its closure that has also only real roots, \tilde{p} has only simple real roots. Then we see that, even if $|\xi| \leq 4R_0$, (34) is valid. Hence the claim is verified.

5. References

- 1). R. Manfrin, On the global solvability of Kirchoff equation for non-analytic initial data. J. Differential Equations, 211, 38-60(2005)
- 2). R. Manfrin, L^p solutions of second order differential equations. Funkcial. Ekvac. 52, 255-279(2009)
- 3). M. Taylor, Partial Differential Equations II, Springer, New York, (1996)
- 4). L. Hörmander, The Analysis Of Linear Partial Differential Operators III, Springer, Berlin, (1994)
- 5). W. Nuij, A Note on hyperbolic polynomials, Math. Scad.,23,69-72 (1968)

An Improved Pedestrian Detection Method for DSS (Driver Supporting System) using an Attitude Measurement Unit

Yukie HASHIMOTO*, THI THI ZIN*, Takashi TORIU* and Hiromitsu HAMA**

(Received September 30, 2011)

Synopsis

This paper proposes an improved method for pedestrian detection using an Attitude Measurement Unit (AMU) in conjunction with multi-slit data. During the next decade, on-board pedestrian detection systems will play a key role in the challenge of increasing traffic safety. The main goal of these systems, to detect pedestrians in urban scenarios, involves overcoming difficulties like processing outdoor scenes from a mobile platform and searching for aspect-changing objects in cluttered environments. Using our new method, it becomes possible to decrease the margin of error of parameters by revising the image width. It is demonstrated that using an AMU as a means of on-road pedestrian detection for automobiles eliminates the need for finding specific configurations on the scene plane. Previously finding these configurations has been too time-consuming for practical use. Our results indicate that the integration of the proposed techniques will give rise to a more economical, accurate, and versatile system.

KEYWORDS: person detection, attitude measurement unit, multi-slit method, vanishing line

1. Introduction

Pedestrian detection is for the safety of both drivers and pedestrians themselves. There are various kinds of hardware and software used for pedestrian detection. As for its applications, a pedestrian detection system can be very useful for monitoring traffic flow, in on-board driver assistance systems, for intelligent pedestrian crossing systems, etc. Using computer vision, pedestrians can be detected and segmented from complex backgrounds. This allows the system to ascertain both the size and position of pedestrians in the camera's field of view. Methods of pedestrian detection can be mainly categorized into two types: motion analysis and shape analysis. In motion analysis¹⁻⁴⁾, a continuous segmentation of pedestrian movement is analyzed. Although these motion-based methods are effective for reducing the rate of false detection of pedestrians, there are still some limitations. They cannot detect motionless pedestrians or any unusual motion of a pedestrian, such as jumping or crawling. Also, a pedestrian's legs must clearly appear in the image for patterns of pedestrian motion to be recognized, but this does not always occur. Furthermore, a sequence of images is required for segmentation and recognition, which cannot be done within a single image. In shape analysis, specific pedestrian characteristics are analyzed for segmentation and recognition^{5,6)}. Obviously, the advantage of almost all of these shape-based methods is that multiple images are not required.

Further improving upon this advantage, we have developed two module systems based on both 2D and 3D sensor cues. The first module uses pitch and roll angles for calculating the vanishing line on the image to select a coherent set of Regions Of Interest (ROIs) to be further analyzed. The second module develops a modified multi-slit method to classify the incoming ROIs into pedestrian and non-pedestrian in order to refine the final results.^{7,8)} Our method utilizes horizontal slicing of the image, called the "multi-slit" method and associates the

* Information and Communication Engineering, Dept. of Physical Electronics and Informatics

** R&D Center of 3G Search Engine, Incubator, Research Center for Industry Innovation
Osaka City University

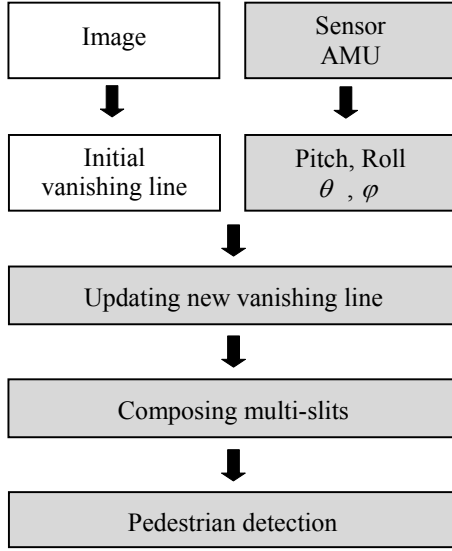
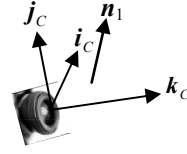
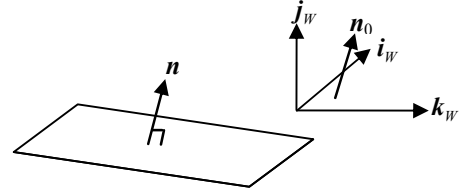


Fig.1 Overview of proposed system.

camera coordinate system



world coordinate system



road surface

Fig.2 Normal vectors of the road surface in two coordinate systems.

multi-slit data with histograms of oriented gradients. In the multi-slit method, the use of vanishing lines is a key feature. The multi-slit approach is a new line of research which utilizes projective geometry and homogeneous coordinates. Depending on the setting, the geometric relationship between the object space and the image space is described via either similarity, affine or projective transformations. It is known that these transformations can be recovered by analyzing the vanishing points and vanishing lines. The most common approach to finding the vanishing line for a scene plane is first to determine two vanishing points from two sets of linear features parallel to the plane, and then construct the vanishing line through the two vanishing points. However, these linear features may not be readily available for every scene and their generation may be prone to errors if the linear features are short in distance. Other methods include estimation from equally spaced coplanar parallel lines and using orthogonal relationships among vanishing points and lines⁹⁾. However, these methods still require parallel lines on the scene plane or specific configurations which are hard to retrieve for practical use.

In contrast to these approaches, in this paper we mainly focus on robust real-time vanishing line estimation for driver assistance applications by using an AMU which measures the altitude or inclinations in both object space and image space (Fig.1). Attitude, pitch and inclination measurement are required in a wide variety of markets such as aerospace, industry and instrumentation. The tilt sensor technique has many advantages; for example, it is low cost, small size, lightweight, and is easy to be intelligent and integrated¹⁰⁾.

The rest of this paper is organized as follows. In Section 2, we establish a technique for constructing the vanishing lines using AMU units. The experimental results are shown in Section 3 and Section 4 contains concluding remarks.

2. Pedestrian detection using multi-slit method

In this paper, we assume a pin-hole camera model. In addition, the normal vector \mathbf{n} on the road surface is expressed as \mathbf{n}_0 in the world coordinate system $(\mathbf{i}_w, \mathbf{j}_w, \mathbf{k}_w)$ and \mathbf{n}_1 in the camera coordinate system $(\mathbf{i}_c, \mathbf{j}_c, \mathbf{k}_c)$ as shown in Fig.2. The vanishing line in an image is obtained from the normal vector \mathbf{n}_1 . The vanishing line is obtained by the following procedure.

[Step1] Suppose \mathbf{j}_C shows \mathbf{j}_W rotated through θ_0 about the x-axis (Pitch) and φ_0 about the z-axis (Roll).

$$\left. \begin{aligned} \mathbf{j}_C = (a_0, b_0, c_0) = a_0 \mathbf{i}_W + b_0 \mathbf{j}_W + c_0 \mathbf{k}_W, |\mathbf{j}_C| = 1, \\ \text{where } \mathbf{i}_W = (1, 0, 0), \mathbf{j}_W = (0, 1, 0), \mathbf{k}_W = (0, 0, 1). \end{aligned} \right\} \quad (1)$$

And a_0, b_0, c_0 are obtained from the next expressions as shown in Fig.3:

$$a_0 = b_0 \tan \varphi_0, b_0 = 1 / \sqrt{\tan^2 \varphi_0 + 1 + \tan^2 \theta_0}, c_0 = -b_0 \tan \theta_0. \quad (2)$$

In addition, the rotating matrices are

$$\mathbf{R}_1(\theta) = \begin{pmatrix} 1 & 0 & 0 \\ 0 & \cos \theta & -\sin \theta \\ 0 & \sin \theta & \cos \theta \end{pmatrix}, \mathbf{R}_2(\varphi) = \begin{pmatrix} \cos \varphi & -\sin \varphi & 0 \\ \sin \varphi & \cos \varphi & 0 \\ 0 & 0 & 1 \end{pmatrix} \quad (3)$$

We obtain θ and φ by resolving the following expressions:

$$\mathbf{j}_C = \mathbf{j}_W \cdot \mathbf{R}(\theta_0, \varphi_0) = \mathbf{j}_W \cdot \mathbf{R}_1(\theta) \cdot \mathbf{R}_2(\varphi) = (a_0, b_0, c_0), \quad (4)$$

$$\theta = -\sin^{-1}(c_0), \varphi = \sin^{-1}(a_0 / \cos \theta). \quad (5)$$

Therefore, the camera coordinate system is obtained by the following expressions:

$$(\mathbf{i}_C, \mathbf{j}_C, \mathbf{k}_C) = (\mathbf{i}_W, \mathbf{j}_W, \mathbf{k}_W) \cdot \mathbf{R}(\theta_0, \varphi_0) = (\mathbf{i}_W, \mathbf{j}_W, \mathbf{k}_W) \cdot \mathbf{R}_1(\theta) \cdot \mathbf{R}_2(\varphi) \quad (6)$$

$$\left. \begin{aligned} \mathbf{i}_C &= (-\cos \varphi, \sin \varphi, 0) \\ \mathbf{j}_C &= (\cos \theta \cdot \sin \varphi, \cos \theta \cdot \cos \varphi, -\sin \theta) \\ \mathbf{k}_C &= (\sin \theta \cdot \sin \varphi, \sin \theta \cdot \cos \varphi, \cos \theta) \end{aligned} \right\} \quad (7)$$

[Step2] We can calculate the road surface normal vector $\mathbf{n}_1 = (a_1, b_1, c_1)$ in the camera coordinate system from vanishing line parameters m, d ($y = mx + d$) to be provided from an input image. We obtain vanishing line parameters by two ways: finding manually and (2) calculating a_1, b_1, c_1 using the next expressions:

$$\sqrt{a_1^2 + b_1^2 + c_1^2} = 1, \tan \theta_1 = d / L_V = -c_1 / b_1, m = \tan \varphi_1 = a_1 / b_1, \quad (8)$$

$$b_1 = 1 / \sqrt{m^2 + 1 + (d / L_V)^2}, a_1 = m \cdot b_1, c_1 = -b_1 \cdot d / L_V. \quad (9)$$

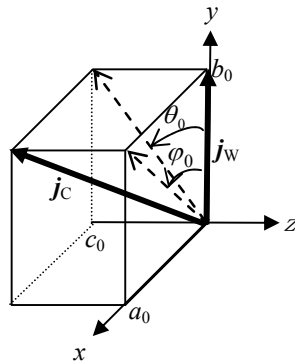


Fig.3 Normal vector.

Here, L_V is expressed for a pixel unit for relative role and imagination as a vertical angle and a vertical resolution of image at distance from the lens center to screen. We illustrate by Section 3 in more detail. Therefore, when the normal vector of \mathbf{n}_0 is expressed as (a_0', b_0', c_0') in the world coordinate system, the \mathbf{n}_0 is converted from the camera coordinate system into in the world coordinate system the following expression:

$$\mathbf{n}_0 = (a_0', b_0', c_0') = a_1 \mathbf{i}_C + b_1 \mathbf{j}_C + c_1 \mathbf{k}_C. \quad (10)$$

The road surface normal vector \mathbf{n}_0 in the world coordinate system is fixed.

[Step3] When the camera attitude is changed, we calculate the new camera coordinate system $(\mathbf{i}_C', \mathbf{j}_C', \mathbf{k}_C')$ from the new camera attitude angles by Eq.(7). Therefore, we calculate \mathbf{n}_1 by the following expressions from Eq.(10):

$$a_1' = \mathbf{n}_0 \cdot \mathbf{i}_C', b_1' = \mathbf{n}_0 \cdot \mathbf{j}_C', c_1' = \mathbf{n}_0 \cdot \mathbf{k}_C'. \quad (11)$$

[Step4] And, we obtain new vanishing line parameters $m', d' (y = m'x + d')$ by the following expressions from Eq.(9):

$$d' = L_V \cdot c_1' / b_1', m' = a_1' / b_1'. \quad (12)$$

Therefore, when the camera attitude is changed, we can update the new vanishing line from new attitude using the road surface normal vector in the world coordinate system.

This section explains processing that extracts head nominators by multi-slit method. The multi-slit method calculates the position (slit) with the possibility with the pedestrian on the image, and it tries to improve the detection accuracy by judging whether there is pedestrian's feature in each slit. The multi-slit method utilizes y-position of vanishing line as the scale factor. The effectiveness of this technique is proven by the reference^{7,8)}.

3. Experimental Results

The effectiveness of the proposed method is confirmed through our experimental results. We took pictures in a variety of camera attitude angles (pitch and roll angles), and we estimated the vanishing line to each image by using pitch and roll angles obtained from an AMU at the same time.

L_V is expressed for a pixel unit for relative role and imagination as a vertical angle and a vertical resolution of image at distance from the lens center to screen as shown in Fig.4. Specifically, because the verticality angle of view of the camera used by the experiment is 37.8° and the verticality resolution of image 2448 pixels, the value of L_V is obtained by the following expression:

$$L_V = 1224 / \tan(18.39^\circ) = 3575.015. \quad (13)$$

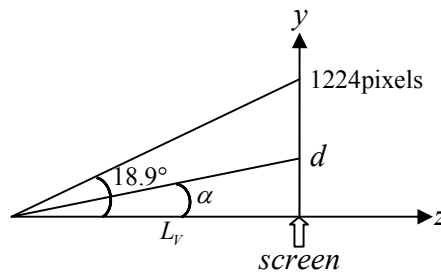


Fig.4 Image of L_V .

Calculation using L_V may cause error between d' and d . It is also necessary to revise the magnification of image width to correct for error between m' and m as shown in Fig.5. Therefore, we introduce a correction coefficient on experimental basis by the following expression:

$$L_V' = L_V \times 0.863 = 3085.238. \tag{14}$$

$$x' = 1/0.9968 \cdot x. \tag{15}$$

Then, the mean of the error margin of d and d' has been improved from 44 to 9 and that of m and m' from -0.0031 to -0.0029 as shown in Table 1. Fig.6(a),(b) shows the error margin of the vanishing line parameters. Examples of multi-slit drawn using vanishing lines estimated by L_V' are shown in Fig.7.

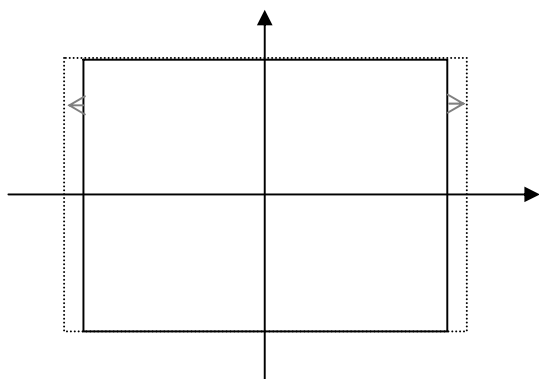
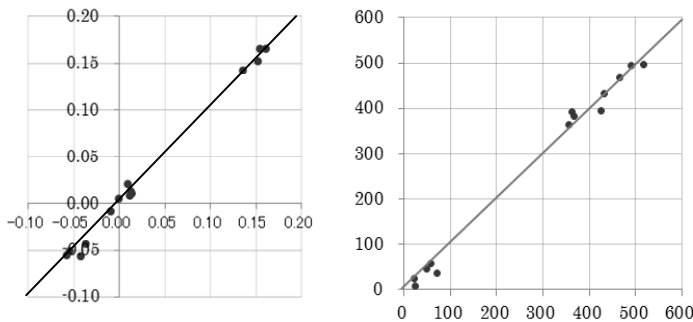


Fig.5 To revise the magnification of image width.



(a) m and m'

(b) d and d'

Fig.6 The error margin of the vanishing line parameters using L_V' and x' .

Table1. The error margin using L_V, x and L_V', x'

		SD	MEAN			SD	MEAN
L_V, x	$m'-m$	0.0044	-0.0031	L_V', x'	$m'-m$	0.0043	-0.0029
	$d'-d$	33	44		$d'-d$	28	9



Fig.7 Examples of multi-slits using L_V' and x' .

4. Conclusion

We have developed an improved method for pedestrian detection using an AMU in conjunction with multi-slit data. In this paper, we proposed a fast and simple technique for obtaining the vanishing lines using an AMU. This system was shown to keep the necessary precision. Therefore, it is possible to combine the multi-slit lines with the data from an AMU mounted in a vehicle in real-time even when the car moves or wobbles around while driving. The effectiveness of our proposed method was confirmed by our experimental results. However, it has here been assumed that the road surface is perfectly level and smooth. As this is of course not always the case, it will be for future research to develop a real-time system for practical use that can handle more generally encountered conditions.

Acknowledgment. This work is partially supported by KAKENHI 21500176 Grant-in-Aid for Scientific Research(C).

5. References

- 1) C. Wöhler, U. Kressler and J. K. Anlauf, Pedestrian Recognition by Classification of Image Sequences. Global Approaches vs Local Spatio-Temporal Processing, *Proc. IEEE Int. Conf Patt. Rec. CVPR2000*, Barcelona, Spain (2000)
- 2) C. Curio, J. Edelbrunner, T. Kalinke, C. Tzomakas and W. von Seelen, Walking Pedestrian Recognition, *IEEE Trans. Int Transp. Sys*, Vol.1(3), pp.155-163 (2000)
- 3) R. Cutler and L. S. Davis, Robust Real-Time Periodic Motion Detection, Analysis and Applications, *IEEE Trans. Patt. An. Mach. Int.*, Vol.22(8), pp.781-796 (2000)
- 4) C. Bregler, Learning and Recognizing Human Dynamics in Video Sequences, *IEEE Conf. Comp. Vision and Pattern Recognition.*, San Juan, Puerto Rico (1997)
- 5) A. Broggi, M. Bertozzi, A. Fascioli and M. Sechi, Shape-Based Pedestrian Detection, *Proc. IEEE Intell. Veh. Symp.*, pp.215-220 (2000)
- 6) F. Suard, A. Rakotomamonjy, A. Benschair and V. Guigue, Pedestrian Detection using Stereo-Vision and Graph Kernels, *Proc. IEEE Intell. Veh. Symp.*, Las Vegas (2005)
- 7) Thi Thi Zin, Hideya Takahashi and Hiromitsu Hama, "Robust Person Detection in Far Infrared Images – Methods based on Multi-slits and GC Movement Patterns–", *IJICIC*, vol.5, No.3, pp.751-761 (2009)
- 8) Thi Thi Zin, Pyke Tin and Hiromitsu Hama, "Bundling Multislit-HOG Features of Near Infrared Images for Pedestrian Detection", *Proc. of ICICIC2009*, Kaohsiung, Taiwan, pp.302-305 (2009)
- 9) Havasi, L. and Sziranyi, T., Extraction of Horizontal Vanishing Line Using Shapes and Statistical Error Propagation, *Symposium of ISPRS Commission III. Photogrammetric Computer Vision*, pp.167-173 (2006)
- 10) Qiushi Han and Chen Chen, 2008. Research on Tilt Sensor Technology. Knowledge Acquisition and KAM Workshop 2008. *IEEE Intl. Symp. on Modeling Workshop*: pp.786-789 (2008)

A Numerical Model to Simulate the Time Dependent Behavior of Rock

Kenichi NAKAOKA^{*}, Koji HATA^{**}, Hiroaki KITO^{***} and Yujing JIANG^{****}

(Received September 30,2011)

Synopsis

To simulate the time-dependent deformation of the rock, we propose herein a numerical creep model. The model can evaluate consistently from immediately after loading up to collapse considering the confinement effect. In this paper, firstly, a rheological relaxation model consisting of spring and damper components is explained to rock under a constant compressive stress and also under a constant strain rate are simulated using the proposed model. As a result, the obtained time history of strain rate under the constant stress, and also the relation between stress and strain including strain softening behavior under the constant rate are fairly agreed with the test's results.

KEYWORDS: creep, numerical model, strain rate effect, strain-softening

1. Introduction

Under the swelling rock, there is sometimes increasing of ground deformations around the tunnel with time though while the tunnel is not under excavation. And it often make difficulty to continue tunnel excavation, so cause the cost up, and delay the schedule For radioactive waste disposal tunnel, long-term evaluation of deformation is needed for performance assessment because it is concerned that the creep phenomenon continues.

It is known that creep deformation of rock specimen under tri-axial compression test with constant stress-which called "creep test" hereafter, shows three phases of their states. Firstly, strain rate decrease by degrees from fast to slow. Next, the slow strain rate condition continues. Finally, strain rate increase rapidly and collapse. Each of these states is called primary creep, secondary creep, and, tertiary creep, respectively.

By contrast, under tri-axial compression test with constant strain rate, which called "loading test" hereafter, axial stress of specimen decrease beyond its peak stress to residual stress, which is called strain softening.

As the numerical models that can evaluate both the creep deformation and strain softening behavior, there are the elasto-viscoplastic model proposed by Adachi and Oka¹⁾, and, the model that varies the compliance depending upon time duration and current stress proposed by Okubo and Fukui et al²⁾.

For the model by Adachi and Oka¹⁾, materials parameters have to be modified depend on confined pressure to simulate the tri-axial tests. To make simulation easy, it is desirable to use same parameters through the analysis if the stress changes even in analysis step. Considering the confinement effects easily, Azuma and Ohtsuki et al.^{3),4)} modified the Adachi-Oka model by adding the new eight model parameters. While, in Okubo's model, the confinement effect is not considered. Furthermore, for the model, the determination of the model parameters using creep tests results is difficult when evaluation of primary to tertiary creep deformation needed.

In this study, the numerical model introducing a non-dimensional parameter s which represents the degree of creep development. The features of the model are easiness of estimating the model parameters because the numbers of parameters are not many. It can evaluate the effect of compression pressure based on Mohr – Coulomb criteria. At first, the numerical model is formulated, and the rheological relaxation model consisting of spring and damper is explained. Next, the model is installed into a finite difference method framework. Then, calculations of creep test and loading test are carried out about the existing tests data using one element model. By comparison between the results of numerical analysis and tri-axial compression test, applicability of the model is discussed.

* Student, Doctor Course of Department of Civil Engineering (Obayashi Corporation)

** Obayashi Corporation

*** Associate Professor, Department of Civil Engineering, Osaka City University

**** Professor, Division of System Science, Nagasaki University

2. Creep model

(1) Introduce of non-dimensional parameter s

The non-dimensional important parameter s indicates the degree of creep development. It is assumed, herein, that the value of s increases with repeating of many stop and forward sequences as shown in Fig.1. As shown in the figure, the number of repetition is to be $ds \cdot n$ within an interval ds , so the increment value of s with the repetition is $1/n$. Introducing the stationary time f for the stop sequence dependent upon current stress state, moreover, increasing rate of s can be described as eq. (1). It is noted that in Fig. 1, the duration for the forward sequences is to be zero, and it for the stop is to be the sum of the time f . Strain rate, so called creep strain is proportional to the increasing rate of s to be described later in detail.

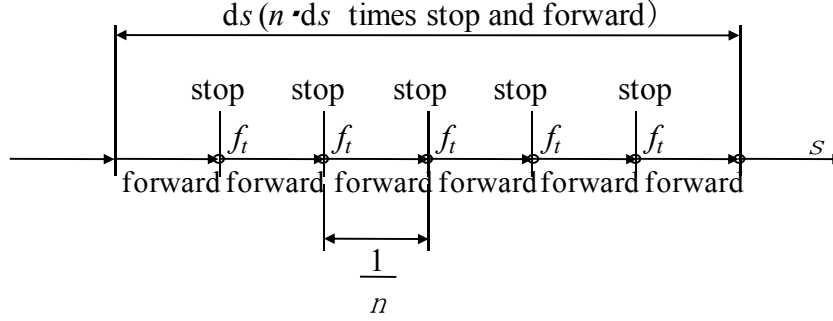


Fig.1 Concept of increasing s .

$$\dot{s} = \frac{1}{nf} \quad (1)$$

The parameter n is that means density of the stop sequence duration in unit interval s . It is assumed that the parameter n varies depending on increments of s , and the function of stopping density $n=g'(s)$ is defined by eq. (2), which is never decrease.

$$n = g'(s) = \frac{\alpha_1}{b_n \sqrt{2\pi}} \exp \left\{ - \left(\frac{s - a_v}{\sqrt{2} b_n} \right)^2 \right\} \quad (2)$$

Here, b_n and a_v are material constants, these called as variance and mean, respectively, as follows. Parameter α_1 is the maximum value of $g'(s)$, and π is circular constant. It is assumed, furthermore, that the stationary time f is the function of stress p , so called $f'(p)$. Thus, increasing rate of s (after, \dot{s}) is described by eq. (3) based on eq. (1) and (2). Now, stress p is defined as the distance from coordinate of principal stress to hydrostatic axis in three-dimensional principal stress space as shown in Fig.2, which is described as eq. (4). Here, J_2 in eq. (4) is second invariant of deviatoric stress, which is as eq. (5), δ_{ij} in eq. (6) is Kronecker's delta. The increasing concept of s is shown in Fig.3 with consideration of stopping density. For creep test's condition, $f'(p)$ is constant so that every stationary durations of stop sequences is same.

$$\dot{s} = \frac{1}{g'(s)f'(p)} \quad (3)$$

$$p = \sqrt{2J_2} \quad (4)$$

$$J_2 = \frac{1}{2} s_{ij} s_{ij} \quad (5)$$

$$s_{ij} = \sigma_{ij} - \delta_{ij} \sigma_m \quad (6)$$

$$\sigma_m = \frac{1}{3} \sigma_{ii} \quad (7)$$

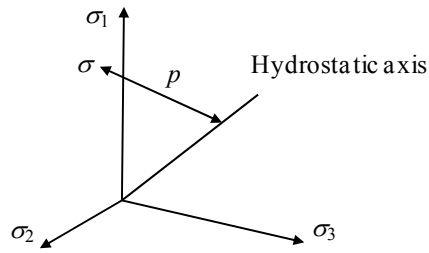


Fig.2 Stress p to increases s .

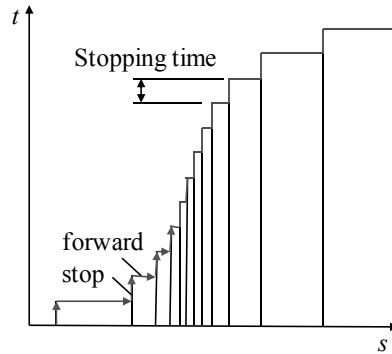


Fig.3 Concept of s increase with consider of stopping density.

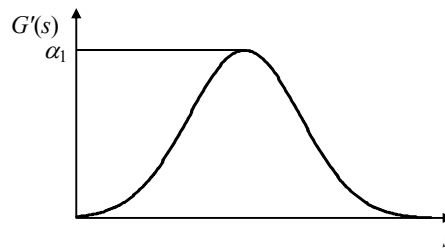


Fig.4 An example of stopping density function.

The concept of this model is based on the assumption as follows: In the case of unconfined material, contact and disconnections will occur between grains, while, in case of rock, the micro cracks will develop and penetrate. At every time of both of the events occurs, the increase of parameter s expressing creep development stops each time. Afterward, the parameter goes forward until next event occurs. For example, at beginning stage of loading under low strain condition, almost grains do not contact each other, or almost micro cracks do not develop so that the number of stopping is small. Subsequently, when the loading stage proceeds, the number increases, because the both events occur evidently. Consequently, approaching at final stage, the number decreases owing to the gradual termination of the both events.

Furthermore, another assumption is introduced here as follows: strain increment with each event is proportional to the deviatoric stress p . It is based on that the event under high stress condition causes considerable large slips or crack extensions, so the strain increment becomes also larger than under low stress condition. Now, consider creep tests, we set parameters $\alpha_1=f_i(p)=1$. \dot{s} curves are obtained as shown in Fig.5 and Fig.7 as numerical solutions for eq. (3). Moreover, the functions of stopping density are as shown in Fig.6 and 8. The s values at \dot{s} minimum in Fig.5 and Fig.7 correspond to the s values at maximum stopping density in Fig.6 and 8.

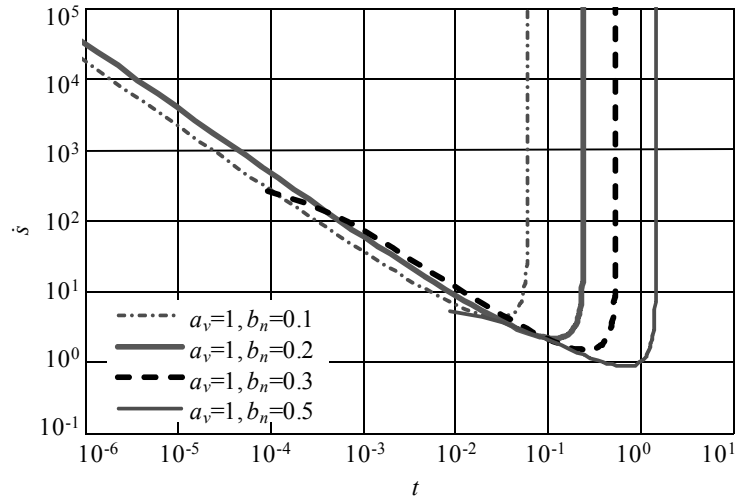


Fig.5 Time history of \hat{s} with various variances: b_n .

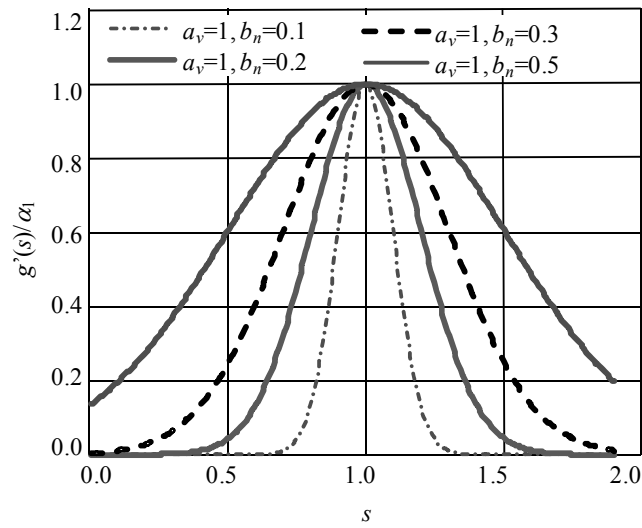


Fig.6 Function of stopping density with various variances: b_n .

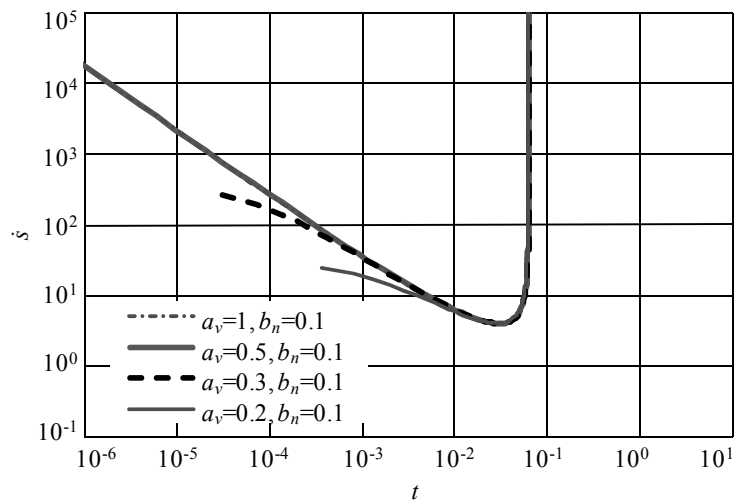


Fig.7 Time history of \hat{s} with various means: a_v .

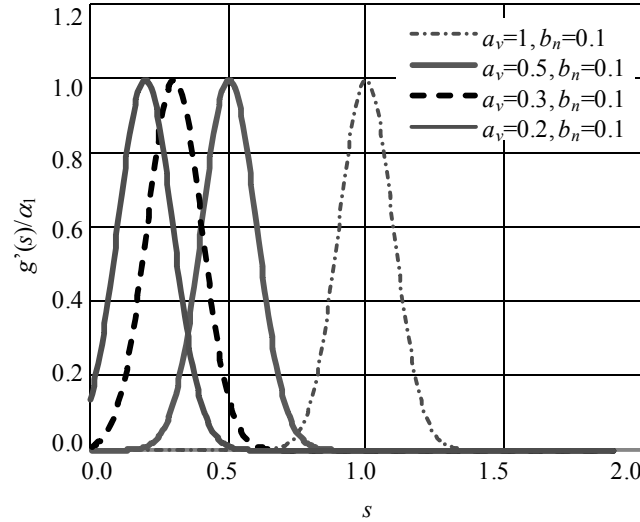


Fig.8 Function of stopping density with various means: a_v .

From these dual logarithmic figures; Figs. 5 and 7, it can be found that, with same mean, the times when \dot{s} is minimum become later with variance increase. While, as the same manner, with same variance, the times when \dot{s} is minimum are similar with variable mean. Inclined straight line lengths before the time of minimum \dot{s} become longer with the mean increase, and become shorter with mean decreasing. Creep strain rate curve calculated by the creep model is similarity shape to Fig.5 or 7. From these figures, the gradient of the length are similar and the value is about 0.9, even though mean and variances are varied. To vary the gradient, parameter n has to be added into stopping density function as eq. (8). With smaller n , the gradient become smaller and curvature near the time when minimum \dot{s} occur become larger. With large n , the gradient become larger and curvature become smaller. The distribution of stopping density is shown by Fig.10.

$$g'(s) = \frac{\alpha_1}{b_n \sqrt{2\pi}} \exp \left\{ - \left(\frac{s^n - a_v^n}{\sqrt{2} b_n} \right)^2 \right\} \quad (8)$$

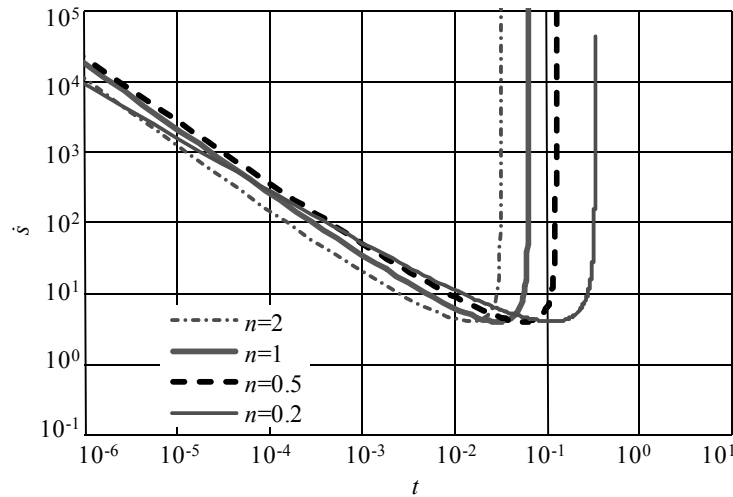


Fig.9 Time history of \dot{s} (variation of n , at $a_v=1$ and $b_n=0.1$).

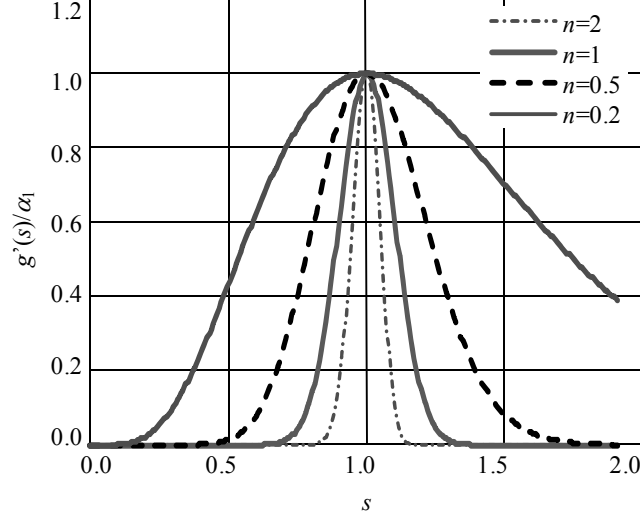


Fig.10 Function of stopping density (variation of n at $a_v=1$ and $b_n=0.1$).

Because, many reports about creep tests of rock show that the gradients of straight intervals are near the value 0.9, hereafter, we regard $n=1$. Next, the function of stopping time is assumed as eq. (9) according to the Arrhenius equation, which rapidly decrease with the intensity of invariant stress p became larger than that of h relevant to shear strength. Parameter h in eq. (9) is obtained from eq. (10) based upon the Mohr-Coulomb criteria.

$$f'(p) = \alpha_2 \exp\{q(h - p)\} \quad (9)$$

$$h = c + \sigma_m \tan \phi \quad (10)$$

Parameters of α_2 and q define the relation between stopping time and p . Furthermore, parameters of c and ϕ define the strength depend on hydrostatic pressure σ_m . By changing of eq. (2) and (9) to eq. (11) and (12), eq. (14) is obtained from eq. (3). The parameter that has to be defined is α in eq. (14).

$$g(s) = \exp\left\{-\left(\frac{s - a_v}{\sqrt{2}b_n}\right)^2\right\} \quad (11)$$

$$f(p) = \exp\{q(h - p)\} \quad (12)$$

$$\alpha = \frac{b_n \sqrt{2\pi}}{\alpha_1 \alpha_2} \quad (13)$$

$$\dot{s} = \frac{\alpha}{g(s)f(p)} \quad (14)$$

(2) Calculation of deviatoric stress p

To install the proposed creep model into a finite difference method framework, FDM, variation of stress due to relaxation is calculated in each loading step previously. By using the stress modifying process additionally, residual force is calculated firstly. Subsequently, after a current incremental stage is convergent, new stress and strain are calculated with the residual force that assumed as load in the FDM. Using obtained residual force, next step to convergence is also done. Finally, next loading step with relaxation calculation is done.

Now, consider a rheological model with spring and damper as shown in Fig.11. The normal force of spring is assumed equal to p shown in Fig.2. It's both ends of the model do not move in process of relaxation calculation. With increments of time step in each loading step, displacement of damper increase and then the force of spring p become smaller. At this process, strain does not change. Next loading step, increment load is added onto spring force, relaxation calculation is repeated again.

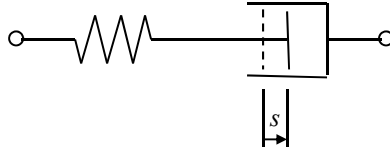


Fig.11 Rheological model

As shown in Fig.11, the displacement of damper is assumed as s indicating degree of the creep development. Being the increment of creep strain by the event of stop and forward sequences as shown in Fig.1 proportional to stress, spring constant is defined as eq. (15). When the spring constant is proportional to stress, relaxation rate becomes faster owing to large stress, and become slower owing to small stress. As the result, the creep strain obtained from convergence calculations satisfies the proportional relation to product of stress p and s . Parameter k' is material constant.

$$k = k'p \quad (15)$$

The flowchart of calculation of relaxation and decreasing of p with time step involved in loading step is shown in Fig.12. The creep strain in Fig.12 is 0. The parameter r in Fig.12 is the stress that increases with creep development to be explained later. It is also assumed that p does not become smaller than r .

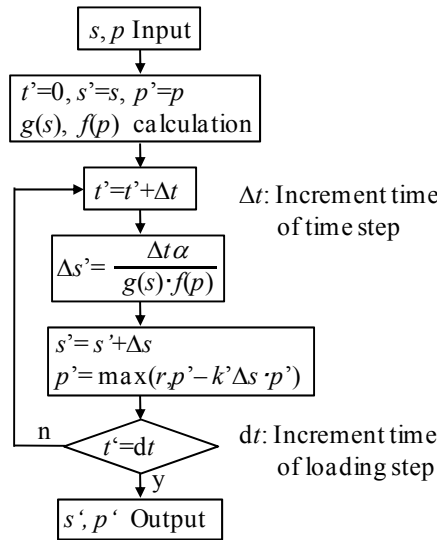


Fig.12 Flowchart of relaxation calculation.

(3) Defining of strength parameter r

The strength parameter r in Fig.12 is to be increases with the accumulated events number as shown in Fig. 1. Thus, r becomes residual strength that is defined by Mohr-Coulomb criteria in eq. (16). Strength parameter r is finally defined by eq. (17).

$$S_r = c_r + \sigma_m \tan(\phi_r) \quad (16)$$

$$r = \frac{S_r}{2} \left\{ 1 + \operatorname{erf} \frac{s - a_v}{\sqrt{2} b_n} \right\} \quad (17)$$

Where, parameters c_r and ϕ_r are cohesion and friction angle at residual stress state, respectively, and σ_m is hydrostatic pressure, erf is error function.

(4) Modifying method of stress using p

Amount of decrease in spring force p is put as dp . Modified spring force is put as p' ($= p - dp$), and, thus stress calculated from p' is updated as σ_{ij}' . As shown in Fig.13, the direction of stress shift by modifying in

principal stress space is normal according to the well-known von Mises's yield surface. In this case, hydrostatic pressure does not change by modifying of stress. As shown in the figure, at point B, the σ_i is principal stress before modify, point A is hydrostatic pressure σ_m . Point C is principal stress after modifying, and C rides on line A-B. Stress s_i is deviatoric principal stress before modify, $s_i = \sigma_i - \sigma_m$. From figure, deviatoric principal stress after modify s'_i that is described by eq. (18) is same with vector AC. The derivation method of modify the principal stress from point B to C is discussed as follows:

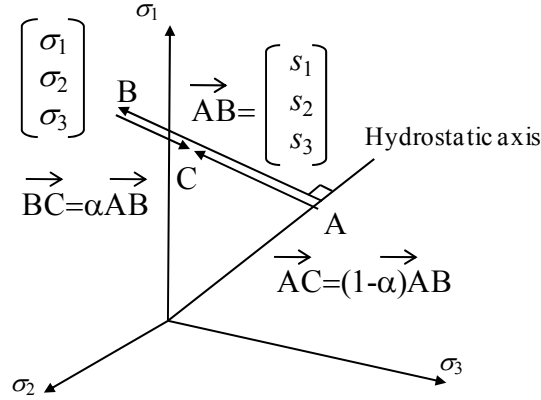


Fig.13 Modify of principal stress

$$s'_i = (1 - \alpha)s_i \quad (18)$$

Deviatoric principal stress s_i is defined by eq. (19). Parameter of J_3 is third invariant of deviatoric stress that is defined by eq. (20).

$$s_i^3 - J_2 s_i - J_3 = 0 \quad (19)$$

$$J_3 = \frac{1}{3} s_{ij} s_{jk} s_{ki} \quad (20)$$

Deviatoric stress after modifying is put s'_{ij} as eq. (21).

$$s'_{ij} = (1 - \alpha)s_{ij} \quad (21)$$

Second and third stress invariants after modifying of J_2' and J_3' are defined by eq. (22) using invariant stress before modifying.

$$J_2' = \frac{1}{2} s'_{ij} s'_{ij} = \frac{1}{2} (1 - \alpha)^2 s_{ij} s_{ij} = (1 - \alpha)^2 J_2 \quad (22)$$

$$J_3' = \frac{1}{3} s'_{ij} s'_{jk} s'_{ki} = \frac{1}{3} (1 - \alpha)^3 s_{ij} s_{jk} s_{ki} = (1 - \alpha)^3 J_3 \quad (23)$$

From eq. (22) and (23), stress invariants before modifying are defined as eq. (24) and (25).

$$J_2 = \frac{J_2'}{(1 - \alpha)^2} \quad (24)$$

$$J_3 = \frac{J_3'}{(1 - \alpha)^3} \quad (25)$$

By substitution of eq. (24) and (25) into eq. (18) and multiplying by $(1 - \alpha)^3$, next equation is obtained.

$$\{(1 - \alpha)s_i\}^3 - J_2'(1 - \alpha)s_i - J_3' = 0 \quad (26)$$

Comparing with eq. (19) and eq. (26), it is found that the stress s'_i defined in eq. (18) is same as deviatoric

principal stress of deviatoric stress s_{ij} after modifying. So the hydrostatic pressure σ_m' after modifying is equal to hydrostatic pressure σ_m before modifying eq. (27) is given from eq. (21).

$$\sigma'_{ij} - \delta_{ij}\sigma'_m = \sigma'_{ij} - \delta_{ij}\sigma_m = (1 - \alpha)(\sigma_{ij} - \delta_{ij}\sigma_m) \quad (27)$$

Stress σ'_{ij} after modifying is given as eq. (28) from eq. (27). Parameter α is given by eq. (29) that is derived from eq. (24).

$$\begin{aligned} \sigma'_x &= \sigma_x - \alpha\sigma_x + \alpha\sigma_m \\ \sigma'_y &= \sigma_y - \alpha\sigma_y + \alpha\sigma_m \\ \sigma'_z &= \sigma_z - \alpha\sigma_z + \alpha\sigma_m \\ \tau'_{xy} &= (1 - \alpha)\tau_{xy} \\ \tau'_{yz} &= (1 - \alpha)\tau_{yz} \\ \tau'_{zx} &= (1 - \alpha) \end{aligned} \quad (28)$$

$$\alpha = 1 - \frac{\sqrt{J'_2}}{\sqrt{J_2}} \quad (29)$$

If we consider the volumetric creep strain, it is possible to use the elasto-plasticity constitutive equation based on flowing rule. Here, creep strain is assumed as plastic strain ε^p_{ij} . Calculation method of stress modified using constitutive equation is discussed below. Strain increment in an incremental loading step $d\varepsilon_{ij}$ is given by sum of elastic strain $d\varepsilon^e_{ij}$ and plastic strain $d\varepsilon^p_{ij}$ as shown by eq. (30).

$$d\varepsilon_{ij} = d\varepsilon^e_{ij} + d\varepsilon^p_{ij} \quad (30)$$

Incremental creep strain is defined by eq. (31).

$$d\varepsilon^p_{ij} = H \frac{\partial g}{\partial \sigma_{ij}} \quad (31)$$

Here, function g defines the direction of creep strain in principal stress field. In the case of the direction is normal with the von Mises's yield surface, the function become as eq. (32). Parameter H defines the amplitude of creep strain. In the process in relaxation calculation, total increment strain $d\varepsilon_{ij} = 0$, eq. (33) is obtained from eq. (30) and (31).

$$g = \sqrt{2J_2} \quad (32)$$

$$d\varepsilon^e_{ij} = -d\varepsilon^p_{ij} = -H \frac{\partial g}{\partial \sigma_{ij}} \quad (33)$$

Using the vector of partial differential of $g(\sigma)$ by each stress component, eq. (34) is obtained from eq. (33). After here, vector representation of stress is used.

$$\{d\varepsilon^e\} = -\frac{H}{\sqrt{2J_2}}\{F\} \quad (34)$$

$$\{F\} = \{\sigma_x - \sigma_m, \sigma_y - \sigma_m, \sigma_z - \sigma_m, 2\tau_{xy}, 2\tau_{yz}, 2\tau_{zx}\}^T \quad (35)$$

Relation of incremental elastic strain and incremental stress is defined with strain-stress matrix D .

$$\{d\sigma\} = D\{d\varepsilon^e\} \quad (36)$$

By putting β as eq. (37), the difference of stress $\{d\sigma\}$ by modifying is obtained by eq. (38) from eq. (34).

$$\beta = -\frac{H}{\sqrt{2J_2}} \quad (37)$$

$$\{d\sigma\} = \beta D\{F\} \quad (38)$$

From eq. (38), by multiplication of D and $\{F\}$, $\{d\sigma\}$ is obtained as eq. (39). Here, G is the shear elasticity modulus.

$$\{d\sigma\} = 2G\beta\{\sigma_x - \sigma_m, \sigma_y - \sigma_m, \sigma_z - \sigma_m, \tau_{xy}, \tau_{yz}, \tau_{zx}\}^T \quad (39)$$

Also $\{d\sigma\}$ is described as eq. (40), the relation $\sigma_m' = \sigma_m$ is obtained by solving for stress after modify using eq. (39) and (40). And by solving for deviator stress eq. (41) is derived.

$$\{d\sigma\} = \{\sigma_x' - \sigma_x, \sigma_y' - \sigma_y, \sigma_z' - \sigma_z, \tau_{xy}' - \tau_{xy}, \tau_{yz}' - \tau_{yz}, \tau_{zx}' - \tau_{zx}\}^T \quad (40)$$

$$\begin{aligned} \sigma_x' - \sigma_m' &= (1 + 2G\beta)(\sigma_x - \sigma_m) \\ \sigma_y' - \sigma_m' &= (1 + 2G\beta)(\sigma_y - \sigma_m) \\ \sigma_z' - \sigma_m' &= (1 + 2G\beta)(\sigma_z - \sigma_m) \\ \tau_{xy}' &= (1 + 2G\beta)\tau_{xy} \\ \tau_{yz}' &= (1 + 2G\beta)\tau_{yz} \\ \tau_{zx}' &= (1 + 2G\beta)\tau_{zx} \end{aligned} \quad (41)$$

By square the both side of eq. (41), relation of J_2 and J_2' is obtained as eq. (42). And substitution of β described in eq. (37) into eq. (42) give H as eq. (43).

$$J_2' = (1 + 2G\beta)^2 J_2 \quad (42)$$

$$H = \frac{\sqrt{2J_2'} - \sqrt{2J_2}}{2G} \quad (43)$$

By substitution of $1 + 2G\beta$ that is described using J_2 and J_2' using eq. (42) into eq. (39), same result of eq. (28) is derived. Volumetric strain with creep deformation becomes zero by solving of the $d\varepsilon_x + d\varepsilon_y + d\varepsilon_z$ using eq. (34) and (35). Evaluation of dilatancy effect enable by giving the gradient of the surface that is defined by g in eq. (32) about hydrostatic axis in principal stress field. Here, direction of creep strain depends on the stress only. Degree of creep s has no relation with the direction.

(5) Method of calculation of creep strain

The strain is evaluated by the calculation that the residual force assumed as load. The residual force is calculated by stress that modified by using decreased p .

3. Simulation of tri-axial confined test

(1) Condition of test and material parameters

The stress modified by the process previously discussed is introduced into the FDM. While, tri-axial confining test with constant axial strain rate so-called loading test and with constant axial load so-called creep test are simulated. Here, one element FDM model is used. Target tests are two^{4), 5)} (Case1 and Case2 each). Sedimentary rock is used as specimen for both tests. Each creep tests of Cases1 and 2, such as 70%, 80%, and 90% loads of peak deviator stress resulted from loading tests is applied. Table 1 shows condition of tri-axial compression tests. Table 2 shows model parameters for calculation. Each parameter is adjusted to fit the results of calculation with tests results. Parameters relevant to the time dependence are α , a_v , b_n , k , c , ϕ , q . Herein, α is assumed 1, and b_n is assumed $a_v/5$ to the straight line length before the time of minimum strain rate in Fig.7 becomes longer. These parameters can be also adjusted separately from residual strength parameters c_r and ϕ_r . It is confirmed by test calculation that Poisson's ratio ν has almost no influence with results. It is assumed $\nu = 0.3$.

Table 1 Conditions of tests.

	unit	Case1 ⁴⁾	Case2 ⁵⁾
Confine stress σ_c (loading, creep test)	MPa	0.6	0.5
Strain rate (loading test)	%/min	0.1	0.01

Table 2 Material parameters.

	unit	Case1	Case1
E (Young's modulus)	MPa	900	900
ν (Poisson's ratio)	-	0.3	0.3
α (Parameter for increase rate of s , set as 1)	1/min	1	1
a_v (mean)	-	400	200
b_n (variance, set as $a_v/5$)	-	80	40
k (spring modulus of rheological model)	-	0.0035	0.01
c (cohesion)	MPa	0.16	0.7
ϕ (friction angle)	drgree	47	47
q (coefficient of sensitivity for stopping time)	1/MPa	22	22
c_r (cohesion of residual stress state)	MPa	0	0
ϕ_r (friction angle of residual stress state)	drgree	51	56

(2) Results

Comparison between calculation and test results of Case1 and Case2 are shown in Fig.14 to 17. From Fig.14 and 16, it is shown that the specific curves of creep rate were simulated satisfactory. The time rapidly strain rate increases, furthermore, were also agreed with that for each case. In Fig.14, the reason of the lines did not continue at tertiary creep is that the overflow of \dot{s} occurred along the iteration for convergence. However, the time of that was considered as frailer time. While, for the loading tests, peak values of each case obtained numerically corresponded well, and strain – stress relations were also fairly agreed. From Fig.18 of the time history of strain, it can be seen the behavior from primary creep to tertiary creep was satisfactory simulated consistently.

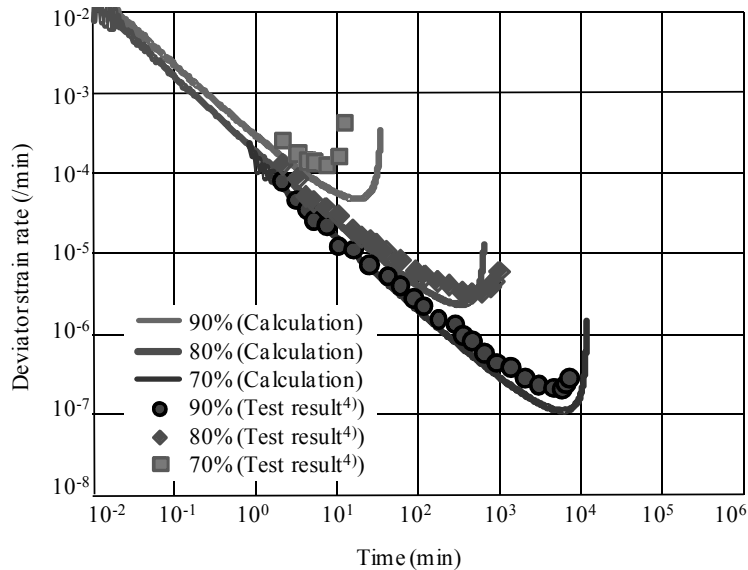


Fig.14 Strain rate by calculation of creep test (Case1, confined pressure $\sigma_c=0.6$ MPa).

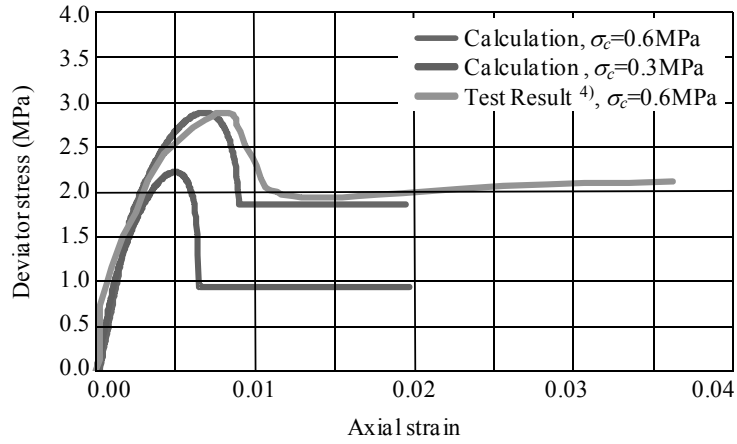


Fig.15 Stress – strain relation by calculation of loading test (Case1, $\sigma_c=0.6$, 0.3MPa).

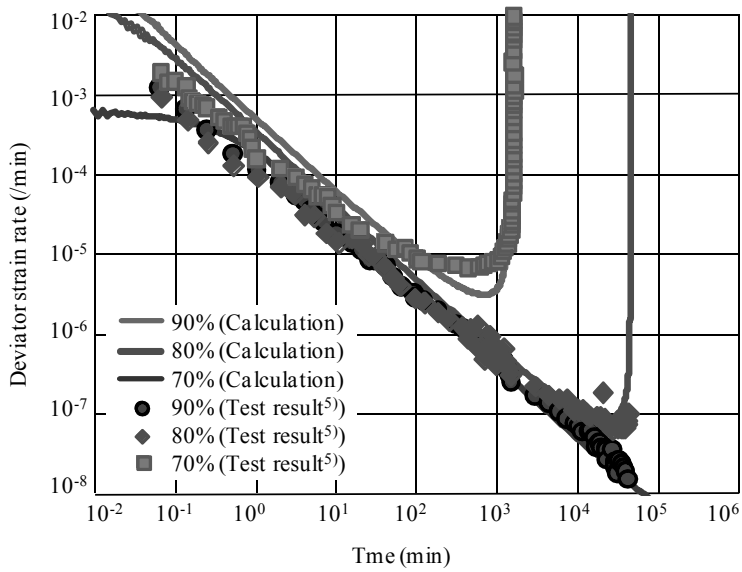


Fig.16 Strain rate by calculation of creep test (Case2, $\sigma_c=0.5$ MPa).

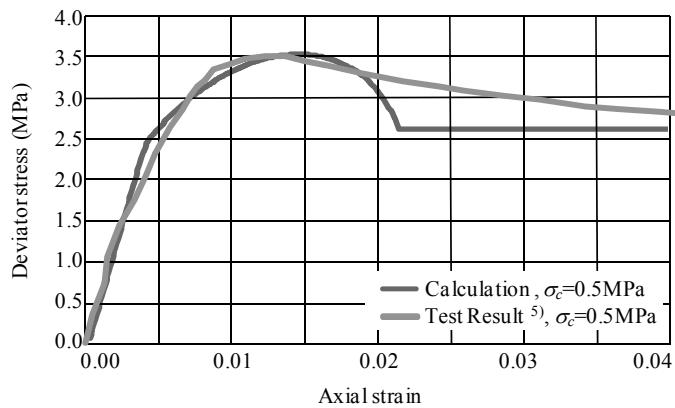


Fig.17 Stress – strain relation by calculation of loading test (Case2, $\sigma_c=0.5$ MPa).

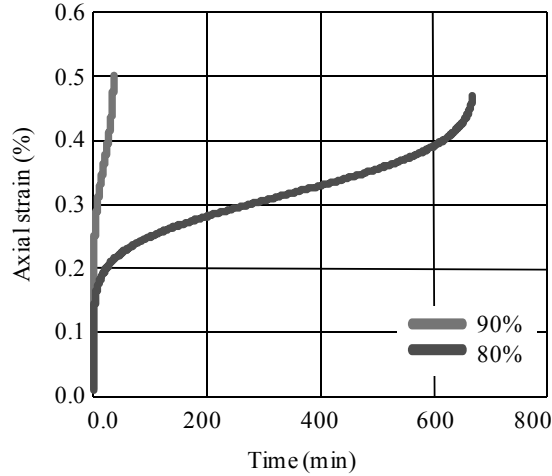


Fig.18 Time history of strain (Case1, $\sigma_c=0.6\text{MPa}$).

Fig.19 shows the relation between strain rate and peak stress obtained numerically relevant to loading test. The peak stress was larger at the region when strain rate became faster. The relation of peak stress and strain rate in dual logarithm graphs was liner, which was caused by the derivation of this relation in eq. (9). Because it is reported that the peak stress is proportional to logarithm strain rate⁶⁾ as described by eq. (44), the relation obtained by calculation is identical to eq. (44).

$$p_j = p_0 + a \log \frac{\dot{\epsilon}}{\dot{\epsilon}_0} \quad (44)$$

where, p_j is deviator stress, p_0 and $\dot{\epsilon}_0$ are basis deviator stress and strain rate, respectively, and, a is gradient of line as shown in Fig.19.

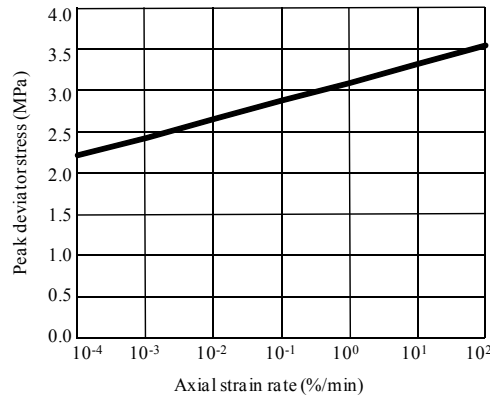


Fig.19 Peak stress vary with strain rate obtained by calculation (Case1, $\sigma_c=0.6\text{MPa}$).

Fig.20 shows the relation of deviatoric stress and the time obtained numerically when strain rate became the minimum for creep test. The time of minimum strain rate increases exponentially with stress decreasing. The liner relation of stress and logarithms time as shown in Fig.20 is also suitable to eq. (9).

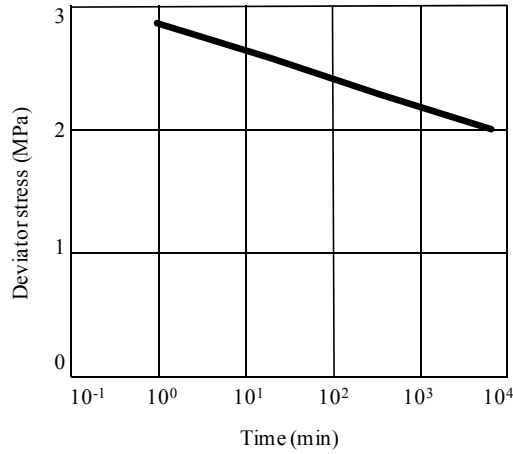


Fig.20 Time at minimum strain rate (Case1, $\sigma_c=0.6\text{MPa}$).

Fig.21 shows an obtained result on the relation of confined stress and peak stress for loading test. It is shown that the peak stress increase linearly with confined stress, which agree with the Mohr – Coulomb failure criterion. The gradient of the line is dependent upon loading strain rate. For example, when loading rate is very slow, peak stress become equal to residual strength, so the gradient coincide with ϕ_r .

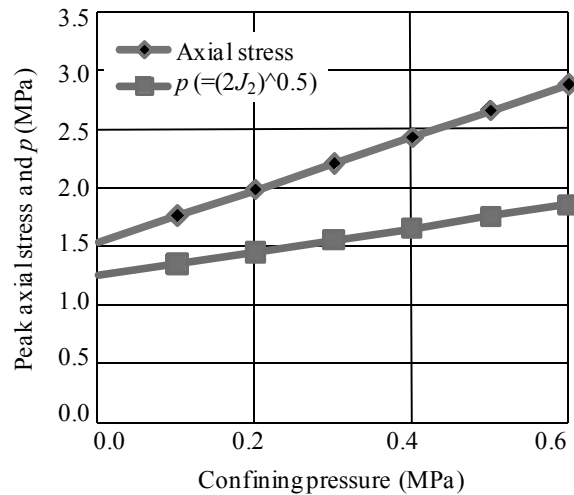


Fig.21 Peak deviator stress vary with confining pressure obtained by calculation (Case1, $\sigma_c=0.6\text{MPa}$).

4. Conclusion

In this paper, a numerical model to evaluate the creep behavior including strain softening of rock is proposed. The predominant parameter s which corresponds to degree of creep development is introduced. To describe the strain rate depend on time or creep strain increase, the function of normal distribution is used as reference. Furthermore, dependence of stress is described by refer to Arrhenius equation. The rheological model consisted of spring and dumper is also developed, which is remarkable that the spring force is equal to deviator stress, to install into the finite difference framework. Numerical simulation for an existing evidence of creep and loading test under the tri-axial confining condition were performed. From creep test simulation, the strain rate curve with primary to tertiary creep was obtained. While, from loading test simulation, stress – strain relation curve with strain softening behavior was also obtained. The both simulation results have a good agreement with test results using same model parameters.

The concern of this model is indicated as follows: The parameter s for the rock, under higher stress than residual stress, absolutely increases. Accordingly, parameter s becomes higher than a_v and then stress approaches to residual stress under natural conditions. However, many creep tests show the creep behavior from primary to tertiary creep. It follows that the initial s of many specimens is lower than a_v . If there is rock that has stress higher than residual strength under natural conditions, it is may be difficult to simulate the

creep behavior of such a rock by using the proposed model herein.

- 1) Adach, T., Oka, F.: An elasto-viscoplastic constitutive model for frozen sand, Proceedings of the JSCE, no.454(III-20), pp.75-81, 1992. (in Japanese)
- 2) Okubo, S., Fukui, K., Hashiba, K.: Extension of constitutive equation of variable compliance type and its validation based on uniaxial compression and tension tests of Sanjome Andesite, Shigen – to – Sozai, Vol. 119, pp.541-546, 2003. (in Japanese)
- 3) Azuma H., Tasaka, Y., Uno, H., Zhang, F, Yasima, A: Improvement of strain softening type elasto-viscouse-plastic model considering confining pressure and strain rate dependency of deformation and strength characteristic, 58th National Science Convention, CS7-056, 2003
- 4) Nishi, K.: Study on elast-plastic behavior of geological materials and application to design of foundations, CRIEPI report, No. 304, pp. 93, 103, 1982. (in Japanese)
- 5) Ohtsuki, H., Tasaka, Y., Suzuki, Y., Ohmori, T., Kishida, K., Adachi, T.: Expansion of a soil-water coupled elasto-visco-plastic model and its application to cavern excavation in soft rock, Proceedings of the 35th Symposium on Rock Mechanics, pp.231-236, 2006. (in Japanese)
- 6) Yong, R. N. and Japp, R. D.: Stress-strain behavior of clays in dynamic compression, vibrational effects of earthquakes on soil and foundations, ASTM, STP, 450, pp.233-262, 1969

Evaluation of the Bolt Axial Force in High Strength Bolted Joints by Using Strain Gauges

Chao PAN^{*}, Takashi YAMAGUCHI^{**} and Yasuo SUZUKI^{***}

(Received October 11, 2011)

Synopsis

In Japan, high strength bolted joints frequently used in steel bridge structures, because high strength bolted joints are easy to joint members than welding from the view point of construction and qualification. On the other hand, performance based design method for bridge structures is being established in Japan to be possible to consider various limit states. Therefore, the high strength bolted connections must be considered various limit states, such as slip state, bearing state, and tearing state. It is important point to understand such behaviors to know the change of bolt axial force at the various limit states. The objective of this study is to collect information of the change of bolt axial force experimentally by using strain gauges in which fastened the connected members until the ultimate limit state and to find the preferable measuring method of it by strain gauges.

KEYWORDS: slip state , bearing state, tearing state ,axial force, strain gauges

1.Introduction

In this study, two methods are taken into consideration. One is the method to glue two strain gauges on the bolt shank and the other is the method to glue the strain gauges on the surface of the bolt head as shown in Fig. 1 respectively. The former method is needed to make two small holes for wires of strain gauges and it is wondering that they might be cut after slip state for friction type connection. The latter method does not need to make holes and less possibility of cutting wires. In order to understand the characteristics of two methods precisely, the experiment and finite element analysis (FEA) has been carried out and discussed about influenced factors, such as the position of glued strain gauges, the measured length of the strain gauge.

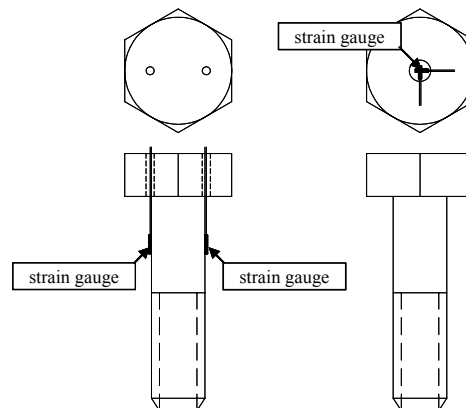


Fig.1 Strain gauges on bolt shank and on head

2. Calibration experiment

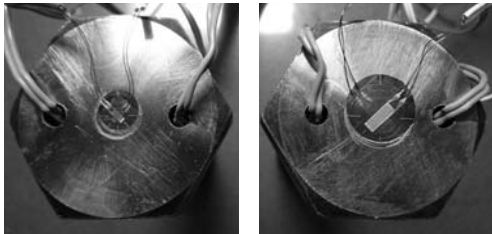
Calibration experiment¹⁾ is conducted to find relationships between load (bolt axial force) and strain (from strain gauge). In experiment, 22mm diameter bolts which grade is 1000MPa are used. Both of the head strain and shank strain were measured by 90° double-element cross strain gauge and single element strain gauge²⁾.

* Student, Doctor Course of Dept. of Civil Engineering, Osaka City University

** Professor, Dept. of Civil Engineering, Osaka City University

*** Associate Professor, Dept. of Civil Engineering, Utsunomiya University

In Fig.2, single element gauge which gage length is 5mm are glued to bolt shank for measuring shank strain. 90° double-element cross strain gauges which gauge length is 2mm/5mm, are used for measuring head strain. Two types of specimens are named, K2 (90° double-element cross strain gauge length 2mm) and K5 (90° double-element cross strain gauge length 2mm) respectively as shown in Fig.3.



(a) length 2mm (b) length 5mm

Fig.2 90° double-element cross strain gauge



(a) specimen K2 (b) specimen K5

Fig.3 Specimen K2 and K5

Specimens are loaded by jigs as show in Fig.4. Each K2 and K5, had executed three times of each specimens. The results are shown in Fig.5 and Fig.6 . Fig.5 shows a results of load versus head strain curves and Fig.6 shows results of load versus shank strain.

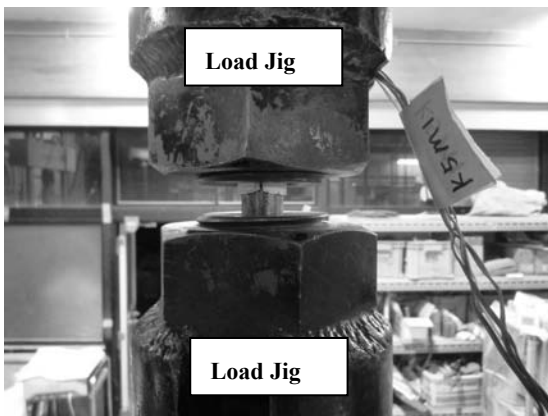


Fig.4 Calibration experiment

Each of load versus strain relationships (which is measured by head strain gauge and shank strain gauge) is alignment as show in Fig. 5 and Fig. 6. Variation of gradient of the curve from head strain is larger than that from shank strain . The results of calibration experiment also show in Table.1 for discussion.

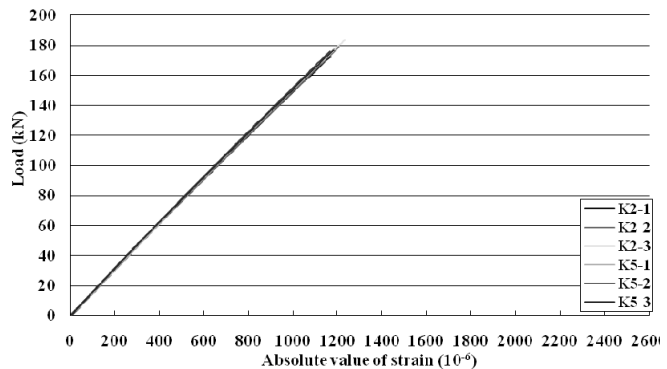


Fig.5 Load versus head strain

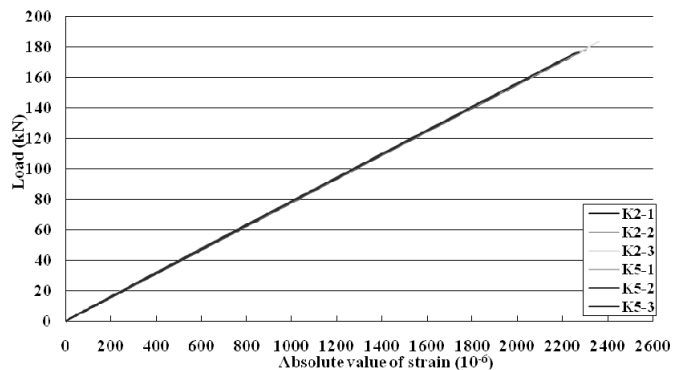


Fig.6 Load versus shank strain

Table.1 Statistics of K2 and K5

	K2		K5	
	Load/ Shank strain	Load/ Head strain	Load/ Shank strain	Load/ Head strain
Average value	77.56	147.29	77.65	149.33
Standard deviation	0.18	1.07	0.14	0.98
Coefficient of variation	0.0024	0.0073	0.0018	0.0066

In Table.1, the accuracy of the measurement results of strain by shank and head strain gauge are compared. In the results of specimen K2, the standard deviation of load/shank strain is 80% off than the standard deviation of load/head strain, the coefficient of variation is 65% off. In the results of specimen K5, the standard deviation of load/shank strain is 85% off than the standard deviation of load/head strain, the coefficient of variation is 70% off. By the results, the accuracy of the measurement by using shank strain is better than that by using head strain. Comparing the length of head strain gauge for accuracy of the measurement, 5mm length (K5) is better than 2mm length (K2).

3.Finite element analysis (FEA)

Finite element analysis (FEA) is conducted to simulate bolt that is fastened in bolt hole. Two case were set, bolt is fastened on bolt hole axial or off bolt hole axial. FEA software ABAQUS³⁾ is used in this study. In the case of bolt off bolt hole axial, bolt axial offside bolt hole axial 2mm are set. FEA model is show in Fig.7.

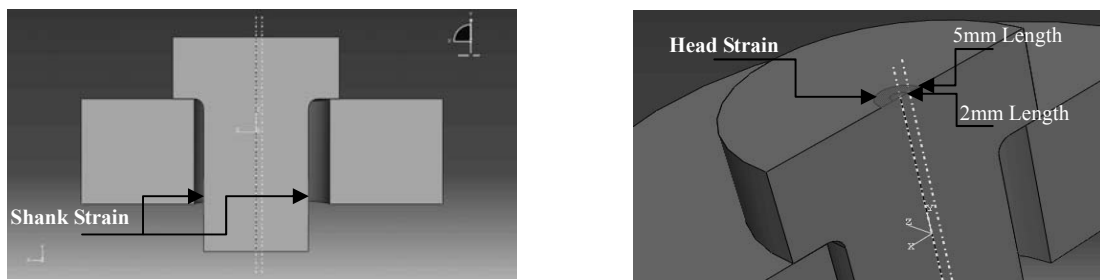


Fig.7 FEA model

The FEA result and experimental result are shown with bolt axial force versus shank strain in Fig.8. Bolt axial force versus head strain (2mm strain gauge length) show in Fig.9. Bolt axial force versus head strain (5mm strain gauge length) show in Fig.10.

In Fig.8, both FEA results and experimental results are on a same line. It means that accuracy of the measurement by shank strain got a better quality. Other results show in Fig.9 and Fig.10.

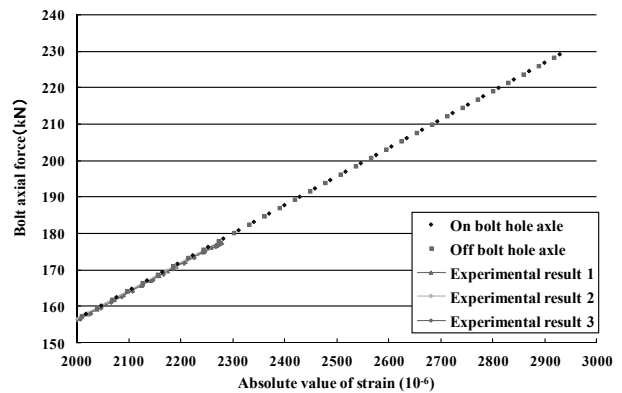


Fig.8 Bolt axial force versus shank strain

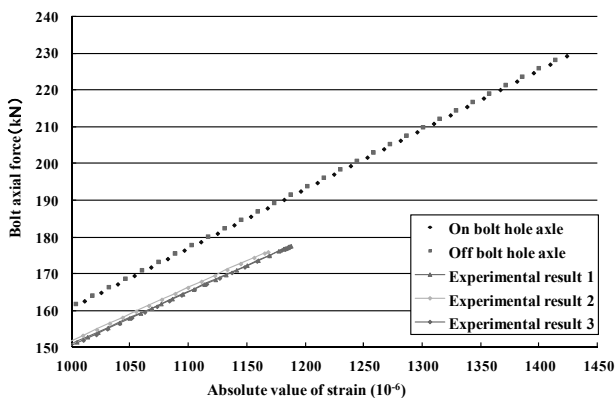


Fig.9 Bolt axial force versus head strain (2mm)

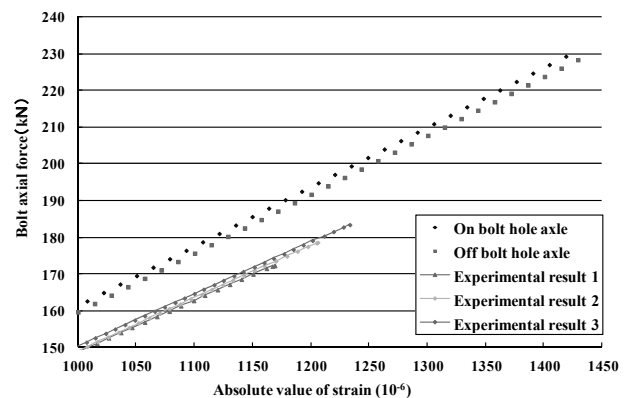


Fig.10 Bolt axial force versus head strain (5mm)

Table.2 Statistics of head strain and shank strain

	Head (gauge length 2mm)		Head (gauge length 5mm)	
	on bolt hole axial	off bolt hole axial	on bolt hole axial	off bolt hole axial
Load/Head strain	161.52	159.72	161.02	161.51
Average value	160.62		161.26	
Standard deviation	0.90		0.24	
Coefficient of variation	0.0056		0.0015	
	Shank			
	on bolt hole axial	off bolt hole axial		
Load/Shank strain	78.35	78.31		
Average value	78.33			
Standard deviation	0.02			
Coefficient of variation	0.0003			

Table.2 show statistics of head strain and shank strain by FEA. In Table.2, the standard deviation value of shank strain which is 95% off than head strain, the coefficient of variation of shank strain which is 90% off than head strain. By the result, using shank strain can get a very good accuracy of the measurement. However, using head strain can't get accuracy of the measurement as good as shank strain, but between gauge length 2mm and gauge length 5mm, gauge length 5mm get a better accuracy of the measurement than gauge length 2mm.

4. Fasten experiment

Actually, bolt is fastened by a torque wrench⁴⁾. In this experiment, use a torque wrench to fasten each specimen, that which can just fasten bolt by need torque value. Same bolts (22mm diameter 1000MPa grade high strength bolt) are used for the specimen for K2 and K5. Three specimens are used to get shank strain by 5mm length single element gauge, named shank strain 1,2,3. The other three specimens are used to get head strain by 5mm length 90° double-element cross strain gauge, named head strain 1,2,3. Use load/strain relation to convert that both shank strain and head strain to bolt axial force. Plot equivalent bolt axial force versus torque in Fig.11. Input torque values are set from 100 N · m to 800N · m, each per 100 N · m are raised.

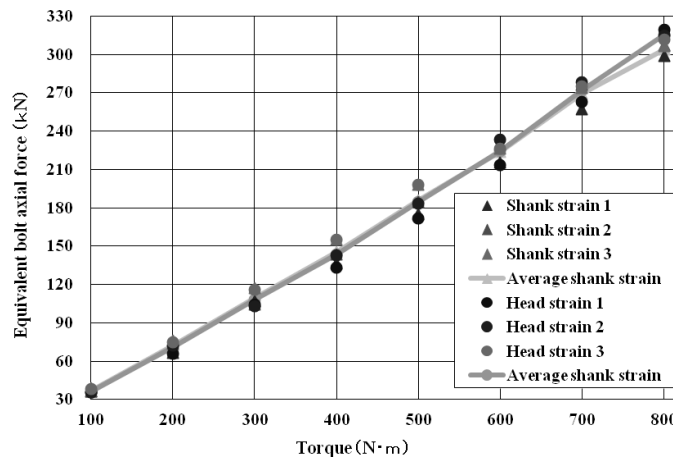


Fig.11. Bolt axial force versus torque

In Fig.11, under 600 N · m torque value, both shank strain and head strain average value nearly on a same line . Over 600 N · m torque value, the equivalent bolt axial force by measuring from head strain gauge, is larger than the equivalent bolt axial force by measuring from shank strain gauge. At 800 N · m torque value, the equivalent bolt axial force of head strain is larger than the equivalent bolt axial force of shank strain. Therefore, both the two way under torque value 600 N · m, can put out a nice equivalent bolt axial force.

5. Conclusion

The main results of the present study are summarized as followings:

- 1) The method of measuring bolt shank strain by 5mm length single element gauge, it can get higher precision to convert bolt axial force than measuring bolt head strain by 90° double-element cross strain gauge. Even if bolt is fastened off bolt hole axial, it also can get high precision.
- 2) In the method of measuring bolt head strain by 90° double-element cross strain gauge, the gauge length of 5mm is recommended, because it can get higher precision than gauge length 2mm.
- 3) On bolt bearing state, the method of measuring bolt head strain by 5mm length 90° double-element cross strain gauge is recommended, because it don't about cutting wires.

6. References

- 1) Recommendations on Design, Construction and Maintenance for Friction Type of High Strength Bolted Connections, *Subcommittee on Design of Friction Type of High Strength Bolted Connections Committee on Steel Structures Japan Society of Civil Engineers, December 2006* .
- 2) Specifications for Highway Bridges, *Japan Road Association, 2002*.
- 3) ABAQUS Analysis User's Manual. *SIMULIA*.
- 4) Preset Type Torque Wrench Instruction Manual, *MAEDA Metal Industries, LTD*

Finite Element Analysis on the Mechanical Behavior of High Strength Bolted Friction Type Joints Considering Fluctuation of Bolt Axial Forces

Xue PENG* and Takashi YAMAGUCHI**

(Received October 11, 2011)

Synopsis

Recent years, from the viewpoint of rational fabrication of the steel bridges, there are some applications using extremely thick plates for primary members of bridge structures. In case of joining such thick plates by using high strength bolted friction type joints, the bolt axial force is specified by the design code. However, the actual bolt axial force tightened is varied, and then mechanical behavior of such multiple joints is not clear. In this study, the finite element analysis (FEA) for such joints has been carried out in order to investigate the mechanical behavior considering fluctuation of bolt axial forces..

KEYWORDS: extremely thick steel plates, high strength bolted friction type joint, many bolts in a line, variation of the bolt axial force, slip coefficient

1. Introduction

Recent years, from the viewpoint of rational fabrication of steel bridges, there are some examples to use extremely thick plates for primary members. In case of joining such thick plates, welding are ordinary used. However, the cost of welding will increase due to its qualification. On the other hand, joints with high strength bolts are not adopted in general due to lack of enough technical information of them.

In order to solve these problems, the experiment¹⁾²⁾ and FEA³⁾ had been carried out in these years. In case of joining such thick plates by using high strength bolted friction type joints, the bolt axial force is specified by the design code. However, the actual bolt axial force tightened is not the constant value specified by the design code, and mechanical behavior of such multiple joints is not clear. In this study, FEA has been conducted in order to understand the influence of the variation of the bolt axial forces to its mechanical behavior.

2. FEA model

2.1 General

In this study, the FEA program ABAQUS has been used. The connected plate, splice plate and high strength bolt are meshed by solid elements of 8 nodes. The material property is referred to the experimental data²⁾. The surface boundary which can simulate contact are installed between the connected plate and splice plate, the connected plate and the splice plate and bolt. The friction coefficient is assumed

* Student, Doctor Course of Dept. of Civil Engineering Osaka City University

** Professor, Dept. of Civil Engineering Osaka City University

0.5 in the FEA model. There are two steps for the model advancing. The first step is that the connected plate and splice plate are tightened by high strength bolts, and the second step is that tensile load is applied at the edge of the model.

2.2 FEA model

The FEA model is 1/8 of experimental specimen²⁾ as shown in Fig. 1. The thickness of the connected plate is 50mm, the thickness of the splice plate is 28mm, and the size of bolt is M16. Structural dimensions of all models are tabulated in Table 1. The first character set of model's name denotes nominal diameter of bolt, the second character set denotes the number of the bolts in a line, and the third character set denotes slip/yielding strength ratio β . The last character set denotes the number of bolts with 120% bolt axial force. For example, M16-4-0.72-1 means; the bolt is M16, the number of bolts in a line is 4, the slip/yielding strength ratio β is 0.72, and the bolt number with 120% bolt axial force is bolt1.

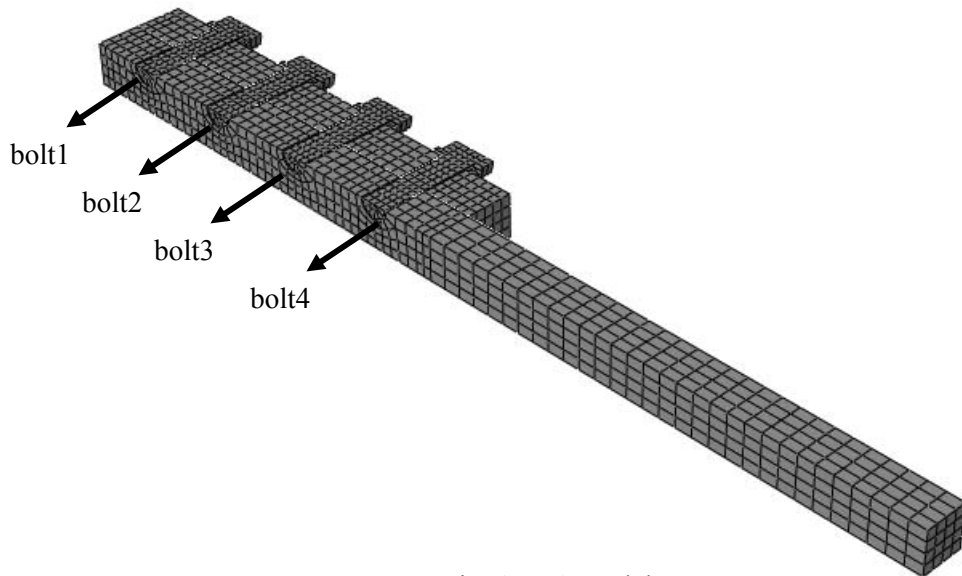


Fig. 1 FEA model

Table 1 Structural dimensions of all models

Specimen's name	M16-4-0.72	M16-4-0.72-1	M16-4-0.72-4	M16-8-0.72	M16-8-0.72-1	M16-8-0.72-4	M16-8-0.72-8
Nominal diameter of bolts	16	16	16	16	16	16	16
Steel grade	SM490	SM490	SM490	SM490	SM490	SM490	SM490
Yield stress (N/mm ²)	295	295	295	295	295	295	295
Thickness of connected plate(mm)	50	50	50	50	50	50	50
Thickness of splice plate(mm)	28	28	28	28	28	28	28
Width of the plate (mm)	50	50	50	82	82	82	82
friction coefficient	0.5	0.5	0.5	0.5	0.5	0.5	0.5
bolt axial force (kN)	bolt1	106	127	106	106	127	106
	bolt2	106	106	106	106	106	106
	bolt3	106	106	106	106	106	106
	bolt4	106	106	127	106	106	127
	bolt5	-	-	-	106	106	106
	bolt6	-	-	-	106	106	106
	bolt7	-	-	-	106	106	106
	bolt8	-	-	-	106	106	106

3. FEA results and discussion

3.1 Load vs. Relative Displacement between the connected plate and splice plate.

Table 2 shows the summary of FEA results. There are slip load, slip coefficient, and reduction rate of bolt axial force. Fig. 2 shows location of relative displacement between the connected plate and splice plate. And Slip occurrence is defined by the relative displacement when it has been reached 0.2mm in Fig. 3. Slip coefficient equal the ratio of slip load divided by design bolt axial force. Fig. 4 shows the curves of load vs. relative displacement between the connected plate and splice plate. The vertical axis shows the tensile load P , and the horizontal axis shows relative displacements. From Fig. 4, whichever bolt was tightened by 120% bolt axial force, the slip load of model is constant as the number of the bolt in a line is same. It is also found that slip load become high as bolt axial force tightened increase. And, comparing model M16-4-0.72, the slip coefficient of model M16-4-0.72-1 and M16-4-0.72-4 increase 5.2%. Comparing model M16-8-0.72, the slip coefficient of model M16-8-0.72-1, M16-8-0.72-4, and M16-8-0.72-8 increase 2.5%. However, focusing on the slip coefficient evaluated by bolt axial force before loading, in case of 4 or 8 rows, slip coefficients are constant.

Table 2 Summary of FEA results

Specimen's name	M16-4-0.72	M16-4-0.72-1	M16-4-0.72-4	M16-8-0.72	M16-8-0.72-1	M16-8-0.72-4	M16-8-0.72-8
Slip load P_{SL} (kN)	408.3	428.8	428.8	817.5	837.8	838.0	838.0
Slip coefficient μ	0.481	0.506	0.506	0.482	0.494	0.494	0.494
Reduction rate of bolt axial force (%)	bolt1	4.8	4.5	5.1	5.9	5.6	6.1
	bolt2	3.9	4.0	4.1	5.1	5.2	5.3
	bolt3	3.8	3.9	4.0	4.9	5.0	5.1
	bolt4	3.1	3.3	2.8	4.8	4.9	4.2
	bolt5	-	-	-	4.6	4.7	4.7
	bolt6	-	-	-	4.5	4.6	4.6
	bolt7	-	-	-	4.3	4.4	4.4
	bolt8	-	-	-	4.1	4.2	4.2

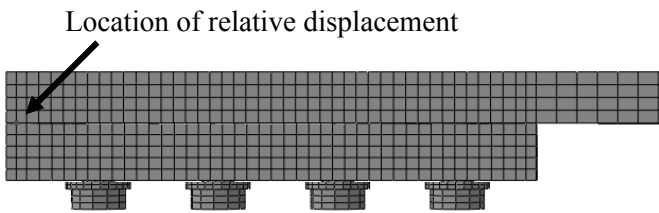


Fig.2 Location of relative displacement

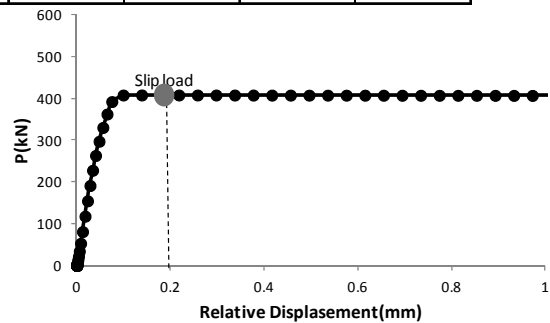
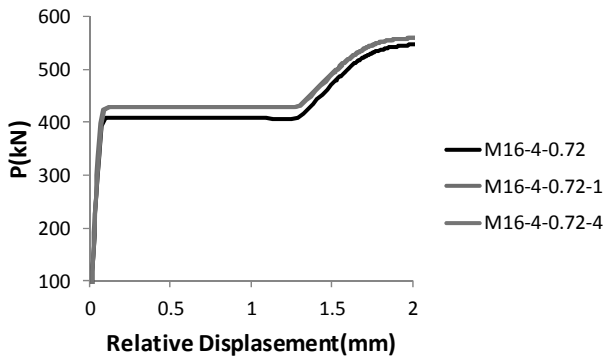
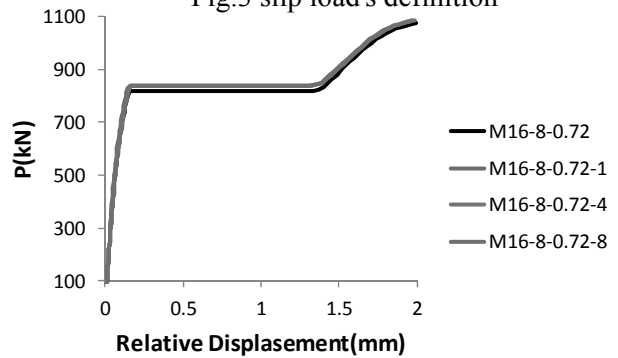


Fig.3 slip load's definition



(a) M16-4-0.72



(b) M16-8-0.72

Fig. 4 Load vs. relative displacement curves

3.2 Reduction rate of bolt axial force

Reduction rates of each bolt axial force at slip load are shown in Fig. 5. The horizontal axis shows the bolt number as shown in Fig. 1. In this figure, reduction rate means normalized decrease of bolt axial force at slip divided by bolt axial force before loading. It is confirmed that reduction rate of bolt axial force with 120% bolt axial force is smaller than that with 100% bolt axial force. Comparing the model that the bolt number in a line is 4, the reduction rate of bolt axial force of model that the bolt number in a line is 8 become high. The reason is plate stress of in model of 4 rows become higher than that in model of 8 rows.

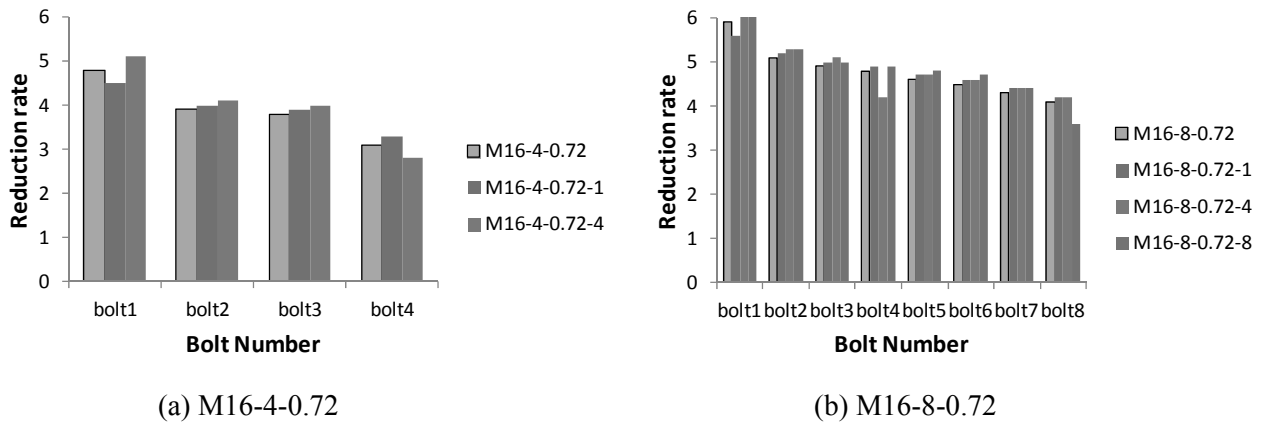


Fig. 5 Reduction rate of bolt axial force

3.3 Stress distribution along the plate's axial direction

Fig. 6 shows stress distribution along the plate's axial direction of models which has four bolts in a line. Fig. 7 shows stress distribution along the plate's axial direction of models which has 8 bolts in a line. It can be found that stress along the plate's axial direction of M16-4-0.72 smaller than that of M16-8-0.72. Also, about model M16-8-0.72, local yielding has occurred at the neighborhood of the bolt1.

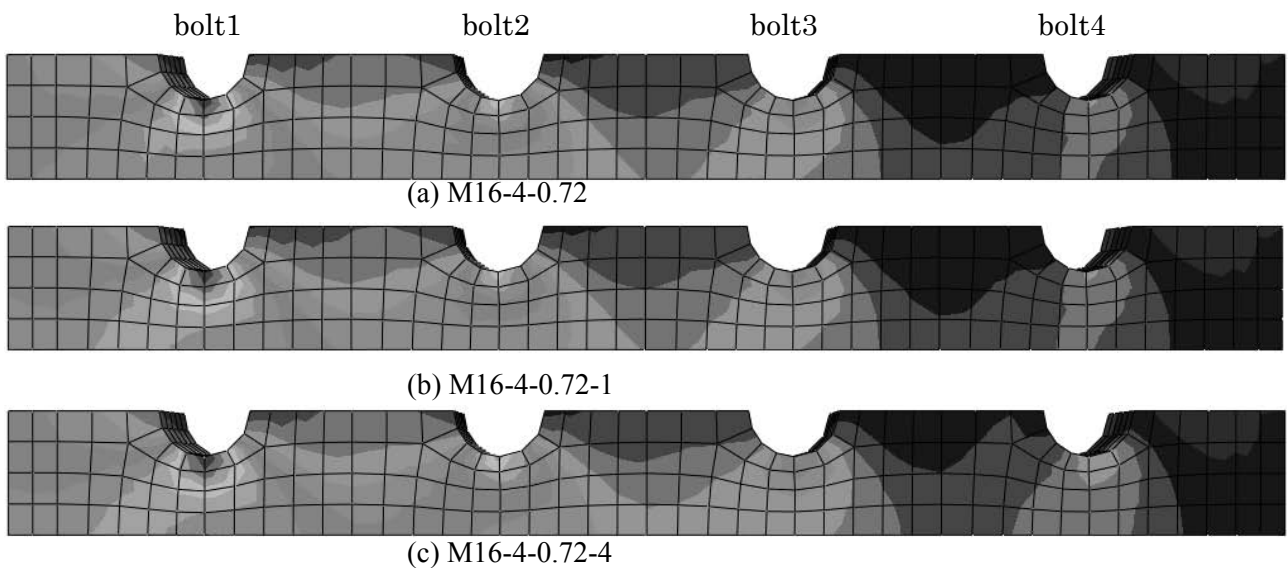


Fig. 6 Stress distribution along the plate's axial direction

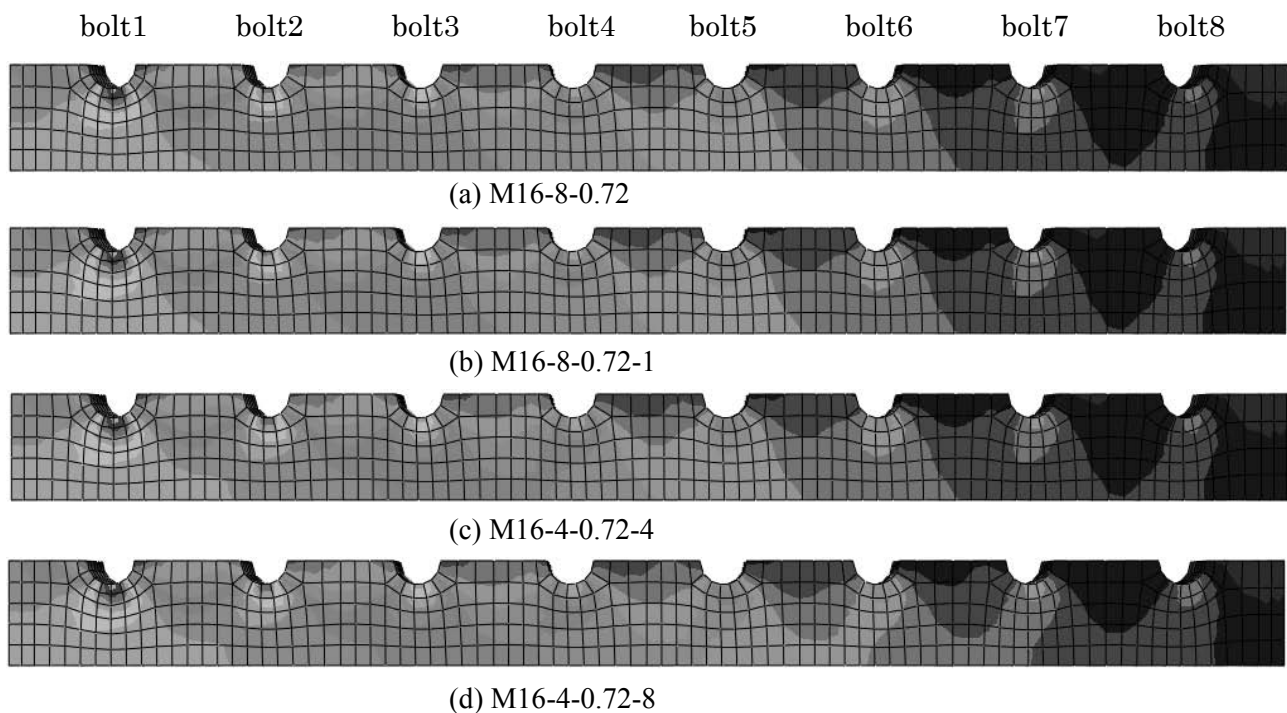


Fig. 7 Stress distribution along the plate's axial direction

4. Concluding remarks

In this study, the finite element analysis (FEA) for high strength bolted friction type joints has been carried out to understand the mechanical behavior of them. As the bolt axial force tightened is various, obtained concluding remarks are as followings:

- (1) Focusing on slip coefficient evaluated by design bolt axial force, in model of 4 rows, slip coefficient is higher than that of 8 rows. However, focusing on slip coefficient evaluated by bolt axial force tightened, in model of 4 or 8 rows, slip coefficient is constant.
- (2) For model that bolt number in a line is 4 or 8, as relative displacement is 0.2mm, the major slip has occurred. So that, the fluctuation of variation of the bolt axial force is small.

5. References

- 1) Xue Peng, Takashi Yamaguchi, Masahide Matsumura, Jun Murakoshi, Naoki Yanadori, Tosiki Yshizawa: Experimental study on the slip behavior of high strength bolted friction type joints with many bolts in a line and extremely thick plate, Japan Society of Civil Engineers 2010 Annual Meeting, I-471.
- 2) Takashi Yamaguchi, Xue Peng, Yasuo Suzuki, Shuhei Miyao: Experimental study on the mechanical behavior of high strength bolted friction type joints with extremely thick plates and many bolts in a line, Japanese Society of Steel Construction, Vol.17, No.66, 2010.
- 3) Xue Peng, Takashi Yamaguchi, Jun Murakoshi, Mamoru Sawada, Naoki Toyama, Atsuo Ookate: Finite element analysis study on the slip behavior of high strength bolted friction type joints with many bolts in a line and extremely thick plate, Japan Society of Civil Engineers 2011 Annual Meeting, I-252.

An Analysis on Influence of Regional and Individual Conditions to Intended Needs and Actual Demands of Bus Service

Naoki OKAMOTO* and Yasuo HINO**

(Received September 30, 2011)

Synopsis

Recently, the vicious circle of decline of bus service and decrease of bus passengers has become remarkable, as the automobile-based life style has popularized with progress of motorization. On the other hand, the mobility of aged people has become important and serious problems because of progress aging society. Therefore, many local governments tried to introduce bus services depended on public subsidy into the inconvenient areas on public transport service¹⁾. However, as the bus passengers must be limited, there are not few cases that were not sustainable due to increase of subsidy.

In this study, the influence of regional and individual conditions to intended needs and actual demands of bus service was analyzed through the experimental case study^{2), 3)}. As a result, some interesting findings came out as follows; 1) the number of actual bus passengers may be estimated as a half of the number of persons intended needs for bus, because many residents did not consider the cost subsidized by tax, but 2) some intended needs with obligated purpose and/or without any alternative modes must be actual demands, and also the service level as the distance to bus stop must influence to actual use.

KEYWORDS: Bus service, Social experiment, Needs and actual demands, Questionnaire survey

1. Introduction

In order to secure the mobility of vulnerable people, some of bus services have been supported by the cooperation of bus company, local government and academic staff. In such cases, it is general that an experimental bus service may be introduced based on the intended needs of bus use which will be obtained by a questionnaire survey. And also, it is true the number of actual demands may be a half of the number of intended needs. Therefore, it is not easy to continue the experimental bus service. That is, it must be important to correctly evaluate the actual demands based on the estimation by analyzing the intended needs from the questionnaire survey.

Then in this study, the relation between the intended needs and the actual demands was analyzed through the before-after analysis, as a case study of the experimental bus service in Kawachi-nagano City located at the south-east area of Osaka Prefecture, Japan. And also, the estimation method of the actual demands of bus use was referred based on the results of the questionnaire survey.

2. Case study

The case study area was the mountain area located at the suburb of the city. This area has 900 population including 26% aged people, and was divided into three zones as shown in Figure-1.

*Student, Master Course of Department of Civil Engineering

**Professor, Department of Civil Engineering

As the longest distance between residences and bus stops of the existing bus route was 1.1km, this area was defined as the inconvenience on public transport service. Therefore, the local government intended to introduce the experimental bus service with no fare to improve the inconvenience of this area. Then the questionnaire survey was executed to estimate the needs before introducing this bus service. As the average number of the intended needs for bus use was 40%-80% according to the location of zone, the circular service to connect the existing bus route was introduced during the limited period. The concern of local government must be put on the actual demands in order to evaluate this bus service. That is, it should be important to reveal how many persons of intended needs became the actual passengers of this bus service.

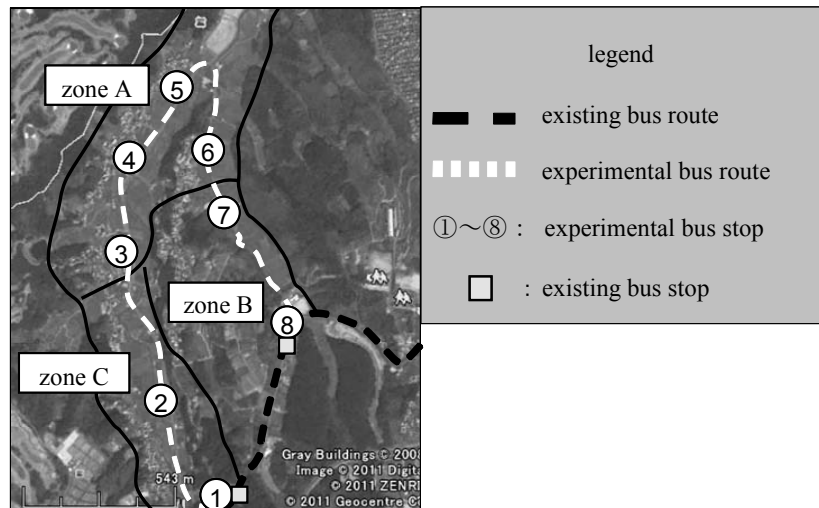


Figure-1 Case study area and bus route

Questionnaire surveys were planned twice before and after introducing the experimental bus service as shown in Table-1. Questionnaires were distributed to residents over the age of primary child, 38 and 64% of respondents were obtained. At the before survey, the ratio of respondents was lower because of the lack of reality for this bus service.

Table-1 Outline of questionnaire survey

	before survey	after survey
implementation	December, 2009	June-July, 2010
distribution/collection	posting	
target	residents of primary school children and older	
distributed	880	1000
repondents	289	640
collected ratio	32.8%	64.0%

3. Analysis of relation between intended needs and actual demands

Here, in order to understand the results of analyses after this section, we define the difference between the intended needs and the actual demands, as follows.

- 1) The intended needs mean the number of respondents who show intention of use after introducing the bus service.
- 2) The actual demands show the actual users as passengers of bus service.

It is clear that the actual demands were 60-80% of the intended needs and both number are

depended on the location of zone as shown in Figure-2. Then, in order to estimate the bus passengers (actual demands) based on the intended needs before introducing the bus service, these differences must be investigated by using some factors which influence to bus use.

Table-2 shows the shortened distance from residence to bus stop of the experimental bus service. From Figure-2 and Table-2, it should be clear that both ratio of actual demands and intended needs were higher in zone-A where is far from the existing bus stop.

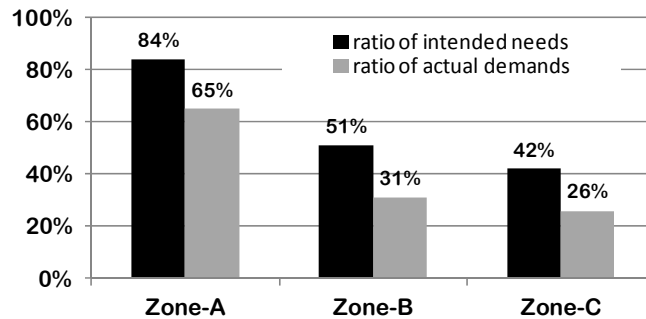


Figure-2 Intended needs and actual demands by each zone

Then, we analyzed the relation between the shortened distances as the improvement level of convenience and the ratio of realization of intended needs, as shown in Figure-3. As a result, some major findings came out of this analysis as follows.

- 1) The larger the shortened distance become, the higher the ratio of intended needs and actual users become.
- 2) The ratio of actual users (demands) realized from intended needs must be high in case of 300m or over of shortened distance.

Table-2 Shortened distance by using experimental bus use

Zone	Location of residence for bus stop	distance to existing bus stop(m)	distance to experimental bus stop(m)	shortened distance(m)	average (m)
A	most far	1050	170	880	600
	nearest	520	200	320	
B	most far	720	160	560	280
	nearest	120	120	0	
C	most far	530	290	240	200
	nearest	380	220	160	

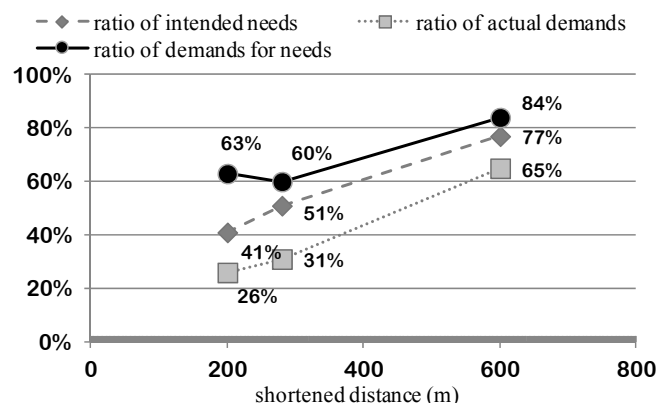


Figure-3 Change of needs and demands according to shortened distance by using bus service

Next, the relation between the intended needs and actual demands was directly analyzed as shown in Figure-4. It is easy to distinguish the difference of results between zone-A and others. That is, the result of zone-A shows the linear relation of them. On the other hand, the relation of them in zone-B and C is not correlative and rather constant in spite of the ratio of intended needs. Here we have to note the peculiar point of zone-C which is the value of respondents for school children who need bus services for going to school.

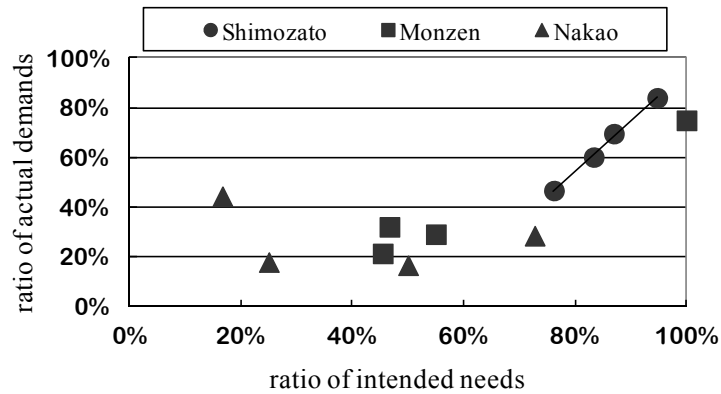


Figure-4 Relation between intended needs and actual demands

Then the relation between the shortened distance and the ratio of intended needs and actual demands were analyzed, as shown in Figure-5, 6. From these figures, three major findings came out as follows.

- 1) The needs of school children for bus service are remarkably high, because they have to go to school.
- 2) The results of elderly people show the high necessity of bus service, because many of them have to go to hospital.
- 3) Most respondents except school children and elderly people show the intention according to the shortened distance.

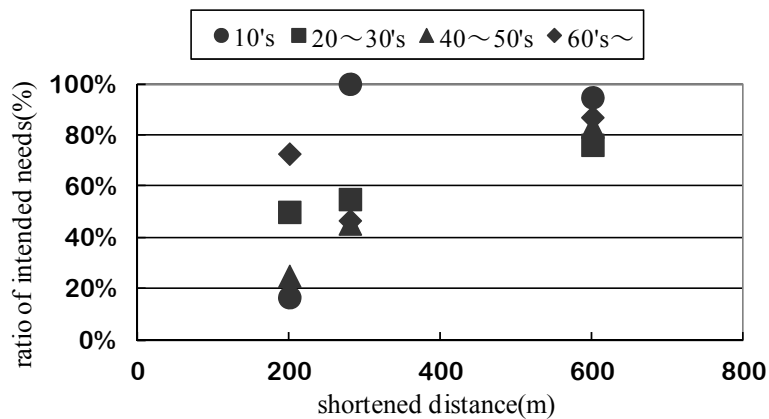


Figure-5 Intended needs according to shortened distance by age rank

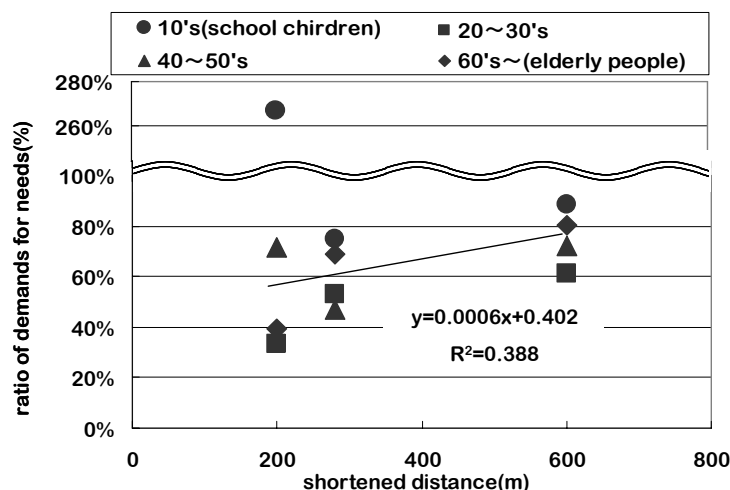


Figure-6 Ratio of demands for needs according to shortened distance by age rank

4. Actual demands for necessity of school children and elderly people

Generally, the public service with no charge may be acceptable for many people. However, these needs must be depended on the intention to only keep the service, as shown in some results mentioned above. On the other hand, it was revealed that there were some cases with the high necessity for bus service according to the specified purposes by age rank.

Table-3 shows the cases of relatively high ratio of needs and demands. Here, we can confirm the necessity for bus in case of going to school. However as for medical use, both needs and demands are not always high. This trend may be depended on the possibility of alternative modes and the lower convenience than expected convenience. On the other hand, the ratio of actual demands for shopping was higher than the ratio of intended needs. This trend means some people may evaluate the importance of convenience for shopping use.

Table-3 Comparison of needs and demands for school children and elderly people

	purpose	1) shortend distance (m)	2) ratio of intended need (%)	3) ratio of actual demands (%)	3)-2)
10's as school chirdren	school	600	72.2	80.6	8.4
		280	100.0	100.0	0.0
		200	0.0	75.0	75.0
60's and more as elderly people	hospital	600	42.9	25.0	-17.9
		280	40.0	23.5	-16.5
		200	50.0	45.5	-4.5
	shopping	600	36.7	43.0	6.3
		280	40.0	41.2	1.2
		200	25.0	36.4	11.4

5. Summary and next step

Some major findings concerned with the relation between intended needs and actual demands of bus use came out of this study as follows.

- 1) It is clear that the actual demands were 60-80% of the intended needs and both number are depended on the location of zone. That is, both ratio of actual users and intended needs were higher in the zone where is far from the existing bus stop.

- 2) The larger the shortened distance become, the higher the ratio of intended needs and actual users become. Especially, the ratio of actual users (demands) realized from intended needs must be high in case of 300m or over of shortened distance.
- 3) It is easy to distinguish the difference of the relation between the intended needs and actual demands among zones. That is, the result of zone which was located far from the existing bus stop shows the linear relation of them. On the other hand, the relation of them in other zones which were near the bus stop is rather constant in spite of the ratio of intended needs.
- 4) The needs of school children for bus service are remarkably high, because they have to go to school. And elderly people show the high necessity of bus service to go to hospital.
- 5) Although the public bus service with no charge may be generally acceptable for many people, these needs must be depended on the intention to only keep the service.
- 6) It was revealed that there were some cases with the high necessity for bus service according to the specified purposes by age rank. However, this trend may be depended on the possibility of using alternative modes and the level of convenience in comparison with the expected convenience

These findings may be useful not only to introduce an experimental bus service but also to consult with residents who need bus service. That is, these data will be able to help residents to understand that the actual demands will not always expected even if the intended needs are observed in the questionnaire survey before introducing bus service. On the other hand, local government will be able to make plans for bus services to improve the inconvenient areas on public transport.

6. Acknowledgement

This study was implemented as a part of a joint research with Kawachi-nagano city. We would like to thank members of research group, cooperators in the questionnaire surveys.

7. References

- 1) Noboru Ise and Yasuo Hino: A Modeling for a Lifecycle of Housing Estate based on Change of Resident's Life Stage, The City Planning Institute of Japan, City Planning Review, No.43-3, pp.493-498, 2008 (In Japanese)
- 2) Noboru ISE, Yasuo HINO and Koichi KAWASAKI: Investigation of Bus Demand and Service in Future based on Lifecycle Model and Scenario Analysis, EASTS, Proceedings of the Eastern Asia Society for Transportation Studies, Vol.7, 13pages, 2009
- 3) Naoki OKAMOTO, Yasuo HINO, Noboru ISE and Yutaka TAWA: A Study on Relationship between Intention and Actual Need for Experimental Bas Service in Inconvenient Area on Public Transport, Japan Society of Civil Engineers, Kansai Chapter, Proceedings of the Annual Conference of JSCE Kansai Chapter, IV-48, 2011 (In Japanese)

Waterfront Functions Required from a Ship Transport Perspective

Yasumasa FUKUSHIMA* and Takashi UCHIDA**

(Received September 30, 2011)

Synopsis

Waterfronts perform various functions such as sites of ‘bustling’ and ‘healing’. From the viewpoint of the involvement of river area residents with rivers, it is important to develop waterfronts utilizing these functions. Devoting attention to needs related to ship transport which used to be an important interface between river and residents along the Yodo River, this study elucidates concrete measures for activation of ship transport and investigates functions that are required at the waterfront of the Yodo River.

KEYWORDS: waterfront development, river ship transport, activation of ship transport, wharf, crisis management

1. Background and Objectives of Research

In recent years, the maintenance of urban rivers involves activities for waterfront development that include environment improvement and recreational utilization, in addition to flood control and water utilization. However, no method for waterfront development that is suitable for urban rivers has been established to date, because conditions and environments for the development include diverse and complicated factors for every river and region.

This study, with examination from perspectives of facility, utilization, landscape, and social involvement, advances research for the overall concept of waterfront development in urban rivers. By using questionnaire/hearing survey results, current problems are examined according to needs for ship transport which used to be an important interface between river area residents and the old Yodo River. Then the orientation of functions necessary for the waterfront at present is investigated. Concrete measures for the activation of ship transport are discussed.

Since ancient times, the Yodo River has served as a main artery of ship transport, supplying needs for goods distribution and passenger transportation between Osaka Bay and the Kyoto area. At the zenith of its prosperity, from the Muromachi Period to the Edo Period (until 19th century), more than 1,000 vessels (Sanjukkoku-bune junks, Kurawanka-bune junks, and river ferries; see Figure 1) came and went along the river; the wharfs and posting stations which served as their bases were invariably crowded¹⁾. However, at the end of the Meiji Period (early 20th century), ship transport started to follow a course of decline after land transportation was developed because of provisions and improvements of railroads and roads. At present,

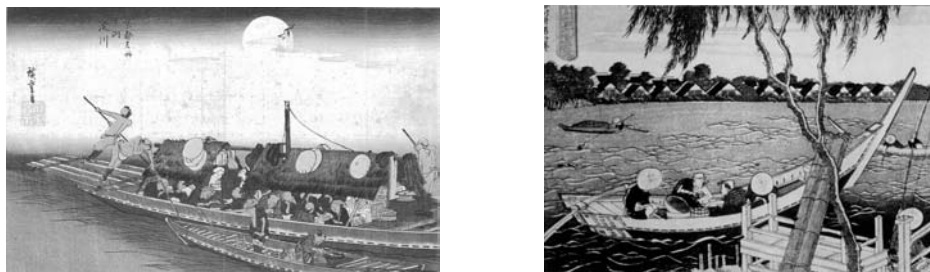


Figure 1 Left: Sanjukkoku-bune junk and Kurawanka-bune junk (“Yodo River”, *Kyoto Beauty Spots*, painted by Hiroshige). Right: Landscape of ferry (“Miyado River, Naganawa”, *Chienoumi*, painted by Hokusai).

* Student, Doctor Course of Department of Civil Engineering

** Associate Professor, Department of Civil Engineering

their connection with residents and society has become extremely tenuous. Recently, ship transport is being reconsidered for sightseeing purposes during normal times and as an alternative transportation in land traffic paralysis in a wide-scale disaster such as an earthquake. Various measures are now being promoted towards the activation of ship transport. The reality, however, is that only gravel carriers and unscheduled sightseeing ships are operating, which have not become a part of people's lives

2. Present Needs and Problems related to Ship Transport

2.1 Ship transport needs

We use the result summary of investigations performed by the Yodo River Office, Kinki Regional Development Bureau to ascertain needs for ship transport along the river²⁾. This investigation was conducted to examine basic concepts for evaluating ship transport and to obtain basic data for preparation of a 'Target picture of ship transport along the Yodo River (draft)'. The objective is to elucidate needs related to ship transport along the Yodo River, and particularly, the following items were surveyed through a questionnaire and hearing (see Table 1): a) Awareness and utilization consciousness of ship transport facilities for 2,035 residents along the Yodo River; b) Willingness to use ship transport and to bear financial burdens for municipalities along the Yodo River (2 prefectures, 9 cities, 1 town); c) Willingness to use ship transport facilities and to launch projects for 65 shipping agents (including 5 agents located upstream of the Yodo River great weir). The surveys with the questionnaire and the hearings were conducted during year of 2002–2003.

2.2 Results of surveys of needs and problems related to ship transport

Here are collected results of questionnaires and hearing of needs related to ship transport along the Yodo River below. Present problems are extracted from survey results.

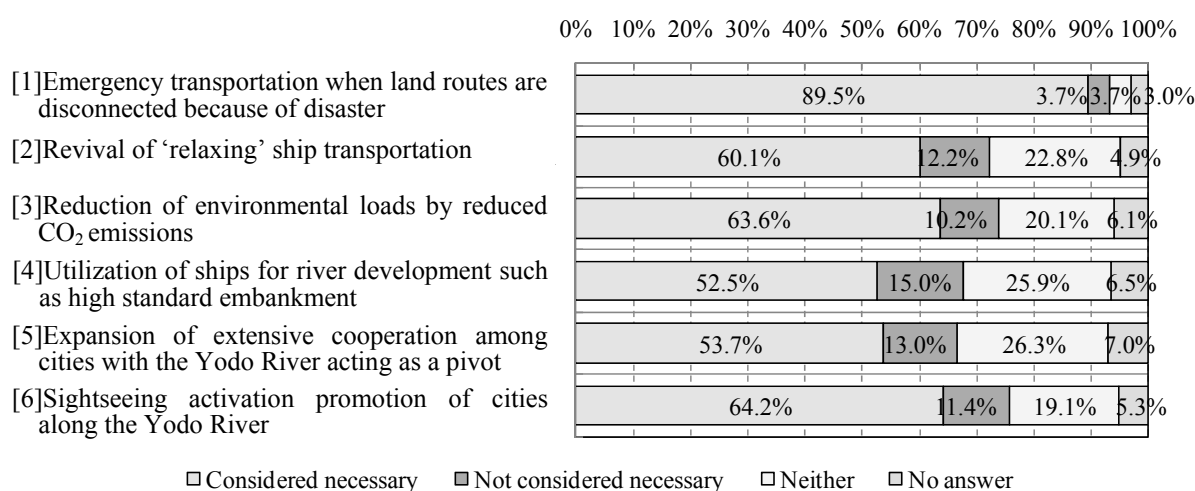
Table 1 List of surveys related to ship transport needs along the Yodo River

Survey name	Survey type	Outline of survey
Questionnaire of Yodo River Ship Transport (2003)	Questionnaire administered to residents (2003)	Sample: residents (2,035 people) along the Yodo River. Questions: Yodo River utilization status, frequency of use, demand for facility development, ship transport image, awareness of emergency wharf, intention for utilization by sightseeing, <i>etc.</i>
Survey of Municipalities along the Yodo River (2003)	Hearing from municipalities (2003)	Sample: municipalities along the Yodo River (2 prefectures -- Osaka, Kyoto, 9 cities -- Hirakata, Neyagawa, Osaka, Moriguchi, Settsu, Takatsuki, Kyoto, Uji, Yawata, 1 town -- Shimamoto) Questions: willingness to independent use of emergency wharf, willingness to bear financial burdens, ranking of Yodo River ship transport in urban planning, willingness of regional activation using Yodo River ship transport, cooperation of watershed cities, <i>etc.</i>
Survey of Business Institutions Related to Yodo River Ship transport (2002)	Questionnaire administered to the shipping agents (2002)	Sample: ocean and river shipping operators (65 operators including 5 parties located upstream of the Yodo River great weir) Questions: willingness to use emergency wharf, willingness to provide vessels in emergencies, willingness to launch a project along the Yodo River, <i>etc.</i>

a) Questionnaire administered to residents (2003)

First, to show items regarded as necessary to attain revival and activation purposes of Yodo River ship transport, results of six questionnaire items are presented in Figure 2. Needs for sightseeing activation promotion [6] and reduction in environmental loads [3] are high, revealing that more than half of respondents felt the necessity for ship transport. Particularly, the necessity of ship transport [1] as emergency transportation when land routes are disconnected at the time of disaster was highly appreciated (about 90%).

Furthermore, utilization of emergency wharfs for sightseeing, traffic and transportation during normal times (Table 2) is highly evaluated (about 70%), reflecting higher needs of utilization of ship transport by residents along the river. Awareness on the provisions and the improvements of the emergency wharf is low (Table 3) reflecting that ship transport is not presented efficiently to the public by administrative authorities (nation, municipalities along the river).



Item	Considered necessary	Not considered necessary	Neither	No answer	Total
[1]Emergency transportation when land routes are disconnected because of disaster	1,822	76	76	61	2,035
	89.5%	3.7%	3.7%	3.0%	100.0%
[2]Revival of 'relaxing' ship transportation	1,224	248	463	100	2,035
	60.1%	12.2%	22.8%	4.9%	100.0%
[3]Reduction of environmental loads by reduced CO ₂ emissions	1,294	207	410	124	2,035
	63.6%	10.2%	20.1%	6.1%	100.0%
[4]Utilization of ships for river development such as high standard embankment	1,069	305	528	133	2,035
	52.5%	15.0%	25.9%	6.5%	100.0%
[5]Expansion of extensive cooperation among cities with the Yodo River acting as a pivot	1,093	264	536	142	2,035
	53.7%	13.0%	26.3%	7.0%	100.0%
[6]Sightseeing activation promotion of cities along the Yodo River	1,307	232	388	108	2,035
	64.2%	11.4%	19.1%	5.3%	100.0%

Figure 2 Items considered necessary to achieve revival and activation purposes of Yodo River ship transport (n = 2,035) (Questionnaire administered to residents (2003), Question 3)

Table 2 Evaluation of emergency wharf of the Yodo River, emergency transportation, and utilization of emergency wharf for sightseeing, traffic and transportation (Questionnaire administered to residents (2003), Question 6 (3))

Response	%
I recognize the value	72.0%
I do not recognize the value	10.0%
Neither	15.0%
No answer	3.0%
Total	100.0%

Table 3 Evaluation of emergency wharf of the Yodo River and emergency transportation, and awareness that the emergency wharf is already provided (Questionnaire administered to residents (2003), Question 6 (1))

Response	%
I know it	13.0%
I did not know it	68.0%
I want to know details	16.0%
No answer	3.0%
Total	100.0%

b) Hearing from municipalities (2003)

From the results of a hearing from municipalities along the river, the ship transport is expected to improve regional development (Table 4), but willingness for utilization of facilities for activation of regional industries is low (Table 5), and opposing exists on the emergence of effects of extensive cooperation among cities (presence or absence of advantages). Therefore, municipalities seem skeptical (Table 6).

Although the attractiveness of ship transport is apparent, municipalities are hesitant to embark voluntarily on ship transport because financial circumstances are strained now. It is considered that they are seeking cooperation with the national government and the shipping industry.

Table 4 Recognition that ship transport can improve regional development (n = 12)
(Public hearing from municipalities (2003), 3-1)

Response	Answer	%
It is possible	9	75.0%
It is not possible	3	25.0%
Total	12	100.0%

Table 5 Willingness to utilize ship transport for regional industrial activation (n = 12)
(Public hearing from municipalities (2003), 3-2)

Response	Answer	%
I want to use it	4	33.3%
I do not want to use it	6	50.0%
No answer	2	16.7%
Total	12	100.0%

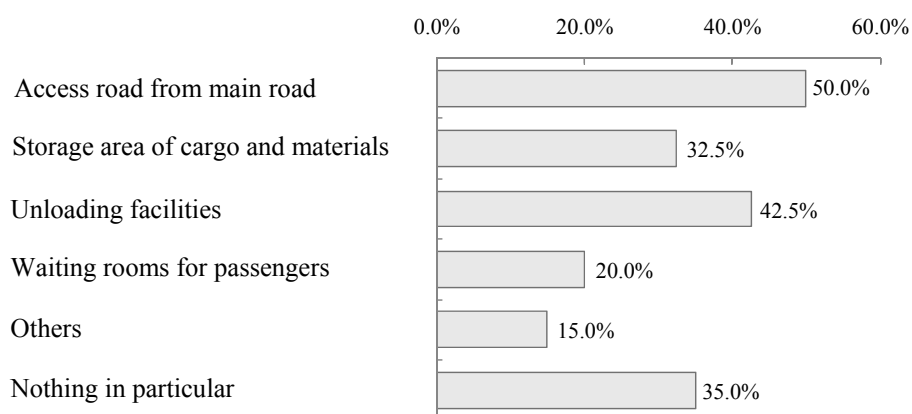
Table 6 Advantages of Yodo River ship transport for extensive cooperation among cities (n = 12)
(Public hearing from municipalities (2003), 4-1)

Response	Answer	%
There is advantage	5	41.7%
There is no advantage	5	41.7%
No answer	2	16.7%
Total	12	100.0%

c) Questionnaire administered to the shipping agents (2002)

As facilities to be provided to emergency wharfs (Figure 3), shipping agents cited road access, unloading facilities, and waiting rooms. However, according to the willingness to use emergency wharfs (Table 7), fewer than 30% of respondents consider using them, even after these are provided, which reveals that half of them hesitate to make judgments about utilizing them at present.

Even though direct access from Osaka Bay to the Yodo River upstream would become possible after installation of locks at the Yodo River great weir, 40% do not think of establishing businesses and more than half have no opinion (Table 8) although demands exist for the installation. In the present economic deterioration as typically represented by the fact that respondents have no ships to use and can not afford to invest (Figure 4), judgments to establish a business solely by shipping agents are difficult from a commercial profit perspective.



Response	Number of times cited	%
Access road from main road	20	50.0%
Storage area of cargo and materials	13	32.5%
Unloading facilities	17	42.5%
Waiting rooms for passengers	8	20.0%
Others	6	15.0%
Nothing in particular	14	35.0%
Total (Number of votes)	78	
Total of valid responses	40	100.0%
No answer	25	
Total	65	

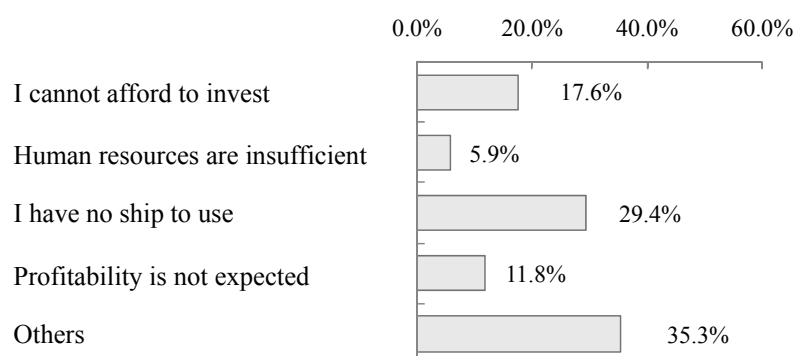
Figure 3 Facilities provided for emergency wharfs (Multiple answers, n = 40)
(Questionnaire administered to the shipping agents (2002), Question 19)

Table 7 Willingness to use when facilities in Question 19 (Table 8) are provided (n = 41)
(Questionnaire administered to the shipping agents (2002), Question 20)

Response	Number of times cited	%
I want to use it	11	26.8%
I do not want to use it	9	22.0%
No opinion/difficult to answer	21	51.2%
Total	41	100.0%
No answer	24	
Total	65	

Table 8 Willingness to establish a business after installation of locks is realized at the Yodo River great weir (n = 46)
(Questionnaire administered to the shipping agents (2002), Question 21)

Response	Number of times cited	%
I want to establish	6	13.0%
I do not want to establish	18	39.1%
No opinion/difficult to answer	22	47.8%
Total	46	100.0%
No answer	19	
Total	65	



Response	Number of times cited	%
I cannot afford to invest	3	17.6%
Human resources are insufficient	1	5.9%
I have no ship to use	5	29.4%
Profitability is not expected	2	11.8%
Others	6	35.3%
Total (Number of votes)	17	
Total of valid responses	17	100.0%
No answer	1	
Total	18	

Figure 4 Reasons for not wishing to establish a business even after installation of locks at the Yodo River great weir (Multiple answers, n = 18)
(Questionnaire administered to the shipping agents (2002), Question 24)

Although it cannot be shown directly, based on the results of hearings from shipping agents held to date, cooperation with facilities operated by the nation or municipalities along the river—acting as a basis of sightseeing—has been demanded, as have been administrative support through public relations activities, and installation of facilities such as public restrooms and waiting rooms. It is considered that businesses are seeking cooperation with public administrative entities (the nation or municipalities along the river).

3. Concrete Measures for Activation of Ship Transport

For the improvement of ship transport activation, to date we have devoted attention to the promotion of utilization during normal times. Recently, with the Great Eastern Japan Earthquake, and the anticipated occurrence of the Tokai, Tonankai, and Nankai earthquakes, now is the time to tackle it from the viewpoints of the aggressive utilization during emergencies while the nation and municipalities along rivers, and eventually the entire nation, act in an integrated manner based on these people's understanding.

For the nation responsible for the management of ship transport facilities, hardware support with installation of facilities that are necessary for shipping agents is important, and also so it is to promote software aspects for support promptly and accurately, such as the provision of navigation route charts, the flexible application of ship transport facilities, and aggressive appeals by holding events *etc.* For municipalities which remain passive about utilization of ship transport considering that it can improve regional development, momentum can be gathered for appealing to residents along the river and for promotion of support measures required for shipping agents if they share the target that active involvement in ship transport during normal times might engender its smooth utilization during emergencies.

As seen from the above we propose the following concrete measures for activation of ship transport³⁾ considering viewpoints of emergency use as well as normal times.

3.1 Measures from viewpoints of normal circumstances

Although residents along the river have needs, shipping agents must continue as a business, and also municipalities must connect it to regional activation. For these reasons, concrete measures for activation of utilization during normal times are presented below.

a) Regional activation for ship transport by municipalities along the river, consciousness improvement of cooperation of watershed cities, and further promotion of cooperation between the public and private sectors should be promoted. Sightseeing ship transport taking advantage of the history and culture of the Yodo River are planned by which improvement of civil needs can be most expected.

Examples:

- Attractive events using land-based facilities (municipalities along the river) to highlight the history of the Yodo River (Kema locks, *etc.*) and nature (wando-biotopes, *etc.*)
- Events for improvement of customer satisfaction from Kema to Hirakata, where the landscape becomes monotonous (slide shows and lectures by a narrator to instruct people on the Yodo River history).

b) Although it is important to secure revenues and expenditures of business of civil business institutions, it is hard to improve the present situation since willingness to use facilities remain low. Therefore, the hardware measures should be administrated through adequate infrastructure provision by the nation and municipalities along the river for the improvement of various needs. Furthermore, the same should be the software provision such as support for flexible operation of the facility and public relations activities.

Examples:

- Provision of public restrooms and waiting rooms at emergency wharfs attending to the needs of the users.
- Development of wharfs and effective utilization of the Hirakata wharf which enable to avoid unavailable time of the Kema locks.
- Extension of available time at the Kema locks for weekends, public holidays and the night time: the locks are available 8:30am – 17:00pm on weekdays at present. Simplification of passing procedures.

c) Investigation of information presentation methods that contribute to safe and smooth navigation for the shipping agents should be performed.

Examples:

- Early provision of navigation route charts and ship navigation rules.
- Construction of information presentation systems through the combination of prior information and

real-time information (river bed transitory condition after flooding, *etc.*) of navigation route charts using the internet and other means.

3.2 Measures from viewpoints of emergencies

Shocked by the tragic results of the Great Eastern Japan Earthquake, public consciousness of crisis management has been increasing. At present, improvement of needs related to utilization of ship transport during and after disaster occurrence is expected more than ever.

It can become motivation to the improvement of needs to encourage interest of people by actively publicizing the roles to be played during emergencies as well as sightseeing activities of ship transport during normal times, promoting earthquake-resistance measures of emergency facilities used during and after wide-scale disasters. Concrete measures are described below.

a) Hold events incorporating opportunities to ascertain the roles of ship-transport-related facilities and river terrace parks to be developed in the event of a wide-scale disaster.

Examples:

- Experience events of the transportation utilizing the facilities such as navigation route, emergency wharfs, emergency river terrace roads so as to aware the effectiveness of alternative transportation for lifesaving and critical materials in a wide scale disaster.
- Training events for residents along the river to set up the evacuation area at the river terrace park, in addition to learn the place and the function of the park set as the regional evacuation site.

b) Promote the provision of a management plan sheet for utilization of ship-transport-related facilities. Make their presence known to related institutions and establish a cooperative framework. In these measures, develop and share momentum for ship transport activation during normal times, which are regarded as supporting the smooth utilization during emergencies.

Examples:

- Advancing the provision of rules for ship transport utilization by municipalities in wide scale disaster.
- Promoting information share such as; emergency river terrace roads (construction and standards, approaching positions, and route restrictions); emergency wharfs (construction and navigable ship standards); and navigation routes (positions and depth) *etc.* so as to act effectively with the cooperation by agreement among building industry, consultants association, gravel gathering union.

4. Conclusions

Recent development of ship transport facilities has been performed for utilization during and after wide-scale disaster occurrence. The active utilization in normal times might be regarded as training for the former, and might foster efficient and effective maintenance, and might be connected directly to the smooth utilization during and after a wide-scale disaster. Based on these perspectives, activation of ship transport in the future is expected to be undertaken recognizing that actions to be taken during normal times and during emergencies are linked inextricably and should not be considered separately.

In this study, using needs related to ship transport as the subject, themes for its activation are assessed using existing survey data. Some concrete measures are proposed. The authors intend to investigate future community renovation considering how waterfront development should be performed for urban rivers, particularly using various functions of rivers and waterfronts while bringing both utilization during normal times and emergencies into perspective.

Finally, the authors wish to express their heartfelt thanks to the Yodo River Office, Kinki Regional Development Bureau who presented us valuable survey data.

References

- 1) Y. Fukushima, T. Adachi, K. Kawamura, K. Motobayashi: "Decoding waterfront cities from mechanism of "bustle", Collection of papers to be presented at a meeting for presentation of research papers, Research Institute of Environmental Technology, pp. 185–186, 2003. (in Japanese)
- 2) Yodo River Office, Kinki Regional Development Bureau: "Business report of investigations of basic concept and rules related to ship transport", pp. 6-1 – 6-37, 2008. (in Japanese)
- 3) Yodo River Office, Kinki Regional Development Bureau: "Summary of transition data related to ship transport", Business report summarizing Yodo River ship transport, pp. 8-1 – 8-5, 2010. (in Japanese)

**Abstracts of Papers
Published in Other Journals**

Mechanical Engineering

Practice and Problem of the Solar Energy Use

Nobuya NISHIMURA

Trans. of Jpn Soc. for Multiphase Flow, Vol.25(3), pp.221-228(2011) (in Japanese)

This paper summarizes the results of author's studies on solar energy resource utilization. One is the development of a micro solar power generation which was combined with micro wind power generation at urban area. The other is the solar thermal utilization by an absorption heat pump for air conditioning. Daily fluctuations of energy supply in Osaka city both by electricity and by town gas were presented precisely in order to understand the energy consumption of urban area. Then, field test results about a micro hybrid power generation system were presented at urban coastal area where there is few wind power resource. Lastly, the performance of a solar-assisted absorption chiller heater of 352 kW refrigeration capacity has been introduced through a long series of proof examination of 17 months.

The Application of a Low Cost Hydroponic Roof Planting by Sweet Potato for Mitigating Urban Heat Island in Summer

Keiko MASUMOTO, Yuko FURUICHI, Misaki SONOYAMA, Atsusi KATO, Takasi ORITA, Hiroshi GODA and Nobuya NISHIMURA

3rd Int. Conf. on Passive and Low Energy Cooling for the Built Environment (CD-ROM), Greece (2010)

The sweet potato (*Ipomoea batatas(L.)Lam.*) grows up in summer and the rate of evapotranspiration is high. When it is cultivated in the roof, the effect of the heat island mitigating is expected as the cool roof. The simple hydro-cultivation system using plastics gutters with automatic water supply was examined. The runner of the sweet potato grew up remarkably, and covered the roof widely. Experimental measurements of thermal environment were carried out at some small-sized buildings which thermal-insulation are not high. The cooling performances were compared by the shadow that the leaves of the sweet potato made, and also the energy consumption reductions were calculated. A "Workshop on the Sweet-Potato Green Carpet Environment" for elementary school children was held and the effect of heat island mitigating by this system were announced to public through the media and internet. This low-cost heat island mitigating system is expected to spread widely to the citizens and the private sectors.

Effects of Porosity And Pore Size Distribution on Capillary Water Transfer In Porous Media

Tamotsu INOUE and Hiroyuki IYOTA

Proc. of 7th Asia-Pacific Drying Conference, No.T1-2(CD-ROM), Tianjin, China (2011)

In this study, we built a simple experimental apparatus for measuring water transfer rate. The experimental results were then used to investigate the effects of porosity and pore size distribution on capillary water transfer in porous media. Several types of cylindrical porous ceramics were used as sample porous media. In addition, we considered a method for predicting the moisture transfer coefficients on the basis of the pore size distribution. The results showed that the water transfer rate increased with the porosity. In addition, the water transfer rate for unit porous area was affected by the pore size distribution. Further, we developed a method for predicting the moisture transfer coefficients of the samples using theoretical analysis.

Defatting and Dehydration of Meat Products during Heating in Steam Convection Oven

Junko YAMAGATA, Hiroyuki IYOTA, Kuniko SUGIYAMA and Nobuya NISHIMURA

J. of JSEM, Vol.11, Special Issue, pp.86-91 (2011)

In this study, we investigated the effects of steam on the reduction in fat and/or water content during the heating of foods. Experiments were performed at 250°C with steam and without steam by using three types of heating equipments; the equipments had different heat transfer coefficients and rates of increase of gas humidity. Sausage and raw pork pate were used as model sample materials. During roasting with steam, the amounts of weight loss and fat loss were greater in the raw pork pate than in the sausage because the amount of protein shrinkage in the pork pate was greater than that in the sausage.

Effects of Placed Conditions on The Internal Temperature Change After Oven Heating of Meat and Poultry

Sadako TAKASAKI, Yoshiko ABE, Kimiko ISHIWATA, Keiko NAKAMURA, Tomoko HARA, Yasuko MATSUDA, Junko YAMAGATA, Hiroyuki IYOTA, Kuniko SUGIYAMA and Shoko SHIBUKAWA

Journal of Cookery Science of Japan, Vol.44(4), pp.277-285(2011) (in Japanese)

The effects on the internal temperature of meat and poultry after oven heating (residual heat), of the oven heating conditions, of the kind of placement medium, and of the presence of a cover were investigated by actual measurements. The time for maintaining a temperature of over 75°C due to the residual heat was also predicted by a numerical analysis using a simplified heat transfer model. No marked difference was apparent in the three kinds of placement medium (stainless steel, wood or gotoku) which had different thermophysical properties. This was due to the small contact area between the medium and the oven plate. The effect of a cover was strong in retaining the residual heat. The time predicted by the simplified numerical model for maintaining over 75°C of internal temperature in the meat was similar to that of the actual measurements, confirming the validity of the heat transfer model.

Development and Evaluation of Directional Retroreflective Materials -Directional Retroreflective Materials as a Heat Island Countermeasure Part 1-

Hideki SAKAI, Hiroyuki IYOTA, Kazuo EMURA and Norio IGAWA

J. Struct. Constr. Eng., AIJ, Vol. 76(665), pp.1229-1234(2011) (in Japanese)

Two kinds of directional retroreflective materials are manufactured, which are designed to show abrupt change in reflectance at the incident angle (θ) of around 30 degrees. The measured solar reflectances are 39.0 percent for $\theta \leq 20$ deg. and 17.7 percent for $\theta \geq 40$ deg. for one type; 54.4 percent and 40.8 percent for the other. Building materials having these kinds of incident angle dependences can be used as cool roofs free of side effect; they can be high-reflective exclusively against summer sunlight, and low-reflective against other light sources, such as, winter sunlight, head lights of cars, and street lights.

Investigating of the Actual Awareness of Energy Consumption among Mass Cooking Staff and Attempt at the "Visualization Method" of Energy Consumption in the Registered Dietitians' Training Course

Junko YAMAGATA, Hiroyu IYOTA, Azumi YAMAGISHI, Tadashi AKAO, Hiroe KIKUSAKI, Nobuya NISHIMURA and Masayoshi FUJIWARA

Japan Journal of Food Service Management, Vol.5(1), pp.29-37(2011) (in Japanese)

In this study, we administered a questionnaire to the food service staff at a hospital in order to clarify the food service staff's awareness level with regard to energy consumption. For the result, both registered dietitians and dietitians were significantly more aware of energy consumption and wastage than other kitchen staff members such as cooks, cooking assistants, and washing staff. It is necessary for registered dietitians to learn the basic knowledge of energy in order to promote energy conservation in the kitchen and improve the cooking staff's awareness of energy conservation without causing any problems and strain during the cooking task. Further, during institutional food service management practicum in the registered dietitians training course, we displayed the numeric value of gas consumption of a steam convection oven. This "visualization method" helped us investigate the change in students' awareness of energy consumption via the questionnaire. Displaying the value of gas consumption during the practicum gave almost all the students an accurate idea of energy consumption. This made them aware of the importance of energy conservation. Our study revealed that the use of a display to indicate the value of gas consumption is effective in training the students about energy. Furthermore, the education for energy conservation should be incorporated into the registered dietitians training course.

Development of Equipment and Software for Evaluating Surface Color Change of Baked Food Using Digital Camera

Hiroyuki IYOTA, Hideki SAKAI, Hiroyuki TAKASAGO and Hideki SHIMADA

Japan Journal of Food Engineering, Vol.11(4), pp.203-213(2010) (in Japanese)

Visual images are one of the most important means of determining whether food has been cooked to perfection, especially while baking, which is a popular cooking method. In this study, equipment for recording the images of the food surface and image editing software were developed in order to record color images having generality and to evaluate the color change due to baking. A spherical dome with a diameter of 500 mm, whose inner surface was painted white, was used as the integrating sphere. The subject (food) was placed in the middle of the dome. Two D65 fluorescent lamps powered by a high-frequency inverter power supply were placed below the subject as the light source. Thus, the subject could be illuminated only by indirect light. The X-Rite White Balance Card and X-Rite ColorChecker were used for color correction. The colors with Munsell chroma, C, less than 5 were in a good agreement with the standard value obtained from the color chart after color correction. The color change of breadcrumbs during re-baking under 200 °C airflow is evaluated from a histogram of L* values versus the number of pixels of the corrected image as a

test case.

Bubble Formation from an Air Jet Injected into a Turbulent Boundary Layer (On a Single Bubble)

Kenji KATOH and Tatsuro WAKIMOTO

J. Fluid Science and Technology, Vol. 5, pp. 528-541 (2010)

The diameter of small bubbles separated from an air jet injected into a turbulent boundary layer from a nozzle on the wall is evaluated. There exist three patterns of bubble separation that are dependent on the jet velocity, i.e., single bubble, coalesced bubbles, and a continuous air jet. The mechanism of bubble separation from the jet is theoretically considered for the single-bubble region. First, the bubble volume is calculated when the force separating the bubbles, such as the drag or lift from the free stream, overcomes the surface tension acting on the wall. Then the total volume of the separating bubble is obtained by adding the volume supplied from the nozzle until the final separation. The diameter of a single bubble was measured for various experimental conditions. The results are well approximated by the results obtained from the theoretical considerations described in the present study.

Bubble Formation from an Air Jet Injected into a Turbulent Boundary Layer (Bubble Separation from a Continuous Jet)

Kenji KATOH, Yusuke ARII and Tatsuro WAKIMOTO

J. Fluid Science and Technology, Vol. 6, pp. 487-498 (2011)

A theoretical and experimental study is conducted to investigate the bubble separation from an air jet injected into a liquid turbulent boundary layer. The following three patterns of bubble separation are dependent on the jet velocity: (a) a single bubble, (b) a coalescent bubble, and (c) a continuous jet. The critical jet velocity from (a) to (b) is theoretically estimated from the condition that the jet from the nozzle overtakes the rear end of the separated bubble, which shrinks due to surface tension. The calculated results generally reproduce the experimental results observed by a high-speed video camera. In addition, the process of bubble separation from the continuous jet (c) is classified into two patterns: (i) the bubble separates from the swell at the front end of the jet, or (ii) the jet breaks due to the instability at the liquid-gas interface. The separated bubble diameter of pattern (i) is theoretically determined by considering the force balance at the front end of the jet between the surface tension, the drag from the free stream, and the virtual mass force. The bubble diameter of pattern (ii) is calculated from the most unstable wavelength of Rayleigh instability. Both of these theoretical results also agree well with those obtained experimentally.

Effect of Air Injection on Drug-Reducing Surfactant Solution Flow in Horizontal Pipe

Koichi ARAGA, Ryosuke MATSUI, Tatsuro WAKIMOTO, Keiji MURATA and Kenji KATOH

J. of JSEM, Vol. 10, pp. 46-53 (2010) (in Japanese)

It is known that small quantities of surfactant additives can greatly reduce the friction factors during the flow of a heat transfer medium. The friction factors are reduced because the generation of turbulent vortices is suppressed by the formation of rod-like micelles, and the flow remains laminar in the high Reynolds number range. However, the values of heat-transfer coefficients decrease during flow laminarization; as a result, heat exchangers with a larger heat transfer area are required. The objective of this research is to study the heat transfer enhancement effect of microbubble injection. This paper presents an experimental investigation of the heat transfer and flow characteristics of the two-phase flow of an air-surfactant solution through a horizontal pipe. In the experiment, microbubbles were injected through three types of porous metal. The experimental results are as follows: The size of the bubbles in a bubbly flow decreases with a decrease in the filtering accuracy of a porous metal. The flow patterns of the two-phase flow of an air-surfactant solution depend on the size of the microbubbles. The heat-transfer coefficient is promoted by microbubbles injection, but the effect depends on the flow pattern or the size of microbubbles. If the diameter of the microbubbles is approximately 100 μm , there is little enhancement in heat-transfer, but a remarkable enhancement in heat transfer is observed when the diameter of the microbubbles is approximately 400 μm or more.

Volume of a Liquid Drop Detaching from a Sphere

Kenji KATOH, Hiroyuki IYOTA, Tamotsu INOUE and Tomoya TSUJINO

Heat Transfer Asian Research, Vol. 39, pp. 396-409 (2010)

A theoretical and experimental study is conducted to investigate the detached volume from a pendant drop on the surface of a sphere. Observation of drop detachment by high-speed video camera reveals that the movement of the upper part of the neck of the drop is quite slow compared to that of the detaching lower part. The surface profile of the upper part was calculated approximately as a static problem using the

axisymmetric Laplace equation. Using the drop profile, the system energy, including the work done by the solid-liquid wetting behavior, was calculated. Based on the condition of minimum energy, the volume of the detached part V was calculated. The volume V increases with the sphere diameter and approaches the value for the pendant drop attached to a plate. In addition, V is strongly dependent on the wettability between the sphere and the liquid and decreases with the receding contact angle. The detached volume of the water drop was measured for spheres of porous brick of various diameters. The experimental and theoretical results were found to be in good agreement.

A New Method to Precisely Measure Contact Angles by Combining Tilting Plate and Optical Methods

Kenji KATOH, Tatsuro WAKIMOTO and Masahiro SUMITANI

Trans. of Jpn Soc. Mech. Engrs., Ser. B, Vol. 76, pp. 1508-1515 (2010) (in Japanese)

A new method was proposed to measure the advancing and receding contact angles by combining the tilting plate and the optical methods. Because of its too high sensitivity, the optical method is usually not applied to measure the contact angles which may widely change from 0 to 180 degrees. In the method proposed in this study, first the liquid-gas interface attached to the test plate was set horizontally as possible by adjusting the inclination of the plate (tilting plate method). Since the interface should not be perfectly horizon, the small inclination angle of the liquid-gas interface at the plate was detected by using the reflection of Laser beam that was directed vertically on the interface. The contact angle can be obtained from the difference of the inclination between the test plate and the interface measured by the optical method. Based on the proposed method, the contact angles were actually measured for each combination between various test plates and liquids. The experimental results were in good agreement with those of another method within the experimental uncertainty. The contact angles can be measured with the accuracy of 0.01 degs. Also the local contact angle can be measured by the space resolution of 50 μm corresponding to the diameter of Laser beam.

A New Method to Actuate a Droplet on a Plate by Use of Laser and Ultrasonic Oscillation

Kenji KATOH, Tatsuro WAKIMOTO and Ryohei MASUDA

Trans. of Jpn Soc. Mech. Engrs., Ser. B, Vol. 76, pp. 2135-2142 (2010) (in Japanese)

A new method to actuate a small droplet on a plate was proposed. In order to reduce the resistance to the droplet movement, which is typically represented by the resultant of surface tension acting on the three-phase contact line, i.e., $\sigma (\cos\theta_R - \cos\theta_A)$ (σ : liquid surface tension, θ_R, θ_A : receding and advancing contact angles), a supersonic oscillation was imposed on the plate to suppress the contact angle hysteresis ($\theta_R - \theta_A$). The experimental results using SAMs (Self-Assembled Monolayers) plates showed that the resistance was reduced by 80 % due to the oscillation having the frequency of 28 kHz and the amplitude of few micrometers. Then the Laser beam was directed to one end of the droplet. The contact angle was remarkably decreased due to the local heating of SAMs plate and the droplet moved to the end of the Laser beam, since the tangential component of surface tension at the heated end overcomes that on the other. The droplet can be actuated by about 0.6 mm/s by the method combining the oscillation and the local heating by the Laser beam.

Characteristics of Liquid Film Flowing around Side Wall of a Horizontal Circular Cylinder (Separation of Liquid Film)

Kenji KATOH and Tatsuro WAKIMOTO

J. of JSEM, Vol. 11, Special Issue, pp. 97-102, (2011)

A standing wave with a peak line toward downstream appears on the surface of a liquid film flowing around a horizontal circular cylinder. The amplitude of the wave grows in the downward direction and finally a part of the wave separates from the film. A theoretical model was proposed to explain the physical mechanism of separation. The wave peak would separate when the resultant of the centrifugal force, gravitational force, surface tension and negative pressure acting on the wave root is not sufficient to supply the flow rate necessary to maintain the wave amplification. The points of separation on the cylinder were calculated theoretically for three kinds of test liquids, i.e., water, ethanol and glycerin solutions. The results agree with those from experiments for various flow rates of the film flow.

Disintegration Process of a Fan Liquid Sheet Formed with Surfactant Solution

Tatsuro WAKIMOTO and Kenji KATOH

J. of JSEM, Vol. 11, Special Issue, pp. 107-111 (2011)

Disintegration process of aqueous surfactant solutions injected from a fan spray nozzle has been clarified. Adsorption of surfactant molecules on the liquid surface causes time-dependent surface tension referred to as "dynamic surface tension". Therefore, when a new liquid surface is formed, surface tension decreases from the value of solvent to equilibrium value with time. This relaxation time of surface tension can be critical for the disintegration process of a liquid sheet that breaks up in comparable timescale. In this study, poly(oxyethylene)(10)octylphenyl ether was used as the surfactant, and the dynamic surface tension of the surfactant solution depending on concentration was measured by oscillating jet method. The break-up length of the liquid sheet and the amplitude of flapping waves inducing the disintegration were also measured by photography and laser induced fluorescence (LIF) method, respectively. The addition of the surfactant decreased the relaxation time of surface tension, and promoted the growth of the wave. However, break-up length increases with surfactant concentration. This discrepancy may be due to surface-stabilizing effect by the surfactant molecules, which is usually seen in a soap film.

Nonlinear Growth of Disturbance Waves in a Radial Liquid Sheet

Tatsuro WAKIMOTO and Kenji KATOH

Proc. of 3rd International Conference on Jets, Wakes and Separated Flows (ICJWSF), CD-ROM, 6pages (2010)

Nonlinear growth of disturbance waves in a radial liquid sheet has been clarified. The radial liquid sheet was formed by releasing of a radial water film flowing along the disk into still air. In this liquid sheet, a velocity profile with an inflection point is formed during the relaxation of the velocity profile. This velocity profile causes instability and amplifies disturbances in the liquid sheet. Consequently, disturbed liquid surface forms a wave, referred as a disturbance wave. In this study, the growth of the disturbance waves depending on the wave amplitude was analyzed by numerical simulation and experiment under the condition of 80 μ m sheet thickness and 14.2m/s surface velocity. The simulated disturbance waves demonstrated that the growth rate decreases when the amplitude exceeds 15 μ m, which is 19% of the sheet thickness. Measured growth rate also showed similar dependence of the growth rate on the amplitude. This implies that disturbance waves are strongly decayed by nonlinear effect.

Basic Seminar on Atomization Mechanism Caused by Rayleigh Instability

Tatsuro WAKIMOTO

Atomization, Vol. 19, pp. 116-122 (2010) (in Japanese)

In a cylindrical liquid jet injected at relatively slow speed, axisymmetric disturbance is amplified because of surface tension. This instability is widely known as Reylegh instability and is the most fundamental mechanism of liquid atomization. In this article, governing equation and boundary condition of multiphase flow is explained in advance, and then the concept and formulation of the Rayleigh instability theory are described. In Rayleigh instability theory, non-viscous fluid and infinitesimal disturbance are assumed. The equation giving temporal growth rate of the disturbance is derived based on the linear stability theory. Rayleigh instability theory predicts that the only axisymmetric disturbance with a wavelength, which is about 3 times longer than the diameter of liquid cylinder, becomes unstable. The most unstable wavelength is about 4.5 times as long as the cylinder diameter.

Vibration Test of a 1/10 Reduced Scale Model of Cylindrical Water Storage Tank

Akira MAEKAWA, Yasutaka SHIMIZU, Michiaki. SUZUKI (Institute of Nuclear Safety System), Katsuhisa FUJITA

ASME Journal of Pressure Vessel Technology, Vol.132 / 051801-1-051801-11 (2010)

In this paper, vibration tests by shaking table are conducted using a reduced scale tank model to investigate the seismic-proof safety of tanks. Sinusoidal excitation tests and seismic excitation tests are conducted. The measured values are compared with the calculated ones by some conventional seismic design methods. The results reveal that the distribution shape and magnitude of the dynamic fluid pressure are different between the positive side and the negative side, and depend on the magnitude of input acceleration. Further examination concludes that the oval-type vibration, which is a high-order vibration mode, affects the distribution shape and magnitude of dynamic pressure. However, it is certified that the vibration does not act as a seismic load in the conventional evaluation of seismic-proof safety.

Effect of Structural Dimensions on Dynamic Stability of Elastic Beam Subjected to Axial Flow in

Confined Narrow Passage

Katsuhisa FUJITA, Ayumi OHKUMA

JSME Journal of System Design and Dynamics, Vol.4, No.6, pp.809-821 (2010)

The evaluation methodologies for the flow-induced vibration of an elastic beam subjected to an axial flow in confined narrow passage are reported. One of authors has already proposed an analytical method using the Navier-Stokes equation for the dynamic stability of an elastic beam subjected to an axial flow confined in a narrow passage. In this paper, by using the proposed analytical methods, the numerical studies are performed taking three kinds of support conditions as parameters, that is, a cantilever fixed at the upstream end, a cantilever fixed at the downstream end, and a simple support beam, respectively. Moreover, the parameter-studies are also performed concerning with a width of annular gap, viscosity of a fluid, and structural damping. And the effects of support conditions of a structure, structural damping, and fluid characteristics on the dynamic stability of an elastic beam are clarified.

Dynamics of Two-Wheels Modeling Roller Coaster Running on a Complicated 3 Dimensional (3D) Trajectory Considering Air Resistance

Katsuhisa FUJITA, Koichi KATSUOKA, Hiroaki TOSHIMITSU

JSME Journal of System Design and Dynamics, Vol.5, No.3, pp.403-415 (2011)

The motion and vibration of a moving body running on a complicated 3 dimensional (3D) trajectory considering an air resistance are investigated. A roller coaster is a concrete example of moving body. The equations of motion of a roller coaster in which a trajectory and a vehicle are coupled are derived by using differential algebraic equation. Although a roller coaster has been modeled as a one-wheel vehicle, it is modeled as a two-wheel vehicle here. The Baumgarte method is adopted for numerical stabilization. The influence of air resistance and rolling resistance, and the interaction between a vehicle and passengers so on are investigated. And also, the transmissibility of vibration through its suspensions is studied. Besides, a part of simulations are compared with the experiments reported by the previous paper.

Stabilization or Destabilization Effect of Fluid Viscosity, Structural Damping on the Vicinity of Critical Velocity of Elastic Beam Subjected to Axial Flow Confined in Narrow Passage

Katsuhisa FUJITA, Ayumi OHKUMA

Transactions of the Japan Society of Mechanical Engineers, Vol.77, No.777, C, pp.1938-1948 (2011) (in Japanese)

The evaluation methodologies for the flow-induced vibration instability of an elastic beam subjected to an axial flow confined in a narrow passage have been reported. In this paper, by using this proposed method, the parameter-studies are performed on the dynamic stability of an elastic beam. The effects of support conditions of structures, structural damping, and fluid characteristics on the dynamic stability are clarified. Especially, paying an attention on the vicinity of critical velocity, the effects as for stabilization or destabilization effect on flutter and divergence phenomena are investigated by changing fluid viscosity and structural damping.

Active Control of Annular Flow-induced Vibration of Axisymmetric Elastic Beam by the Local Gap Width Control

Shoji TAKADA, Atsuhiko SHINTANI, Tomohiro ITO (Osaka Prefecture University) and Katsuhisa FUJITA

JSME Journal of System Design and Dynamics, Vol.5, No.4, pp.577-588 (2011)

In this paper, for the purpose to avoid vibration troubles, the active control of vibration of an axisymmetric elastic beam subjected to annular flow is investigated. An air-pressured actuator is attached on the surface of the circular cylinder for the vibration control. As the shape of the actuator changes by control, the gap width changes, which causes the change of the fluid pressure. Therefore, the vibration of the fluid-structure coupled system can be suppressed. The fluid-structure coupled equation based on the Euler-Bernoulli type of partial differential equation and the Navier-Stokes equations is analytically derived including control terms. By applying the optimal control law to the coupled system, the unstable behavior is stabilized. The stability of the coupled system is investigated by eigenvalue analyses of controlled coupled equations.

Pressure Pulsation Behavior in Actual Size Mock-Up Piping System

Akira MAEKAWA, Tsuneo TAKAHASHI, Takashi TSUJI (Institute of Nuclear Safety System),

Michiyasu NODA (Kansai Electric Power), Minoru KATO (Kobelco Kaken) and Katsuhisa FUJITA

JSME Journal of System Design and Dynamics, Vol.5, No.4, pp.603-611 (2011)

In this study, the influence of valve closing and opening operations to change inner pressure during pump

operations was investigated to improve the prediction accuracy of pressure pulsation. Vibration experiments were conducted by using an actual size mock-up piping system. A drastic change in the boundary condition of the acoustic resonance by a slightly different valve opening ratio to set a different inner pressure was seen experimentally. The simulation using the method of characteristics showed that the boundary condition of the acoustic resonance changed when the valve opening ratio was changed slightly from 10 % to 15 %. It was concluded that the boundary condition of the acoustic resonance was sensitive to a slight change of the valve opening ratio and this was one of the reasons why it is difficult to predict the pressure pulsation behavior accurately in actual plants.

A Consideration on Nonlinear Sloshing of a Rectangular Liquid Storage Container Subjected to Seismic Excitations

Katsuhisa FUJITA, Sho ASANO

Proceedings of ASME Pressure Vessels and Piping Division Conference, Baltimore, Maryland, USA, PVP2011-57116 in CD-ROM (2011)

The liquid storage container (tank) in industrial facilities, is listed as one of the facilities which are apt to be damaged by an earthquake. As for seismic damages of containers, the sloshing phenomenon of the liquid free surface and the bulging phenomenon which is due to the interaction between the container structure rigidity and the liquid pressure become problems. Here, we investigate a nonlinear sloshing. In this paper, a modal method which superposes linear solutions using Fourier series' representation depending time is proposed as for a nonlinear solution. Furthermore, this nonlinear method is applied to the seismic response analysis on the nonlinear sloshing of a rectangular liquid storage container in nuclear plants.

Influence of Fluid Viscosity and Structural Specifications on Stability in the Vicinity of Critical Velocity of an Elastic Beam Subjected to Confined Axial Flow

Katsuhisa FUJITA

Proceedings of ASME Pressure Vessels and Piping Division Conference, Baltimore, Maryland, USA, PVP2011-57117 in CD-ROM (2011)

Evaluation methodologies for the flow-induced vibration of an elastic beam subjected to an axial flow confined in a narrow passage are reported. In this paper, by using the analytical method already proposed by the author, a parameter study is performed on the dynamic stability of an elastic beam subjected to axial flow confined a narrow passage. The effects of support conditions of structures, structural damping, and fluid characteristics on the dynamic stability are clarified. Especially, paying attention on the vicinity of critical velocity, the effects of stabilization or destabilization on flutter and divergence are investigated by changing fluid viscosity and structural damping.

Experiment and Simulation on Pressure Pulsation Accompanied by Acoustic Resonance and Piping Vibration

Takashi TSUJI, Akira MAEKAWA, Tuneo TAKAHASHI (Institute of Nuclear Safety System), Michiyasu NODA (Kansai Electric Power), Minoru KATO (Kobelco Kaken), Katsuhisa FUJITA

Proceedings of ASME Pressure Vessels and Piping Division Conference, Baltimore, Maryland, USA, PVP2011-57221 in CD-ROM (2011)

To improve condition-based maintenance (CBM) techniques for operating plants, it is necessary to investigate on the behavior of fluid inside piping system in detail. This study was conducted using the full-scale piping system under conditions that could seriously threaten the plant operation, by matching pressure pulsation, acoustic resonance and piping natural frequency. Although piping vibration is reported to influence fluid pressure pulsation, there were few examples of such influence in the conditions of this experiment. Knowing that the opening ratio of the pressure control valve affects the boundary condition for acoustic resonance, the experiment and numerical simulation at different opening ratios were conducted. It was suggested that there are cases in which a valve partially open at 25% or less shouldn't be taken as a closed end. This finding conflicts with widespread design assumption.

Seismic Safety Margin of Cylindrical Liquid Storage Tanks in Nuclear Power Plants

Akira MAEKAWA, Tsuneo TAKAHASHI (Institute of Nuclear Safety System), Katsuhisa FUJITA

Proceedings of ASME Pressure Vessels and Piping Division Conference, Baltimore, Maryland, USA, PVP2011-57241 in CD-ROM (2011)

In Japanese nuclear power plants, the quantitative evaluation for seismic safety margin of the equipment is an important issue. In this study, the seismic safety margin of cylindrical liquid storage tanks used in nuclear

power plants was investigated experimentally and analytically. The buckling load of the tanks was examined. The test tanks were the reduced-scale models of large-scale liquid storage tanks in nuclear power plants. The experimental buckling load was compared with the design value. Furthermore, dynamic and static elastic-plastic buckling simulations by finite element analysis using a three dimensional model were made. The simulated and experimental results agreed well. The design value was lower than the nearly-true buckling load, indicating the difference is the seismic safety margin.

Diagnosis of Air-conditioner by SVM

Tadao KAWAI, Seiya. KUSHIZAKI

Proceedings of COMADEM 2010, pp.575-582 (2010)

To avoid failures of an air-conditioner, we need suitable condition monitoring technique. Unfortunately, an air-conditioner has many parameters in it, i.e., inlet temperature, outlet temperature of a condenser or an evaporator, pressure at each component and input power to compressor and so on. Furthermore, we need expensive sensors to measure pressure. It is very difficult to monitor so many parameters from viewpoint of cost, setup in an air-conditioner and calculation cost of diagnosis technique. This is one of reasons why we must select suitable parameters for diagnosis. In this paper, we checked suitable parameters to monitor the condition of an air-conditioner by experiment. And then we applied neural network, i.e., NN, and support vector machine, i.e., SVM, with two types of kernel function to diagnose its failure. We also checked the effect of parameters on diagnosis performance to reduce the number of input parameter for NN or SVM. Finally, we selected several parameters for input data and showed good diagnosis ability of SVM with polynomial kernel.

Diagnosis of Engine Mount

Tadao KAWAI, Sigeto IMAMURA

Proceedings of D&D2010, in CD-ROM (2011)

Because in many cases damage of mount could be assumed to reduce a spring constant, we estimated spring constant of each engine mount by solving inverse problem to detect a damage of mount in this paper. We built physical model of engine and engine mounts by modelica language and modified spring constant of mount to simulate failure of engine mount. Finally, we can identify spring constant of mount in the vertical direction with high accuracy.

Diagnosis of Air-conditioner by using its Dynamic Property

Tadao KAWAI, Seiya. KUSHIZAKI

Proceedings of D&D2010, in CD-ROM (2011)

To avoid failures of an air-conditioner, we need suitable condition monitoring technique. Unfortunately, an air-conditioner has many parameters in it, i.e., inlet temperature, outlet temperature of a condenser or an evaporator, pressure at each component and input power to compressor and so on. Furthermore, it is very difficult to identify failures in an air-conditioner because of small difference of parameter between normal and abnormal condition. In this paper, we proposed diagnosis technique by using SVM (support vector machine) with identified system parameters by ARX model. Because dynamic property of an air-conditioner identified by ARX model, did not depend on operation condition, i.e., room temperature, outside temperature, our proposed technique did not need a lot of data. Finally, our proposed technique well identified clog in heat exchanger very well.

Walking Guide Interface Mechanism and Navigation System for the Visually Impaired

Atsushi IMADU, Tadao KAWAI, Yogo TAKADA, and Tomoki TAJIRI

Proc. of 2011 4th Int. Conf. on Human System Interactions, Yokohama, Japan, May 19-21, IEEE CFP1121D-CDR, 34, (2011).

We propose a new mechanism, with an intuitive interface, for a walking guidance system for the visually impaired. The user pushes the mechanism using a long handle like walking stick, and the mechanism steers to navigate along a given route using environmental sensors, communicating the steering angle to the user by twisting the handle. Using the interface, users are aware of their direction to go and can walk without hesitation. A navigation method incorporating simple topological map information is proposed for the mechanism, and a prototype system that follows the walls surrounding a route is developed. Experiments illustrate the usability and performance of the proposed interface and system.

Prediction of Soot Emission from a Direct Injection Diesel Engine by Means of Three-dimensional

Chemical Kinetics Calculation

Hideki TAKASE, Yukitoshi SHIDA, Yogo TAKADA and Tomoyuki WAKISAKA

Transactions of Society of Automotive Engineers of Japan, Vol.41, No.5, (2010), pp.1083-1088 (2010) (in Japanese)

The elementary reaction scheme including a soot model for a diesel surrogate fuel by Golovitchev and the soot oxidation model for surface reaction by Nagle, et al. have been incorporated into the GTT-CHEM code constructed by the authors' group, in order to numerically predict soot emission from a direct injection diesel engine. The reaction rate constants have been optimized to reasonably reproduce the ϕ -T map for soot generation and the ignition delay data. As a result, the experimental results of soot and NO emissions as well as the rates of heat release under various injection conditions have been reproduced reasonably well by means of three-dimensional chemical kinetics calculation using the GTT-CHEM code.

Development of Small Fish Robot with Built-in Fuel Cells

Yogo TAKADA, Hiroki MASUDA, Tomoki TAJIRI and Tomoyuki WAKISAKA

Proc. of Int. Symp. On Techno-Ocean 2010, Kobe, Japan, 008.pdf (CD-ROM)(2010)

A polymer electrolyte fuel cell (PEFC) has high energy density and robots move for a long time with the PEFC. Therefore, the series-connected PEFCs are attractive as practical power supplies for robots. Authors originally developed a small and lightweight passive-type polymer electrolyte fuel cell "Power Tube". Additionally, a submersible small fish robot with a magnetic actuator was made. The fish robot has an external power supply composed of four Power Tubes and a voltage booster. Next, authors tried to put Power Tubes in another fish robot. When PEFC is used in the robot body inside, it is necessary to consider the method of aerating in the body. Therefore, the hydrogen peroxide solution was used as an oxidant of PEFC in this study. With the oxygen supply system in the fish robot, it was able to swim in water for one hour or more.

Stabilization of Walking on Uneven Road for a Small Humanoid Robot

Tomoki TAJIRI, Rei OGAMI, Kazuya SUGIMOTO, Yogo TAKADA and Tomoyuki WAKISAKA

Trans. of Jpn Soc. Mech. Engrs., Ser.C, Vol.76, No.772, pp.440-447 (2010) (in Japanese)

Recently, humanoid robots have widely researched, and they have become possible to be controlled robots with complicated kinetic characteristics. However, in the cases that the robot walks on an unknown undulating road or receives disturbances such as collision with an object from the outside, the robot loses stability and falls even if the inverted pendulum model is used. In this paper, an impedance control of a swing leg and a PI control of the rotation of a humanoid robot's waist are used to stabilize the dynamic walk on the unknown undulating road. For an impedance control, force sensors on the soles of the humanoid robot are used to measure the torque and force of a swing leg that collide with the unknown undulating road. An angular velocity sensor and acceleration sensor in the body of the humanoid robot are used to measure the rotation of the waist and its error signal are used for the PI control of humanoid robot motion. As a result, it has been confirmed that the humanoid robot can walk on an unknown undulating road with proposed walking method.

Effects of Tail Fin Flexibility on Propulsive Performance in Small Fish Robots (Investigation by Fluid-Structure Interaction Analysis Considering Elastic Deformation of Tail Fin)

Yogo TAKADA, Ryosuke ARAKI, Toshinori OCHIAI, Tomoki TAJIRI and Tomoyuki WAKISAKA

Transactions of the Japan Society of Mechanical Engineers (Ser.C), Vol.77, No.778, pp.183-194 (2011) (in Japanese)

Fish robots that swim with the tail fin do not give the caution to underwater creatures. Therefore, they become useful for the investigation of ecosystem in water and the usage of the environmental surveillance and so on. However, the propulsive velocity of fish robots is extremely slower than that of live fishes. It is necessary to examine the difference of how to swim between live fishes and fish robots in order to put the robots to practical use. In this study, the modification has been added to the CFD code that had been developed up to now, so as to clarify the relation between tail fin's flexibility and the propulsive performance of the fish robot. The new code can calculate fluid-structure interaction analysis considering elastic deformation of tail fin. By using the modified CFD code, effects of tail fin flexibility on propulsive velocity and flow pattern of water around the fish robot have been examined.

Effect of Titanium Layer on Low-Velocity Impact Damage Behaviour of Ti/GFRP Laminates

Hayato NAKATANI, Tatsuro KOSAKA, Katsuhiko OSAKA and Yoshihiro SAWADA

J. of the Soc. of Materials Science, Japan, Vol.59, No10, pp.792-799 (2010) (in Japanese)

In the present paper, effects of titanium skin layer on impact damages in GFRP core of Ti/GFRP laminates as Fibre-Metal Laminates under impact loadings were investigated. Low-velocity impact tests using a drop-weight tower were conducted on Ti/GFRP laminates with single titanium layer as a face sheet. In these tests, the titanium skin or GFRP layer were considered to be as an impact surface, and damages in the GFRP layer after the impact loading were observed in each case. From the experimental evidence, it was found that out-of-plane deformation and internal damages of GFRP layer were constrained by the titanium layer which was set at the opposite side of impact. Furthermore, four-point bending tests were conducted using the GFRP core derived from Ti/GFRP laminates after impact loadings. Experimental results showed that the specimens impacted from the GFRP layer side exhibited superior residual bending strength and bending stiffness compared to those impacted from the titanium layer side. Numerical analyses of impact damages in Ti/GFRP laminates using a finite element method were executed in order to evaluate damage development in the GFRP layer. The calculated damage state in the GFRP layer agreed well with the experimental results. As a consequence, it was revealed that the titanium layer at the opposite side of impact plays a major role in preventing damages in the GFRP core under low-velocity impact loading on Ti/GFRP laminates.

Measurement of Cure Shrinkage Strain of Resin by Optical Fiber Strain Sensors

Tatsuro KOSAKA, Katsuhiko OSAKA and Yoshihiro SAWADA

J. of the Soc. of Materials Science, Japan, Vol.60, No.5, pp.432-438 (2011) (in Japanese)

Strain monitoring of resin during cure process is an effective method to manufacture high-quality FRP products because it is known that residual stress generated during molding decreases strength of final products. Although both cure and thermal shrinkage occur during cure process, it is difficult to measure cure shrinkage of FRP products due to dramatic changes in mechanical properties of resin by cure reaction. Among cure monitoring methods, it is proven that fiber optic embedded strain sensors can measure cure shrinkage of resin. However, quantitative evaluation of cure shrinkage strain measured by optical fiber strain sensors has not been conducted. In the present paper, we monitored curing shrinkage of epoxy resin by an embedded EFPI sensor. Mechanical and thermochemical properties of the resin during cure process were experimentally obtained by several methods. Volume shrinkage of resin during cure process was also measured by a dilatometer. In this paper, a viscoelastic model during cure process was driven and the model was used for FEM analysis of cure shrinkage strain generated in the embedded EFPI sensor. From the results, it appeared that the calculated cure shrinkage strain of the EFPI sensors agreed well with the measured strain especially when the degree of cure was high. Therefore, it was concluded that an embedded EFPI sensor can measure cure shrinkage strain quantitatively.

Damage Characterization of Titanium/GFRP Hybrid Laminates Subjected to Low-velocity Impact

Hayato NAKATANI, Tatsuro KOSAKA, Katsuhiko OSAKA and Yoshihiro SAWADA

Composites Part A: Applied Science and Manufacturing, Vol.42, No. 7, pp.772-781(2011)

Low-velocity impact-induced damage in Ti/GFRP laminates as titanium-based Fibre-Metal Laminates (FMLs) was investigated to reveal the extent of internal damage in the in-plane direction and to evaluate the effects of titanium facesheets on impact damage in the GFRP core. It was found that interlaminar delamination in the GFRP layer expands widely due to crack initiation in the titanium layer on non-impacted side. However, matrix cracks and residual out-of-plane deformation are suppressed by energy absorption achieved by the bottom titanium layer. Furthermore, impact responses and damages obtained by finite element analysis with detailed modelling agree well with the experimental results. Thus, this study confirmed that the impact behaviour of the Ti/GFRP laminates is dominated by a fracture in the titanium layer on non-impacted side that fails in tension and that this layer plays a major role in preventing impact damages in the GFRP core.

Resin Cure Monitoring in RTM Process by Electromagnetic Acoustic Transducer

Tomohiro YAMASAKI

Proc. 4th Japan-US Symposium on Emerging NDE Capabilities for a Safer World, pp.186-192 (2010)

Degree of resin cure is measured using electromagnetic acoustic transducer (EMAT) in manufacturing process of fiber reinforced plastics (FRP) by resin transfer molding (RTM). RTM method is suitable for

fabrication of FRP products of complicated shape. In order to reduce the cost by minimizing the cycle time, cure monitoring of resin is necessary. Dielectric sensors have been used for such a purpose. However, they may affect the strength of the products, since they should be embedded in the mold. Furthermore, effect of conductivity of the carbon fibers must be removed. Ultrasonic methods, such as velocity measurement, have also been applied. In this study, attenuation of shear standing wave in the mold is measured by the EMAT. As resin cure proceeds, increase in the resin viscosity causes decrease in reflection coefficient at the interface between the resin and the mold. Then the attenuation coefficient of the standing wave in the mold gives us the information about the resin cure. In the cure process of resin without reinforcement, attenuation coefficient is compared with the results of dielectric sensor, showing that the cure index can be evaluated by the attenuation measurement. Cure monitoring is also executed in the molding process of CFRP.

On the transition from serrated to non-serrated plastic flow in metallic glasses at low temperatures

A. VINOGRADOV, D. LAZAREV, V. LOUZGUINE-LUZGIN, Y. YOKOYAMA, S. LI, A. R. YAVARI and A. INOUE

Acta Materialia Vol.58, pp. 6736-6743 (2010)

The mechanical behavior and the kinetics of shear banding in bulk metallic glasses was investigated at room and liquid nitrogen temperature using the acoustic emission (AE) technique. It was demonstrated that the intensive AE reflecting the activity of strongly localized shear bands at room temperature vanishes at the transition of plastic flow from serrated to non-serrated with a reduction in temperature. The disappearance of AE clearly suggests that the shear band propagation velocity significantly decreases at low temperature, and sliding along the principle shear band is observed at the machine-driven rate.

Comparative Analysis of Inhomogeneous Plastic Flow in Bulk and Ribbon Metallic Glasses Monitored by Acoustic Emission

A. LAZAREV, A. VINOGRADOV and S. HASHIMOTO

Int. Journal of Alloys and Compounds, Vol. 504S, pp. S60-64 (2010)

Aiming to gain a better insight into the phenomenological description and mechanisms of inhomogeneous plastic deformation in metallic glasses, we review the currently available experimental data on the acoustic emission (AE) behaviour in these materials under load and compare the results for typical ribbon-shaped and bulk metallic glasses. It is shown that the AE patterns reflecting the kinetics of shear banding are very much alike for both kinds of glasses (as-cast and as-spun) despite a gross difference in the quenching rate during manufacturing, geometry and loading conditions. It is also shown that the stress drops during serrated plastic flow in BMGs are triggered by short time localised shear events having a comparatively large scale although no simple correlation between the stress drops and AE amplitudes is found.

Acoustic Emission Analysis of Fracture of Metallic Glasses

A. LAZAREV and A. VINOGRADOV

Proc of Int. Symp. on Acoustic Emission, IAES-20, ed by S.Wakayama et al., Kumamoto, Japan, JSNDI pp. 121-126 (2010)

This is the first report where the crack velocity is measured in metallic glasses. From the high speed AE waveform records we argued that the crack velocity in the melt-spun ribbon metallic glass amounts to 180 ± 20 m/s. The wavelet analysis has been shown to be a practical tool for extraction of scales corresponding to fracture process in these materials.

On the reversibility of dislocation slip during cyclic loading of Al alloys containing shear-resistant particles

W. HAN, A. VINOGRADOV and C. HUTCHINSON

Acta Materialia, Vol. 59, pp. 3720-3736 (2011)

The cyclic deformation behavior of a model Al-4Cu-0.05Sn (wt.%) alloy containing a homogeneous and well-defined distribution of shear-resistant θ_0 (Al₂Cu) precipitate plates was used to study the effect of precipitate state on the cyclic slip irreversibility. The precipitate spacing was controlled so that it was less than the self-trapping distance of dislocations. The cyclic deformation tests were conducted under constant plastic strain amplitude mode and the evolution of the cyclic stress and cyclic hardening rate with cumulative plastic strain were monitored. The deformed and undeformed microstructures were characterized using transmission electron microscopy. The cyclic deformation behavior and the corresponding dislocation structures depend on both precipitate state and imposed plastic strain amplitude. An expression for the cyclic slip irreversibility that explicitly depends on microstructural and deformation parameters was derived based

on proposed mechanisms of interaction between the mobile dislocations and the precipitates. The cyclic deformation curve was calculated using the expression for the slip irreversibility and shown to describe most features of the cyclic deformation curves well, as a function of precipitate state and imposed plastic strain amplitude, as well as describing the results of plastic strain amplitude jump tests.

Dynamic Precipitation During Cyclic Deformation of an Underaged Al-Cu Alloy

W. HAN, Y. CHEN, A. VINOGRADOV and C. HUTCHINSON

Materials Science and Engineering A Vol 528, pp. 7410-7516 (2011)

The cyclic deformation behavior of Al-4Cu alloy containing shear-resistant particles was investigated systematically as a function of precipitate state. Pronounced cyclic hardening was observed in the under aged Al-4Cu-0.05Sn (wt.%) alloy strained under various imposed plastic strain amplitudes at room temperature. Such cyclic hardening is absent from the longer aging treatments. Microstructural characterization reveals that the pronounced cyclic hardening of the under aged alloy is due to the dynamic precipitation of GP zones. The dynamic precipitation occurs during all the cyclic loading process and only at the peak stress, where the hardening increment from dynamic precipitation saturates, does strain localization occur which is soon followed by failure of the material. The dynamic precipitation of GP zones has a positive effect on the low cycle fatigue performance of this alloy, and can significantly elevate the strength of this alloy without loss in ductility. Experiments performed to test the dependence of the cyclic hardening on plastic strain amplitude and strain-rate illustrate a relatively strain-rate independent and strain amplitude dependent behavior. Such kinetic behavior is approximately consistent with that expected if the GP zone formation is controlled by the vacancies production process during plastic deformation.

The influence of temporary hydrogenation on ECAP formability and low cycle fatigue life of CP titanium

A. CZERWINSKI, R. LAPOVOK, D. TOMUS, D. ORLOV, Y. ESTRIN and A. VINOGRADOV

Journal of Alloys and Compounds, Vol. 509, pp. 2709-2715 (2011)

It is generally believed that thermo-hydrogen processing has a beneficial effect on tensile ductility and fatigue properties of titanium. This study was concerned with investigating whether this also applies to titanium of commercial purity (CP) with an ultrafine-grained structure obtained by equal-channel angular pressing (ECAP). It was shown that despite the possibility to manipulate the microstructure of titanium the thermo-hydrogen processing offers, temporary hydrogenation was not able to improve ductility and low cycle fatigue life of CP titanium over the levels achievable by straight ECAP.

Reversible nature of shear bands in copper single crystals subjected to iterative shear of ECAP in forward and reverse directions,

H. MIYAMOTO, T. IKEDA, T. UENOYA, A. VINOGRADOV and S. HASHIMOTO.

Materials Science and Engineering A. Vol.528, pp.2602-2609 (2011)

Copper single crystals were subjected to equal-channel angular pressing for two passes via the routes A and C, in order to examine the effect of iterative shear in forward and reverse directions on the development of shear bands in a crystallographic aspect. Shear bands were clearly revealed metallographically after one pass, which accompanies splitting of distinct crystallographic orientations. These shear bands remained after the second pass via route A, where shear was given in a forward direction with regard to the previous shear. Micro-indentation tests show that the shear bands were harder than the matrix, and both the shear bands and the matrix became harder progressively by the second pass. In route C, where the second shear is given in the parallel plane, but in the reverse direction with regard to the previous shear, most of these shear bands were less visible in metallographic and EBSD observations. Besides, the distribution of microhardness became homogeneous across the traces of shear bands and the matrix. It is suggested that the shear bands were dissolved by merging with the matrix by diffusion of the geometrically necessary dislocations (GND) delineating the shear bands and the matrix.

Deformation and Fracture Behavior of Metallic Glassy Alloys and Glassy-Crystal Composites

D. LOUZGUINE, A. VINOGRADOV, S. LI, A. KAWASHIMA, G. XIE, A. R. YAVARI and A. INOUE

Metallurgical and Materials Transactions A, Vol 42, pp.1504-1510 (2011)

The present work demonstrates the deformation behavior of Zr-Cu-Ni-Al bulk glassy alloys and Zr-Ni-Cu-Al-Pd glassy foils as well as Ni-Cu-Ti-Zr bulk crystal-glassy composites. Fracture of Zr₆₀Cu₁₆Ni₁₄Al₁₀ and Zr_{64.13}Ni_{10.12}Cu_{15.75}Al₁₀ bulk glassy alloys is featured by nearly equal fraction areas of cleavage-like and vein-type relief. The observed pattern of alternating cleavage like and vein-type

patterns illustrates a result of dynamically self-organizing shear propagation at the final catastrophic stage. The deformation behavior of Zr_{64.13}Ni_{10.12}Cu_{15.75}Al₁₀ alloy has also been tested at LN₂ temperature. The strength of the sample decreases with temperature, and no clear serrated flow typical for bulk glassy samples tested at room temperature is observed in the case of the samples tested at LN₂ temperature. We also studied the deformation behavior of Zr-Ni-Cu-Al-Pd glassy foils thinned to electron transparency in situ in tension in a transmission electron microscope. We also present a Ni-Cu-Ti-Zr crystal-glassy composite material having a superior strength paired with a considerable ductility exceeding 10 pct. The metastable cP2 crystalline phase promotes a strain-induced martensitic transformation leading to pseudoelastic behavior as well as enhanced plasticity at room temperature.

Nanostructurization assisted by twinning during Equal Channel Angular Pressing of Metastable 316L Stainless Steel

H. UENO, A. VINOGRADOV, K. KAKIHATA, Y. KANEKO and S. HASHIMOTO

Journal of Materials Science, Vol. 46, pp.4276-4283 (2011)

A conventional SUS 316L low carbon stainless steel has been processed by Equal channel angular pressing (ECAP) to the equivalent shear strain equal to 2, 4, 6 or 8 at different temperatures ranging from 250 °C to room temperature. The aim of this study is to gain extra control over the “strength-ductility” combination via nanostructure formation, involving twinning and/or strain-induced phase transformation. The resultant microstructure is examined by transmission electron microscopy, X-ray diffraction and electron back scattered diffraction (EBSD) techniques. Substantial structure refinement down to nanoscale is observed in parallel with significant enhancement of tensile yield and ultimate tensile stress, both exceeding 1GPa. A considerable resistance to fracture during localized plastic flow and a fairly good elongation to fracture in tension is reported.

Mechanical Properties and Wear Resistance of Nano-Multilayers Fabricated by Electrodeposition

T. HATTORI, Y. KANEKO and S. HASHIMOTO

Tribologist, Vol. 56 pp.155-160 (2011) (in Japanese)

Mechanical properties and wear resistance of multilayered metallic structures were reviewed. The multilayers were composed of alternate stack of two kinds of thin metallic films. First, method of Ni/Cu and Co/Cu multilayers fabrications, which are based on electrochemical-potential dependence of deposit composition, were explained. Then, the high strength of the multilayered structure is explained in terms of blockage of lattice dislocation by the misfit dislocation networks which are located at interlayer interfaces. It is shown that the Ni/Cu multilayer had apparently high wear resistance with compared to a conventional nickel electrodeposit. The wear resistance of the Ni/Cu multilayer

Multi-Scale Modeling of Irradiation Effects in Spallation Neutron Source Materials

T. YOSHIE, T. ITO, H. IWASE, Y. KANEKO, M. KAWAI, I. KISHIDA, S. KUNIEDA, K. SATO, S. SHIMAKAWA, F. SHIMIZU, S. HASHIMOTO, N. HASHIMOTO, T. FUKAHORI, Y. WATANABE, Q. XUA and S. ISHINO

Nuclear Instruments and Methods in Physics Research B, Vol.269, pp. 1740-1743 (2011).

Changes in mechanical property of Ni under irradiation by 3 GeV protons were estimated by multi-scale modeling. The code consisted of four parts. The first part was based on the Particle and Heavy-Ion Transport code System (PHITS) code for nuclear reactions, and modeled the interactions between high energy protons and nuclei in the target. The second part covered atomic collisions by particles without nuclear reactions. Because the energy of the particles was high, subcascade analysis was employed. The direct formation of clusters and the number of mobile defects were estimated using molecular dynamics (MD) and kinetic Monte-Carlo (kMC) methods in each subcascade. The third part considered damage structural evolutions estimated by reaction kinetic analysis. The fourth part involved the estimation of mechanical property change using three-dimensional discrete dislocation dynamics (DDD). Using the above four part code, stress-strain curves for high energy proton irradiated Ni were obtained.

Synthesis and characterization of bioactive hydroxyapatite-calcite Nanocomposite for biomedical applications

G. S. KUMAR, E. K. GIRIJA, A. THAMIZHAVEL, Y. YOKOGAWA and S. N. KALKURA

J. Colloid and Interface Sci., Vol.349, pp.56-62 (2010)

In a number of recent reports on the synthesis of hydroxyapatite (HA) by sol-gel method using citric acid as an organic modifier, washing was an essential step to remove the byproducts and citric acid. In the present

study we made an attempt to synthesize HA by sol-gel method in the presence of citric acid, wherein we have employed calcination technique instead of the conventional washing process. The products thus obtained were analyzed by X-ray diffraction (XRD), Fourier Transform-Infrared (FT-IR) spectroscopy, thermogravimetry and scanning electron microscopy which confirmed the formation of a nanocomposite of HA and CaCO₃ (calcite) when citric acid was added during synthesis. HA is known to be bioactive and bioresorbable but the rates are too low. On the other hand, CaCO₃ is highly biodegradable. The combination of HA and CaCO₃ compromised the demerits of each others. The dissolved Ca ions from CaCO₃ enhanced the supersaturation of the surrounding fluid which resulted in higher bioactivity of HA.

Biomolecules Loading and Mesoporous SBA-15 Pore Sizes

Y. YOKOGAWA, T. TOMA, A. SAITO, A. NAKAMURA and I. KISHIDA

Bioceramics Development and Applications, Vol.1, (2010). Article ID D110126, 3 pages

The encapsulation and immobilization of biomolecules on solid materials, mesoporous SBA-15, have been studied. Highly ordered hexagonal mesoporous silicates (MPS) with different mean pore sizes have been synthesized using two kinds of triblock copolymers (P123 or L123) as a template. The mixture of tetraethyl orthosilicate (TEOS) and the triblock copolymer (poly(ethylene glycol)-poly(propylene glycol)-poly(ethylene glycol)) was stirred and hydrothermally treated at various temperatures to form the MPS structure. Higher temperatures during stirring and hydrothermal treatment led to the enlargement of pore size. UV-spectrometry was performed to determine the amount of bovine serum albumin (BSA) encapsulated in MPS. It was found that the adsorption processes of BSA on/in MPS could be well described by intraparticle diffusion model.

Synthesis of Microporous Materials and their Adsorptive Properties of H₂S for Dental Application

I. KISHIDA, H. UTAKA, H. MORIKAWA, A. NAKAMURA and Y. YOKOGAWA

Bioceramics Development and Applications, Vol.1, (2010), Article ID D110130, 3 pages

The microporous materials, Zeolite A and ZSM-5 were hydrothermally synthesized and their H₂S adsorption was studied. The obtained samples were put into a separable glass flask filled with H₂S gas, and the change in concentrations of H₂S was measured for 1–48 h at rt. Then the samples were taken out and put into a pyrolysis plant attached to gas chromatography-mass spectroscopy to determine the amount of H₂S desorbed from samples. The amount of H₂S adsorbed on Zeolite A was found to be larger than that on ZSM-5. That is 46% of H₂S was desorbed from Zeolite A when heated at 400 °C, while 24% of H₂S was desorbed from ZSM-5. The adsorption/desorption behavior of H₂S from zeolite materials could be interpreted by the electrostatic interaction between H₂S and adsorbent.

Formation of the Microstructure of TiO₂ Film Through Anodic Oxidation of Titanium

Y. YOKOGAWA, T. YASUKI, T. HIROTOMI, A. NAKAMURA and I. KISHIDA

Mater. Sci. Eng., Vol. 18, (2011) 182003

Recent titanium oxide nanotube arrays have attracted attention for their applications. Titanium oxide nanotubes were prepared under potentiostat conditions (10 - 60 V) for various times (1 min - 3 hr). SEM observations revealed that the pore sizes of the nanotubes have a tendency to increase with an increase in the applied potential in the NH₄F-glycerol-H₂O electrolyte. Some corrosive pores were observed on the surface of titanium substrate at 40 V for 1 minute at 40°C. The pores covered the surface of the titanium substrate after 10 minutes, and some small pores were observed in the inner part of the pores, which should correspond to the combining of some small adjacent pores into a large one. The combining of the tubes were observed after 2 h and 3 h anodization times, and the nanotube arrays seem to be formed upward from the SEM side-views. The photocatalytic activity of the titanium oxide nanotubes was evaluated according to the JIS standard (JIS R 1703-2). The R factor of the titanium oxide nanotube arrays formed at 40 V and 40°C for a 3h the anodization time was 9.71 n mol/l·min, which was twice that of the titanium oxide thin film obtained by the rf-sputtering method.

Synthesis of Microporous Materials and Their VSC Adsorption Properties

Y. YOKOGAWA, H. MORIKAWA, M. SAKANISHI, H. UTAKA, A. NAKAMURA and I. KISHIDA

Mater. Sci. Eng., Vol. 18, (2011) 192011.

Oral malodor is caused by volatile sulfur compounds (VSC) such as hydrogen sulfide (H₂S), methyl mercaptan and dimethyl sulfide produced in mouth. VSC induces permeability of mucous membrane and oral malodor formation. Thus, the adsorbent which highly adsorbs VSC should be useful for health in mouth and may prevent teeth from decaying. The microporous material, hydrotalcite, was synthesized by a wet

method, and the H₂S adsorption was studied. The samples, identified by powder X-ray diffraction method, were put into glass flask filled with H₂S gas. The initial concentration of H₂S was 30 ppm. The change in concentrations of H₂S was measured at rt, and the amount of H₂S adsorbed on the hydrotalcite for 24 h was 300 micro L/g. The samples were taken out from the above glass flask and put into a pyrolysis plant attached to gas chromatography-mass spectrometry to determine the amount of H₂S desorbed from samples. Only 3 % of H₂S was desorbed when heated at 500 °C. H₂S in water was also found to adsorb into hydrotalcite, which was confirmed by the headspace gas chromatography with flame photometric detector. The hydrotalcite material should be expected to be an adsorbent material, useful for health in mouth.

TEM Observation of Biomolecules on/in Mesoporous SBA-15

Y. YOKOGAWA, A. SAITO, N. OGAWA, A. NAKAMURA and I. KISHIDA

Key Engineering Materials, Vols. 493-494, pp. 728-731 (2012)

The encapsulation and immobilization of biomolecules on/in mesoporous silica materials (MPS) have been studied by using transmission electron microscopy (TEM). The mixture of tetraethyl orthosilicate (TEOS) and the triblock copolymer as a template was stirred, hydrothermally treated to form the mesoporous SBA-15 structure, and heat-treated at 550 °C. SEM observation indicated that long and narrow particles were linked together in the long axis direction to form secondary particles of SBA-15. UV-spectrometry was performed to determine the amount of bovine serum albumin (BSA), cytochrome C, myoglobin or β-lactoglobulin encapsulated on/in SBA-15. The time profiles for adsorption of proteins can be well described by intraparticle diffusion model. The TEM observations of proteins on/in mesoporous SBA-15 revealed that proteins were embedded on/in mesoporous SBA-15 and the protein behaviors given by TEM observations may correspond to the intraparticle diffusion model.

Synthesis of Ag-doped zeolite materials and their sulfide adsorption properties

Y. YOKOGAWA, H. MORIKAWA, M. SAKANISHI, H. UTAKA, A. NAKAMURA and I. KISHIDA

Arch. BioCeram Res., Vol.10, pp. 6-9 (2010)

Halitosis is reported to be caused by volatile sulfide compounds (VSCs) such as hydrogen sulfide (H₂S) and methyl mercaptan yielded in mouth. The VSCs also have a bad influence on parodontium, and it may cause periodontitis. Thus, material which adsorbs VSCs should be useful to keep health in mouth. Previously, we reported the H₂S adsorptive properties of zeolite and hydrotalcite materials with micro pores. The amount of H₂S adsorbed on the zeolite was found to be around 300-400 ppm, and depend on their Si/Al ratio. These materials are sparingly soluble in water, and are expected to be likely absorbents for VSCs. In this study, Ag-doped LTA zeolite materials and its H₂S adsorption were investigated. The materials were hydrothermally synthesized and identified by powder X-ray diffraction method. The specimens were put into H₂S gas sealed in glass flask, and then the change in concentrations of H₂S was measured using FPD gas chromatography (GC) and GC- mass spectrometer (MS). Then the materials were heated in a pyrolysis equipment attached to GC-mass spectroscopy to determine an amount of H₂S desorbed from the materials quantitatively. The H₂S adsorptive property of zeolite was remarkably improved by the addition of Ag. Instructions for preparing papers for ABC Proceedings Series are presented. They are intended to guide the authors in preparing camera-ready hardcopy and electronic form of their papers. Only papers prepared according to these instructions will be published.

Synthesis of hybrid films of surface-modified ceramic platelets by Langmuir-Blodgett method for biosensor

Y. YOKOGAWA, S. SAKABE, H. KURIBAYASHI, H. UTAKA, A. NAKAMURA and I. KISHIDA

Arch. Bio Ceram. Res., Vol.10, pp. 91-93 (2010).

Recent, nano-structured films have been attracted interest because of their potential applications to sensor, optical device, electronic device, and so on. Langmuir-Blodgett (LB) method is of use to produce multi-layered organic and inorganic nano-structured film. In this paper, formation of hybrid film of inorganic platelets and an amphiphilic molecule by LB method was studied. NL-BIO40-MWCT (Nippon Laser Electron) was used to measure a π-A plots, and to prepare the hybrid film. Kaolin treated using a silane coupling reagent, and arachidic acid as amphiphilics on mica as substrate were used. Also the inorganic/organic hybrid film formation by in-situ inorganic crystal precipitation on amphiphilic monolayers was investigated. The hydroxyapatite crystals precipitated from SBF solution on LB monolayers / mica substrate was reported.

Cation diffusion along basal dislocations in sapphire

T. NAKAGAWA, A. NAKAMURA, I. SAKAGUCHI, N. SHIBATA, T. MIZOGUCHI, T. YAMAMOTO, H. HANEDA, N. OHASHI and Y. IKUHARA

Acta Materialia, Vol. 59, pp. 1105-1111 (2011)

The diffusion behavior of impurity cations was examined in deformed α -Al₂O₃ single crystals (sapphire) that had a high density of unidirectional basal dislocations. This behavior was examined in the temperature range of 1150–1400 °C by secondary ion mass spectrometry depth profiling techniques. In order to investigate different pipe diffusion behaviors with different diffusing elements, diffusion behaviors of Cr and Ti were studied. Cr was expected to exhibit behavior similar to that of Al because both are isovalent and because of the complete mutual solubility of Cr₂O₃ and Al₂O₃ at high temperatures. Ti was selected because it is representative of an element that is hardly soluble and thus is expected to segregate at dislocations. A drastic decrease in the activation energy for Ti penetration was observed; however, such behavior was not observed for Cr penetration. This fact well explains that the electrical conductivity of deformed sapphire, which results from diffused Ti nanowires along the dislocations of the crystal. The behavior of Cr was similar to that of 18O, examined previously, in that their activation energies for lattice and pipe diffusion were similar. Because Cr diffusion was expected to mimic cation self-diffusion, it was assumed that the activation energy for pipe diffusion was not very low compared to that for bulk diffusion. This assumption is consistent with the fact that the activation energy for grain boundary diffusion in alumina and other ceramics is equal to or higher than that of bulk diffusion. Thus, the absolutely low temperature dependence of Ti pipe diffusion in sapphire may not be because of the enhanced migration of Ti along dislocations but because of other effects, such as the segregation of Ti or Ti clustering at dislocations.

Dislocation Structures in a $\{-1104\}$ / $\langle 11-20 \rangle$ Low-angle Tilt Grain Boundary of Alumina (α -Al₂O₃)

E. TOCHIGI, N. SHIBATA, A. NAKAMURA, T. YAMAMOTO and Y. IKUHARA

J. Mater. Sci., Vol. 46, pp. 4428-4433 (2011)

An alumina (α -Al₂O₃) bicrystal with a $(-1104)/[11-20]$ 2° low-angle tilt grain boundary was fabricated by diffusion bonding at 1500 °C in air, and the grain boundary was observed by transmission electron microscopy (TEM). High-resolution TEM observations revealed that the grain boundary consists of at least two kinds of dislocations. One is a perfect dislocation which has a Burgers vector of $1/3[-12-10]$. The other is dissociated into two partial dislocations with a stacking fault on the (0001) plane, and each partial dislocation has a $1/6[-1101]$ edge component. It is suggested from structural considerations that the dissociated-dislocation pair originates from a $b = 1/3[02-21]$ perfect dislocation (i.e., $1/3[02-21] \rightarrow 1/6[02-21] + 1/6[02-21]$). This dissociation produces a stacking fault in the anion sublattice. The stacking fault energy is estimated to be roughly 1.3 J/m² based on the elastic theory. The authors discuss the dislocation structures and the stacking fault formed on the (0001) plane in detail.

Strain-induced Variation of Relaxation Time in Crosslinked Epoxy Glass Evaluated by a Simple Nonlinear Mechanical Model

Shin'ya YOSHIOKA and Mariko IWAMOTO

Zairyo (J. Soc. Mat. Sci., Jpn), Vol.60, pp.51-56 (2011) (in Japanese)

The single relaxation time of epoxy glass, a thermoset having crosslinked molecular structures, was evaluated during tensile yielding process by using a nonlinear single relaxation model. The model consisted of two elastic springs expressing linear viscoelastic behavior and a dashpot with variable viscosity as a single parameter representing strain-induced structural change. We calculated the strain-dependent relaxation time τ_{SS} by fitting the model to experimental stress-strain curves observed at various strain rates and temperatures. The relaxation time τ_{SS} steeply decreased with increasing strain at the beginning of stretching, and then attained to low steady values at strains slightly larger than the yield strain. The steady values of τ_{SS} were almost inversely proportional to the strain rate, and slightly shorter at a higher stretching temperature. These dependences of τ_{SS} for epoxy glass on strain, strain rate and temperature were qualitatively identical to those for thermoplastic glassy polymers without crosslinked molecular structures. Strain-dependent relaxation times for thermoplastic glassy polymers are known as the result of change in glassy structures. Thus, it is concluded that the nonlinear viscoelastic behavior of crosslinked epoxy glass arises from strain-induced structural change.

Electrical Engineering

Study of a Multi-Pinhole Retinal Projection Display

Hideya TAKAHASHI, Kenji NISHIMURA, Masaru KOBAYASHI (Wear Vision Inc.), Junichi HIRAMOTO (Wear Vision Inc.), Eiji SHIMIZU (Wear Vision Inc.), and Seiji YAMAGUCHI (Times Corporation Ltd.)

J. Jpn. Soc. Low-vision Research and Rehabilitation, Vol. 10, pp.68-74 (2010) (in Japanese).

Purpose: To determine if use of multiple pinholes is an effective method to increase the viewing zone for a retinal projection display.

Methods: We simulated the proposed method for increasing the viewing area of the retinal projection display by changing the alignment and size of the multiple pinholes. We verified the effectiveness of the proposed method by using the optical system simulator to evaluate the retinal projection display when various pinholes were used. Results: When we evaluated the quality of retinal images using the modulation transfer function, we verified that the image quality of the proposed system was similar to that of the previous system. Moreover, in the simulation of changes in pupil size and alignment, we confirmed by the quality of the retinal images that the new method increased the viewing zone.

Conclusions: The proposed method of using multiple pinholes effectively increased convergence points and the viewing zone for the retinal projection display.

The Method of Area Segmentation of Cancer Using Multispectral Image

Hideya. TAKAHASHI, K. YAMADA (Osaka University), Maki TAKEDA (Osaka University), Shigeto YOSHIDA (Hiroshima University), Thi Thi ZIN, and Tahito AIDA

ICIC Express Letters, Vol.5, 10, pp.3859-3864 (2011).

Transnasal endoscopy has recently become a widely accepted screening method in practical application areas of medical endoscopy. Pain tolerance and safety seem to be the greatest advantage of transnasal endoscopy when compared to those of a conventional peroral endoscopy. Although there are some disadvantages such as poor endoscopic images and less illumination caused by downsizing of scopes, as a whole, slim endoscopy is a safe and less invasive tool for screening purposes. On the other hand, flexible spectral imaging color enhancement (FICE) is one of the diagnostic methods using specific light spectra based on spectral image processing technology. FICE provides comparison of spectral images of diseased and surrounding normal areas for enhancement of the contrast by combining wavelengths with greater differences in signals. It is thus in this paper, we propose a novel method of segmenting tumor region for medical endoscope surgery and investigation by using the narrow-band images on several wavelengths.

Evaluation of Three-Dimensional Endoscope Using Compound Eye Optical System with Multi-Wavelength Band-Pass Filter

Kenji YAMADA (Osaka University) and Hideya TAKAHASHI

International Journal of Innovative Computing, Information and Control, Vol.7, 8, pp.4691-4701 (2011).

Diagnosis and intervention in endoscopy is based on image sequences of a video camera. However, an image sequence provides no depth information. We propose the novel endoscope system with compound eye and wavelength band pass filter. The system is composed of micro-lens array, wavelength band pass filter, separation layer and image sensor. Several wave length band pass filters are covered with each micro-lens. The proposed system makes it possible to take any images from the membrane surface to deep blood vessel simultaneously. With several test targets, the characteristics of the prototype system are evaluated.

Real-Time Updatable Volumetric Display System Based on Inclined-Image Scanning

D. MIYAZAKI, K. OHNO, and T. MUKAI

Sixth International Conference on Intelligent Information Hiding and Multimedia Signal Processing, pp. 684 - 687 (2010).

A new experimental volumetric display system based on inclined-image scanning is reported. A volumetric image is formed as a stack of about one hundred cross-sectional images. A high-speed video interface apparatus for controlling a digital micromirror device, which displays the cross-sectional images, is introduced to achieve real-time updating of volumetric images. The cross-sectional images of a three-dimensional (3D) object are generated from a depth map of the 3D polygon surface model within a video frame rate. In addition, to increase the viewing angle, the numerical aperture of an optical system is increased by use of a larger scanner mirror.

Three-Dimensional Display Using a Roof Mirror Grid Array and a Prism Sheet

Y. MAEDA, D. MIYAZAKI, N. HIRANO, and S. MAEKAWA (NICT)

17th International Display Workshops, pp. 1301-1304 (2010).

We developed a three-dimensional display using a roof mirror grid array, which is an optical imaging element that forms a real image, and a rotating prism sheet. The use of the rotating prism sheet can reduce a blur caused by diffraction at the roof mirror grid array.

Phase conjugate wave generation based on self-pumped four-wave mixing in a broad-area laser diode

K. HARA, M. INOUE, D. MIYAZAKI and T. MUKAI

22nd IEEE International Semiconductor Laser Conference, (ISLC2010), pp. 125 - 126 (2010).

The purpose of this study is to construct the fast-response PCM only made of semiconductor gain material in a self-pumped manner, and to demonstrate the self-oscillation of the PCM cavity which may offer the drastically narrow spectral linewidth, as theoretically proposed by Petersen et al. This paper first demonstrates the destructive interference due to the phase conjugate feature in the self-pumped, angled feedback experiment using a broad-area laser diode (BA-LD).

Self-Pumped Phase Conjugate Mirror Using a Broad-Area Laser Diode

T. MUKAI, K. HARA, M. INOUE, S. NAGIYAMA, and D. MIYAZAKI

Int. Quantum Electronics Conference/ Pacific Rim Conference on Lasers and Electro-Optics (IQEC/CLEO Pacific Rim 2011), 3230-CT-6 (2011).

Self-pumped phase conjugate mirror is successfully constructed using a broad-area laser diode with angled feedback configuration. We demonstrate the light output decrease and the half-axial mode specific to the phase conjugate resonator.

Characteristics of Exciton Polaritons in a ZnO Microcavity

T. KAWASE, S. KOMURA, K. MIYAZAKI, D. KIM, and M. NAKAYAMA

Physica E, Vol. 42, pp. 2567–2570 (2010).

We have investigated the characteristics of exciton polaritons in a ZnO microcavity with HfO₂/SiO₂ distributed Bragg reflectors. The results of the angle-resolved reflectance spectra were analyzed by calculating the cavity polariton dispersions with a phenomenological Hamiltonian for the coupling between the cavity photon and three kinds of excitons labeled A, B, and C peculiar to ZnO. The vacuum-Rabi-splitting energy is estimated to be ~80 meV. The reflectance dips originating from the cavity polaritons shift to lower energy side with an increase in temperature. We discuss the temperature dependence of the cavity-polariton energies of the ZnO microcavity on the basis of the phenomenological Hamiltonian taking account of the temperature dependence of the exciton energies with Varshni's law. DOI:10.1016/j.physe.2009.12.058

Photoluminescence Properties of Exciton–Exciton Scattering in a GaAs/AlAs Multiple Quantum Well

M. NAKAYAMA, T. HIRAO, and T. HASEGAWA

Physica E, Vol. 42, pp. 2644–2647 (2010).

We report on the photoluminescence (PL) properties of a GaAs (20 nm)/AlAs (20 nm) multiple quantum well under high-density-excitation conditions at excitation energies near the fundamental exciton energies. The biexciton-PL band is dominant in a relatively low-excitation-power region. The PL originating from exciton–exciton scattering, the so-called P emission, suddenly appears with an increase in excitation power. The excitation-energy dependence of the intensity of the P-PL band indicates that the excitation energy higher than the fundamental heavy-hole exciton by the energy of the longitudinal optical (LO) phonon is the most efficient for the P PL. This suggests that the LO-phonon scattering plays an important role in the relaxation process of excitons leading to the P PL. The appearance of the P-PL band remarkably suppresses the intensity of the biexciton-PL band; namely, the exciton–exciton scattering process prevents the formation of biexcitons. Furthermore, we have confirmed the existence of optical gain due to the exciton–exciton scattering process with use of a variable-stripe-length method. DOI:10.1016/j.physe.2009.09.021

Upconversion of Photoluminescence due to Subband Resonances in a GaAs/AlAs Multiple Quantum Well Structure

T. HASEGAWA, S. OKAMOTO, and M. NAKAYAMA

Physica E, Vol. 42, pp. 2648–2651 (2010).

We have investigated the upconversion of photoluminescence (PL) due to subband resonances in a simple GaAs(15.3 nm)/AlAs(4.5 nm) multiple quantum well embedded in a *p-i-n* diode structure. The systematic measurements of the PL spectra and the calculated results of the interband transition energies as a function of electric field strength reveal that the PL bands from the electron subbands with $n=3$ (E3) and $n=4$ (E4) sharply appear under the first-nearest-neighbor resonance conditions between the E1 and E3 subbands and the E1 and E4 subbands, respectively, owing to the carrier injection to the E3 and E4 subbands from the E1 subband. This result indicates that the resonant tunneling due to the subband resonance is a dominant mechanism for the carrier population in the higher lying subbands. Utilizing these subband resonances, we have demonstrated the upconversion of PL from the E3 and E4

subbands under the excitation condition of the fundamental interband transition between the E1 and the $n=1$ heavy-hole subbands.

DOI:10.1016/j.physe.2009.10.003

Coherent Control of Terahertz Wave from Coherent Longitudinal Optical Phonon in a GaAs/AlAs Multiple-Quantum-Well Structure

K. MIZOGUCHI, Y. KANZAWA, G. OOHATA, S. SAITO, K. SAKAI, and M. NAKAYAMA

Jpn. J. Appl. Phys., Vol. 49, 120202 (3 pages) (2010).

We report on the coherent control of terahertz (THz) waves emitted from coherent longitudinal optical (LO) phonons in a GaAs/AlAs multiple-quantum-well structure at room temperature using two-pulse excitation. When the time difference between the first pump pulse and second weak control pulse is increased, the intensity of THz waves from the coherent phonons is cancelled and enhanced by the control pulse, and the phase of THz waves shows periodic changes accompanied by a phase jump. The time-difference dependences of the intensity and phase of THz waves are explained in terms of the superposition of two coherent oscillations.

DOI: 10.1143/JJAP.49.120202

Photoluminescence Decay Profiles of Exciton-Exciton Scattering in a ZnO Thin Film

S. WAKAIKI, H. ICHIDA, K. MIZOGUCHI, D. KIM, Y. KANEMATSU, and M. NAKAYAMA

Phys. Status Solidi C, Vol. 8, pp. 116–119 (2011).

We have investigated the photoluminescence (PL) dynamics of a ZnO thin film under intense excitation conditions at 10 K. In the ZnO thin film, a PL band due to exciton-exciton scattering, the so-called P emission, appears. The optical-Kerr-gating method with the ultrashort gating time of 0.6 ps enabled us to obtain precise information of the temporal profiles including the peak energy, the bandwidth and the intensity of the P emission, at various detection energies. We have found that the decay time of the P emission gradually shortens with decreasing detection energy. The change in the decay time can be reasonably attributed to the photon-like characteristics of the lower polariton branch that is the final state of the exciton-exciton scattering. Furthermore, we have shown that the decay time of the P emission is phenomenologically determined by the group velocity of the final state although the origin of the long decay time remains to be elucidated.

DOI: 10.1002/pssc.201000675

Simple Strategy for Enhancing Terahertz Emission from Coherent Longitudinal Optical Phonons Using Undoped GaAs/ n -type GaAs Epitaxial Layer Structures

H. TAKEUCHI, J. YANAGISAWA, S. TSURUTA, H. YAMADA, M. HATA, and M. NAKAYAMA

Phys. Status Solidi C, Vol. 8, pp. 343–345 (2011).

We have explored the feasibility of enhancing terahertz (THz) emission from coherent longitudinal optical (LO) phonons using simple epitaxial layer structures: undoped GaAs/ n -type GaAs (i -GaAs/ n -GaAs) epitaxial layer structures. Initially, using a numerical simulation we have confirmed that a decrease in the i -GaAs layer thickness d increases the built-in electric field in the i -GaAs layer. From the THz wave measurement, it is observed in the THz waveforms of the samples that the monocycle oscillation, the so-called first burst, resulting from the surge current of the photogenerated carriers, accompanies with a clear oscillatory profile with a period of 113 fs corresponding to the GaAs LO phonon frequency (8.8 THz). The Fourier transform spectra show that the intensity of the LO phonon band remarkably increases with a decrease in d that causes the enhancement of the built-in electric field in the i -GaAs layer. Thus, we conclude that the utilization of the i -GaAs/ n -GaAs structure is a useful way to

enhance the THz emission from the coherent LO phonon. We also performed the time-partitioning Fourier transform in order to investigate the decay time of the THz wave from the coherent LO phonon. The decay time of each sample is almost the same: 2.0 ps.
DOI: 10.1002/pssc.201000396

Photoluminescence Properties of Exciton-Exciton Scattering in a Dilute Nitride GaAs_{1-x}N_x Epitaxial Film

M. NAKAYAMA, J. HASHIMOTO, and Y. MAEDA

Phys. Status Solidi C, Vol. 8, pp. 372–374 (2011).

We report on the photoluminescence (PL) properties of a dilute nitride GaAs_{1-x}N_x epitaxial film with $x=0.008$ grown on a (001) GaAs substrate under high-density-excitation conditions. The band-gap energy of the GaAs_{0.992}N_{0.008} film is 1.34 eV at 10 K, which was confirmed by photoreflectance spectroscopy; namely, GaAs_{0.992}N_{0.008} belongs to a category of narrow-gap semiconductors. It has been found that a PL band appears with a threshold-like nature. At the threshold excitation power for the appearance of the PL band, the PL-peak energy is lower than the energy of the fundamental exciton by the exciton binding energy. The results described above indicate that the PL band originates from exciton-exciton scattering, the so-called P emission, which is typically observed in wide-gap semiconductors with large exciton binding energies. Furthermore, we have confirmed the existence of optical gain in the energy region of the P band with use of a variable-stripe-length method.

DOI: 10.1002/pssc.201000387

Exciton Polaritons in ZnO Microcavities with Different Active Layer Thicknesses

T. KAWASE, D. KIM, K. MIYAZAKI, and M. NAKAYAMA

Phys. Status Solidi B, Vol. 248, pp. 460–463 (2011).

We have investigated the characteristics of exciton polaritons in ZnO microcavities with different active layer thicknesses. The microcavity was made from a bulk ZnO active layer and two distributed Bragg reflectors (DBRs) consisting of HfO₂ and SiO₂ layers. We adopted rf magnetron sputtering and pulsed laser deposition for the preparation of the DBR and ZnO active layer, respectively. Angle-resolved reflectance spectra demonstrate the formation of cavity polaritons. From the analysis using a phenomenological Hamiltonian for the coupling between the cavity photon and three kinds of excitons labeled A, B, and C peculiar to ZnO, the vacuum Rabi-splitting energies in the 1/2-microcavity are estimated to be 30, 71, and 84 meV for the A, B, and C excitons, respectively. Moreover, we indicate the potential to control the Rabi-splitting energy by changing the active layer thickness.

DOI: 10.1002/pssb.201000620

Frequency-Tunable Terahertz Electromagnetic Wave Emitters Based on Undoped GaAs/*n*-type GaAs Epitaxial Layer Structures Utilizing Sub-Picosecond-Range Carrier-Transport Processes

H. TAKEUCHI, J. YANAGISAWA, S. TSURUTA, H. YAMADA, M. HATA, and M. NAKAYAMA
J. Lumin., Vol. 131, pp. 531–534 (2011).

We have investigated sub-picosecond-range carrier-transport processes in undoped GaAs/*n*-type GaAs (*i*-GaAs/*n*-GaAs) epitaxial layer structures with various *i*-GaAs-layer thicknesses d ranging from 200 to 2000 nm, focusing on the relation between carrier-transport processes and terahertz electromagnetic wave frequency. Initially, using numerical simulation and photoreflectance measurement, we confirm that a decrease in d enhances the built-in electric field in the *i*-GaAs layer. In the time-domain terahertz waveform, it is observed that the intense monocycle oscillation induced by the surge current of photo-generated carriers, the so-called first burst, is followed by the oscillation patterns originating from the

coherent GaAs longitudinal optical (LO) phonon. From the Fourier power spectra of the terahertz waveforms, it is clarified that the decrease in d causes a high frequency shift of the band of the first burst. Consequently, we conclude that, in the sub-picosecond time range, the photogenerated carriers are monotonously accelerated by the built-in electric field without being affected by intervalley scattering. The present conclusion signifies that the frequency-tunable terahertz emitters are realized by controlling i -GaAs-layer thickness. We also find the intensity of the coherent LO phonon band is enhanced by a decrease in d .

DOI:10.1016/j.jlumin.2010.09.022

Control of Exciton-Photon Interactions in CuCl Microcavities

M. NAKAYAMA, K. MIYAZAKI, T. KAWASE, and D. KIM

Phys. Rev. B, Vol. 83, 075318 (5 pages) (2011).

We have investigated the active-layer-thickness dependence of exciton-photon interactions in planar CuCl microcavities with HfO₂/SiO₂ distributed Bragg reflectors. The active layer thickness was changed from $\lambda/32$ to $\lambda/4$, while the cavity length was fixed at $\lambda/2$. We performed angle-resolved reflectance measurements and clearly detected three cavity-polariton modes, originating from the lower, middle, and upper polariton branches, in a strong-coupling regime of the Z_3 and $Z_{1,2}$ excitons and cavity photon. The incidence-angle dependence of the cavity-polariton modes was analyzed using a phenomenological Hamiltonian for the strong coupling. It was found that the interaction energies of the cavity-polariton modes, the so-called vacuum Rabi splitting energies, are systematically controlled from 22(37) to 71(124) meV for the Z_3 ($Z_{1,2}$) exciton by changing the active layer thickness from $\lambda/32$ to $\lambda/4$. The active-layer-thickness dependence of the Rabi splitting energy is quantitatively explained by a simple theory for quantum-well microcavities.

DOI: 10.1103/PhysRevB.83.075318

Emission of the Terahertz Electromagnetic Wave from Coherent Longitudinal Optical Phonons in a GaAs Buffer Layer Optically Masked by a GaSb Top Epitaxial Layer

H. TAKEUCHI, S. TSURUTA, and M. NAKAYAMA

Appl. Phys. Lett., Vol. 98, 151905 (3 pages) (2011).

We demonstrate that, in a GaSb/GaAs epitaxial structure, the coherent longitudinal optical (LO) phonon in the GaAs layer optically masked by the GaSb top layer is observed utilizing terahertz-electromagnetic-wave spectroscopy. It is confirmed from a Raman scattering measurement that only the optical phonon in the GaSb layer is optically observable, where the photon energy of the excitation laser beam was almost the same as that of the femtosecond pulse pump beam for the terahertz wave measurement. In the terahertz wave measurement, the Fourier power spectrum of the terahertz waveform exhibits both the GaAs and the GaSb LO phonons; namely, the coherent LO phonon in the optically masked GaAs buffer layer is observed in the terahertz wave measurement. This fact demonstrates that the instantaneous surface potential modulation originating from the impulsive carrier excitation by the pump pulses reaches the GaAs buffer layer. Consequently, the above-mentioned surface potential modulation generates the coherent GaAs LO phonon.

DOI:10.1063/1.3574541

Electric Field Effects on Excitonic Quantum Beats in a Single Quantum Well Embedded in a GaAs/AlAs Superlattice

T. HASEGAWA, Y. TAKAGI, and M. NAKAYAMA

Phys. Rev. B, Vol. 83, 205309 (6 pages) (2011).

We have investigated the characteristics of the quantum beat of excitons confined in a GaAs single quantum well (6.4 nm) embedded in the center of a GaAs (3.2 nm)/AlAs (0.9 nm) superlattice (SL) from the viewpoint of the resonant coupling between the subband states in the single quantum well (SQW) and the Wannier–Stark localization states in the SL with the use of a reflection-type pump-probe technique. The resonant couplings, which cause anticrossing behaviors of relevant transition energies, were observed by electroreflectance spectroscopy and analyzed by calculating the eigenenergies as a function of electric field strength. It is found that the frequency and intensity of the quantum beat between the heavy-hole and light-hole excitons in the SQW significantly change under the resonant coupling conditions of the electron states. The changes of the quantum-beat properties result from the formation of bonding and antibonding electron states which modifies the excitonic transition properties in the SQW as a function of electric field strength. The experimental results of the quantum beat are reasonably explained by the electric-field-strength dependence of the energies and transition probabilities of the excitons in the SQW observed from electroreflectance spectra.
DOI: 10.1103/PhysRevB.83.205309

Cavity Polaritons of Heavy-Hole and Light-Hole Excitons in a CuI Microcavity

M. NAKAYAMA, M. KAMEDA, T. KAWASE, and D. KIM

Phys. Rev. B, Vol. 83, 235325 (5 pages) (2011).

We have investigated the exciton-photon coupling phenomena in a CuI bulk microcavity consisting of a CuI active layer with an effective thickness of $\lambda/2$ and HfO₂/SiO₂ distributed Bragg reflectors. In the CuI active layer, a thermal strain removes the degeneracy of the heavy-hole (HH) and light-hole (LH) excitons at the Γ point. Angle-resolved reflectance spectra measured at 10 K demonstrate strong coupling between the HH and LH excitons and cavity photon, resulting in the formation of three cavity-polariton modes: lower, middle, and upper polariton branches. The photoluminescence band from the lower polariton branch was clearly observed. The energies of the three cavity-polariton modes as a function of incidence angle are reasonably explained by analysis using a phenomenological Hamiltonian for the strong coupling. The vacuum Rabi splitting energies are evaluated as 50 and 29 meV for the HH and LH excitons, respectively. The magnitude of the Rabi splitting energy results from the large oscillator strength of the relevant exciton. Furthermore, it is confirmed that the strong coupling regime is fully maintained at room temperature because of the high stability of the excitonic system.
DOI: 10.1103/PhysRevB.83.235325

Terahertz Spectroscopy of Dynamics of Coupling Between the Coherent Longitudinal Optical Phonon and Plasmon in the Surge Current of Instantaneously Photogenerated Carriers Flowing Through the *i*-GaAs Layer of an *i*-GaAs/*n*-GaAs Epitaxial Structure

H. TAKEUCHI, S. TSURUTA, and M. NAKAYAMA

J. Appl. Phys., Vol. 110, 013515 (6 pages) (2011).

We demonstrate the dynamics of coupling between the coherent longitudinal optical (LO) phonon and plasmon of instantaneously photogenerated electrons in an undoped GaAs/*n*-type GaAs (*i*-GaAs/*n*-GaAs) epitaxial structure using time-domain terahertz spectroscopy. Initially, we experimentally and numerically clarify the presence of the built-in electric field in the *i*-GaAs layer of the *i*-GaAs/*n*-GaAs epitaxial layer. Next, we performed the terahertz-wave measurements of the *i*-GaAs/*n*-GaAs epitaxial structure at various excitation conditions from a low density excitation regime to a high excitation regime. The LO-phonon-plasmon coupled (LOPC) mode has been confirmed from the terahertz-wave measurement. It is found that the frequency of the LOPC mode is determined by the pump-beam power. This fact demonstrates that the LOPC mode is formed in the *i*-GaAs layer. In addition, we performed

the time-partitioning Fourier transform in order to reveal the dynamical change in the LOPC mode as a function of time delay. Using this analysis, we have observed that the disappearance of the LOPC mode immediately occurs within the time delay of 0.6 ps. Following the disappearance of the LOPC mode, only the bare coherent GaAs LO phonon dominates the terahertz waves.

DOI: 10.1063/1.3603046

Noncascading THz-wave parametric oscillator synchronously pumped by mode-locked picosecond Ti:sapphire laser in doubly-resonant external cavity

YUMA TAKIDA, SHINGO MAEDA, TATSUYA OHIRA, HIROSHI KUMAGAI and SHIGEKI NASHIMA

Optics Communications **284**, 4663 (2011).

A noncascading terahertz (THz) wave parametric oscillator synchronously pumped by a mode-locked picosecond Ti:sapphire laser whose average power was less than 1 W was demonstrated with a noncollinear phase-matching MgO:LiNbO₃ crystal in an external enhancement cavity doubly resonant for both pump (780 nm) and signal (781–784 nm) waves. In the external cavity, in which the pump wave enhanced so as to reduce the pumping threshold of parametric processes, the signal wave could also resonate and thus be enhanced simultaneously, resulting in a THz wave output at approximately 0.9 THz as the idler wave. The novel dual enhancement of pump and signal waves reduced the threshold pumping intensity to approximately 50 MW/cm², which was much lower than that of a conventional externally pumped THz wave parametric oscillator with a crystal.

High-efficiency second harmonic generation of a mode-locked picosecond Ti:sapphire laser with an external enhancement cavity

YUMA TAKIDA, TATSUYA OHIRA, SHINGO MAEDA and HIROSHI KUMAGAI

Proceedings of LPM2011, 12th International Symposium on Laser Precision Microfabrication, 11-095 (2011)

We reported high-efficiency SHG of a low-power mode-locked picosecond Ti:sapphire laser, whose average output power was less than 1 W, with a BiB₃O₆ (BiBO) nonlinear crystal installed in a four-mirror external enhancement cavity. A 15-mm-long BiBO crystal was cut for collinear critical type I ($e + e \rightarrow o$) phase-matching direction (θ, ϕ) = (149.3°, 90°). UV coherent light at 389 nm with the maximum average power of 506 mW was obtained with the input average power of 805 mW using the external cavity. Considering the reflective loss of the output coupler of the 389 nm light, we could estimate the intrinsic conversion efficiency of 70 %. This value, to the best of our knowledge, is the highest conversion efficiency for SHG with a BiBO crystal, even at the relatively low fundamental power.

Parametric oscillation of terahertz wave pumped by picosecond Ti:sapphire laser with MgO-doped LiNbO₃ installed in external enhancement cavity

YUMA TAKIDA, TATSUYA OHIRA, SHINGO MAEDA, HIROSHI KUMAGAI and SHIGEKI NASHIMA

Proceedings of LPM2011, 12th International Symposium on Laser Precision Microfabrication, 11-096 (2011)

We demonstrated a mode-locked picosecond Ti:sapphire laser pumped terahertz (THz) parametric oscillation (TPO) with a 5 mol% MgO-doped lithium niobate (MgO:LiNbO₃) crystal installed in a simple external enhancement ring cavity. In the external cavity consisted of only four mirrors, the idler (Stokes) wave which made an intersecting angle of about 1 degree with the pump wave was resonated as well as the pump wave automatically and simultaneously in order to reduce the pumping threshold

of TPO and improve the conversion efficiency. As a result, the novel doubly resonant of both pump and idler waves achieved approximately 50 MW/cm² of the threshold intensity and about 2.0×10^{-7} of conversion efficiency. Also, we obtained the tunability of idler wavelength from 781.5 to 786.0 nm, corresponding to the frequency of THz wave of 0.7 to 3.0 THz. A broad output spectrum of THz wave at approximately 0.9 THz of peak frequency was confirmed by constructing a Michelson interferometer with a silicon beam splitter.

TiO₂/sapphire beam splitter for high-order harmonic

YASUTAKA SANJO, MASAKI MURATA, YUJI TANAKA, HIROSHI KUMAGAI and MASAYA CHIKAGE

Proceedings of LPM2011, 12th International Symposium on Laser Precision Microfabrication, 11-097 (2011)

TiO₂/sapphire beam splitter (BS) for high-order harmonics was studied and fabricated through taking advantage of the self-limiting nature of atomic layer epitaxy (ALE). Theoretical calculation indicated that the highest reflectivity of the TiO₂/sapphire BS was 44.8 % at 21.24 nm, which corresponds to the 37th-order harmonics of the 800-nm pump pulse and then the optimal thickness of the TiO₂ layer was 67.4 nm. Incident angle was set at 70.5° for TiO₂, which corresponds to the Brewster's angle of the 800-nm pump pulse. Moreover, experimental results indicated that refractive indices ($\lambda = 632.8\text{nm}$) of the TiO₂ films were almost constant at a value of 2.59 and growth rate of TiO₂ films was 0.077nm/cycle, which corresponds to 885 cycles in order to deposit the TiO₂ layer with the optimal film thickness as an anti-reflection layer.

Sum-frequency generation of continuous-wave tunable ultraviolet coherent light in BBO-installed external cavity

KENTA MUKOYAMA, KAZUHIRO TOKUYAMA, HIROSHI KUMAGAI, NORIHIRO INOUE, NAOAKI FUKUDA and TOSHIO TAKIYA

Proceedings of Photonics West 2012: LASE2012, (CD-ROM), (2012) in press.

We developed a CW, high-power, tunable, and UV light source through sum-frequency generation (SFG) with a BBO nonlinear crystal. We built up a two-stage frequency-conversion system using two external cavities for the enhancement of CW lights. In the first stage, we obtained 532-nm coherent light by the second harmonic generation (SHG) of a 1064-nm light source. The 1064-nm light source was a fiber laser which was able to output up to 10 W. We employed a bow-tie external cavity incorporating four mirrors, whose cavity length was controlled by a Hänsch-Couillaud frequency stabilization method. The mirrors of the cavity were placed on a monolithic brass board to away from any environmental fluctuations. In the second stage, we successfully obtained 312-nm coherent light by SFG of 532-nm light from the first stage and 754-nm light from a single-frequency CW Ti:Sapphire laser.

Quasi phase matching through periodic step structure

TAKAFUMI OHFUCHI, NOBUYUKI HIRANO, HIROYA MATSUKAWA, KOICHIRO NAKAYAMA, HIROSHI KUMAGAI, NORIHIRO INOUE, NAOAKI FUKUDA and TOSHIO TAKIYA

Proceedings of Photonics West 2012: LASE2012, (CD-ROM), (2012) in press.

We report on a new way to generate the second harmonic (SH) by quasi phase matching (QPM). In ordinary, QPM is achieved by polarization inversion, but we suggest the periodic step structure to achieve QPM. The periodic step structure is made by chipping off the region which might be ordinary inversion structure by Focused Ion Beam (FIB). We processed several optical crystals such as lithium

triborate (LBO) and tried to generate the SH. The process cycle was calculated theoretically and conversion efficiency was also simulated.

Novel beam splitter for high-order harmonics with WO₃/TiO₂ bilayer grown on c-plane sapphire substrate by sequential surface chemical reactions YASUTAKA SANJO, MASAKI MURATA, HIROSHI KUMAGAI, YASUO NABEKAWA, KATSUMI MIDORIKAWA and MASAYA CHIKAGE
Proceedings of Photonics West 2012: LASE2012, (CD-ROM), (2012) in press.

We proposed and fabricated a novel beam splitter (BS) for the high-order harmonics with a WO₃/TiO₂ bilayer grown on a c-plane sapphire substrate by sequential surface chemical reactions. In BS for the high-order harmonics, reflection of the fundamental waves should be minimized by entering the p-polarized fundamental waves at the Brewster's angle, which could improve the separation between the fundamental waves and the high-order harmonics. Then, reflection characteristics at the soft-x-ray wavelengths were investigated at the same Brewster's angle using monochromatized synchrotron radiation at Ultraviolet Synchrotron Radiation Facility (UVSOR), Institute for Molecular Science, Okazaki, Japan.

Tunable terahertz parametric oscillator synchronously pumped by mode-locked picosecond Ti:Sapphire laser with MgO-doped LiNbO₃

YUZURU TADOKORO, YUMA TAKIDA, TATSUYA OHIRA, HIROSHI KUMAGAI and SHI-GEKI NASHIMA

Proceedings of Photonics West 2012: LASE2012, (CD-ROM), (2012) in press.

We built a THz parametric oscillator (TPO) in doubly-resonant external enhancement cavity synchronously-pumped by a mode-locked picosecond Ti:sapphire laser with 780 nm of center wavelength. As a result, we developed a widely tunable picosecond TPO just by selecting the resonant idler wavelength. The resonant idler wave was continuously tunable from 781.5 to 786.0 nm by varying the noncollinear phase-matching condition, corresponding to the THz frequency range from 0.7 to 3.0 THz according to the law of energy conservation. In addition, the measured angle between the pump and idler waves inside the crystal showed the good agreement with the theoretical calculation.

Coherent electro-optical detection of THz-wave generated from synchronously pumped picosecond THz parametric oscillator

YUMA TAKIDA, TATSUYA OHIRA, YUZURU TADOKORO, HIROSHI KUMAGAI and SHI-GEKI NASHIMA

Proceedings of Photonics West 2012: LASE2012, (CD-ROM), (2012) in press.

We have been focusing on developing low-laser-power-pumped THz-wave parametric sources and successfully demonstrated a synchronously-pumped picosecond THz parametric oscillation in doubly-resonant external cavity with a bulk 5 mol% MgO-doped lithium niobate crystal. For the purpose of the realization of THz spectroscopy and imaging applications using our THz-wave source, we constructed the coherent THz-wave detection system via electro-optical effect with a <110> ZnTe crystal. As a result, we obtained the temporal waveform and the relatively broad spectrum of the THz-waves generated from our parametric oscillator. Also, we compared this electro-optical detection system with a Fourier transform Michelson interferometer using a high-resistance silicon beam splitter, from the viewpoints of availability, ease of use, and signal-to-noise ratio.

Topology of magnetic field lines: Chaos and bifurcations emerging from two-action systems

T. MIYAGUCHI, M. HOSODA, K. IMAGAWA, and K. NAKAMURA

Phys. Rev. E, **83**, #016205-1-5 (2011).

Nonlinear dynamics of magnetic field lines generated by simple electric current elements are investigated. In general, the magnetic field lines show behavior similar to that of the Hamiltonian systems; in fact, they can be generally transformed into Hamiltonian systems with 1.5 degrees of freedom, obey the Kolmogorov-Arnold-Moser (KAM) theorem, and generate chaotic trajectories. In the case where unperturbed systems are described by two action (slow) and one angle (fast) variables, however, it is found that the periodic orbits of the unperturbed systems vanish for arbitrarily small symmetry-breaking perturbations (a breakdown of the KAM theorem) and drifting or periodic trajectories appear. The mechanism of this phenomenon is investigated analytically by weak nonlinear stability analysis. It is also shown numerically that scattering processes of the perturbed system exhibit typical features of chaotic dynamical systems.

Ubiquitous chaotic magnetic field lines

M. HOSODA

Parity, **26**, No. 06, pp. 34-39 (2011). In Japanese.

We found that a kind of chaos, i.e., chaotic magnetic-field lines (CMFLs) exist everywhere and are ubiquitous in the modern technological world. Although it is commonly believed that magnetic-field lines generated by a wire carrying electric current always have simple closed-loop structures, this belief is wrong, because CMFLs can be generated by simple three-dimensionally crossed-wires. We investigated the existence of CMFLs in realistic systems, and revealed that this chaos exists widely in conventional electrical and electronic products in our daily life, for example, in mobile phones, personal computers, power wires in house etc., although we are unaware of this fact.

Noncascading THz-wave parametric oscillator synchronously pumped by mode-locked picosecond Ti:sapphire laser in doubly-resonant external cavity

Y. TAKIDA, S. MAEDA, T. OHHIRA, H. KUAGAI, AND S. NASHIMA

A noncascading terahertz (THz) wave parametric oscillator synchronously pumped by a mode-locked picosecond Ti:sapphire laser whose average power was less than 1 W was demonstrated with a noncollinear phase-matching MgO:LiNbO₃ crystal in an external enhancement cavity doubly resonant for both pump (780 nm) and signal (781-784 nm) waves. In the external cavity, in which the pump wave enhanced so as to reduce the pumping threshold of parametric processes, the signal wave could also resonate and thus be enhanced simultaneously, resulting in a THz wave output at approximately 0.9 THz as the idler wave. The novel dual enhancement of pump and signal waves reduced the threshold pumping intensity to approximately 50 MW/cm², which was much lower than that of a conventional externally pumped THz wave parametric oscillator with a crystal.

Ultraslow Convergence to Ergodicity in Transient Subdiffusion.

T. MIYAGUCHI and T. AKIMOTO,

Physical Review E **83**, 062101 (2011, June).

We investigate continuous time random walks with truncated α -stable trapping times. We prove distributional ergodicity for a class of observables; namely, the time-averaged observables follow the probability density function called the Mittag-Leffler distribution. This distributional ergodic behavior persists for a long time, and thus the convergence to the ordinary ergodicity is considerably slower than in the case in which the trapping-time distribution is given by common distributions. We also find a crossover from the distributional ergodic behavior to the ordinary ergodic behavior.

DOI: 10.1103/PhysRevE.83.062101

Intrinsic Randomness of Transport Coefficient in Subdiffusion with Static Disorder.

T. MIYAGUCHI and T. AKIMOTO,

Physical Review E **83** 031926 (2011, March).

Fluctuations in the time-averaged mean-square displacement for random walks on hypercubic lattices with static disorder are investigated. It is analytically shown that the diffusion coefficient becomes a

random variable as a manifestation of weak ergodicity breaking. For two- and higher- dimensional systems, the distribution function of the diffusion coefficient is found to be the Mittag-Leffler distribution, which is the same

as for the continuous-time random walk, whereas for one-dimensional systems a different distribution (a modified Mittag-Leffler distribution) arises. We also present a comparison of these two distributions in terms of an ergodicity-breaking parameter and show that the modified Mittag-Leffler distribution has a larger deviation from

ergodicity. Some remarks on similarities between these results and observations in biological experiments are presented.

DOI: 10.1103/PhysRevE.83.031926

Topology of Magnetic Field Lines: Chaos and Bifurcations Emerging from Two-Action Systems.

T. MIYAGUCHI, M. HOSODA, K. IMAGAWA and K. NAKAMURA,

Physical Review E 83 016205 (2011, January).

Nonlinear dynamics of magnetic field lines generated by simple electric current elements are investigated. In general, the magnetic field lines show behavior similar to that of the Hamiltonian systems; in fact, they can be generally transformed into Hamiltonian systems with 1.5 degrees of freedom, obey the Kolmogorov-Arnold-Moser (KAM) theorem, and generate chaotic trajectories. In the case where unperturbed systems are described by two action (slow) and one angle (fast) variables, however, it is found that the periodic

orbits of the unperturbed systems vanish for arbitrarily small symmetry-breaking perturbations (a breakdown of the KAM theorem) and drifting or periodic trajectories appear. The mechanism of this phenomenon is investigated analytically by weak nonlinear stability analysis. It is also shown numerically that scattering processes of the

perturbed system exhibit typical features of chaotic dynamical systems.

DOI: 10.1103/PhysRevE.83.016205

Assessment of Gait in Patients with Neck Disease Using a Wearable Accelerometer.

Namiko AKAMATSU (OCU Hospital), Shinji IMAKUBO(OCU Hospital), Ryoichi KATO(OCU Hospital), Takashi MIYOSHI, (OCU Hospital) Tamotsu NAKATSUCHI (Tsuji Orthopaedic Rehabilitation Hospital), Shigeyoshi NAKAJIMA, Hiroyoshi IWAKI(Grad. School of MED,OCU), Mitsuhiro IKEBUCHI(Grad. School of MED,OCU), Hidetomi TERAJ(Grad. School of MED,OCU), Hiroaki NAKAMURA(Grad. School of MED,OCU) *Japanese Journal of Clinical Biomechanics*, Vol.31, pp.85-90, Oct. (2010).

Patients with neck disease sometimes show instability in walking due to abnormal gait patterns. Evaluation of such abnormalities is often made subjectively. A more objective and quantitative method of gait evaluation for these patients has been desired. We are now studying a wearable accelerometer which is compact in size, simple to use and allows measurement under less limited settings. The present study paid attention to the walking rhythm of patients with neck disease and attempted a new method for quantification of their gait patterns. The method attempted was DCT analysis of the data yielded from a wearable accelerometer and subsequent calculation of peak occupancy with the band pass filter technique. The study involved 37 patients divided into two groups according to preoperative JOA score : the severe group (n=27) and the mild group (n=10). Ten healthy volunteers served as the healthy control group. The preoperative peak occupancy in the severe group was lower than the peak occupancy in the healthy control group, while the preoperative peak occupancy in the mild group was comparable to the peak occupancy in the healthy control group. In the severe group, peak occupancy rose significantly 1 and 3 months after surgery as compared to the preoperative level ($p<0.01$), becoming closer to the peak occupancy in the control group. The mild group showed no significant change in peak occupancy at any point of measurement after surgery as compared to the preoperative peak occupancy. These results indicate that measurement with a wearable accelerometer enables evaluation of gait rhythm in patients with neck disease. The wearable accelerometer is useful as a means of objective and quantitative evaluation of gait and its clinical utilization seems to be possible if the data collected with this device are combined with findings as to instability and other physical features.

Measurement of Absolute Size of Moving Object Using An Omnidirectional Sensor Camera and Laser Range Sensor

Yuuki FUKUI, Shigeyoshi NAKAJIMA, and Takashi TORIU

ICIC(Innovative Computing, Information and Control) Express Letters , Volume 4, Issue 6(B), pp.2451-2456, (2010)

We propose a new method to measure an absolute size of an object in sight using an omnidirectional sensor camera and a laser range sensor. With a camera (omnidirectional or else), an angle of a view of an object or its planer dimension tells us its relative size, but not its absolute size. And a range sensor tells us the distance from the sensor, to an object, also but not its absolute size. The combination of an omnidirectional sensor camera and laser range sensor tells us an absolute size of object and it is good at surveillance for security.

Security and Observation System for Solitary Person Using Accelerometer and Surveillance Camera

Satoshi HASEBE, Shigeyoshi NAKAJIMA, ThiThi Zin and Takashi TORIU

IJCSNS International Journal of Computer Science and Network Security, VOL.11 No.3, March (2011)

Recently people living alone increase according to a change of the state of the society in the world. Notably elderly people living alone increase more and more. The increasing number of hunger deaths and solitary deaths becomes a big social problem. Municipal governments and care service companies provide services monitoring an alone elderly person using a television-phone or a remote camera and deliver a service person in emergency. On the other hand, there were many cases that a turnover accident of an alone elderly person causes a solitary death. Then in this study we propose a system to discriminate human postures and behaviors using camera images and accelerometer data to detect quickly a turnover or else. We can discriminate with a camera and an accelerometer a posture which is not discriminable with only a camera. With an acceleration data we can easily discriminate a face up lie from a face down lie. We show the results of our experiments to discriminate postures

which are not discriminable only with images also not discriminable only with accelerations and show the efficiency of the proposed method.

Separation of Mixed Plural Sound Sources in Instrumental Music Using Butterworth Parallel BPF

Yusuke YAMAGUCHI, Shigeyoshi NAKAJIMA and Takashi TORIU

IJCSNS International Journal of Computer Science and Network Security, VOL.11 No.4, pp.85-90, April (2011).

Many researchers investigated sound source separation as one of themes of music information processing. Sound source separation is a work to separate each sound from a mix of several sound sources such as pianos and violins etc. It is one of very important techniques in automatic music transcription. And also it is assumed as one of early stages in music recognition of human auditory perception and it will take a major role in computer simulations of human perception process. We propose a new method of sound source separation using Butterworth parallel bandpass filter(BPF). We show that the proposed method is superior to a recent work. As a result of experiment the proposed method improves fidelity of output comparing an original single instrument sound in input.

Band Pass Filtering at Harmonics for Visualization of 3D trajectory of Human Periodical Walking Motion from Wearable Accelerometer Data

Shigeyoshi NAKAJIMA, Mitsuhiro IKEBUCHI (Grad. School of MED, OCU) and Takashi TORIU

ICIC(Innovative Computing, Information and Control) Express Letters Part B: Applications, Vol.2, No.3, pp.553-558, June (2011).

A human walk includes many kinds of information about the walking person. For many years a lot of researchers investigated data of human walk. A motion capture system is one of good mechanisms to record 3D motion data of parts of human bodies such as wrists, waists, head and so on and good to record human walking data. But a motion capture systems is heavy, large, not portable and needs much space. A wearable accelerometer is one of portable and light machines to record acceleration data of a human body. An acceleration is the second order differential of a motion. So terms of the motion upper than linear is recovered by twice integrations of an acceleration. Recently a researcher tried it but the result is unsatisfactory. We successfully extracted a periodical trajectory of a 3D human walking motion from acceleration data using DFT, frequency detection and multiple band pass filtering.

Accuracy of Distance of Registration in Orthopedic Navigation System with Visible Radiation 3D Tracking Using X-ray Fluoroscopy Images and CT Images

S. NAKAJIMA, M. IKEBUCHI (Grad. School of MED, OCU), and T. TORIU

ICIC(Innovative Computing, Information and Control) Express Letters, Vol. 5, No. 10, pp. 3853-3857, Oct. (2011).

We developed new navigations for orthopedic operations with X-ray fluoroscopy and CT images and a method to measure accuracies of those navigations. We used 3D tracker with visible radiation. Many navigation systems for orthopedic operations were proposed. But there were no reports about accuracies of distances of those navigation systems. X-ray images using a non-flat fluoroscopy include a distortion. Our system is designed to reduce distance error with correction of such a distortion. Also we developed a navigation using a flat fluoroscopy without a distortion. We show the accuracies of distances of the proposed methods in this paper.

Applied Chemistry

Examinations on 2.5V Li[Li_{1/3}Ti_{5/3}]O₄/Li[Li_{0.1}Al_{0.1}Mn_{1.8}]O₄ Cells at -10, 25, and 55 °C for the first-generation 12V lead-free batteries

Mitsuyasu IMAZAKI, Lina WANG, Toru KAWAI, Kingo ARIYOSHI and Tsutomu OHZUKU

Electrochim. Acta, Vol. 56, pp. 4576-4580 (2011).

Electrochemical behaviors of 2.5V Li[Li_{1/3}Ti_{5/3}]O₄ (LTO)/Li[Li_{0.1}Al_{0.1}Mn_{1.8}]O₄ (LAMO) cells for the first-generation 12 V lead-free battery were examined at -10, 25, and 55 °C. The LTO/LAMO cells showed the same rechargeable capacity in temperature ranging from -10 to 55 °C when the cells were examined at 0.5 mA cm⁻² in cell potential ranging from 0 to 3.0 V. Capacity fading after 250 cycles was negligibly small at -10 °C. Rechargeable capacities, however, faded 5% at 25 °C and 15% at 55 °C after 250 cycles. In the discharged LTO/LAMO cell after 250 cycles at 55 °C, the state of charge (SOC) of the positive electrode was 16% while SOC of the negative electrode was 0%, indicated that the capacity fading was due to an imbalance in SOC between the positive and negative electrodes. To understand the progress of an imbalance in SOC, the LTO/LAMO cell with a lithium auxiliary electrode was fabricated and examined at 55 °C for 400 cycles, and the possible origin of capacity fading was discussed.

Effect of Primary Particle Size upon Polarization and Cycling Stability of 5-V Lithium Insertion Material of Li[Ni_{1/2}Mn_{3/2}]O₄

Kingo ARIYOSHI, Yusuke MAEDA, Toru KAWAI and Tsutomu OHZUKU

J. Electrochem. Soc., Vol. 158, pp. A281-A284 (2011).

The 5-V lithium insertion materials of Li[Ni_{1/2}Mn_{3/2}]O₄ having different primary particle sizes were prepared by the two-step solid-state reaction at several temperatures and characterized by Fourier transform infrared, X-ray diffraction, and scanning electron microscopy. The primary particle size of Li[Ni_{1/2}Mn_{3/2}]O₄ depends on the heating temperature. High temperature synthesis gives highly crystallized Li[Ni_{1/2}Mn_{3/2}]O₄ having large particle sizes with smooth {111} facets of octahedra characteristic of spinel. The steady-state polarization measurements were carried out by applying the sinusoidal voltage of peak amplitude of 1 V at 0.1 Hz to the cell consisting of Li[Ni_{1/2}Mn_{3/2}]O₄ and Li[Li_{1/3}Ti_{5/3}]O₄. The well-developed primary particles prepared at 1000 °C were superior to the small primary particles prepared at temperatures lower than that value in terms of polarization together with cycling stability.

Silicon-Based Negative Electrode for High-Capacity Lithium-Ion Batteries: "SiO"-Carbon Composite

Masayuki YAMADA, Atsushi UEDA, Kazunobu MATSUMOTO and Tsutomu OHZUKU

J. Electrochem. Soc., Vol. 158, pp. A417-A421 (2011).

The silicon-based materials were prepared and examined in lithium cells for high-capacity lithium-ion batteries. Among the materials examined, "SiO"-carbon composite showed remarkable improvements on capacity fading. "SiO" is composed of nanosized silicon crystallites highly dispersed in an amorphous silicon dioxide matrix. The "SiO"-carbon composite materials consisting of "SiO," graphite, and carbon fiber with carbon coatings show the smallest irreversible capacity at the first cycle and the best capacity retention among the other silicon-based materials examined, such as carbon-coated silicon, the one-to-one mixture of "SiO" and graphite, or one-to-one mixture of carbon-coated "SiO" and graphite. Capacity of more than 85% compared to capacities observed for initial ten cycles is retained after 100 cycles when the laminate-type cell with a positive electrode is examined in voltage ranging from 2.5 to 4.2 V, which meets the requirement on the negative electrodes for practical high-capacity lithium-ion batteries.

High-Capacity Lithium Insertion Materials of Lithium Nickel Manganese Oxides for Advanced Lithium-Ion Batteries: Toward Rechargeable Capacity More Than 300 mAh g⁻¹

Tsutomu OHZUKU, Masatoshi NAGAYAMA, Kyoji TSUJI and Kingo ARIYOSHI

J. Mater. Chem., Vol. 21, pp. 10179-10188 (2011).

Lithium nickel manganese oxides Li[Ni_xLi_(1/3-2x/3)Mn_(2/3-x/3)]O₂ ($x = 1/2, 2/7, \text{ and } 1/5$) are prepared and characterized by XRD and FT-IR, and the samples are examined in non-aqueous lithium cells at room temperature and 55 °C. Among these materials LiNi_{1/2}Mn_{1/2}O₂ ($x = 1/2$) shows the highest operating voltage and the smallest polarization with a rechargeable capacity of *ca.* 230 mAh g⁻¹ and Li[Li_{1/5}Ni_{1/5}Mn_{3/5}]O₂ ($x = 1/5$) shows the lowest operating voltage and the largest polarization with a rechargeable capacity more than 300 mAh g⁻¹. Extraordinarily large rechargeable capacity of Li[Li_{1/5}Ni_{1/5}Mn_{3/5}]O₂ together with an

anomalously long voltage plateau at 4.5 V only observed at first charging process is examined by window-opening charge and discharge, continuous charge and discharge combined with differential chronopotentiometry at room temperature and at 55 °C, and possible mechanisms are discussed in terms of lithium insertion scheme.

Low-Temperature Magnetic Properties and High-Temperature Diffusive Behavior of LiNiO₂ Investigated by Muon-Spin Spectroscopy

Jun SUGIYAMA, Yutaka IKEDO, Kazuhiko MUKAI, Hiroshi NOZAKI, Martin MANSSON, Oren OFER, Masashi HARADA, Kazuya KAMAZAWA, Yasuhiro MIYAKE, Jess H. BREWER, Eduardo J. ANSALDO, Kim H. CHOW, Isao WATANABE and Tsutomu OHZUKU

Phys. Rev. B, Vol. 82, pp. 224412-1-11 (2010).

In order to elucidate the effect of Ni ions in the Li layer on magnetism and Li diffusion of LiNiO₂, we have measured muon-spin rotation and muon-spin relaxation (μ^+ SR) spectra for the polycrystalline Li_{1-x}Ni_{1+x}O₂ samples with $x=0.02$, 0.03, and 0.15. Weak transverse-field- μ^+ SR measurements demonstrated the existence of a bulk ferromagnetic transition at $T_m=48(6)$ K for the $x=0.03$ sample and 161(7) K for $x=0.15$ while the $x=0.02$ sample exhibited an antiferromagnetic transition at 18(4) K. Zero-magnetic-field-(ZF) μ^+ SR measurements below T_m clarified the formation of static ferromagnetic (FM) order for the $x=0.03$ and 0.15 samples but only a highly disordered antiferromagnetic (AF) order for the $x=0.02$ sample. Therefore, the variation in the low- T magnetism with x is most unlikely due to the change in the concentration of an AF NiO-type domain or an FM Ni-rich cluster but likely due to a homogeneous change in the whole system. In the paramagnetic state, ZF- and longitudinal-field- μ^+ SR spectra exhibited a dynamic nuclear field relaxation. From the temperature dependence of the field fluctuation rate, a diffusion coefficient of Li⁺ ions (D_{Li}) at 300 K was estimated about $0.39(3) \times 10^{-11}$ cm²/s for the $x=0.02$ sample and $0.12(7) \times 10^{-11}$ cm²/s for $x=0.15$. On the other hand, the related compound, LiCrO₂, did not show any diffusive behavior even at the highest temperature measured (=475 K). Considering the hindrance of diffusion by Ni in the Li⁺ diffusion plane and the fact that LiCrO₂ is electrochemically inactive, the estimated D_{Li} is thought to be very reasonable for the positive electrode material of Li-ion batteries. Furthermore, at low temperatures where the Li⁺ ions are static, the internal magnetic field was still found to be fluctuating, due to a dynamic local Jahn-Teller distortion of the Ni³⁺ ions in a low-spin state with $S=1/2(t_{2g}^6e_g^1)$.

Structural and Chromatic Changes of Host Polydiacetylene Crystals during Intercalation with Guest Alkylamines

Tomoyo SHIMOGAKI and Akikazu MATSUMOTO

Macromolecules, Vol. 44(9), pp. 3323–3327 (2011).

We report a new type of intercalation system using the host polydiacetylene (PDA) crystals including a carboxylic acid in the side chain in combination with various guest alkylamines. The role of the phenylene or methylene spacer between the conjugated main chain and the carboxylic acid on the intercalation property was investigated using three kinds of PDAs, i.e., poly(1,3-hexadecadiynyl-4-benzoic acid), poly(2,4-heptadecadiynoic acid), and poly(10,12-pentacosadiynoic acid), as the host polymer crystals. The color of the PDA crystals changed from blue to red by the addition of the amines. A change in the interlayer distance of the host polymer crystals according to the size of the guest amines was determined and the inclined structure of the alkyl groups was discussed based on the powder X-ray diffraction data. We further succeeded in the direct observation of the intercalation reaction process by monitoring the color change in a large PDA crystal using optical microscopy.

Single-Crystal-to-Single-Crystal Transformation of Di(isopropylammonium) (Z,Z)-Muconate into the (E,E)-Muconate during One-Way Photoisomerization in the Solid State

Natsuko NISHIZAWA, Junya NAKAMURA and Akikazu MATSUMOTO

Cryst. Growth Des., Vol. 11(8), pp. 3442–3447 (2011).

The solid-state EZ photoisomerization of di(isopropylammonium) (Z,Z)-muconate (**ZZ-1a**) into the corresponding EE isomer (**EE-1a**) via a single-crystal-to-single-crystal reaction process was investigated. The molecular motion based on a bicycle-pedal model was directly observed during the photoisomerization in the crystals by an X-ray single crystal structure analysis. The photoirradiation of **ZZ-1a** provided **EE-1a** in a quantitative yield via a one-way isomerization mechanism, being different from the solution products in the photostationary state. The isomerization reactivity was discussed for the ammonium and ester derivatives of muconic acid.

Columnar Mesophases Constructed by Hierarchical Self-Organization of Rod-like Diacetylene Molecules

Tomoyo SHIMOGAKI, Satoshi DEI, Kazuchika OHTA and Akikazu MATSUMOTO

J. Mater. Chem., Vol. 21(29), pp. 10730–10737 (2011).

We report a new class of liquid crystalline system exhibiting columnar mesophases, which are constructed by the hierarchical supramolecular self-organization of a rod-like diacetylene derivative as the primary building block. A series of 1,3-alkadiynyl-4-benzoic acids (**mDA**) with different alkyl chain lengths ($m = 8–16$) were synthesized and their mesophase properties were investigated by differential scanning calorimetry, polarized optical microscopy, and X-ray diffraction under temperature control. The **mDA** exhibited three types of mesophases, i.e., a discotic lamellar phase, D_L , and two columnar rectangular phases, Col_{rd} and Col_{ro} , with disordered and ordered stacking structures of the mesogens in a column, respectively, depending on the length of the alkyl substituent and temperature. We have revealed that the columnar mesophase structures are constructed with the rod-like **mDA** molecules as the starting building blocks by hierarchical self-organization. The hydrogen-bonded dimers of the carboxylic acid with a rigid framework are assembled to provide a disc-like mesogen unit, which consists of a π -stacked core-part and peripheral alkyl-chains. The discotic supramolecular mesogens further stack in ordered and disordered columnar structures, producing the Col_{ro} and Col_{rd} mesophases, or in the layer D_L mesophase. This is a rare example for the discotic mesophases using the rod-like diacetylenes with a non-branched molecular structure.

Highly-Controlled Regiospecific Free-Radical Copolymerization of 1,3-Diene Monomers with Sulfur Dioxide

Naruki TANAKA, Eriko SATO and Akikazu MATSUMOTO

Org. Biomol. Chem., Vol. 9(10), pp. 3753–3758 (2011).

The free-radical copolymerization of alkyl-substituted 1,3-butadienes with sulfur dioxide using a redox initiating system in toluene at -78°C produced poly(diene sulfone)s consisting of a highly alternating and 1,4-regiospecific repeating structure, irrespective of the position and number of alkyl substituents, and the highly regioselective propagation via a free radical reaction mechanism is well accounted for by DFT calculations using model reactions.

Intercalation of Mono- and Difunctional Azobenzenes as the Photoresponsible Guest Molecules into the Host Poly(muconic acid) Crystals

Tomoyo SHIMOGAKI, Shinya OSHITA and Akikazu MATSUMOTO

Macromol. Chem. Phys., Vol. 212(16), pp. 1767–1777 (2011).

An intercalation system consisting of layered PMA crystals as the host material and amino-functionalized azobenzene derivatives as the guests is studied. The intercalation of difunctional guest molecules yields low conversions compared to the intercalation results using the corresponding monofunctional guests. Investigation of the cis-trans photoisomerization of the intercalated azo compounds reveals that the isomerization rate depends on the packing structure and the mobility of the azobenzene moieties in the host crystals. The monofunctional azobenzene moieties with a longer alkyl spacer undergo fast and reversible photoisomerization. XRD and UV results reveal the arrangement of the guest molecules present in the interlayer space of the host PMA crystals.

Mechanical Aging Behavior of Styrene-Butadiene Rubbers Evaluated by Abrasion Test

Takeo NAKAZONO and Akikazu MATSUMOTO

J. Appl. Polym. Sci., Vol. 120(1), pp. 379–389 (2011).

The ring-shaped styrene-butadiene rubbers (SBR) test pieces ran on a rotating stainless-steel ring using an abrasion tester in order to evaluate the changes in the mechanical properties, such as the tensile storage modulus and $\tan\delta$ values, the modulus at 300% elongation, and the strength and extension ratio at the breaking point, after a mechanical aging process. The surface of the SBR test pieces and the formed rubber debris after the running experiment was investigated using scanning electron microscopy (SEM). A change in the cross-linking density of the SBRs and the analysis of the isolated free polymers showed the occurrence of bond scission of the copolymer chains. On the other hand, the mechanical properties of whole SBR samples showed only a small change during the mechanical aging test.

Phase Separation and Thermal Aging Behavior of Styrene-Butadiene Rubber Vulcanizates Using Liquid Polymers as Plasticizers Studied by Differential Scanning Calorimetry and Dynamic Mechanical Spectroscopy

Takeo NAKAZONO, Anri OZAKI and Akikazu MATSUMOTO

J. Appl. Polym. Sci., Vol. 120(1), pp. 434–440 (2011).

Styrene-butadiene rubber (SBR) vulcanizates were prepared using plasticizers including the four liquid types of styrene-butadiene copolymers (LPSB), polybutadiene (LPB), polyisoprene (LPI), and the hydrogenated polyisoprene (LHPI) as well as the conventional process oil, and their phase-separated structures and mechanical properties were investigated by differential scanning calorimetry (DSC) and dynamic mechanical spectroscopy (DMS). The phase separation was observed for the SBR vulcanizates when LPI and LHPI were used as the plasticizers, while the LPSB and LPB gave homogeneous structures because of the good miscibility with the SBR. The phase-separated structure of the SBR vulcanizate prepared using LPI changed to the homogeneous during the thermal aging. We revealed the role of the liquid polymers as the plasticizers in maintaining the physical and mechanical properties of the SBR vulcanizates during the thermal aging process when the plasticizers were miscible to the SBR.

Control of Interface Structure and Properties Using Polymer Reactions

Eriko SATO

J. Adhes. Soc. Japan, Vol. 47(10), pp. 398–404 (2011) (in Japanese).

Polymer reactions change the properties of polymers such as solubility, glass transition temperature, and so on. The introduction of reactive polymers or groups to other polymers such as a branched copolymer, a block copolymer, and a network polymer would enhance property changes by polymer reactions. The investigation of bulk and interface property changes of the reactive polymers and their application to functional materials was introduced.

Change in Mechanical Properties of Styrene-Butadiene Rubber Vulcanizates during Thermal Aging

Takeo NAKAZONO and Akikazu MATSUMOTO

Mem. Fac. Eng., Osaka City Univ., Vol. 51, pp. 1–10 (2010).

The change in mechanical properties was investigated during the thermal aging process of styrene-butadiene rubbers (SBR) with different styrene, 1,2-, and 1,4-butadiene contents and the different types of plasticizers. An increase in the hardness and modulus values during the aging was confirmed to be due to the additional cross-linking reaction between the polymer chains in the SBR vulcanizates and the slow evaporation of the used process oil. We demonstrated the validity of the use of a nonvolatile liquid polymer as the plasticizer to achieve the desired physical properties of the SBR vulcanizate during thermal aging.

Fabrication of Thin-Film Crystals of Muconic Esters by Vapor Deposition and Their Solid-State Reaction

Akikazu MATSUMOTO

Chemical Industry (Kagaku Kogyo), Vol. 2(4), pp. 249–254 (2011) (in Japanese).

Dismantlable Adhesion Technology Using Degradable Polymers

Eriko SATO

Science and Industry (Kagaku To Kogyo), Vol. 85(3), pp. 114–121 (2011) (in Japanese).

Adhesion Using Thermally Degradable Polymers

Akikazu MATSUMOTO

In *Handbook of Bonding and Debonding Technologies: Source, Environment and Energy*, Edited by Hiroo Miyairi, NGT, pp. 339–345 (2011) (in Japanese).

Report on 19th Organic Crystals Symposium

Akikazu MATSUMOTO

Newsletters of Organic Crystals Division, The Chemical Society of Japan, No. 28, p. 73 (2011) (in Japanese).

Reports from Local Divisions: Report from the 57th Polymer Research Symposium (Kobe)

Akikazu MATSUMOTO

Kobunshi, The Society of Polymer Science, Japan, Vol. 60, No. 10, p. 762 (2011) (in Japanese)

Dismantlable Adhesion Using the Main- and Side-Chain Degradation of Polymers

Akikazu MATSUMOTO

The 60th Annual Meeting of the Society of Polymer Science, Japan, Invited Lecture, May 25–27, 2011, Osaka, *Polymer Preprints*, Vol. 60, pp. 61–63 (2011) (in Japanese).

Dismantlable Pressure-Sensitive Adhesion System Responsible for Photoirradiation and Postbaking

Akikazu MATSUMOTO

The 4th Asian Conference on Adhesion, Invited Lecture, Busan, September 25–27, 2011, Abstracts, pp. 27–30.

Control of Interface Structure and Properties Using Reactive Polymers

Eriko SATO

The 60th Annual Meeting of the Society of Polymer Science, Japan, Invited Lecture, May 25–27, 2011, Osaka, *Polymer Preprints*, Vol. 60, pp. 105–107 (2011) (in Japanese).

Synthesis and Application of Block Copolymers Containing Main-Chain Degradable Polyperoxides

Eriko SATO

The 5th Pacific Symposium on Radical Chemistry, Invited Lecture, September 25–28, 2011, Shirahama, Abstract, IL-24.

Experimental Parameters for XRF Analysis of Soils

Yukiko IMANISHI, Atsushi BANDO, Shintaro KOMATANI, Shin-Ichiro WADA and Kouichi TSUJI

Advances in X-ray Analysis, Vol. 53, pp. 248–255 (2010).

Harmful elements (Pb, Se, Cd, etc.) in the soil samples were measured by X-ray fluorescence (XRF) method. We investigated the influence of the thickness of soil layer, the grain size of soils, and the water content in soils on XRF intensity. Since high-energy XRF such as Cd $K\alpha$ was detected in deep inside of soils, a thickness of 10 mm was recommended. The soil sample with a small grain size gave a relatively strong XRF intensity, especially for low-energy x-rays. Therefore, this grain-size effect should be taken into account for quantitative XRF analysis of the soil. It was also confirmed that water in soils decreased the XRF intensity, especially for low-energy x-rays. Preferably, after the soil sample was dried, the soils should be analyzed by XRF. Otherwise, XRF intensity has to be corrected depending on water content in the soil sample.

Development of Laboratory Confocal 3D-XRF Spectrometer and Nondestructive Depth Profiling

Kazuhiko NAKANO and Kouichi TSUJI

J. Anal. At. Spectrom., Vol. 25, pp. 562–569 (2010).

The present paper reports on the laboratory 3D-XRF results applied to industrial and environmental samples. The feasibility of confocal 3D-XRF analysis was characterized with regard to the depth resolution and depth sensitivity. To investigate the depth sensitivity of the confocal 3D-XRF analysis, the multilayered plastic reference samples were prepared by using a spin coating method. It was confirmed that these plastic layered reference materials were useful for evaluating the analytical performance of confocal 3D-XRF. In addition, many applications of 3D-XRF to industrial plastics, chemical microchip, and biological samples were demonstrated under the confocal XRF configuration.

Development of a Transportable μ -XRF Spectrometer with Polycapillary Half Lens

Tasuku YONEHARA, Daisuke ORITA, Kazuhiko NAKANO, Shintaro KOMATANI, Sumito OHZAWA, Atsushi BANDO, Hiroshi UCHIHARA and Kouichi TSUJI

X-Ray Spectrom., Vol. 39, pp. 78–82 (2010).

We developed a transportable micro-XRF (μ -XRF) spectrometer using a polycapillary X-ray focusing half lens, which was placed between the sample and the detector. The total weight of the developed spectrometer was about 2 kg; its dimensions were 18 (W) \times 26 (D) \times 40 (H) cm. The spatial resolution of the spectrometer with the half lens of a working (focal) distance of 30mm was 171 μ m at Fe $K\alpha$, which was evaluated by a wire scanning method. In this setup, it is easy to replace the polycapillary X-ray half lens with one having a different analytical performance, because a precise position-adjustment of the X-ray lens is not required. The

spacial resolution with the half lens of a working distance of 16 mm was 106 μm at Fe $K\alpha$. Depending on analyzing area on the sample and required spatial resolution, we can easily change the X-ray lens, as in a conventional optical microscope. The calibration curves of V, Cr, Mn, and Ni measured for standard steel materials showed good linear relationships (correlation coefficients > 0.993). Clear elemental mapping could be obtained by scanning the sample (Cu mesh). An elemental analysis of a micro-region in an electronic device was also performed by the transportable μ -XRF spectrometer. Sn and Pb were detected at the metallic part (Sn–Pb solder) of the device. Br and Ba were observed at some resin parts of the electronic device.

X-Ray Fluorescence Imaging with Polycapillary X-ray Optics

Tasuku YONEHARA, Makoto YAMAGUCHI and Kouichi TSUJI

Spectrochim. Acta Part B, Vol. 65, pp. 441-444 (2010).

X-ray fluorescence spectrometry imaging is a powerful tool to provide information about the chemical composition and elemental distribution of a specimen. X-ray fluorescence spectrometry images were conventionally obtained by using a μ -X-ray fluorescence spectrometry spectrometer, which requires scanning a sample. Faster X-ray fluorescence spectrometry imaging would be achieved by eliminating the process of sample scanning. Thus, we developed an X-ray fluorescence spectrometry imaging instrument without sample scanning by using polycapillary X-ray optics, which had energy filter characteristics caused by the energy dependence of the total reflection phenomenon. In the present paper, we show that two independent straight polycapillary X-ray optics could be used as an energy filter of X-rays for X-ray fluorescence. Only low energy X-rays were detected when the angle between the two optical axes was increased slightly. Energy-selective X-ray fluorescence spectrometry images with projection mode were taken by using an X-ray CCD camera equipped with two polycapillary optics. It was shown that Fe $K\alpha$ (6.40 keV) and Cu $K\alpha$ (8.04 keV) could be discriminated for Fe and Cu foils.

X-ray Spectrometry (Review article)

Kouichi TSUJI, Kazuhiko NAKANO, Yoshio TAKAHASHI, Kouichi HAYASHI and Chul-Un RO

Anal. Chem., Vol. 82, pp. 4950-4987 (2010).

In this review, we focus on the most significant and essential progress in x-ray spectrometry (XRS) published during the period 2008-2009 covering developments and improvements in x-ray optics, x-ray detectors, new quantification models in x-ray spectra and data evaluation, micro-x-ray fluorescence (μ -XRF) including 3D- x-ray fluorescence (3D-XRF), imaging techniques such as tomography and holography methods for 2D or 3D imaging of microstructures, electron probe microanalysis (EPMA), total reflection x-ray fluorescence (TXRF), particle-induced x-ray emission (PIXE) analysis, and x-ray absorption spectrometry (XAS). In addition, different applications in each subfield of XRS are described including sample preparation, standard materials, energy-dispersive XRF (ED-XRF) and wavelength-dispersive XRF (WD-XRF). This review involves only a selected minority of published papers and impressive figures. We attempt to look over the current trends in this analytical field with a critically selected citing of papers to support the research activity of the community of x-ray scientists.

Sample Surface and Near-surface Analysis by Confocal 3D XRF Spectrometer

Kazuhiko NAKANO and Kouichi TSUJI

Hyomen-Kagaku, Vol. 31, pp. 331-336 (2010) (in Japanese).

We have developed a confocal 3D-XRF spectrometer in combination with polycapillary X-ray lenses and a laboratory X-ray source. The depth resolutions of the 3D-XRF configuration estimated by scanning of Au and Cr thin foils were approximately 50 μm for AuLa, and 100 μm for CrKa, respectively. The capacity of the depth-sensitive analysis of the confocal setup was investigated by scanning a thick plastic reference sample concluding trace metals of Ti, Cr, Co and Pb. The depth sensitivity in deeper region was significantly decreased than that in the surface region because of the absorption of X-ray irradiation and X-ray

fluorescence in the material. The calculated LLD values of Cr at each depth were 9.4 mg/kg at 300 μm , 23 mg/kg at 500 μm , 38 mg/kg at 700 μm , 77 g/kg at 900 μm , and 110 mg/kg at 1100 μm , respectively. 3D elemental analysis with the confocal XRF setup was demonstrated for an electrical Cu cable covered with PVC. The 3D elemental images agreed well with the actual distributions of the sample. The confocal 3D-XRF has a great advantage for 3D elemental analysis as well as nondestructive depth analysis at ambient pressure.

Total Reflection X-ray Fluorescence Analysis of Metals in Leaching Solutions from Plastic Samples

Masaya KAWAMATA, Yukiko IMANISHI, Kazuhiko NAKANO and Kouichi TSUJI

Advances in X-Ray Chemical Analysis, Japan, Vol. 41, pp. 185-193 (2010) (in Japanese).

Total reflection x-ray fluorescence (TXRF) is well known as a trace analysis method. There are many applications of trace elemental analysis by TXRF. Sample preparation technique has been developed depending on the type of the samples to be analyzed. In the case of solution samples, a normal sample preparation is to drop a small amount of solution on a flat sample carrier, then a dried residue is measured by TXRF. We have studied how to measure the metals in surface layers of plastics by TXRF. In some cases, the surface of the plastic products will be dissolved by acid solutions such as acid rain, leading that harmful elements are also dissolved into the solutions or soils. In this study, we have studied dissolving and leaching processes of plastic products for TXRF analysis. A droplet of solutions dissolved by organic solutions was prepared in thin films by spin coating techniques. This sample was analyzed by TXRF with an internal standard solution. In addition, a actual plastic toy (minicar) was dissolved in acid solution. The leaching solution was sampled in the time range from 0.5 min. to 180 min., then they were measured by TXRF. The time-dependent curves of TXRF intensities showed specific shapes depending on the elements. This result indicates that TXRF is useful for monitoring the leaching process of metals from plastic toys.

Photochromism of a Diarylethene with Methoxymethyl Groups at Reactive Carbons: Thermal Irreversible Reaction of the Closed-Ring Isomer

Daichi KITAGAWA and Seiya KOBATAKE

Chem. Lett., 40(1), pp. 93–95 (2011).

A photochromic diarylethene having methoxymethyl groups at the reactive carbons was synthesized, and the thermal stability of the closed-ring isomer was examined. The closed-ring isomer of the diarylethene caused both the thermal cycloreversion and a thermally irreversible reaction at 120 °C. The structure of the thermal product was identified by ^1H NMR, MS, and X-ray crystallographic analysis.

Correlation between Steric Substituent Constants and Thermal Cycloreversion Reactivity of Diarylethene Closed-Ring Isomers

Daichi KITAGAWA, Kyohei SASAKI and Seiya KOBATAKE

Bull. Chem. Soc. Jpn., 84(2), pp. 141–147 (2011).

Two kinds of diarylperfluorocyclopentenes having 5-phenyl-2-propyl-3-thienyl and 2-isobutyl-5-phenyl-3-thienyl group as the aryl groups were newly synthesized, and the thermal stability of their closed-ring isomers was investigated. The bulkiness of the substituent (R) at the reacting positions in photochromic diarylethenes plays an important role in the thermal cycloreversion reactivity of the photogenerated closed-ring isomers. The steric substituent constant was introduced to investigate the relationship between the steric hindrance of the substituent R and the thermal cycloreversion reactivity. We employed three steric substituent constants, $E_s(\text{R})$, $E_s^c(\text{R})$, and $\nu(\text{R})$ values. We found that there is a good correlation between the $E_s^c(\text{R})$ value and the thermal cycloreversion reactivity. Furthermore, the $E_s(\text{CH}_2\text{R})$ value has also a good correlation with the thermal cycloreversion reactivity, while $E_s(\text{R})$ has no correlation. These results indicate that the steric hindrance has an effect on the thermal cycloreversion and there is no hyperconjugation of the α -hydrogen on the 2-substituent on the thiophene ring. Moreover, the activation energy was also found to be related to the steric substituent constant. These findings would give a new useful strategy to design novel diarylethenes having desired thermal stability.

Photoswitching of an Alcohol-Sensitive Photochromic Diarylethene

Seiya KOBATAKE, Shotaro IMAO, Yosuke YAMASHIRO and Yuko TERAOKA

Tetrahedron Lett., 52(16), pp. 1905–1908 (2011).

The closed-ring isomer of diarylethene **1a**, 1-(2-methyl-5-(4-*N,N*-diethylaminophenyl)thien-3-yl)-2-(2-methyl-5-phenylthien-3-yl)perfluorocyclopentene was found to cause the substitution reaction with primary alcohols at room temperature. The open-ring isomer **1a** was stable in the alcohols. The product obtained in methanol was isolated by HPLC, and the structure was identified by ¹H NMR, mass spectrometry, and X-ray crystallographic analysis. It was revealed that two fluorine atoms were replaced with methoxy groups. The substitution reaction was also caused with ethylene glycol to form the five-membered ring. Both the products also showed photochromism, and had absorption maxima and photocycloreversion quantum yields different from those of **1a**.

Cyclization Reaction Dynamics of a Photochromic Diarylethene Derivative as Revealed by Femtosecond to Microsecond Time-Resolved Spectroscopy

Yukihide ISHIBASHI, Mika FUJIWARA, Toshiyuki UMESATO, Hisayuki SAITO, Seiya KOBATAKE, Masahiro IRIE and Hiroshi MIYASAKA

J. Phys. Chem. C, 115(10), pp. 4265–4272 (2011).

Cyclization reaction of a photochromic diarylethene derivative, 1,2-bis(2-methyl-3-benzothienyl)perfluorocyclopentene (BT), in nonpolar alkane solutions with different viscosity was investigated by means of femtosecond-microsecond transient absorption spectroscopy and a time-correlated single-photon counting method. Transient absorption measurements revealed that a ring closure rapidly occurred with a time constant of 450 fs. In addition to this rapid cyclization, transient species with longer lifetimes (ca. 150 ps and ca. 1 μs) were observed. The faster time constant of 150 ps was independent of the solvent viscosity and was assigned to the fluorescence lifetime of a conformer with molecular geometry unfavorable for the ring closure. The longer component was strongly quenched in the solution purged with O₂ and was attributed to the triplet state of the open-ring form. Steady-state measurement and nanosecond transient absorption spectroscopy revealed that the cyclization process did not occur via the triplet state of BT. These results indicate that only the rapid reaction taking place in subpicosecond time region was responsible for the cyclization process. The key factors regulating the cyclization reaction of diarylethene derivatives were discussed on the basis of the solvent viscosity dependence, by comparing the present results with those obtained for other diarylethene derivatives.

Enhanced One-Photon Cycloreversion Reaction of Diarylethenes near Individual Gold Nanoparticles

Hiroyasu NISHII, Tsuyoshi ASAHII and Seiya KOBATAKE

J. Phys. Chem. C, 115(11), pp. 4564–4570 (2011).

The photocycloreversion reaction of a diarylethene upon irradiation with visible light was found to be accelerated in proximity to a gold nanoparticle covered with diarylethene polymers (Au-poly(DE)) dispersed in a solution. Enhancement of the reaction rate by the gold nanoparticle was quantitatively evaluated by kinetic analysis on the basis of absorption spectroscopy. Multicomponent bleaching of the closed-ring form of poly(DE) was observed around the gold nanoparticle upon irradiation with visible light; the irradiation time dependence of the absorbance could be explained using a reaction model with two decay components rather than one. The results indicate that the cycloreversion reaction was enhanced only in the vicinity of the gold nanoparticle. The faster reaction inside the polymer shell was confirmed by numerical spectral simulation of Au-poly(DE) using a double shell model based on Mie theory. The enhancement factor determined as the ratio of the enhanced reaction rate to the nonenhanced rate was estimated to be 2–5, and the enhanced region was evaluated to be 9–12 nm from the surface of the gold nanoparticle. The enhancement factor tended to increase with irradiation at longer incident wavelength, which did not correlate with the spectral shape of the local surface plasmon resonance (LSPR) band of the gold nanoparticle.

High-Convertible Photochromism of a Diarylethene Single Crystal Accompanying the Crystal Shape Deformation

Seiya KOBATAKE, Hiroki HASEGAWA and Kentaro MIYAMURA

Crystal Growth & Design, 11(4), pp. 1223–1229 (2011).

We designed and fabricated thin single-microcrystals of a photochromic diarylethene, 1,2-bis(2-methoxy-5-phenyl-3-thienyl)perfluorocyclopentene, which exhibits photochromic reactions up to high conversion in high efficiency because the diarylethene molecule has extremely small photocycloreversion quantum yield. The thin microcrystals prepared on glass plates by sublimation underwent photochromism upon alternating irradiation with ultraviolet and visible light. The photocyclization reaction proceeded with more than 90% conversion in the crystalline phase, keeping the

crystallinity. In addition to the high-convertible photochromic reaction in the crystalline phase, the crystals were found to exhibit the shape changes, such as contraction, bending, and separation, depending on the thickness of the crystal and the irradiation method with ultraviolet light. The intermolecular interaction between the photogenerated closed-ring isomers plays a significant role in deforming the crystal.

Enhanced Photocycloreversion Reaction of Diarylethene Polymers Attached to Gold Nanoparticles in the Solid State

Hiroyasu NISHI, Tsuyoshi ASAHU and Seiya KOBATAKE

J. Photochem. Photobio. A: Chem., 221(2-3), pp. 256–260 (2011).

The photochromic reactivity of diarylethene polymers attached to gold nanoparticle in the solid state was investigated. The photochromic diarylethene polymers around the gold nanoparticle exhibited reversible photochromism upon alternating irradiation with ultraviolet (UV) and visible light even in the solid state. The local surface plasmon resonance (LSPR) band of the gold nanoparticle in the solid state was red-shifted in comparison with that dispersed in a solution because of the closer interparticle distance. Alternating irradiation with UV and visible light led to the photoreversible changes in the LSPR band because the refractive index of the diarylethene polymer shell changes along with the photochromic reaction of the diarylethene polymers. However, the behavior of the spectral changes significantly depended on the irradiation wavelength. It reveals that the photocycloreversion reaction heterogeneously took place in the shell of the diarylethene polymers upon irradiation at longer wavelength to be enhanced in proximity to the gold nanoparticles. The promotion of the photoreaction is due to the plasmonic enhancement effect both in the vicinity and in the gap of the gold nanoparticles.

Control of Surface Wettability and Photomicropatterning with a Polymorphic Diarylethene Crystal upon Photoirradiation

Daichi KITAGAWA, Itsuka YAMASHITA and Seiya KOBATAKE

Chem. Eur. J., 17(35), pp. 9825–9831 (2011).

A photochromic diarylethene crystal of 1,2-bis(2-methyl-6-nitro-1-benzothiophen-3-yl)perfluorocyclopentene (**1a**) was found to undergo a thermodynamic phase transition at 180 °C to form a needle-like crystal, designated as **1a- γ** . The phase transition involves melting of the initial α -crystal and growth of the γ -crystal. The phase transition temperature decreased with the presence of the closed-ring isomer (**1b**) in the crystal because of the decrease in the melting temperature. Upon irradiation with ultraviolet (UV) light, compound **1a** in the α -crystal was converted into **1b** to an extent of 20%. Consequently, the α -crystal containing 20% of **1b** underwent the phase transition accompanied by melting of the crystal and growth of the γ -crystal even at 170 °C. Photomicropatterning by the phase transition upon irradiation with UV light using a photomask, followed by heating at 170 °C, was successfully accomplished with a resolution in the microcrystalline pattern of about 20 μm . The contact angle with water on the γ -microcrystalline phase on a glass substrate was larger than that on the α -microcrystalline phase by 20°. This can be ascribed to a difference in the roughness of the surface. Furthermore, the γ -microcrystal was also found to be formed upon heating an amorphous film of **1a** in poly(methyl methacrylate) for 2 min at 130 °C. The crystallized area exhibited a higher water contact angle than the amorphous area. Upon irradiation of the amorphous film with UV light, such crystallization did not take place because of the impurity effect of **1b** in **1a**. Photomicropatterning by the crystallization in the polymer showed a pattern with a higher resolution of about 4 μm , which was much better than that of the neat crystal. This photopatterning process represents a useful tool for controlling the surface wettability in relevant applications.

Microcrystallization Patterning Using Photoisomerization of Photochromic Diarylethenes

Seiya KOBATAKE and Daichi KITAGAWA

Chemical Industry (Kagaku Kogyo), 62(4), pp. 313–317 (2011) (in Japanese).

Molecular Design for Photoresponsive Crystal Shape Changes of Diarylethenes

Seiya KOBATAKE

The 6th International Symposium on Organic Photochromism (ISOP2010), Invited Lecture, Yokohama, October 17–21, 2010; Preprints pp. 31–32.

Enhanced Photocycloreversion Reaction of Diarylethene Chromophore Induced by Gold Nanoparticle

Hiroyasu NISHI, Tsuyoshi ASAHU and Seiya KOBATAKE

The 6th International Symposium on Organic Photochromism (ISOP2010), Yokohama, October 17–21, 2010;

Preprints p. 120.

Control of Surface Wettability and Photo-micropatterning with a Polymorphic Diarylethene upon Photoirradiation

Daichi KITAGAWA and Seiya KOBATAKE

The 6th International Symposium on Organic Photochromism (ISOP2010), Yokohama, October 17–21, 2010; Preprints p. 139.

Photochromic Reaction of Diarylethene Polymers Covered on Gold Nanoparticle

Seiya KOBATAKE, Hiroyasu NISHI and Tsuyoshi ASAH

Third Japanese-French Joint Seminar on Organic Photochromism –Innovations in Photochromism–, Yokohama, October 21–22, 2010; Preprints p. 61.

Control of Solid-State Physical Property of Mesoscopic Photofunctional Organic Molecular Crystals

Seiya KOBATAKE

The 19th Symposium on Organic Crystals, Invited Lecture, Osaka, November 11–12, 2010 (in Japanese); Preprints.

Photoresponsive Property Changes of Photochromic Diarylethene Crystals

Seiya KOBATAKE

6th Asian Photochemistry Conference 2010, Award Invited Lecture, Wellington, New Zealand, November 14–18, 2010; Preprints p. 60.

Molecule and Crystal Moving by Photoirradiation

Seiya KOBATAKE

The 2nd Symposium on SPring-8 Upgrade Plan 2019, Invited Lecture, Tokyo, December 4, 2010 (in Japanese); Preprints.

Gold Nanoparticle Enhanced Photochromic Reaction of Photochromic Diarylethene Polymers

Seiya KOBATAKE, Hiroyasu NISHI and Tsuyoshi ASAH

The International Chemical Congress of Pacific Basin Societies (Pacifichem2010), Honolulu, Hawaii, USA, December 15–20, 2010; Preprints.

Synthesis, Optical Property, and Photoreaction of Gold Nanoparticle Covered with Photochromic Diarylethene Polymers

Hiroyasu NISHI, Tsuyoshi ASAH and Seiya KOBATAKE

The International Chemical Congress of Pacific Basin Societies (Pacifichem2010), Honolulu, Hawaii, USA, December 15–20, 2010; Preprints.

Photoinduced Micropatterning by Polymorphic Crystallization of a Photochromic Diarylethene in a Polymer Film

Daichi KITAGAWA and Seiya KOBATAKE

The International Chemical Congress of Pacific Basin Societies (Pacifichem2010), Honolulu, Hawaii, USA, December 15–20, 2010; Preprints.

Development of Photofunctional Photochromic Crystal with Mesoscopic Material

Seiya KOBATAKE

The 10th Chemistry and Material Research Seminar, Kyushu University, Invited Lecture, Fukuoka, January 22, 2011 (in Japanese).

Bioengineering

Cytotoxic Enhancement of a Bispecific Diabody by Format Conversion to Tandem Single-Chain Variable Fragment (taFv): The Case of the hEx3 Diabody

Ryutaro ASANO, Keiko IKOMA, Ippei SHIMOMURA, Shintaro TAKI, Takeshi NAKANISHI, Mitsuo UMETSU and Izumi KUMAGAI

J. Biol. Chem., Vol. 286, pp. 1812–1818 (2011).

Diabodies (Dbs) and tandem single-chain variable fragments (taFv) are the most widely used recombinant formats for constructing small bispecific antibodies. However, only a few studies have compared these formats, and none have discussed their binding kinetics and cross-linking ability. We previously reported the usefulness for cancer immunotherapy of a humanized bispecific Db (hEx3-Db) and its single-chain format (hEx3-scDb) that target epidermal growth factor receptor and CD3. Here, we converted hEx3-Db into a taFv format to investigate how format affects the function of a small bispecific antibody; our investigation included a cytotoxicity assay, surface plasmon resonance spectroscopy, thermodynamic analysis, and flow cytometry. The prepared taFv (hEx3-taFv) showed an enhanced cytotoxicity, which may be attributable to a structural superiority to the diabody format in cross-linking target cells but not to differences in the binding affinities of the formats. Comparable cross-linking ability for soluble antigens was observed among hEx3-Db, hEx3-scDb, and hEx3-taFv with surface plasmon resonance spectroscopy. Furthermore, drastic increases in cytotoxicity were found in the dimeric form of hEx3-taFv, especially when the two hEx3-taFv were covalently linked. Our results show that converting the format of small bispecific antibodies can improve their function. In particular, for small bispecific antibodies that target tumor and immune cells, a functional orientation that avoids steric hindrance in cross-linking two target cells may be important in enhancing the growth inhibition effect.

Mechanism of HSV Infection Through Soluble Adapter-Mediated Virus Bridging to the EGF Receptor

Kenji NAKANO, Masatoshi KOBAYASHI, Kei-ichiro NAKAMURA, Takeshi NAKANISHI, Ryutaro ASANO, Izumi KUMAGAI, Hideaki TAHARA, Michihiko KUWANO, Justus B. COHEN and Joseph C. GLORIOSO

Virology, Vol. 413, pp. 12–18 (2011).

Herpes simplex virus entry into cells requires the binding of envelope glycoprotein D (gD) to an entry receptor. Depending on the cell, entry occurs by different mechanisms, including fusion at the cell surface or endocytosis. Here we examined the entry mechanism through a non-HSV receptor mediated by a soluble bi-specific adapter protein composed of recognition elements for gD and the EGF receptor (EGFR). Virus entered into endosomes using either EGF or an EGFR-specific single chain antibody (scFv) for receptor recognition. Infection was less efficient with the EGF adapter which could be attributed to its weaker binding to a viral gD. Infection mediated by the scFv adapter was pH sensitive, indicating that gD-EGFR bridging alone was insufficient for capsid release from endosomes. We also show that the scFv adapter enhanced infection of EGFR-expressing tumor tissue *in vivo*. Our results indicate that adapters may retarget HSV infection without drastically changing the entry mechanism.

In Vitro and In Vivo Antitumor Effects of Recombinant Bispecific Antibodies Based on Humanized Anti-EGFR Antibody

Yasuhiro WATANABE, Ryutaro ASANO, Kyoko ARAI, Ippei SHIMOMURA, Hiromi OGATA, Hiroko KAWAGUCHI, Hiroki HAYASHI, Hideo OHTSUKA, Hiroshi YOSHIDA, Yu KATAYOSE, Shinichi EGAWA, Takeshi NAKANISHI, Mitsuo UMETSU, Hiroshi YASUI, Tadao ISHIDA, Kohzoh IMAI, Toshio KUDO, Michiaki UNNO and Izumi KUMAGAI

Oncol Rep., Vol. 26, pp. 949–955 (2011).

We performed *in vitro* and *in vivo* experiments of the anti-epidermal growth factor receptor (EGFR) x

anti-CD3 bispecific diabody (hEx3-Db) with the IgG-like bispecific antibodies (BsAbs) (hEx3-scFv-Fc and hEx3-scDb-Fc) and the anti-EGFR therapeutic antibody cetuximab to assess the effect of BsAbs on cancer growth inhibition. *In vitro*, efficacy of the BsAbs and cetuximab were compared by growth inhibition assays of human cell lines of bile duct (TFK-1, HuCC-T1, OCUCh-LM1), epidermoid (A431), gastric (Kato-III), colon (DLD-1, SW480), and breast (SK-BR-3, MCF-7) cancer. *In vivo*, in three mouse models, we evaluated the anti-tumor activity of hEx3-Db and cetuximab, assessed the effect of hEx3-Db alone, and compared the antitumor activity of hEx3-Db with the IgG-like BsAbs. *In vitro*, hEx3-scFv-Fc showed nearly 100% killing activity for all cell lines. Both *in vitro* and *in vivo*, hEx3-Db needed CD3-positive phenotypes to induce a growth inhibitory effect. In contrast, IgG-like BsAbs showed monotherapeutic effects *in vivo* by inducing antibody-dependent cellular cytotoxicity (ADCC) similar to cetuximab. However, enhancement was not observed when lymphokine-activated killer cells with the T-cell phenotype were co-injected. Results suggest that IgG-like BsAbs could not efficiently direct T lymphocytes toward tumor cells to induce ADCC due to steric hindrance on binding to CD3- and Fc-receptor-positive phenotypes. Although hEx3-scFv-Fc showed high cytotoxicity *in vitro*, its high molecular weight limits its usefulness. With an *in vivo* effect comparable to hEx3-scFv-Fc and its realistic molecular weight, hEx3-scDb-Fc shows promise as a novel recombinant therapeutic antibody and may be modified to enhance its potency by prevention of steric hindrance.

Biomimetic Engineering of Modular Bispecific Antibodies for Biomolecule Immobilization

Hideki WATANABE, Kengo KANAZAKI, Takeshi NAKANISHI, Hidenori SHIOTSUKA, Satoru HATAKEYAMA, Masaru KAIEDA, Takeshi IMAMURA, Mitsuo UMETSU and Izumi KUMAGAI
Langmuir, Vol. 27, pp. 9656–9661 (2011).

Modular bispecific antibodies (BsAb's) that interact directly with a gold surface were engineered for immobilization on biosensing devices. The BsAb's consist of the variable fragments of antigold and antilysozyme antibodies connected via one of three linkers derived from naturally occurring proteins. The BsAb's were bound tightly to both the gold surface and to lysozyme, thus functioning as interface molecules between lysozyme and the gold surface without a substantial loss of antigen-binding activity. The antigen-binding capacity (the ratio of the amount of immobilized lysozyme to the amount of immobilized BsAb) on the gold surface reached 82%. An analysis of the correlation between binding capacity and linker characteristics indicated that the presence of a long, rigid linker sequence derived from a cellulase resulted in a higher antigen-binding capacity than did the presence of a long but relatively flexible glycine-rich linker. This result suggests a strategy for designing linkers suitable for BsAb

Development of a Novel Fines-Dissolution Mechanism for Production of Large Crystals in Batch Crystallization

K. IGARASHI, M. ARIMOTO, H NODA and H. OOSHIMA

Proc. of The 9th International Conference on Separation Science and Technology, 2011, Korea

In the industrial crystallization, there are many characteristics of product crystals that must be well controlled. Crystal size distribution (CSD) is one of the most important characteristics of crystals. In many cases, large crystals with a narrow CSD are preferred to make filtration easy. Various methods have been attempted to obtain uniform large crystals. As an effective solution, we have proposed the WWDJ-batch crystallizer, which can dissolve undesirable fine crystals on the heated inner wall of the head space of crystallizer. In the present paper, we propose a novel batch crystallizer suitable for production of large and uniform crystals. The crystallizer is composed of a jacketed-glass vessel, a newly developed fines-dissolver equipped with an induction-heating (IH) system, and an agitation propeller. The fines-dissolver is a connected body of a stainless-steel cylinder and a circular truncated cone at lower side. It was set on a coaxial rotation rod with an agitation propeller. The rotation speed of the dissolver and the agitation propeller can be individually controlled. The lower end of the dissolver is placed in crystallization solution at a given depth from solution level. To heat the fines-dissolver, the IH coil sealed from crystallization slurry is put around the

fines-dissolver. The rotating fines-dissolver was directly heated by a high-frequency alternating current flows through the IH coil. The slurry is lifted up along the inner wall of the heated fines-dissolver by the centrifugal force, and is returned to the crystallization phase from the top of the dissolver. Fine crystals in the lifted slurry can be expected to partially dissolve. The surviving large crystals are also expected to grow further, at the expense of fine crystals, after returning to the crystallization phase. Using the novel crystallizer, cooling crystallization of glycine was performed by controlling the temperature from 50 to 25°C at the initial concentration of glycine of 268 mg/ml. The performance of the crystallizer was compared with that of a conventional batch cooling crystallization without the fines-dissolver. The average particle size obtained in a conventional crystallization was 622 μm . On the other hand, when the novel crystallizer was used, the average size of crystals was 1544 μm .

Effect of Complete Dissolution of Once Appeared Crystals on Induction Period and Crystal Size in Cooling Crystallization of *p*-Acetanisidide

K. IGARASHI, A. KITANO, I. KOZUTSUMI and H. OOSHIMA

Proc. of The 9th International Conference on Separation Science and Technology, 2011, Korea

In crystallization of active pharmaceutical ingredient (API), it may be preferred to produce fine crystals with large specific surface area. It is because fine crystals are desirable to improve bioavailability of low solubility-pharmaceutical compounds. Crystal size and its distribution are depending on the timing of nucleation. If nucleation would occur at the same time under a high super-saturation, lots of nuclei must be generated and result in the formation of many fine crystals. Usually in industrial crystallization, the timing of nucleation is controlled by adding seed crystals. However, if only it were possible in crystallization of API, use of seed crystals should be the second choice to prevent contamination by the third matter. In the present study, in order to produce fine crystals with a narrow size distribution in cooling crystallization without seed crystals, we investigated the effects of the introduction of a process of complete dissolution of crystals once appeared in the first crystallization into the normal cooling crystallization. We expected that the solute molecules and those aggregates once experienced crystals must keep the same conformation of molecules and same structure of molecular aggregates as those of crystal for a while even after complete dissolution of crystals. Such solution, as it were, “a metastable solution”, must be ready to nucleate. In the cooling crystallization from the metastable solution, nucleation may occur easily and furthermore at the same time. A novel experimental apparatus was used to perform cycling of a set of cooling crystallization and complete dissolution of once obtained crystals in the first crystallization. This apparatus was able to cool and heat the solution at a constant rate, and detect scattering light indicating appearance of crystals. *p*-Acetanisidide (PAC) was used as crystallization substances. Four mL of 95 mg/mL PAC/methanol solution was pre-incubated for 12 h in crystallization cell to set the solution at a constant condition. Then the solution was cooled down to a little higher temperature 17°C ($C/C_s=0.95$) than the saturation temperature 15.5°C and incubated for 20 min at the temperature. Then, the solution was cooled down to 5°C ($C/C_s=1.5$) at a constant cooling rate of 2.4°C/min. Appearance of crystals was monitored by a photo sensor and the time when crystals first appeared was recorded. After the appearance, the slurry was further incubated for 30 min and then heated to 17°C at a constant heating rate of 2.4°C /min and incubated at 17°C for 20 min. After that, the second cooling was carried out. The cooling from 17°C was repeated 5 times in one batch crystallization. The same batch experiment was carried out 4 times. As results, the long induction period from 8 to 30 min was observed at the first cooling, and crystal size distribution (CSD) was wide from 5 to 270 μm . However, at the second cooling of the solution once experienced crystals, the induction time was shorten in the range from 6.5 to 13 min. Furthermore, a narrow CSD was obtained from 5 to 50 μm . We confirmed the effect of “metastable” solution on induction period in crystallization and CSD.

Crystallization of Pharmaceutical Compounds Depending on the Structure of Solution

H. OOSHIMA

Proc. of International Conference on Materials for Advanced Technologies (ICMAT), 2011, Singapore

In the manufacturing of crystal products, reliable and reproducible crystallization operation is required as a guarantee that the product crystals always possess the desired characteristics. It is also serious in pharmaceutical industry. There are many compounds that have polymorphs more than two in same solvent. It is strongly required to produce a crystal polymorph selected as a drug with good reproducibility. Seed crystals are not always useful for crystallizing a target polymorph. We always make a lot of efforts to find a good operation condition. In order to understand a causal relationship between crystallization operation (cause) and crystals as a product (result), we need to understand how the solute molecules play in solution before nucleation and what is occurring in supersaturated solution. In the present paper, it will be discussed taking several pharmaceutical compounds and other organic compounds for example that the conformation of solute molecules in supersaturated solution and its change depending on crystallization conditions are important to understand a causal relationship between crystallization operation (cause) and crystals as a product (result).

Crystallization

H. OOSHIMA

In Chemical Engineering Handbook, 7th Edition, Chapter 11, pp. 579-610 (2011).

Membrane Disk and Sphere: Controllable Mesoscopic Structures for the Capture and Release of a Targeted Object

Tsutomu HAMADA, Ryoko SUGIMOTO, Mun'delanji C. VESTERGAARD, Takeshi NAGASAKI, and Masahiro TAKAGI

J. Am. Chem. Soc., Vol. 132, pp. 10528–10532 (2010).

Design of molecules for self-assembled mesoscopic structures with specific functions is an important and interesting challenge that spans across disciplines such as nanosciences. A closed lipid membrane is a good example of a self-assembled mesostructure. In this study, we developed controllable membrane formation by making a subtle change at the molecular level. We utilized a synthetic photosensitive amphiphile (KAON12) to achieve the photobased molecular manipulation of the opening and closing of membranes through reversible transitions between sphere and disk structures. We found that the mechanism is based on the photoswitching of the membrane line tension, as deduced from the fluctuation of the membrane edge, through the action of KAON12. Furthermore, we demonstrated the controllable capture and release of colloidal particles into and from a membrane sphere. The observation of Brownian motion of the particle confirmed colloidal encapsulation. This successful photomanipulation of mesoscopic membrane structures in a noncontact and reversible manner should lead to a better understanding of the mechanism of membrane self-organization and may see wider application, such as in microreactors and drug-delivery systems.

Photochemical control of membrane raft organization

Tsutomu HAMADA, Ryoko SUGIMOTO, Takeshi NAGASAKI and Masahiro TAKAGI

Soft Mat., Vol. 7, pp. 220-224 (2011).

Controllable membrane phase separation through the action of a synthetic photoresponsive amphiphile is reported. We studied multi-component giant vesicles formed from a ternary lipid mixture of saturated and unsaturated phospholipid and cholesterol together with the photoresponsive amphiphile. A change in the conformation of the photoresponsive amphiphile can switch membrane lateral segregation in a reversible manner. Cis-isomerization induces lateral phase separation in one-phase membranes or produces additional lateral domains in two-phase membranes. Membranes that are close to miscibility boundary show high photo-responsiveness. This is the first report on the reversible control of membrane lateral segregation triggered by a conformational change in a membrane-constituting molecule. These findings may lead to new methods for controlling membrane self-organization such as raft engineering.

Ultrasound-mediated Transfection with Liposomal Bubbles Delivers Plasmid DNA Directly into Nucleus

Takeshi KAWAZU, Kazumi HAKAMADA, Yusuke ODA, Jun MIYAKE, Kazuo MARUYAMA and Takeshi NAGASAKI

Chem. Lett., Vol. 40, pp.298-299 (2011).

Transfection using ultrasound exposure in the presence of nanobubbles can overcome the important barrier for non-viral gene delivery, that is entering into nucleus without cell division. The monitoring of a relationship between fluorescent protein expressing and cell division reveals that ultrasound-mediated transfection with liposomal bubbles is independent on the disappearance of nuclear membrane at mitosis.

Lateral phase separation in tense membranes

Tsutomu HAMADA, Yuko KISHIMOTO, Takeshi NAGASAKI and Masahiro TAKAGI

Soft Mat., Vol. 7, pp. 9061-9068 (2011)

The organization of lateral domains, called lipid rafts, in plasma membranes is essential for physiological functions, such as signaling and trafficking. In this study, we performed a systematic analysis of lateral phase separation under membrane tension. We applied osmotic pressure directed toward the outside of vesicles to induce membrane tension. Microscopic observations clarified the shifts in phase structures within bilayer membranes with change in tension and temperature. The miscibility transition temperature between one-liquid and two-liquid states was shown to increase under tension. We also observed a shift in the transition temperature between two-liquid and solid-liquid states in membranes under tension. We determined a quantitative phase diagram of phase organization with respect to the applied pressure and temperature. The results indicate that membrane tension can induce phase separation in homogeneous membranes. Our findings may provide insight into the biophysics of bilayer phase organization under tension, which is an intrinsic mechanical property of membranes.

Tumor accumulation of ϵ -poly-lysines-based polyamines conjugated with boron clusters

Masayuki UMANO, Kazuhiro UECHI, Takatoshi URIUDA, Sayuri MURAYAMA, Hideki AZUMA, Atsuko SHINOHARA, Young LIU, Koji ONO, Mitsunori KIRIHATA, Hironobu YANAGIE and Takeshi NAGASAKI

Appl. Radiat. Isot., in press.

Boron Neutron Capture Therapy (BNCT) is one of the potent cancer radiotherapies using nuclear reaction between $(10)\text{B}$ atoms and the neutron. Whether BNCT will succeed or not depends on tumor selective delivery of $(10)\text{B}$ compounds. ϵ -Poly-L-lysine is a naturally occurring polyamine characterized by the peptide linkages between the carboxyl and ϵ -amino groups of L-lysine. Because of high safety ϵ -PLL is applied practically as a food additive due to its strong antimicrobial activity. In this study, we focus on a development of a novel polymeric delivery system for BNCT using biodegradable ϵ -PLL conjugated with $(10)\text{B}$ -containing clusters (BSH). This polymeric boron carrier will be expected to deliver safely and efficiently into tumor tissues based on Enhanced Permeability and Retention (EPR) effect.

1'-Acetoxychavicol acetate enhances the phase II enzyme activities via the increase in intranuclear Nrf2 level and cytosolic p21 level

Keisuke YAKU, Isao MATSUI-YUASA, Hideki AZUMA and Akiko KOJIMA-YUASA.

Am. J. Chin. Med. Vol. 39, pp. 789-802 (2011).

(1'*S*)-acetoxychavicol acetate ((*S*)-ACA) exhibits chemopreventive effects on chemically induced tumor formation. It has been shown that ACA inhibited the development of azoxymethane-induced colon carcinogenesis through its suppression of cell proliferation in the colonic mucosa and its induction of glutathione S-transferase and quinone oxidoreductase 1 in vivo. In this study, we investigated how ACA induced these enzymes by using rat intestine epithelial cells (IEC6) in vitro. ACA induced glutathione

S-transferase (GST) and NAD(P)H: quinone oxidoreductase 1 (NQO1) activities, increased intracellular glutathione (GSH) level, and upregulated intranuclear Nrf2 and cytosolic p21. It suggested that activation of phase II enzymes via Nrf2 associated with p21 is one of possible mechanisms of ACA to prevent advance of carcinogenesis.

Biological Activity of Water-Soluble Inclusion Complexes of 1'-Acetoxychavicol Acetate with Cyclodextrins

Hideki AZUMA, Yui AIZAWA, Nao HIGASHITANI, Takashi TSUMORI Akiko KOJIMA-YUASA, Isao MATSUI-YUASA and Takeshi NAGASAKI

Bioorg. Med. Chem., Vol. 19, pp. 3855-3863 (2011).

1'-Acetoxychavicol acetate (ACA), isolated from the rhizomes and the seeds of the *Zingiberaceae* plant, has a variety of biological activities such as anti-tumor, antiallergic and repellent effects. However, ACA seems to have some disadvantages which may limit for future possible clinical applications, for example, its poor water solubility. Furthermore, ACA is not stable in aqueous solutions and undergoes hydrolysis and/or isomerization. To improve the solubility and stability of ACA in water, we prepared the inclusion complexes with various β -cyclodextrins (β -CDs). In aqueous solution, the association constants of ACA with various CDs were estimated at 662 ± 95 (β -CD), 336 ± 70 (methyl- β -CD, Me β -CD) and 322 ± 44 M⁻¹ (hydroxypropyl- β -CD, HP β -CD), respectively, by a spectrofluorometric displacement method based on competition between a guest and a fluorescent probe for CDs. It was revealed that almost all ACAs existed as a free molecule in the CD-containing aqueous solution. However, in the case of preparing the inclusion complexes of CDs with ACA by a solid phase "high-speed vibration milling" technique, the average inclusion rates of the obtained water-soluble complexes were calculated as $88 \pm 13\%$ (β -CD), $70 \pm 1\%$ (Me β -CD) and $63 \pm 2\%$ (HP β -CD), respectively, by ¹H NMR analysis. To characterize the structures of the CD·ACA complexes, 2,3,6-trimethyl- β -CD (TMe β -CD)·ACA complex was prepared as a model compound (inclusion rate: 40%). As a result of 2D ROESY experiments, it was considered that the aromatic ring of ACA is located in the narrow side of the hydrophobic cavity of the TMe β -CD and both 1'- and 4-acetoxy groups of ACA positioned in the vicinity of the secondary and primary methoxy groups of TMe β -CD, respectively. Furthermore, we examined the apoptogenic activity of CD·ACA complexes to evaluate whether or not the bioactivities of ACA were affected by their inclusion. Although the cytotoxicity of all CD·ACA complexes in human epithelial carcinoma HeLa cells and murine adenocarcinoma colon26 cells were diminished as compared with the ACA alone, only HP β -CD·ACA maintained high levels of activity. In addition, HP β -CD·ACA and Me β -CD·ACA showed suppressive effect for the transcription factor NF- κ B activation on LPS-activated murine macrophage RAW264.7 cells and the former was more active complex. Furthermore, HP β -CD·ACA inhibited the in vivo tumor growth of tumor-bearing mice, although the activity was slightly weak compared with that of free ACA. These results indicate that HP β -CD is the best host molecule for ACA to form a water-soluble complex with the similar biological activity of free ACA.

Controlled release of antibiotics from HA used in bone cement with HA (IBBC) as prevention of infection in joint replacement

Hiroyuki OONISHI Jr., Tomonori ARITA, Akira TACHIBANA, Toshizumi TANABE, Shigekazu MIZOKAWA and Hironobu OONISHI

The 23rd Annual Congress of the International Society for Technology in Arthroplasty, 2010, Dubai UAE

Controlled release of antibiotics from β -TCP used in bone cement with β -TCP and HA (IBBC) as prevention of infection in joint replacement

Hiroyuki OONISHI Jr., Tomonori ARITA, Akira TACHIBANA, Toshizumi TANABE, Shigekazu MIZOKAWA and Hironobu OONISHI

The 23rd Annual Congress of the International Society for Technology in Arthroplasty, 2010, Dubai UAE

Controlled release of antibiotics from bone filling materials

Hiroyuki OONISHI Jr., Tomonori ARITA, Akira TACHIBANA, Toshizumi TANABE, Shigekazu MIZOKAWA and Hironobu OONISHI

Combined Meeting of the Orthopaedic Research Societies, 2010, Kyoto Japan

Characterization of acyl-coenzyme A: diacylglycerol acyltransferase (DGAT) enzyme of human small intestine

Yasushi. HIRAMINE and Toshizumi TANABE

J. Physiol. Biochem., Vol. 67, pp. 259-264 (2011).

Acyl-coenzyme A:diacylglycerol acyltransferase (DGAT) plays a significant role in dietary triacylglycerol (TAG) absorption in the small intestine. However, the characteristics of human intestinal DGAT enzyme have not been examined in detail. The aim of our study was to characterize the human intestinal DGAT enzyme by examining acyl-CoA specificity, temperature dependency, and selectivity for 1,2-diacylglycerol (DAG) or 1,3-DAG. We detected DGAT activity of human intestinal microsome and found that the acyl-CoA specificity and temperature-dependency of intestinal DGAT coincided with those of recombinant human DGAT1. To elucidate the specificity of human intestinal DGAT to 1,2-DAG or 1,3-DAG, we conducted acyl-coenzyme A:monoacylglycerol acyltransferase assays using 1- or 2-monoacylglycerol (MAG) as substrates. When 2-MAG was used as acyl-acceptor, both 1,2-DAG and TAG were generated; however, when 1-MAG was used, 1,3-DAG was predominantly observed and little TAG was detected. These findings suggest that human small intestinal DGAT, which is mainly encoded by DGAT1, utilizes 1,2-DAG as the substrate to form TAG. This study will contribute to understand the lipid absorption profile in the small intestine.

Cross talk between distinct nuclear import pathways enables efficient nuclear import of E47 in conjunction with its partner transcription factors

Rashid MEHOOD, Noriko YASUHARA, Masahiro FUKUMOTO, Souichi OE, Taro TACHIBANA and Yoshihiro YONEDA

Mol. Biol. Cell, in press.

Nuclear import of karyophilic proteins is carried out by a variety of mechanisms. We have previously shown that two basic helix-loop-helix proteins, NeuroD1 and E47 synergistically affect each other's nuclear import. In this study, we dissected the molecular pathways underlying nuclear import of the NeuroD1/E47 heterodimer. In vitro nuclear import assays indicated that importin α family members are the major nuclear import receptors for E47. However, inhibition of importin α resulted in cytoplasmic retention of E47 that could be rescued by its binding partner, NeuroD1, through heterodimerization. Additionally, nuclear import of NeuroD1 was importin α -independent but importin β 1-dependent. In primary neurons, localization of endogenous E47 was not affected by importin α inhibition, suggesting that neuronal E47 could be imported into the nucleus as a heterodimer with NeuroD1 by utilizing importin β 1 alone. We also found that E47 had similar nuclear import characteristics in C2C12 cells, where E47 heterodimerized with MyoD, another helix-loop-helix protein, suggesting functional conservation within the same family transcription factors. Collectively, our data reveal that E47 is imported into the nucleus via multiple pathways depending on the molecular binding mode, establishing a previously uncharacterized cross talk between two distinct nuclear import pathways.

Enzymatic actions of Pasteurella multocida toxin detected by monoclonal antibody recognizing the deamidated alpha subunit of the heterotrimeric GTPase Gq

Shigeki KAMITANI, Shinpei AO, Hirono TOSHIMA, Taro TACHIBANA, Makiko HASHIMOTO, Kengo KITADOKORO, Aya FUKUI-MIYAZAKI, Hiroyuki ABE and Yasuhiro HORIGUCHI

FEBS Journal, Vol. 278, pp. 2702-2712 (2011).

Pasteurella multocida toxin (PMT) is a virulence factor responsible for the pathogenesis of some Pasteurellosis. PMT exerts its toxic effects through the activation of heterotrimeric GTPase (G(q), G(12/13) and G(i))-dependent pathways, by deamidating a glutamine residue in the α subunit of these GTPases. However, the enzymatic characteristics of PMT are yet to be analyzed in detail because the deamidation has only been observed in cell-based assays. In the present study, we developed rat monoclonal antibodies, specifically recognizing the deamidated G α (q), to detect the actions of PMT by immunological techniques such as western blotting. Using the monoclonal antibodies, we found that the toxin deamidated G α (q) only under reducing conditions. The C-terminal region of PMT, C-PMT, was more active than the full-length PMT. The C3 domain possessing the enzyme core catalyzed the deamidation in vitro without any other domains. These results not only support previous observations on toxicity, but also provide insights into the enzymatic nature of PMT. In addition, we present several lines of evidence that G α (11), as well as G α (q), could be a substrate for PMT.

Steroidogenic Factor 1 (NR5A1) resides in centrosomes and maintains genomic stability by controlling centrosome homeostasis

LAI PY, WANG CY, CHEN WY, KAO YH, TSAI HM, TACHIBANA T, CHANG WC and CHUNG BC.

Cell Death Differ. in press.

SF-1 (Steroidogenic Factor 1, NR5A1) is a tissue-specific transcription factor critical for the growth, development and differentiation of steroidogenic and a few other endocrine tissues. But how SF-1 regulates cell growth is not entirely clear. Here we found that SF-1 was localized to the centrosome in addition to the nucleus, and SF-1 depletion by shRNA caused centrosome over-duplication, aberrant mitosis and genomic instability, leading to a reduction of cell number. Centrosome amplification defect was rescued by both wild-type SF-1 and transcription-defective SF-1-G35E, suggesting a non-genomic activity of SF-1 involved in centrosome homeostasis. In addition, we identified in SF-1 a centrosome localization signal, whose overexpression led to reduced localization of both SF-1 and γ -tubulin to the centrosome. Our results uncover a novel role of SF-1 in the control of centrosome homeostasis and genomic stability.

Mitochondrial prohibitins and septin 9 are implicated in the onset of rat hepatocarcinogenesis

Anna KAKEHASHI, Naomi ISHII, Takeshi SHIBAT, Min WEI, Etsuko OKAZAKI, Taro TACHIBANA, Shoji FUKUSHIM and Hideki WANIBUCHI

Toxicol Sci. Vol.119, pp. 61-72 (2011).

In the present study, protein lysates from microdissected glutathione S-transferase placental-form-positive (GST-P(+)) foci and hepatocellular carcinomas from livers of rats treated with N-diethylnitrosamine followed by phenobarbital at doses of 0 and 500 ppm in the diet for 10 and 33 weeks were analyzed using QSTAR Elite liquid chromatography with tandem mass spectrometry and iTRAQ technology. Among 75 proteins, a total of 27 and 50 proteins displaying significant quantitative changes comparing with adjacent normal-appearing liver tissue were identified in GST-P(+) foci of initiation control and promotion groups, respectively, which are related to transcription, protein folding, cytoskeleton filaments reorganization, cell cycle control, nuclear factor (erythroid-derived 2)-like 2 (NRF2)-mediated oxidative stress responses, lipid metabolism, glutathione metabolism, oxidative phosphorylation, and signal transduction. Furthermore, Ingenuity Pathway and bioinformatic analyses revealed that expression changes of genes encoding proteins with altered expression detected in GST-P(+) foci are likely to be controlled by c-myc, NRF2, aryl hydrocarbon receptor, nuclear factor kappa B, and hepatocyte nuclear factor 4 transcriptional factors. Coordinated overexpression of mitochondrial chaperons prohibitin (PHB) and prohibitin 2 (PHB2), septin 9 (SEPT9), neurabin 1, and other cytoskeletal and functional proteins in areas of GST-P(+) foci during initiation and/or promotion stages of rat hepatocarcinogenesis was associated with induction of cell proliferation and might be responsible for the neoplastic transformation of rat liver preneoplastic lesions. Newly discovered elevation of PHB, PHB2, and SEPT9 in GST-P(+) foci and tumors, imply that they might

play important role in the onset of liver cancer and be of potential values in the studies of hepatocarcinogenesis.

Specific Monoclonal Antibody Against the Nuclear Pore Complex Protein, Nup96

Chiaki MIZUGUCHI, Masahiro OKA, Tetsuji MORIYAMA, Taro TACHIBANA and Yoshihiro YONEDA
Hybridoma, Vol. 29, pp. 551-553 (2010).

Nup96 is a component of the Nup107-160 complex, the largest subunit of the nuclear pore complex. Nup96 is generated as a precursor protein with Nup98. However, the mechanism by which Nup96 contributes to cell function is not clear. We report here on the preparation of a monoclonal antibody (MAb) directed against mouse Nup96. The antibody was produced by the hybridization of mouse myeloma cells with lymph node cells from an immunized rat. The antibody, MAb 4H5, specifically recognized Nup96, as evidenced by immunoblotting using the whole cell lysates. In immunostaining using MAb 4H5, a nuclear rim staining pattern was observed. This antibody will be useful in immunoblotting and immunolocalization experiments, as well as further analyses of the biological function and cellular dynamics of this protein.

Architecture and Building Engineering

Relation between Load-Carrying Capacity and Seismic Motion Level of Dynamic Collapse for Lattice Arch and Cylindrical Roof

Yoshiya TANIGUCHI and Risa FUKUSHIMA

Journal of Structural and Construction Engineering (Transactions of AIJ), Vol.75, No.658, pp.2189-2196, 2010. (in Japanese)

Lattice structures consisting of various mesh patterns show different static buckling and post-buckling behaviors even if the compression members have the same slenderness ratios. There are not sufficient studies in the literature to find a document to know the effect of these static characteristics on the seismic resistant capacity. In this paper as for plane lattice arches and double-layer cylindrical lattice roofs, the relation between dynamic collapse behavior and static collapse behavior, under excessive vertical loads, is numerically investigated to present a prediction method for the load level of dynamic collapse. The prediction method can be done with the information of load-deformation curves, natural periods and velocity response spectrum of seismic motions. The value predicted may be modified with the information of the elastic and plastic strain energies at a limit state of structures.

Seismic Motion Level of Dynamic Collapse or Limit State Deformation for Lattice Arch and Cylindrical Roof

Yoshiya TANIGUCHI

Abstract Book and CD-ROM of Structural Engineers World Congress, Como, Italy, 2011, p.176.

Lattice structures consisting of various mesh patterns show different static buckling and post-buckling behaviors even if the compressive members have the same slenderness ratios. There are not sufficient studies in the literature to find a document to know the effect of these static characteristics on the seismic resistant capacity. In this paper as for plane lattice arches and double-layer cylindrical lattice roofs, the relation between dynamic collapse behavior and static collapse behavior, under excessive vertical loads, is numerically investigated to present a prediction method for the load level of dynamic collapse. The prediction method can be done with the information of load-deformation curves, natural periods and velocity response spectrum of seismic motions. The predicted value is modified with the information of the elastic and plastic strain energies at a limit state of structures.

Vibration Test of TMD with Initial Displacement under Impulse Loading

Susumu YOSHINAKA, Shuji NISHIYAMA and Yoshiya TANIGUCHI

Proceedings of IABSE-IASS2011, London, UK, September 20-23, CD-ROM 0175 (pp.1-8) (2011)

We propose TMDs with initial displacement to effectively control transient responses. The initial displacement of a TMD can change the phases of beat envelope curves resulting from superposition of two vibration modes with closely spaced natural frequencies. In this paper, we describe a vibration test under impulse loading to verify the effect of the proposed system experimentally and show that an experimental model of the TMD with initial displacement works. Firstly, we study analytically the effect of vibration control using the proposed method with a plate model. Then, we explain the experimental results. Finally, we compare the experimental results with the analytical results.

Experimental Form-Finding Using Thermoplastic Resin

Sho WATANABE, Kouichi WADA, Susumu YOSHINAKA and Yoshiya TANIGUCHI

Proceedings of IABSE-IASS2011, London, UK, September 20-23, CD-ROM 0430 (pp.1-6) (2011)

In this study, in order to make the finding shape easy without the expert technique and knowledge, we extend the experimental finding method by using acrylic materials. The acrylic material changes its material property in the hot state and becomes with in-plane stress state when it is hanged, that is we can introduce stretch of materials in finding a shape. We describe the experimental method using the heating acrylic plate in detail. Then, we explain about analytical results using coordinates measured from shapes obtained by experimental results. Moreover, we compare this method with the method using the Moore-Penrose generalized inverse matrix

simulating the experimental hanging method without stretch of materials from the view of shapes and the difference of the stress distribution. The method using Moore-Penrose generalized inverse matrix is the analytical form finding method in the equilibrium state with unstable link structures.

Limit State of Double-layer Lattice Domes of Different Member Layouts

Chongbing YAN, Yoshiya TANIGUCHI and Susumu YOSHINAKA

Proceedings of IABSE-IASS2011, London, UK, September 20-23, CD-ROM 0767 (pp.1-7) (2011)

To consider safety of double-layer lattice structures, it is important to determine the load carrying capacity and the deformation performance in the ultimate state. The initial yield load and the maximum load may be evaluated by post-buckling behavior or elastic-plastic behavior. Therefore, in this paper the effect of member layouts on the post-buckling behavior and limit state load is investigated for double layer lattice domes. Analytical models are 6 double-layer lattice domes whose half span angle is 30 degrees. The joints of the models are treated as rigid-joints under the assumption that the strength and stiffness of the joints are sufficiently large. The analytical models are subjected to two loading cases, which are the uniform vertically distributed load and the asymmetric vertically distributed load respectively. The ultimate states of six latticed patterns are investigated with the coefficient β , which is the ratio of the limit state load against the initial yield load. The limit state load estimated with the load-deformation relationship obtained by push-over analyses. The study shows that the structural characteristics of lattice structures depend upon mesh patterns and member layout. In addition, the usefulness of the method to estimate the effective strength by the segment consisting of 3×3 structural units is discussed.

Evaluation of elementary school lawn grounds in Osaka urban regions

Noriko Umemiya, Akemi Nakanaga, Yuta Sakurai, Ryota Matsui, Toshiki Naotsuka, Takayuki Harada and Ryoji Okura

Proceedings of the 10th International Symposium on Building and Urban Environmental Engineering, Seoul, pp.111-116, 2010.

A survey related to school ground lawn planting was administered to elementary school maintenance managers in Osaka city. From all 297 elementary schools in Osaka city, 100 responses were received. Comparison of the answers of respondents from schools where lawn grounds had been 'completed', 'planned', and 'not-planned' revealed the following: 1) 'completed' schools have larger grounds and fewer children; 2) 'not-planned' schools have lower PTA and exchange activity levels between the school and the local community; 3) 'planned' schools are more anxious about efforts at maintaining a lawn; and 4) 'not-completed' schools expect lawn planting to mitigate the thermal environment in summer, but 'completed' schools do not regard those effects as important. Sky factors and sunshine duration at the summer and winter solstice and the equinox were estimated for 36 schools. 5) Only 35.3% of the schools satisfy the condition of sunshine duration for raising a lawn. 6) Subjective evaluation of sunshine and contentment with school grounds strongly relate to sky factors and sunshine duration. 7) The sunshine duration is shorter and sky factors are less for 'completed' schools.

Effects of weather conditions on thermal control use in apartments during summer–autumn

Noriko Umemiya and Koichi Taniguchi

Proceedings of the International Air Infiltration and Ventilation Centre Conference on low energy and sustainable ventilation technologies for green buildings, 6A-3, pp.1-13, 2010.

Air conditioner use and window opening were recorded in Osaka during summer–autumn. The measured period was divided into four seasons according to the change of ratio of air conditioner use. In the former questionnaire survey of the reasons for opening and closing windows, 'fine weather' or 'rain' were ranked highly. This study investigated effects of weather conditions on the relation between temperature and humidity and thermal control use. Cloud cover was used as indices of weather conditions. Results showed that the ratio of opening was higher 1) for fine weather during the natural ventilation season for equivalent outdoor temperatures, 2) for cloudy weather in the late cooling season for equivalent indoor temperatures, 3) for cloudy weather in the late cooling season for equivalent outdoor humidity, and 4) for fine weather in the cooling season and for cloudy weather in the late cooling season for equivalent indoor humidity.

Seasonal and regional differences in neutral temperatures in Nepalese traditional vernacular houses

Hom B. Rijal (Tokyo city university), Harunori Yoshida (Okayama university of science) and Noriko Umemiya

Building and Environment, 45, pp.2743-2753, 2010.

Two surveys of the thermal environment and thermal sensations were conducted in the indoor and the semi-open spaces of traditional houses, during both summer and winter, in five districts of Nepal: Banke, Bhaktapur, Dhading, Kaski and Solukhumbu. The surveys were carried out for 40 days, gathering a total of 7116 thermal sensations from 103 subjects. The results show that residents are highly satisfied with the thermal condition of their houses, since they adjust well to the thermal conditions. The residents have higher neutral temperatures in semi-open spaces such as verandas than in indoor spaces. The findings reveal that people in the regions studied adapt well to the natural environment, as a result of which neutral temperatures are different in different climates. They are lowest in the cool climate, medium in the temperate climate and highest in the sub-tropical climate.

Numerical Study on Buckling Behavior of Single Layer Two-way Grid Dome with Tension Member as Diagonals

M. FUJIMOTO, S. KUSHIMA(Takenaka Corporation), K. IMAI(Osaka University), S. KATO(Toyohashi University of Technology),and T. OGAWA(Tokyo Institute of Technology)

Proceedings of IASS Symposium 2010, Shanghai, Nov. 8- 12, pp. 326-337 (2010)

The purpose of this study is to obtain the anti-buckling data on single layer two-way grid dome with tension member as diagonals by the numerical calculation. The tension member is used to stiffen the in-plane rigidity of two-way grid as diagonals. Circular hollow tubes are used as two-way grid members and PC bars as tension members. The numerical parameters of this study are installation of tension member, initial axial forces of tension members, loading patterns, half open angle of dome and so on. As a result, it is confirmed that the buckling load of two-way grid dome increases effectively by the attachment of tension members and the introduction of the initial axial forces to them. Then the comparison between the numerical results and continuum treatment method is shown.

Effect of Tension Member on Buckling and Strength Behavior of Single Layer Two-way Grid Cylindrical Shell Roof

Z. ZHANG and M. FUJIMOTO

Proceedings of IASS Symposium 2010, Shanghai, Nov. 8- 12, pp. 2178-2187 (2010)

This paper addresses the buckling behavior of a single layer two-way grid cylindrical shell roof with tension members to stiffen the rigidity of the two-way grid. The effect of tension member arrangement pattern on the buckling load and strength of a single layer grid shell is discussed by the numerical calculations. The numerical calculation parameters are number of units in the grid cylindrical shell roof, half open angle, aspect ratio and the arrangement pattern of tension member. It is confirmed that the tension member arrangement in a single layer two-way grid cylindrical shell roof caused increases in buckling load and strength. In linear buckling analysis, tension member arrangement with strut is the most effective pattern. In nonlinear analysis, four tension member arranged in each two-way grid is more effective pattern.

Development of a Numerical Model for Predicting Flow Induced by Sediment Dumped into a Vertical Pipe

T. HIRANO, T. SHIGEMATSU, Tsuyoshi KANAZAWA

Journal of JSCE, Ser. B2 (Coastal Engineering), Vol. 66, pp. 751-755 (2010) (in Japanese)

In order to predict fluid motion induced by sediment dumped into a vertical pipe, a numerical model is developed. The numerical model is based on fundamental equation of incompressible fluid with the Boussinesq approximation and the Volume Of Fluid method is applied to trace water surface in a vertical pipe. According to comparison with laboratory experimental results, calculated results reasonably agree with experimental ones in qualitatively. The estimation results by the developed model on thickness and progressive velocity of turbidity mass on the bottom are presented with maximum ambient fluid velocity.

Numerical Simulation of Fluid Force acting on Solids placed in Unidirectional Flow

Y. TAKEOKA, T. SHIGEMATSU, S. NAKAJO

Journal of JSCE, Ser. B2 (Coastal Engineering), Vol. 66, pp. 761-765 (2010) (in Japanese)

There is few research on fluid force acting on solids and turbulent flow in a pore of porous media because of the difficulty of measurement in experiments. In order to get fundamental knowledge of them, 2-D unidirectional fluid flow is investigated numerically using the Immersed Boundary method, which rigorously satisfies with the boundary condition on the solid surface with Cartesian grid and Lagrangian grid. Calculation results on pressure drop through circular cylinders reasonably agree with experimental formula by Ergun. In addition, fluid force acting on each cylinder, which varies markedly in time and space, is also presented.

A Fundamental Study on the Nonlinear Turbulent Modeling Based on Results of Image Velocimetry for the Flow Passing Through a Porous Media

S. NAKAJO and T. SHIGEMATSU

Journal of JSCE, Ser. B2 (Coastal Engineering), Vol. 66, pp. 771-775 (2010) (in Japanese)

The modeling of turbulence for the flow passing through a porous media is analyzed experimentally by using a priori tests. Velocity field inside and around a porous media is obtained with PTV. Two turbulence models, linear eddy viscosity model and nonlinear model, are tested on different Reynolds number conditions. There is a high correlation in the turbulent stress and the nonlinear velocity gradient. The applicability of the latter model is higher than the former. The model coefficient doesn't depend on the Reynolds number and the size of the spatial average area.

A Study on Remediation Index of Sea Bottom Environment and Its Estimation Method by Field Investigation

T. SHIGEMATSU, K. MIZUTA, T. ENDO

Journal of JSCE, Ser. B2 (Coastal Engineering), Vol. 66, pp. 1031-1035 (2010) (in Japanese)

Oxygen consumption by bottom sediment in a eutrophied port and harbor is modeled based on field investigation. The model consists of factors of biological contribution and chemical-physical contribution. It is presented that these factors can be estimated by water temperature and dissolved oxygen above the sea bottom. Through modeling sediment oxygen consumption it is found that a penetration depth of oxygen is a useful parameter to represent sea bottom environment as a remediation. Further, estimation method of penetration depth of oxygen is improved to take into the change of the dissolved oxygen above sea bottom consideration.

Numerical Simulations of Urban Heat Release into Osaka Bay Considering Meteorological Data

N. MORI, Y. SACHI, T. SHIGEMATSU, M. NAKAO, S. YAMOCHI, H. MASE

Journal of JSCE, Ser. B2 (Coastal Engineering), Vol. 66, pp. 1296-1300 (2010) (in Japanese)

The stratification of upper layer of coastal water can be regarded as an unused energy source in summer. The coastal water has large capability to store the urban heat owing to the heat capacity difference between the air

and water. The estimated urban heat over Sumiyoshi ward in Osaka is equivalent to 10 m³/s warm water if we allow 7 degree water temperature increase from stagnant environment. The numerical simulation of the urban heat release into coastal zone is performed. The larger warm water discharge gives absorption effect of short wave radiation from the atmosphere to the ocean due to enhancement of vertical mixing at the upper ocean.

Estimation Method of Oxygen Penetration Depth into the Bottom Sediment at Strongly-Enclosed Sea Area

T. SHIGEMATSU and T. ENDO

Journal of Coastal Research, Special Issue 64, pp. 1633-1637 (2011)

Oxygen consumption by bottom sediment is modeled based on field investigation in a eutrophied port and harbor through a whole year. Based on measured sediment oxygen consumption flux using a chamber and a dark bottle with fluorescence type oxygen sensors, biological and physical-chemical oxygen consumption processes are modeled with water temperature and dissolved oxygen concentration near the sea bottom. It is presented that these factors can be estimated by water temperature and dissolved oxygen above the sea bottom. Through modeling sediment oxygen penetration depth is a useful parameter to represent sea bottom environment as a remediation. Further, estimation method of oxygen penetration depth is improved to take into the change of the dissolved oxygen above sea bottom consideration.

Numerical Simulation of Fluid Force acting on Circular Cylinders in Unidirectional Flow

S. NAKAJO, Y. TAKEOKA, and T. SHIGEMATSU

Proc. of 7th International Symposium on Turbulence and Shear Flow Phenomena (2011)

There is few research on turbulent flow in a pore of porous media and fluid force acting on solids because of the difficulty of measurement in experiments. In this paper, in order to get fundamental knowledge of them, 2-D unidirectional flow passing through circular cylinders is investigated numerically using the Immersed Boundary Method with Physical Virtual Model, which rigorously satisfies with the boundary condition on the solid surface with Cartesian grid and Lagrangian grid. Calculation results on pressure drop through circular cylinders reasonably agree with experimental formula by Ergun. Transition of flow pattern with increase in the Reynolds number is presented. In addition, fluid force acting on each cylinder, which varies markedly in time and space, is also presented.

Experimental Verification of Turbulence Modeling for the Flow through a Porous Media by Using PTV

S. NAKAJO and T. SHIGEMATSU

Proc. of 7th International Symposium on Turbulence and Shear Flow Phenomena (2011)

Most of existing turbulence models for porous media flow which many researchers have proposed were macroscopic models based on the knowledge of pressure drop along a porous media. Therefore they can not present distribution of turbulent properties in a porous media at all. In the present study, we validated a linear and a nonlinear turbulence models by a priori testing based on the measurement data of velocity inside a porous media using a high resolution PTV with the refractive index matching method. As a result, it was cleared that a nonlinear turbulence model with nonlinear velocity gradient agree to the experimental results much better than a linear turbulence model for the flow through a a porous media. Moreover, it was presented that the coefficient in the nonlinear model is constant and independent with the Reynolds number and spatial averaging area size.

Strain softening behavior of reinforced concrete member under axial load

Wataru KURAMOTO, Yohei KOTANI, Yuki TAKAI, Hiroaki KITOH, Hajime OHUCHI

Journal of Structural Engineering, Vol.57A, pp.916-925 (2011) (in Japanese)

For deformation capacity improvement of reinforced concrete members, it is significant to increase ductility of compressive concrete with providing effective lateral confinement. The purpose of the present study is to predict a strain softening behavior of the confined concrete based on an uniaxial compressive loading test of the reinforced concrete column models with lateral hoops. The present study has been conducted in the following approach; (1) axial compressive forces acted on longitudinal reinforcement and on cover concrete section are

respectively estimated and then, (2) axial force on confined concrete section is identified. (3) stress-strain relationship of confined concrete is predicted up to strain softening region, which is compared with the design equation proposed in the existing specification.

Strengthening Technique of the Marine Pier Beam by DFRCC

Tetsuya OGASAWARA, Chunri JIN, Yuji INOKI, Hisao TSUNOKAKE, Hajime OHUCHI

Structural Engineers World Congress 2011, 8pages, (CD-ROM) (2011)

Ductile Fiber Reinforced Cementitious Composite (DFRCC) can be expected as plastic tensile material. It has high performances that can prevent chloride penetration by the multiple crack characteristic, and also that can be applied to repair combined seismic retrofit. In the present study, focusing on ordinal pier beam member classified into deep beam as a proto type model, monotonic loading tests has been conducted into two programs, i.e. 1) flexural strengthening and 2) shear strengthening.

Shear Test of Concrete-Filled Steel Tubular Short Columns with Thin Walled Cross Section

Hisao TSUNOKAKE, Yoshihiro YAMADA, Tetsu SUGANUMA and Hajime OHUCHI

Proceedings of the Japan Concrete Institute, JCI, Vol.33, pp.1141-1146, (CD-ROM) (2011)(in Japanese)

Fundamental Study to Pier Beam on Effect of Thickening Bending Reinforcement by DFRCC

Tetsuya OGASAWARA, Yuji INOKI, Hisao TSUNOKAKE and Hajime OHUCHI

Proceedings of the Japan Concrete Institute, JCI, Vol.33, pp.1255-1392, (CD-ROM)(2011) (in Japanese)

Experimental Study on Strengthening Method of Lower Flange Plate of I Shaped Steel Girder with Bolted Connection by High Modulus CFRP Strips

Nobuhito OCHI (Akashi National College of Technology), Masahide MATSUMURA and Nobuhiro HISABE (Mitsubishi Plastics, Inc.)

Journal of Structural Engineering, Vol.55A, JSCE, pp. 43- 51 (2009) (in Japanese)

The installation of CFRP strips of high modulus can be effective for strengthening a superannuated existing steel I girder with regard to improving its load carrying capacity. Here, shear plates of the bolted connections become obstacles in installing the CFRP strips onto the lower flange plate of I shaped steel girder. Then, experimentally investigated in this study is the strengthening effect of the methods to prevent the CFRP strips of high modulus from debonding in the vicinity of the bolted connection of lower flange plate of I shaped steel girder through a bending test. It is concluded that the proposed methods are effective to prevent debonding of the CFRP strips and further investigations are needed to develop more effective methods.

Bending and Shear Behavior of a Steel I-Shaped Girder with a Transversely Profiled Steel Web Plate

Kunitaro HASHIMOTO (Kyoto University), Takashi YAMAGUCHI, Kosuke OTSUKA (Kyoto University), Kunitomo SUGIURA (Kyoto University), Yasuo SUZUKI (Utsunomiya University) and Takuji KUMANO (JFE Engineering Corp.)

Journal of Structural Engineering, Vol.55A, JSCE, pp. 144- 153 (2009) (in Japanese)

Steel plates with varied thickness have a potential for rationalization of steel bridge design. For example, longitudinally profiled steel plates already have been adapted to flanges of an I-shaped girder / a box girder to reduce the weight of the bridge and the process of bridge construction. Recently, the analytical study on the mechanical behavior of steel girders with a transversely profiled web plate has been carried out, and it has been concluded that there exists the preferable cross sectional shape of steel plate from the viewpoint of the load carrying capacity and ductility. In this paper, the static loading tests for I-shaped girders with a profiled web plate in thickness are carried out. It is found that the web plate whose thickness is larger at the middle height of the girder has superiority for shear buckling strength; on the other hand, that the web plate whose thickness is larger at the close to flange plate has superiority for bending strength.

Seismic Performance Evaluation of a Viaduct Supported by Steel Bridge Piers with EPS

Masahide MATSUMURA, Satoshi UCHIDA (NEWJEC Inc.) and Toshiyuki KITADA
Journal of Structural Engineering, Vol.55A, JSCE, pp. 653- 661 (2009) (in Japanese)

Embedded Plastic Segment (EPS), which has been developed as a seismic retrofitting technique for existing steel bridge piers, can enhance the ductility with less increment in the ultimate strength of the column members. In this paper, the seismic performance of a viaduct of the total length 200m with 5 spans supported by the steel bridge piers with the EPS is analytically investigated. The effectiveness of the steel bridge piers with the EPS is revealed in comparison with a viaduct supported by concrete filled steel bridge piers. It is concluded that the EPS enables the reduction of the construction cost of piles and footing concrete and the enhancement of redundancy of the viaduct.

Measurements of Initial Imperfections of Longitudinally Profiled Steel Plates and Their Applied Box Cross Section

Takuji KUMANO (JFE Engineering Corp.), Yasuo SUZUKI (Utsunomiya University), Takeshi KITAHARA (Kanto Gakuin University), Kunitomo SUGIURA (Kyoto University) and Takashi YAMAGUCHI
Journal of Structural Engineering, Vol.55A, JSCE, pp. 977- 984 (2009) (in Japanese)

Recently, various kinds of high-performance steel have been developed in order to reduce construction costs and improve structural performances. LP steel plate is applied to flange plates of steel girders with a view to reduction of process for fabrication and simplifying structures. On the other hands, it is generally known that initial imperfections of steel plates affect on the characteristics of strength and deformation of steel girders. Therefore, in this study, the fabrication error of plate thickness and the residual stress distribution subjected to metal rolling and welding are measured for the actual LP plate and box cross section in order to correct the basic information of initial imperfections of LP steel plates.

Analytical Study on Mechanical Behavior of the High Strength Bolted Friction Joints with F18T Grade Super High Strength Bolts Subjected to Compression

Takashi YAMAGUCHI, Toshiyuki KITADA, Takayuki IKEDA (NTT Data Corp.) and Natsuki YOSHIOKA
Journal of Structural Engineering, Vol.55A, JSCE, pp. 1005- 1013 (2009) (in Japanese)

Recent years, rationalization of the joint structures is required from the viewpoint of reduction of the total cost of steel structures. As one of such effective solutions, adoption of super high strength bolts for friction type joints, which strength is more than 1,600 MPa is considered in order to be a compact joint section with a few bolts and lines. However, the mechanical behavior of such joints, especially the behavior under compressive load, is not clear. Therefore, in this study, the mechanical behavior of the friction type joints with super/normal high strength bolts subjected to compressive load is discussed based on the FE analytical results paying attention to the maximum spacing of the bolts and contact between joint surfaces.

Experimental Study on the Strengthening of Bolted Tensile Joints with a Deformable Filler Plate

Yasuo SUZUKI (Utsunomiya University), Takashi YAMAGUCHI, Akinori NAKAJIMA (Utsunomiya University) and Takahiro SHIMIZU (Utsunomiya University)
Journal of Structural Engineering, Vol.55A, JSCE, pp. 1014- 1023 (2009) (in Japanese)

In the split tee joints, the prying force occurs due to the deformation of the tee flange plates, and the prying force reduces the strength of the joint. Therefore, it is very important for this type of joints to suppress the prying force. In order to make it possible to reduce the prying force of split tee joints easily, we propose to apply the sealant named as deformable filler plate for the split tee joints consists of soft rubber and steel rings. In this study, the mechanical behavior of split tee joints with the deformable filler plate is investigated experimentally. Particularly the influence of the sealant and shapes of the tee flange plates on strength and deformation of these joints are mainly discussed.

Dynamic Response of Isolated Bridge System Considering Knocking-off of Side Block as Displacement Restrainer of Superstructure

Masahide MATSUMURA, Nobuhito OCHI (Akashi National College of Technology), Masahiko YOSHIDA (Kawaguchi Metal Industries Co., Ltd), Minoru SAKAIDA (Sakaida Bridge Engineering & Consulting) and Toshiyuki KITADA

German-Japanese Bridge Symposium, Munich, (7 pages, CD-ROM) (2009)

Displacement restrainer of the superstructure in the transverse direction of the isolated bridge, like side block, is usually installed to protect expansion joints from damage during earthquake. Here, a more rational response of the isolated bridge to mitigate damage to bridge pier and/or base structure and to enhance redundancy against a strong earthquake like the Level 2 Earthquake can be considered to be that the displacement of the superstructure against a small and a moderate earthquake like the Level 1 Earthquake is restraint and the displacement against the Level 2 Earthquake is released. For instance, steel side block, improved to have a knock-off function, will provide these responses. This study presents the outline of the side block with the knock-off function, which is the side block with a slit and developed by the authors to control the breaking load accurately, reveals the effectiveness of the knocking-off in the isolated bridge system through dynamic loading test using a small-size shaking table and verifies the influences of the breaking characteristics of the side block with the knock-off function through the dynamic response analysis of the system.

Experimental Study on Static Mechanical Properties of Glass Plate Materials for Use as Structural Members

Yugo NAGAMACHI, Toshiyuki KITADA, Takashi YAMAGUCHI and Masahide MATSUMURA

German-Japanese Bridge Symposium, Munich, (4 pages, CD-ROM) (2009)

Developments of the glass technology and fundamental researches for the structural use of the glass enable the applications of the glass plate to structures. The glass plate has been widely used in architectural structures both as structural and non-structural members and the use of the glass plate as structural members creates more attractive and functional structures. On the other hand, the use of the glass to structures in civil engineering field is not so popular, because the cost-effectiveness may be first priority in the structural design and planning. Here the use of the glass plate for structures in civil engineering field, for instance, for principal structural members of bridge can be considered to create more attractive and fascinating bridge and construction, which will bring a drastic change to images of the bridge. In the study, fundamental material properties of the glass plate are clarified through material tests. Then, a new type of glass plate beam with a joint is proposed through numerical calculations based on the material test results. Here, SGP foils is used for the joint in the beam.

Inspection and Damages of Bridge Expansion Joints in Urban High Way in Japan

Masahide MATSUMURA, Takashi YAMAGUCHI, Yoshihiko TAKADA (Hanshin Expressway Management Technology Center) and Toshiyuki KITADA

German-Japanese Bridge Symposium, Munich, (7 pages, CD-ROM) (2009)

Bridge expansion joints, installed at the edges of the girders and subjected to the impact loading of moving vehicles, take important roles in providing smooth running of the vehicles. A proper type of the expansion joint, which can secure enough interspaces between the girders, should be selected to prevent their interaction against expansion movements with the changes in temperature and during the earthquake. Adoption of the finger joint is a general solution when larger interspaces between the girders are required. However, the finger joint is designed only against the static vertical design load corresponding to the truck live load according to the present design method in the Japanese Specification of Highway Bridges (JSHB), however some damages of the finger joint are reported. Presented in this paper are the outlines of inspection results and damages of the expansion joints, which is carried out by Hanshin Expressway Corp., and the discussion based on the test results of the two kinds of the field test passing the vehicles over the joints. It is concluded that the impact loading derived from the vehicle passing and enlarged by the faulting between the joints is not negligible in the design of the finger joint.

Slip Behavior of High Strength Bolted Friction Joints for Composite Girders Subjected to Bending

Natsuki YOSHIOKA, Takashi YAMAGUCHI, Masatsugu NAGAI (Nagaoka University of Technology) and Takeshi MIYASHITA (Nagaoka University of Technology)

German-Japanese Bridge Symposium, Munich, (8 pages, CD-ROM) (2009)

In recent years in Japan, various studies on rational design of steel bridges focusing on cost reduction, such as consideration of plastic behavior for ultimate state are performed. In Euro Code, AASHTO-LRFD, plastic moment is already adopted to the ultimate strength for the positive bending state of the composite girder. However, in Japan, there are a few researches about it and as a result, plastic moment is not allowed to the ultimate strength in the design specifications. Accordingly, in this study, in order to collect basic information for design of composite girder connection, FE analyses were executed referring to the experiment which has been carried out by authors. Finally, based on these analytical results, the evaluation method of ultimate bending strength of the composite girder with high strength bolted friction joints are proposed and desirable design concept of the friction type joints for composite girder bridges are summarized.

Analytical Study on Residual Load Carrying Capacity of Damaged Steel Bridge with Large Crack

Takashi YAMAGUCHI, In ho KIM (Miyaji Iron Works Co., Ltd.), Toshiyuki KITADA and Kazuyuki MURAMOTO (Japan Bridge Engineering Center)

Steel Construction Engineering, Vol.16, No.63, JSSC, pp. 15- 25 (2009) (in Japanese)

In recent, much damage has been detected in superannuated bridges. Especially, the fatigue problems of aged steel bridges become serious in the maintenance of bridges. Recently, the serious and large crack of approximately 1.1m length was detected. In the web plate of interior main girder at the intersection of the main girder and the transverse girder, and at the location near the interior support in the center span of a three-span continuous girder bridge. If such a large crack occurs, the load carrying system of bridge should be changed and its capacity will be decreased. Accordingly, it is important to evaluate the residual load carrying capacity of damaged bridges with a large crack from the viewpoint of the management of the bridge system. The objective of this study is to investigate analytically change of the load carrying system of the various damaged three-span continuous girder bridges with four main girders.

Friction Test for High-Strength Bolted Joints with Long-Exposed Weathering Steel

Minoru SAKAIDA (SAKAIDA Bridge Engineering & Consulting), Kunitomo SUGIURA (Kyoto University), Takashi YAMAGUCHI, Shigeyuki MURAKAMI (Gifu University) and Kunitaro HASHIMOTO (Kyoto University)

Steel Construction Engineering, Vol.16, No.63, JSSC, pp. 37- 48 (2009) (in Japanese)

Strength and slip factor of high strength bolted friction joints were obtained through loading tests. Specimens were assembled from weathering steel base members and blasted splicing members. Weathering steel plates were cut out from lower flange plate of a bridge that was exposed for 8 years in open inland field, and it has been generated protective rust on its surface. Base members were treated in some levels of rust removing. Applied treatments are blasting, disk sanding, powered wire brushing, manual wire brushing and cloth wiping. Protective rust decreases the slip factor, and thin crystalloid rust increases it, but thick rust over 100 μm decreases it.

Assessment on Fatigue Cracks in Orthotropic Steel Decks

Kunitomo SUGIURA (Kyoto University), Kunitaro HASHIMOTO (Kyoto University), Yoshinobu OSHIMA (Kyoto University) and Takashi YAMAGUCHI

Steel Construction, Vol.2, No.3, Ernst & Sohn, pp. 175- 180 (2009)

In this study, proposed is the new health evaluation system for fatigue cracks of orthotropic steel bridge decks by measuring strain changes of the asphalt pavement on steel plate decks. In order to consider applicability of this system, carried out are parametric FE analyses in which the type of cracks, their position, and their length are varied. From these analytical results, it is found that strain changes of the asphalt pavement on steel plate decks by the length and the positions of cracks can be significant enough to be detected.

Experimental Study on Vibration Control of Pole Type Steel Structures on Bridges by Using Damping Members/Elements

Tomohiko ISHIBASHI (Nasu Denki-Tekko Co., Ltd.), Takashi YAMAGUCHI and Kazuyuki HENMI (Nasu Denki-Tekko Co., Ltd.)

Journal of Constructional Steel, Vol.17, JSSC, pp. 247- 254 (2009) (in Japanese)

Recently, it is pointed out that the bridge vibration due to traffic may cause fatigue damages to pole type steel structures like a lighting pole or a marker pole on bridges. As such damage tends to cause severe accidents, the vibration damage is to be eliminated as soon as possible. It is important to avoid resonance phenomenon and to increase damping effect of the steel poles with possible fatigue damages by economical techniques, because the number of pole type steel structures on bridges is large. Authors suggest two vibration controlling techniques for these steel poles, by using wire ropes and by using chloroprene rubber plates underneath the lower end plate of the steel pole. It is verified through a vibration experiment that both techniques are effective and the response displacement of the pole can be reduced substantially.

Fundamental Study on Characteristics of Extremely Low Cycle Fatigue Crack of Steel Members in Bridges

Shigeharu YAMANE (Mitsubishi Heavy Industries Bridge & Structures Engineering Co., Ltd.), Toshiyuki KITADA, Takashi YAMAGUCHI and Masahide MATSUMURA

Journal of Constructional Steel, Vol.17, JSSC, pp. 289- 294 (2009) (in Japanese)

Extremely low cycle fatigue crack phenomenon is not yet clarified enough. In this paper, crack initiation mechanism in a range of the repetition number of several times to 20 is clarified by the extremely low cycle fatigue experiment focusing on strain at crack initiation point and fractography of the crack fracture. It is concluded that the crack is not brittle but ductile in the case of the extremely low cycle experiment using the specimens with welding part and notches at their central part.

A Fundamental Experiment on Mechanical Behavior of Panel Point of Steel Truss Bridges

Shinsuke YOSHIDA (Kyoto University), Takashi YAMAGUCHI, Kunitaro HASHIMOTO (Kyoto University) and Kunitomo SUGIURA (Kyoto University)

Journal of Constructional Steel, Vol.17, JSSC, pp. 391- 398 (2009) (in Japanese)

In this study, in order to clear the mechanical behavior of panel point of steel bridges using high strength bolted frictional connection, tensile loading experiment is carried out. In the experiment, two specimens modeled the panel points of steel truss bridges which the gusset plate and the diagonal member are connected by high strength bolts are prepared. One has the ordinal gusset plate whose thickness is 9 mm, and the other has thin (6 mm) gusset plate in which is considered the decrease of the thickness due to corrosion. From the result of this experiment, it is found the collapse behavior of panel points of steel truss bridges and it is suggested the optimum calculating method for yielding strength of such panel point.

Study on Methods for Effectively Using Down-Sized Vibration Table to Evaluate Seismic Performance of Bridge Structures

Yasuyuki NAKANISHI (NEWJEC Inc.), Masahide MATSUMURA, Toshiyuki KITADA and Takashi YAMAGUCHI

Journal of Constructional Steel, Vol.17, JSSC, pp. 415- 420 (2009) (in Japanese)

Dynamic response analysis requires many idealizations regarding the unknown factors, such as dumping coefficient, dynamic characteristics of material, etc, but simulates the dynamic behavior the idealized of structure, although it's unknown whether the predicted behavior is exact. While shaking table test without idealizations shows dynamic response. Using a down-sized specimen, the dimensional reduction from a full scale is same question as to the realization of exact behavior, but the cost effectiveness will be much attractive. Then the shaking table test using down-sized specimens are carried out in this study to examine the advantages and disadvantages. Also the experimental results are compared with the numerical ones using the idealized analytical models. Effectiveness of using down-sized specimen in the small shaking table in evaluating seismic performance of steel structures is discussed comparing experimental and analytical results.

Repairing Design of Stiffeners on the Support of a Plate Girder for Highway Bridges

Kennichi SATO (New Structural Engineering, Ltd.), Yukiko MITSUGI (New Structural Engineering, Ltd.), Takashi YAMAGUCHI, Kunitaro HASHIMOTO (Kyoto University) and Kunitomo SUGIURA (Kyoto University)

Journal of Constructional Steel, Vol.17, JSSC, pp. 673- 680 (2009) (in Japanese)

In this paper, the repairing design of stiffeners on the support of a plate girder for Highway Bridges is studied referring the literature and executing simple calculation. We treated the stiffener on the support, whose effective sectional area is decreased by corrosion at the end of the bottom portion. From the viewpoint of the performance based design, we considered the role of the each member/element that consists of the girder on the support. The mechanics of resistance and the limit states of them are discussed. In the case that the thickness of the plate at the bottom end is decreased by the corrosion, the bearing limit state of the bottom-end is dominant.

Fatigue Failure Assessment Considering Actual-working Load and Running Position of Orthotropic Steel Deck by Using BWIM

Yoshihiko TAKADA (Hanshin Expressway Management Technology Center) and Takashi YAMAGUCHI

Memoirs of the Faculty of Engineering, Osaka City University, Vol.50, pp. 55- 61 (2009)

Recent considerable increase in traffic intensity and wheel loads causes fatigue cracks in orthotropic steel decks in Hanshin Expressway. From results of the periodic inspection, fatigue cracks are detected by 167 spans in 1347 spans in orthotropic steel decks as of April, 2009. Under traffic loading, in particular the effect of local wheel loads, longitudinal welds between deck plate and trough are subjected to local transverse bending moments and are susceptible to fatigue cracks. The stress in trough to deck plate welds is strongly influenced by actual-working load and run position. Then, in orthotropic steel decks in Kobe route of Hanshin Expressway, measurement of the load of actual-working traffic and generating stress is performed by Bridge-Weigh-In-Motion. This paper presents the outline of fatigue failure in orthotropic steel decks. Next, Fatigue failure assessment based on this measurement results are described.

A Consideration on Seismic Response Analysis Result of Steel Truss Bridge by Focusing on Modeling Method of Connections in Steel Truss Bridge

Hiroaki TANIUE (Osaka University), Kiyoshi ONO (Osaka University), Masahide MATSUMURA and Takao MIYOSHI (Osaka University)

Proceedings of the 13th Symposium on Ductility Design Method for Bridges, JSCE, 8 pages (2010) (in Japanese)

Elasto-plastic and finite element analysis of a steel truss bridge is carried out by focusing on modeling method of connections, which are designed as pinned connections so that only axial forces are subjected to the chords members in a steel truss bridge. That is, the influences of flexural rigidity of the connections on the ultimate strength of the truss bridge and on the working stress against the Level 2 Earthquake defined in the Specifications for Highway Bridges in Japan are investigated through the FEM analysis.

Ultimate Strength and Repairing Design Method for Stiffeners on the Support of a Plate Girder End for Highway Bridges

Makoto USUKURA (Tokyo Consultants Co., Ltd.), Akihisa KONDO (Sogo Engineering Inc.), Takashi YAMAGUCHI, Akira HATANAKA, Yukiko MITSUGI (New Structural Engineering, Ltd.), Kunitaro HASHIMOTO (Kyoto University) and Kunitomo SUGIURA (Kyoto University)

Journal of Structural Engineering, Vol.56A, JSCE, pp. 722- 732 (2010) (in Japanese)

In this paper, the ultimate strength of the girder end with corrosion of a plate girder for Highway Bridges is studied by FEM analysis. We have dealt with the stiffener or web on the support, whose effective sectional area is lost by corrosion at the end of the bottom portion. The vertical stiffener on the support is designed as a column subjected to compression. But in the case that the thickness of the plate at the bottom end is decreased by the corrosion, it is considered that the limit state of the bottom-end is dominant. Finally, the design concept of the stiffener is also discussed.

Study on Mechanical Behavior of Single-Riveted Joint Damaged by Corrosion

Kunitaro HASHIMOTO (Kyoto University), Takashi YAMAGUCHI, Yukiko MITSUGI (New Structural Engineering, Ltd.) and Kunitomo SUGIURA (Kyoto University)

Journal of Structural Engineering, Vol.56A, JSCE, pp. 756- 765 (2010) (in Japanese)

In this study, in order to clarify the mechanical behavior, and the relationship between corrosion and residual strength of single-riveted joint damaged by corrosion, experimental and analytical studies are carried out. In the experiment, are used the specimens, which cut from the demolished steel bridge members. Two types of the specimens, light and the heavy corroded joints, are prepared and tensile tests are executed. In FE analysis, corroded condition of rivet head is varied and parametric analysis is carried out. From the result, it is found that there is the influence to strength when a rivet head is corroded heavy, in case of the single riveted joint.

Stress Analysis of Existing Orthotropic Steel Deck for Evaluation of Fatigue Cracks Originating from Root of Weld

Yoshihiko TAKADA (Hanshin Expressway Management Technology Center), Akiko TABATA (Hanshin Expressway Corp.), Kunitaro HASHIMOTO (Kyoto University), Kunitomo SUGIURA (Kyoto University) and Takashi YAMAGUCHI

Journal of Structural Engineering, Vol.56A, JSCE, pp. 766- 778 (2010) (in Japanese)

Significant increases in traffic intensity and wheel loads are causing fatigue cracks in orthotropic steel decks. Under traffic loading, in particular the local effect of wheel loads, longitudinal welds between deck plate and trough rib are subjected to local transverse bending moments and are susceptible to fatigue cracks. For the purpose of evaluation of crack originating from root of weld, FEM analysis modeling the full-scale orthotropic steel deck of two span continuous box girder bridge is carried out. The stress of welds which originates in a deformation of large range in deck plate is calculated. From these analytical results, it became clear that the state of the stress under different loading location affects fatigue cracks.

Application Effect of Rapture Controllable Steel Side Blocks for Viaduct with Isolation Bearings

Masahide MATSUMURA, Nobuhito OCHI (Akashi National College of Technology) and Masahiko YOSHIDA (Kawakin Core-Tech Co.,Ltd.)

Journal of Structural Engineering, Vol.56A, JSCE, pp. 554- 563 (2010) (in Japanese)

Steel side blocks are set besides the seismically isolating bearings of a viaduct and are designed as a joint protector against the Level 1 earthquake. The authors suggested the CSB as rapture controllable steel side block with knock-off function and as a trigger to provide isolation effect not only in the direction of the bridge axis but also in the transverse direction against the Level 2 earthquake. In this study, the knock-off effect of the CSB in a vibration system consisting of bridge pier-rubber bearing-mass is investigated through shaking table test. Also the installation effect of the CSB is verified through seismic response analysis of a viaduct with isolating bearings.

Experimental Study on the Mechanical Behavior of High Strength Bolted Friction Type Joints with Extremely Thick Plates and Many Bolts in a Line

Takashi YAMAGUCHI, Xue PENG, Yasuo SUZUKI (Utsunomiya University) and Syuhei MIYAO

Steel Construction Engineering, Vol.17, No.66, JSSC, pp. 23- 33 (2010) (in Japanese)

Resent years, from the viewpoint of rational fabrication of the steel bridges, there are some applications using extremely thick plates which thickness is more than 75mm for primary members of bridge structures. In case of joining such thick plates by using high strength bolted friction type joints, the number of bolts in a line along the member axis might be more than 10. However, the mechanical behavior of such multiple joints is not clear. In this study, the experiment for such joints has been carried out to understand the mechanical behavior of them. Discussed herein is the mechanical behavior of such joints based on the experimental results.

Seismic Devices for Isolated Bridge

Masahide MATSUMURA

Proceedings of the 3rd Taiwan-Japan Workshop on Bridge Engineering, pp.36-40, NCREE (2010)

Several types of seismic devices of isolated bridges in Japan are introduced and explained in this paper. Through the discussions it is concluded that seismic retrofit scheme for bridge structures are gradually changing by assembling some advanced features and seismic devices. Then the combination use of several seismic devices for damage control enables seismic retrofit of existing bridge structures to satisfy the design requirements. Also development and widespread uses of seismic response analysis and experimental approach to assure the performance of seismic devices surely help in evaluating the seismic safety of bridge structures.

Experimental Study on Vibration Control of Pole Type Steel Structures on Bridges

Tomohiko ISHIBASHI (Nasu Denki-Tekko Co., Ltd.), Takashi YAMAGUCHI and Daisuke OKAZAKI (Nasu Denki-Tekko Co., Ltd.)

Steel Construction Engineering, Vol.17, No.66, JSSC, pp. 35- 44 (2010) (in Japanese)

Recently, it becomes a large problem that bridge vibration induced by vehicles causes damages to not only the bridge but also a pole type steel structures, such as lighting poles, marker poles on the elevated bridge. Since such damage tends to cause more severe damage, the vibration problem should be solved. As a number of such poles is large enough, it is important to improve damping performance of the steel pole with cheap cost. Then the authors suggested a vibration controlling technique for a steel pole by using wire ropes. It was found through the vibration experiment that the technique functions effectively and the vibrations of the pole can be reduced.

Study on Bending Strength Evaluation of Non-Composite and Composite I Girders by Reliability Analysis

Kunitaro HASHIMOTO (Kyoto University) and Takashi YAMAGUCHI

5th International ASRANet Conference, 14-16 June, Edinburgh, UK (8pages, CD-ROM)

In this study, in order to evaluate bending strengths of non-composite and composite I girders, sensitivity analysis by FE analysis and reliability analysis by RSM are carried out. At First, sensitivity analysis is carried out for non-composite and composite I girders by using FE analysis because there are many uncertain factors relating to their bending strengths. Next, reliability analysis is carried out by RSM. In RSM, two random variables are determined by the results of the sensitivity analysis. From the results of these analyses, it is found that reliability index and fracture probability are almost same values for composite girders of two models in this study. And it is also cleared that reliability indexes and fracture probability are different values between non-composite and composite girders.

Study on Probabilistic Fatigue Assessment of Existing Orthotropic Steel Decks

Yoshihiko TAKADA (Hanshin Expressway Management Technology Center), Masaki OCHI, Takashi YAMAGUCHI and Masahide MATSUMURA

5th International ASRANet Conference, 14-16 June, Edinburgh, UK (8pages, CD-ROM)

Recent considerable increase in traffic intensity and wheel loads are causing fatigue cracks in orthotropic steel decks in urban expressway in Japan. Under traffic loading, longitudinal welds between deck plate and trough rib are subjected to local transverse bending moments due to local wheel loads, and are susceptible to fatigue cracks. The stress occurred in trough rib to deck plate welds is strongly influenced by actual-working load and run position of vehicles. In order to evaluate the remaining fatigue life and fatigue durability of existing orthotropic steel decks rationally, probabilistic fatigue evaluation should be needed. At first, weight distributions of various vehicles are modeled by log normal distribution based on the Live load simulation results., And FE analysis for an orthotropic steel deck of the actual steel bridge is performed to estimate the stress ranges due to running vehicles. Secondary, The stress range and frequency by various vehicles are clarified by Reign flow method considering running position along the transverse direction of the vehicles. Finally, probabilistic fatigue assessment of existing orthotropic steel decks is carried out by using obtained results.

On Method for Reducing Earthquake Force of the Pier Foundation Using Energy Absorption Connectors

Kentaro TANAKA (Kanto Gakuin University), Takeshi KITAHARA (Kanto Gakuin University), Hiroshi ZUI (Setsunan University) and Masahide MATSUMURA

Memoirs of the Faculty of Engineering, Kanto Gakuin University (2010) (in Japanese)

In this paper, the energy absorption performance of the steel bellows as one of the energy absorbing bridge girder connectors is examined for reducing earthquake force of the pier foundation by means of a non-linear time-history analysis. The effectiveness of the steel bellows on the seismic response is verified using a three-span girder bridge model supported on lead rubber bearings.

Dynamic Response of Bridge System with Knocking-off Members

Masahide MATSUMURA, Masahiko YOSHIDA (Kawakin Core-Tech Co.,Ltd.) and Nobuhito OCHI (Akashi National College of Technology)

LABSE Symposium Venice 2010, Vol.97, pp.344-345, Venice (2010)

Displacement restrainer restrains transverse movement of superstructure of isolated bridges to protect expansion joints from damage during earthquake. Here to mitigate damage of bridge pier and/or its foundation and to enhance redundancy of the isolated viaducts in a strong earthquake, it can be considered that the displacement of the superstructure against a small and moderate earthquake is restraint and the displacement against a strong earthquake is freed to shift to isolated condition. Knock-off members will provide these responses of the vibration system. This study presents the outline of some of displacement restrainers having the knock-off function and reveals the effectiveness of the knock-off in the isolated bridge system through dynamic loading test using small-size shaking table. It is also analytically verified the influences of the breaking characteristics on seismic response of the system.

Technical Front of Steel Bridges in Japan

Toshiyuki KITADA, Takashi YAMAGUCHI and Masahide MATSUMURA

Festschrift zum 60. Geburtstag von Univ.-Prof. Dr.-Ing. Ingbert Mangerig, pp.255-262, UniBwM-BKI, ISSN 1431-5122 (2010)

Described in this paper is the technical front on the design method, design load, seismic design, buckling stability, connection and maintenance of steel bridges in Japan. That is to say, shown is what has been clarified, in particular, what is not still clarified in the behavior and design of steel bridge structures, and what should be developed in the future, in order to hand down the information on the technical front of the steel bridge engineering from the generation who constructed many laborious steel bridges such as the Akashi Strait Bridge, the longest suspension bridge in the world to the next generation. Also included in the paper are items which the first author could not achieve in Osaka City University until his retirement for the age limit. The technical front on the wind-resistance design, fabrication method and erection method is out of the subject of the paper, because of a little knowledge of the authors in these fields.

Repair Design for Fatigue Crack by Adding Steel Plates with High Strength Bolts

Yukiko MITSUGI (New Structural Engineering, Ltd.), Takashi YAMAGUCHI, Akihisa KONDO (Sogo Engineering Inc.) and Kunitaro HASHIMOTO (Kyoto University)

Journal of Constructional Steel, Vol.17, JSSC, pp. 507- 514 (2010) (in Japanese)

In case of adding steel plates for repairing a fatigue crack, fit bolts are generally used considering high load transferring capacity compared with high strength bolted frictional joints. But it is reported that execution of this repairing method is difficult from the viewpoint of constructability. In this paper, repairing method for fatigue cracks by adding steel plates with high strength bolted joints are discussed. First of all, the required performance of this method is summarized. Secondary, considering such required performance, applicability of adding method with high strength bolted frictional and bearing joints is discussed based on the mechanical behavior of this type of joints by using actual application examples.

Consideration on Seismic Design Method of Viaduct with Steel Bellows as Semi-rigid Girder Connectors

Hiroshi ZUI (Setsunan University), Kentaro TANAKA (Kanto Gakuin University), Masahide MATSUMURA and Masahiko YOSHIDA (Kawakin Core-Tech Co.,Ltd.)

Journal of Constructional Steel, Vol.18, JSSC, pp. 413- 418 (2010) (in Japanese)

Mutual interactions like contacts and collisions between superstructures and devices attached at the ends of the superstructures influences on seismic response of a viaduct with some seismic isolation devices. Preferably recommended is to adopt an analysis model, which can consider their interactions, in order to ensure seismic safety of the viaduct in the seismic design. Then, focused on in this study is a combination use of steel bellows and 2 types of the expansion joints, which have different allowable displacement, and the steel bellows are designed to have different load-displacement relationships to prevent their contacts and collisions. The effectiveness of the combined use of them is investigated and clarified through seismic response analysis.

A Consideration of Seismic Response of a Viaduct Considering Collisions of Expansion Joints and Knocking-off Effect of Mounting High Strength Bolts of Them

Masahide MATSUMURA, Kazuyuki ISHIHARA, Toshiyuki KITADA and Takashi YAMAGUCHI
Journal of Constructional Steel, Vol.18, JSSC, pp. 419- 424 (2010) (in Japanese)

Expansion joints may disturb an isolating function of a viaduct when the transverse displacement of the superstructures is influenced by the collision of the expansion joints during a strong earthquake. In this paper, seismic response of a viaduct is clarified on condition that the expansion joints limit the transverse displacement of the superstructures during a strong earthquake and the necessity of the expansion joints with knock-off function is described. Then, the high strength bolts installed a slit is considered to provide the knock-off function of the expansion joints and the breaking characteristics of them are verified through static breaking test.

Experimental Study on Installation Effect of Longitudinal Stiffener Bolted to Steel Bridge Piers

Masahide MATSUMURA, Toshiyuki KITADA and Yoshihiko TAKADA (Hanshin Expressway Public Corporation)

Journals of Japan Society of Civil Engineers, Ser. A1 (SE/EE), Vol.66, No.1, pp.216-223 (2010) (in Japanese)

Stiffener strengthening technique, adding additional stiffeners and strengthening flange plates, is adopted to enhance ductility and buckling strength of existing stiffened plate in an existing steel bridge pier. However, in this technique, the additional stiffeners are welded and the flange plates are bolted. That is, quality assurance of the welded part and workability in a narrow space in the steel bridge pier are to be improved to suggest more economical and rational strengthening technique for retrofitting the existing stiffened plate. Then focused on in this study is a strengthening technique using L-shaped strengthening member joined with high strengthening bolts to the plate panel between the existing stiffeners. The effectiveness of this technique against cyclic load is investigated through cyclic loading test. It is concluded that the L-shaped and bolted stiffener effectively works in changing the buckling mode of the plate panel and shows a sound strengthening effect as in the case of the welded stiffeners.

Effects of Information Provision to Encourage Public Involved Consciousness Toward Sustainable Bus Service

Noboru ISE and Yasuo HINO

Osaka City University, Memoirs of the Faculty of Engineering, Vol. 51, pp. 11-19 (2010)

Recently, the public involved approach has been introduced to local public transportation planning, because the operation of bus service based on taxes was not sustainable. However, it seems that public involved approach has not yet fully generated, and much more still remains to be improved, such as information provision, components of approach and division of roles. This study focused on the effectiveness of information provision in cooperative activities to encourage the public involved consciousness. As a result, it was revealed that it was important to provide information for understanding the future situation of individual and area through the cooperative activities, in order to realize the sustainable bus transportation services

Information Provision via Traceability for Civil Structures

Hirokazu MATSUMOTO and Takashi UCHIDA

Osaka City University, Memoirs of the Faculty of Engineering, Vol. 51, pp. 19-26 (2010)

Recently, public administration is increasingly required to disclose information. Now, therefore, the law related to information disclosure is enhanced and local governments are increasingly releasing their information.

However, citizens rarely access that information, partly because of the procedural time and effort necessary. It is important that people be able to know information about civil structures easily, especially that which is closely associated with daily life. We propose a “Traceability System for Civil Structures” as one information service system. This paper shows a process to produce the system and experimentation using a prototype system. The results show citizens’ high interest in administrative information and the feasibility of the system.

Quantify Benefits of Cycling Space Development in Jakarta

Muhammad ZULKIFLI, Yasuo HINO, AM PATTINAJA, Indra TJAHJANI

Journal of the Eastern Asia Society for Transportation Studies, Vol.9, in press (2011)

This study aims to quantify the benefit of cycling space development in Jakarta. There are very few studies which evaluate benefits of cycling, especially if cyclist’s conditions including road facilities are improved. Improvements on health, accidents, air pollution, travel time, saving on parking costs, vehicle cost and security-enjoyments were considered as benefits in this study. As quantifying was done without established data and value available, the Contingent Valuation Methods (CVM) including Willingness to Pay (WTP) and Willingness to Use with considerations and realistic assumptions were introduced as methodology. The results show that development of cycling space is valuable measures, especially on saving of user cost. This is because the higher interest to cycling among the large number of motorized vehicles in Jakarta. This study is designed to discuss the framework of methodology, therefore the finding could be developed to be more comprehensive quantifying for the further research.

New Measure of the Level of Service for Basic Expressway Segments Incorporating Customer Satisfaction

Takashi Sakai, Kiko Yamada-Kawai, Hirokazu Matsumoto and Takashi Uchida

ISHC2011, Procedia Social and Behavioral Sciences, Vol.16, pp.57-68 (2011)

Using an empirical approach, we produced a level of service (LOS) measure that is consistent with a driver’s subjective evaluation from the viewpoint of customer satisfaction (CS). The study consists of (1) analysis of the causal relation between the level of CS and drivers’ perceptions related to traffic flow conditions using individual response data obtained through in laboratory experiments with video images, (2) construction of practical driver satisfaction models segmented by the number of lanes of which independent variables are selected among ordinary indices of traffic flow considering results of the analysis.

An Experimental Study on Measure of Speed Separation to Improve Road Safety on Bicycle Way

Tomota SANO, Yasuo HINO, Nagahiro YOSHIDA, Akinori TATUMI

Japan Society of Traffic Engineers, Papers on Traffic Engineering, No. 31, pp. 409-412 (2011) (in Japanese)

Recently, although many bicycle ways have been constructed, various problems came into existence because they were kept within the limited road space. Especially, the difference between higher speed and lower speed may become dangerous among cyclists and pedestrians. In this study, the video survey and questionnaire survey were executed on the sections where both the bicycle lane and side walk with bicycle way were provided. As a result, some major findings came out of these surveys as follows. 1) the dangerous conditions which low speed use by mainly aged people used the bicycle lane, on the other hand, higher speed by younger people used the side walk were revealed, 2) the speed of bicycles was relatively high at peak time. Then we tried to introduce the signboards to separate the users according to speed. Some major results show that the speed of bicycles became reduced and this system was evaluated as a high valuation. As a result, these results may be able to provide the important information in order to operate safely the bicycle ways.

Important Issues in Future based on Comparison Analysis of BRT Systems in China

Li HAN HAN and Yasuo HINO

Japan Society of Traffic Engineers, Papers on Traffic Engineering, No. 31, pp. 477-480 (2011) (in Japanese)

Recently, some BRT (Bus Rapid Transit) systems were introduced as a major public transport or the complement system of rail way systems, in China. However, there are some cases which the BRT system could not fulfill its function, because the placement of BRT system was not clear in the transport system. In this paper, BRT systems in China were classified into 3 types according the level of rail way system, and some important conditions such as traffic condition before introducing BRT system, purpose and characteristics of BRT system and system evaluation through the before-after analysis, were investigated based on 4 typical systems according

to the classification. As a result, not only the common problems but also each condition according to urban characteristic was revealed. These results may be useful to consider the guide line to introduce BRT systems in future.

Influences on Road Safety by Desert Weather in Uighur

Kelem ZULPIKAL and Yasuo HINO

Japan Society of Traffic Engineers, Papers on Traffic Engineering, No. 31, pp. 25-28 (2011) (in Japanese)

In Uighur, as the road construction has been extended to the desert area, the influences of desert weather to road safety have become important issues. However, the data of weather and accidents in Uighur were not enough. Then in this study, two major issues were treated. At first, the actual conditions of desert weather in Aral-Hotan desert and Taklamakan desert were analyzed based on the existed data by the Meteorological Agency of Uighur. Secondly, the conditions of occurrence of traffic accidents on main road in each desert area were also analyzed based on the data of the research institute in Uighur. However, as their data were not enough, the questionnaire survey was executed to bus drivers on these roads. As a result, it was clear that the influence of high temperature to automobile tire and brake, the influence of sandstorm to the driving visibility, as well as the speed over and desultory driving due to the long and straight road, may bring high risk of traffic accidents.

Actual Condition and Major Problems of School Education on Prevention of Traffic Accidents according Bicycle Use

Yusuke KOTAKE, Yasuo HINO, Nagahiro YOSHIDA and Kazuyuki SHUNDO

Japan Society of Traffic Engineers, Papers on Traffic Engineering, No. 30, pp.137-140 (2010) (in Japanese)

Recently, the ratio of bicycle accidents involved children has become higher. Therefore, the safety education at school and home must be important. However, the actual conditions are not revealed. In this study, the large scale of questionnaire survey was executed to public school including primary school, junior high school and high school, in Hyogo Prefecture, Japan. As a result, some major findings came out as follows. 1) Although the experience type education was introduced at many primary schools, there were few curriculums at junior high schools and high schools. 2) There was lack of staffs and teaching materials for road safety education. These findings may be useful to deepen awareness of road safety and realize the cooperation of school and local government including police office.

An Experimental Study on the Relationship between Visual Information and Behavior for Bicycle Facility Design

Takanori OKAWA, Nagahiro YOSHIDA, Yasuo HINO and Takashi Uchida

Japan Society of Civil Engineers, Proceedings of Infrastructure Planning, No.43, 4p (CD-ROM)(2011) (in Japanese)

Recently, it is spreading to prepare the cycle lane. However the standard of information presentation to control, to lead and to direct bicycle is unclear. In a previous study, there are little case that treated both view user and behavior of bicycle. Therefore, knowledge of promoting method of pavement marker, signage and road sign based on there is a high degree of usability. In this study, we aimed to clarify the relationship between visual information and behavior on cycle lane. We did experiment to measure visual information and behavior on cycle lane in Amagasaki, Hyogo Prefecture, and confirmed the perception of pavement marker and so on by hearing. We compared data by type of lane and by gazed object, and analyzed a relationship between visual information and behavior on cycle lane and a perception of pavement marker and so on.

A Case Study on Evaluation and Major Problems of Bicycle Way on Sidewalk from Viewpoint of Pedestrians

Tomoya Sano, Yasuo HINO, Nagahiro YOSHIDA and Kazuyuki SHUNDO

Japan Society of Traffic Engineers, Papers on Traffic Engineering, No. 30, pp.325-328 (2010) (in Japanese)

In recent years, the promotion of bicycles utilization that, on the wide pavement has increased the separation of pedestrian and bicycle maintenance. However, the problem that caused by the coexistence of pedestrians and cyclists are not obvious. In this study, we aimed to clarify the evaluation and improvement of bicycle ways considering the use of pedestrians. Therefore, the experiment revealed by interviews with pedestrians on the pavement, that understanding the usage of bicycles, risk perception felt by pedestrians to bicycle and approach to

the separation of pedestrian and bicycle ways. As a result, pedestrians are asked to avoid the conflicting separation of bicycles. In addition, there's "run fast" and "run along" I feel very dangerous. Also, in the event is not aware of the relative risks and their evaluation depends on age and whether or not bicycle. Therefore, in the mixed space, pointed out that it is a pressing issue that the safety of the elderly do not use a bicycle.

A Study about Freedom of Information System to Aspire for Trust in Administrative Agency

Hirokazu MATSUMOTO and Takashi UCHIDA

Japan Society of Civil Engineers, Proceedings of Infrastructure Planning, No.42, 4p (CD-ROM)(2010) (in Japanese)

Trust for public administration has attracted attention in actual practice and conventional theory. Therefore we focus on confidence-building by measures aiming stable and delayed effective like information disclosure. In this paper, we consider the possibility based on a flow of citizens' consciousness. And with relationships between administrative activities and factors of trust, we consider concrete measures to develop a trusting relationship. Hearing with local governments which have many advanced projects is conducted to investigate their situation.

Quantifying Cost Benefit of Cycling and Walking Facilities Improvement; A Preliminary Study for Methodology and Application in Jakarta,

Muhammad ZULKIFLI, Yasuo HINO and Indra TJAHJANI

Japan Society of Civil Engineers, Proceedings of Infrastructure Planning, No.42, 4p (CD-ROM)(2010)

Cost benefit Analysis is used to evaluate the impacts of road improvement projects in Jakarta and many Indonesia other cities. However, analysis was not yet used to assess the impacts on Non Motorized Transports (NMT) facilities improvements. The reason for this might be that the evaluation of impacts are very difficult to make an adequate valuation, therefore the results of estimation will be uncertain. This study is designed to discuss the framework of methodology, in order to quantify the cost and benefits of space developments for cycling and walking, in case if they are improved in Jakarta. Several methods using Contingent Valuation Methods (CVM) such as Willingness to Use, Willingness to Pay (WTP) were ex-pored as methodology. Some benefits are particularly hard to be valued. On this condition, we have to use several consideration and realistic assumptions with evaluating reliable indicators for Jakarta. The results come of net benefit show B/C ratio is 1: 22.2 for cycling space and 1: 4.1 for pedestrian developments, which vehicle cost saving hold the major share on value benefits of approximately 60 percents on the total benefits. The results will be able to identify cycling and walking as one profitable measure and optimal solution against the rapid increase of motor vehicle usage in Jakarta. These findings are not only important in the context of the current promotion of NMT in Jakarta but also become highlights of the need for further research.

Study on the process of bus service planning and its evaluation method based on public involved approach

Noboru ISE, Yasuo HINO, Koichi KAWASAKI and Yutaka TAWA

Traffic Science Society of Osaka, Proceedings of Traffic Science, Vol.40, No.2, pp.17-20 (2010) (in Japanese)

In this paper, as one of practical stages of a series of studies for the sustainable bus service in Kawachi-nagano City, the utility of public involved process was referred by using the new indicators concerned with public involvement. As a result, the discussions by workshop procedure were effective to make agreement from wider viewpoint of the lifestyle and urban transport problem in future. In addition, based on the introduction of new indicators, both the possibility of the gradual evaluation of bus service and adequacy evaluation of subsidy from local government, were referred.

A Traceability System for Civil Structures to Equalize Consciousness of Private and Public Sectors

Hirokazu MATSUMOTO and Takashi UCHIDA

Proceedings of Applied Computing in Civil Engineering, Vol.35, pp.5-8, (CD-ROM) (2010) (in Japanese)

Lots of information which public administration has stored in business affairs are not provided to citizens. For civic society, information gap separating citizens and administrative officers should be solved. "Traceability System for Civil Structures" which is proposed in this study is one information service systems for easy information query. The implementation could ensure accountability and raise civil awareness. This paper shows a process of information in prototype system which is built in based on past achievement. And experimentation

using the system to know citizens' concern in administrative information is conducted. We reflect the results in the system and describe future prospects.

Comparative Analysis on the Conflict between Left-Turning Vehicles and Bicycles at Various Type of Signalized Intersection with Cycle Lane

Takuya IWAMI and Nagahiro YOSHIDA

Proceedings of Infrastructure Planning, No.41, 4p, (CD-ROM) (2010) (in Japanese)

In Japan, almost all of space for cycle is bicycle-pedestrian track. It has caused increasing accidents between cycle and pedestrian recently. Road Traffic Act was revised in 2008, and it is spreading to promote cycle lane on a trial basis. However, there is little standard needed to consider how to promote cycle lane in Japan. In this study, conflict between left-turning car and cycle is important to safety at the signalized intersection with cycle lane, and it aims to define features of each intersection with cycle lane by comparing the speed and distance by video analysis. In Analysis, showing the features by conflicting behavior and vehicular swept path of each intersection, and analyzes the behavior in Copenhagen as an example.

Analysis of Driver's Satisfaction of Basic Freeway Segments and Satisfaction Rating Model

Takashi SAKAI and Takashi UCHIDA

Infrastructure Planning Review, Vol.27, pp.595-604 (2010) (in Japanese)

The objective of this study is to analyze the relationship between traffic conditions and driver's satisfaction with level of services (LOS) for basic freeway segments. Driver's perception and satisfaction about the traffic conditions has large difference among individuals, however, the aggregate satisfaction tends to be constant. Then, by using the covariance structure analysis, causal relationships between drivers' satisfaction and both traffic indices and perceptions of traffic condition. Finally, for each number of lanes, a satisfaction rating model with traffic indices as independent variables is proposed.

A Method for Measuring Driver's Mental Reactions by Using Near Infrared Sensor

Masataka IHARA and Takashi UCHIDA

Infrastructure Planning Review, Vol.27, pp.483-492 (2010) (in Japanese)

There are a lot of measures for the prevention of the traffic accident now. However, whether these measures work effectively from the perspective of the psychological condition is not considered, because the method for measuring driver's mental reactions has not been established. Then, the purpose of the study is to propose a method for measuring driver's mental reactions by using Near Infrared Sensor. The sensor gives a physiology index that is an oxygen saturation of the hemoglobin. This paper shows the utility of the technique and stability of this method.

A Study of Pedestrian Flow Index for Grasping Pedestrian Space's Features

Takashi UCHIDA, Kentaro MATANO, and Tomoka TSUJI

Infrastructure Planning Review, Vol.27, pp.743-750 (2010) (in Japanese)

Recently, the activation of the urban area is becoming a serious problem. As an example, open terraces are set up to improve the usage of street spaces. The street spaces are evaluated by the index of flowing quantity of the space density and the pedestrians, today. However, these indexes cannot be applied to the space where multiple ways of flow exist. Therefore, it cannot be clarified whether or not if this is effective. So in order to clarify the effect, it is important to understand the situation of the flow. The study proposes the index quantitatively expresses the flow situation. And the utility was confirmed by the walking experiment that simplified the flow situation. Also in an actual urban area that showed complex flow, it was shown that the index was able to be applied. The influence of the analytical condition and the spatial condition on the index was examined by using the walking experiment data.

A Study of Navigation System for Visually Handicapped to Support Town Walk - Media and Messages for Guidance -

Takashi UCHIDA and Yoshiaki YOSHII

Infrastructure Planning Review, Vol.27, pp.831-839 (2010) (in Japanese)

Recently, navigation systems for pedestrian are widespread with advancing positional specific technology, *e.g.* GPS. However, the accuracy of a positional specific technology is after low, and even audio guide is difficult for visually handicapped people. In the study, a navigation system for the visually handicapped was experienced by using the signal of sound and the verbal map in the condition similar to practical use. In this paper, the classification of facilities intended for suburbs, a margin for error of timing, and the priority level of the element of the verbal map are clarified from the experiment and hearing. Then, the proposal of the practical use of the navigation is discussed.

Environmental Urban Engineering

A research on the inhibition factor to upward migration of juvenile Ayu *Plecoglossus altivelis* at downstream of the Yamato River, Osaka – Effects on free ammonia on the survival of juvenile Ayu-

Hiromitsu ONCHI and Susumu YAMOCHI

Journal of Japan Society for Impact Assessment, Vol. 9, No. 2, pp. 62-68 (2010) (in Japanese)

Field surveys were conducted on the seaward drifting of larval Ayu *Plecoglossus altivelis* and their distributions at the mouth of the Yamato River, central Japan from 2007 to 2009. Total numbers of drifting Ayu were estimated to be about three million individuals in 2007, while no individuals of Ayu were observed in 2008. This is partly due to the change of grain size distributions of the riverbed around the spawning site. 34 individuals of Ayu were caught at the most seaward reach of the river, while none of the juvenile Ayu was collected at the upper areas of the river mouth. Values of ORP were low (min.-156mV) in sediments of the upper site of the river mouth when compared with its seaward sites. These findings indicate that the deterioration of the bottom sediment may partly inhibit the upstream migration of the Ayu at seaward areas of the mouth of the Yamato River.

Outbreaks of Green Tide on the Artificial Salt Marsh along the Coast of Osaka Bay, Japan

Susumu YAMOCHI

EMECs9: Managing for Results in our Coastal Seas, Abstract books, 166 p (2011)

Field surveys and indoor experiments were conducted to reduce the outbreak of green tide by *Ulva pertusa* at Osaka Nanko bird sanctuary. Reduction of biomass of *Ulva* spp. was observed at stations where the exposure rate to air was from 30 to 40%. In addition, the exposure rate of 30 to 40% to air showed no negative impacts on the biomass of benthic microalgae, infauna and non-motile epibenthos. Laboratory experiments revealed that photosynthetic activity of *Ulva pertusa* decreased when exposed to air for 4 to 7 hours at 25-35°C. Salinity decrease from 30 to 25 or 20 psu in accompanied with exposure to air drastically inhibited the photosynthesis of this species. These results suggest the possibility of controlling a green tide of *Ulva pertusa* without serious physico-ecological damages to benthic microalgae, infauna and non-motile epibenthos by the combination of exposure to air with low salinity.

Field investigation of oxygen consumption characteristic of sediment in hypoxic enclosed coastal sea

Toru ENDO, T. SHIGEMATSU and S. YAMOCHI

EMECs9: Managing for Results in our Coastal Seas, Abstract books, 41 p (2011)

In this study, we found out the oxygen consumption characteristic of sediment that the oxygen consumption rate becomes large during summer hypoxic season. Therefore, it is important to consider the effect of the oxygen consumption potential of sediment when restoration technologies for promoting oxygen supply are applied in hypoxic sea.

Research on Characteristics of the Organic Matter Degradation at the Artificial Tidal Flat –The North Pond of Osaka Nanko Bird Sanctuary-

Tetsuro FUJITA, Yuri OTANI and Susumu YAMOCHI

Proceedings of Japan Society for Impact Assessment, pp. 67-72 (2011) (in Japanese)

We measured carbon dioxide (CO₂) emissions from tidal-flat sediments using the chamber method to investigate the characteristics of organic matter degradation at a tidal flat of Osaka Nanko bird sanctuary. In addition, we determined concentrations of pCO₂ in the underground water. The amount of organic matter degradation at low tide in tidal-flat varies depending on season and also tidal variability of a day. CO₂ emission is highest when water table is lowest and temperature is highest. Flux of CO₂ shows a clear relation with temperature, water table levels and biomass.

An Experimental Study on Effect of Oxygen Supply to the Bottom of Hypoxic Sea on Oxygen Consumption Characteristic and Sea Bottom Environment

T. ENDO and T. SHIGEMATSU

Journal of JSCE, Ser. B2 (Coastal Engineering), Vol. 66, pp. 1031-1035 (2010) (in Japanese)

To understand oxygen consumption characteristics of sediment for the case of oxygen supply to the bottom of sea under the hypoxic condition, we carried out a laboratory experiment by using sediment and artificial-seawater. It is found that the oxygen consumption pattern of sediment is changing while sediment consumes oxygen. Immediately after oxygen supplying, dissolved oxygen of seawater was consumed by the chemical reaction in the sediment. And then dissolved oxygen consumed by the biological reaction.

Adsorption Characteristics of Heavy Metals to Humic Acid

Mukedes ABDURISHIT, Yoshinori KANJO and Satoshi MIZUTANI

Journal of Environmental conservation engineering, Vol.39, No.7, pp.30-36 (2010) (in Japanese)

Humic acid, which is widely distributed in the soil and natural water, has high complexation ability with various kinds of heavy metals, and gives strong effects on the mobility and solubility of heavy metals. In this paper, we focused on the adsorption characteristics of heavy metals to humic acids, which were extracted from different soils based on the extraction method of International Humic Substance Society, compared with the results of molecular weight distributions of heavy metals absorbed to humic acid with gel filtration chromatography. Judging from the results, lead was detected at the same points to the humic acid, and Zinc was absorbed to the organic matter which molecular weight was more than 100,000. But copper was absorbed to wide range of humic acid. In addition, we could obtain that the absorbed amounts of heavy metals were correlated with the amounts of functional groups of humic acids.

Deconjugation Characteristics of Natural Estrogen Conjugates by Acid-catalyzed Solvolysis and its Application for Wastewater Samples

Ze-hua LIU, Yoshinori KANJO and Satoshi MIZUTANI

Journal of Environmental monitoring, Vol.12, pp.1594-1600 (2010)

Deconjugation reactions of natural estrogen conjugates were studied here by three different solutions of 1 M hydrochloric acid (HCl) in methanol. Estrogen sulfates could be easily deconjugated even at low temperature, while deconjugation conditions of estrogen glucuronides required a higher temperature and longer time. For 1 M HCl in methanol with 8% water, the deconjugation efficiencies of the three studied estrogen glucuronides were below 59.4% at 80°C for 360 min, while the corresponding deconjugation efficiencies were above 80.6% for anhydrous HCl methanol at 80 °C for 210 min, which suggested trace water in the solution of 1 M HCl methanol retarded the deconjugation rates of estrogen glucuronides. On the other hand, their corresponding deconjugation rates increased with the addition of ethyl acetate, and their corresponding deconjugation efficiencies were above 86.7% at 80 °C for 120 min. As water is a highly polar solution, and the polarity of ethyl acetate is lower than that of methanol, this may suggest that a low polar substance would favor the reaction, while a highly polar solution would prohibit the reaction. All reactions were in pseudo first-order, and higher temperature increased the reaction rate. Finally, a GC-MS method for simultaneous analysis of free estrogens and estrogen conjugates in wastewater with acid-catalyzed solvolysis was developed, and satisfactory recovery efficiencies were obtained by spiking the standard target chemicals into the influent and effluent of one municipal wastewater treatment plant (WWTP), which demonstrated the feasibility of the developed method. Compared with enzymatic hydrolysis, the acid-catalyzed solvolysis method developed here to deconjugate estrogen conjugates is cost effective and time-saving, giving it a greater potential for use with environmental samples.

Adsorption Behavior of Mercuric Compounds on Soils under Different pH Condition

Satoshi MIZUTANI, Kazushi KADOTANI and Yoshinori KANJO

Environmental Engineering Research, Japan Society of Civil Engineering, Vol.47, pp.267-272 (2010) (in Japanese)

pH dependency of the solubility and adsorptive behavior of HgSe, HgS, HgCl₂, HgO on soils was studied. HgSe was the most stable in the four compounds under all pH area and its solubility were 0.01 - 0.2 µg/L. Because the solubility in the alkaline solution was higher than acidic one, the behavior at high pH should be paid attention to.

Adsorption ability of seven kinds of soils for mercury was evaluated based on Freundlich type adsorption isothermal line. Kurotuti-soil and Akadamado-soil, which are main soils in loamy layer of the Kanto region, and Arakidado-soil showed high adsorption abilities. The interaction of mercury and humic materials in the soil are also studied. They are extracted from Kurotuchi-soil and Arakidado-soil, and their solution with mercury was fractionated based on the molecular weights by gel filtration chromatography. The mercury was detected in the fraction with humic materials, and it suggested that mercury adsorbed on them.

Development of Drainage Collection System for Early Stabilization of Sea-based Landfill Site

Mitsuyasu TAKATA(Osaka Bay Regional Offshore Environmental Improvement Center), Takayuki SHIMAOKA(Kyushu Univ.), Yoshinori KANJO, Tamihiro NAKAMICHI(Kobe City), Yoshio YAGI and Takuji NISHIDA(Japan Waste Research Foundation)

Journal of water and waste, Vol.52, No.11, pp.912-920 (2010) (in Japanese)

Simultaneous Analysis of Natural Free Estrogens and their Sulfate Conjugates in Wastewater

Ze-hua LIU Yoshinori KANJO and Satoshi MIZUTANI

Clean-soil, air, water, Vol.38, No.12, pp.1146-1151 (2010)

Natural estrogens from humans increasingly attract attention because of their strong endocrine disrupting potency. The discharge of sewage water is considered as the most important source of these endocrine disrupting chemicals (EDCs) in the environment. Therefore, a GC-MS method was developed for the simultaneous analysis of six natural free estrogens and their sulfate conjugates in municipal wastewater, in which natural free estrogens and sulfate conjugates were successfully separated from an Oasis HLB solid phase extraction (SPE) cartridge with two different eluents, and the sulfate conjugates were then transformed to their corresponding free estrogens by acid solvolysis. Before the analysis with GC-MS, samples were derivatized by N,O-bis (trimethylsilyl) trifluoroacetamide (BSTFA) plus 1% trimethylchlorosilane (TMCS) at 80°C for 40 min. Satisfactory recoveries ranging from 64 to 112% were obtained by spiking ultra-purified water, raw, and treated municipal wastewater with the six estrogens at 50, 100, and 50 ng/L, respectively. The method was successfully applied to wastewater samples from one WWTP, which suggested that E1 was the dominant natural estrogens in effluent and E3-3S was one of the conjugates possibly occurring in the effluent.

Removal of Natural Free Estrogens and their Conjugates in a Municipal Wastewater Treatment Plant

Ze-hua LIU Yoshinori KANJO and Satoshi MIZUTANI

Clean-soil, air, water, Vol.39, No.2, pp.128-135 (2011)

Removal of natural free estrogens and estrogen conjugates in a municipal wastewater treatment plant (WWTP) was investigated and analyzed by GC-MS, in which estrogen conjugates were first transformed to their corresponding free estrogens with an acid solvolysis procedure before their analysis. Natural free estrogens, E1-3-sulfate (E1-3S), and E3-3-sulfate (E3-3S) were detected with high concentrations in both the influent and effluent of the primary settling tank (PS), while no estrogen glucuronides were detected in any of the monitored wastewater samples. Regarding their removal efficiencies, all were almost completely removed, except for E1 with only a minor decrease. The estrogenic/androgenic removal of the same WWTP was also evaluated with estrogen receptor (androgen receptor) (ER (AR))-binding assays, in which the removal efficiencies for E2 equivalents (EEQ) or testosterone equivalents (TEQ) were 68.5 and 72.2%. In addition, the chemically calculated EEQ from natural estrogens were about 20.6–39.3% that of the ER-binding assay, in which E3 contributed the biggest proportion in both the influent and PS, while the calculated value of E1 increased from only 6.7% in the influent to as high as 20.6% in the effluent.

Recovery of Indium from Waste-LCD by Chemical Extraction Method

Satoshi MIZUTANI, Yoshinori KANJO and Hiroshi HASEGAWA(Kanazawa Univ.)

Proceedings of the 26th International Conference on Solid Waste Technology and Management held in Philadelphia, U.S.A., pp.1188-1193 (2011)

Indium is an important metal for our society. It is used for liquid crystal display (LCD) for portable computer, television, monitor etc. Although about 86 % of demand of the world is used in Japan, Japan imports almost all of the indium. Therefore indium recycling is very important. In this study, recovery of indium from waste-LCD by solvent extraction followed with solid phase extraction is studied. Old laptop computer was taken to pieces, and only glass board containing ITO (Indium Tin Oxide) in LCD is taken off. It is crushed and pulverized by planetary mill. Then the samples are extracted with some solvents. A variety concentration of hydrochloric acid and aqua regia are used as solvents. Higher liquid per solid ratio and higher concentration of acid raised the recovery rate of indium.

